

University of Nottingham
UK | CHINA | MALAYSIA

FILLING NANOTUBES FOR PHOTOCATALYSIS

Kate E. Walker, MSci

Thesis submitted to the University of Nottingham

for the degree of Doctor of Philosophy

September 2017

Abstract

The work presented in this thesis describes the preparation, characterisation and applications of novel classes of one-dimensional nanostructures comprising guest-species encapsulated within host-boron nitride and carbon nanotubes (BNNT and CNT respectively). A number of methods to open, shorten and purify the tubular host-nanostructures were evaluated in order to provide the most accessible route for guest-species into the internal volume of the nanotubes and maximise the filling yield. C_{60}-fullerene was inserted into BNNT from the gas-phase and found to exhibit unusual and diameter-dependent stacking arrangements and temperature-dependent dynamic behaviour inside nanotubes. Subsequent heating of this material resulted in the formation of a CNT inside BNNT – an important step toward realisation of the world's smallest co-axial cable, now affordable on a preparative scale. Both liquid- and gas-phase impregnation of CNT and BNNT with ionic cadmium precursors, followed by confined reactions with sulphur-containing compounds, lead to the templated formation of cadmium sulphide quantum dots inside nanotubes. These novel photocatalytic nanoreactors were applied for the degradation of methylene blue, exploring the effects of quantum dot location (inside *versus* outside nanotubes) and the type of nanotube (CNT *versus* BNNT) on the rates of reaction. No effect of spatial confinement inside nanotubes was observed, but BNNT were seen to outperform CNT, a feat that has been attributed to the transparency of BNNT to visible light. These results further demonstrate the outstanding ability of CNT and BNNT to act as nanoscale containers and reaction vessels for molecules, affording unique materials with potential applications in electronic and catalytic devices.

Publications

(1) Walker, K. E.; Rance, G. A.; Pekker, A.; Tóháti, H. M.; Fay, M. W.; Lodge, R. W.; Stoppiello, C. T.; Kamarás, K.; Khlobystov, A. N., Growth of Carbon Nanotubes inside Boron Nitride Nanotubes by Coalescence of Fullerenes: Toward the World's Smallest Coaxial Cable. *Small Methods*, 2017, **1**, 1700184.

(2) Chamberlain, T. W.; Biskupek, J.; Skowron, S. T.; Markevich, A. V.; Kurasch, S.; Reimer, O.; Walker, K. E.; Rance, G. A.; Feng, X. L.; Mullen, K.; Turchanin, A.; Lebedeva, M. A.; Majouga, A. G.; Nenajdenko, V. G.; Kaiser, U.; Besley, E.; Khlobystov, A. N., Stop-Frame Filming and Discovery of Reactions at the Single-Molecule Level by Transmission Electron Microscopy. *ACS Nano*, 2017**, 11**, 2509.

(3) Pekker, A.; Nemeth, G.; Botos, A.; Tohati, H. M.; Borondics, F.; Osvath, Z.; Biro, L. P.; Walker, K.; Khlobystov, A. N.; Kamaras, K., Cloaking by π-electrons in the infrared. *Phys. Status Solidi B*, 2016, **253**, 2457.

Acknowledgements

The journey through my PhD has taught me so much, both academically and personally. I could not have completed this without the help of so many people, of which there are too many to name them all, so I shall mention just a few.

The first person I wish to thank is my supervisor, Prof. Andrei Khlobystov. Throughout my PhD he has continued to provide an inspiring level of scientific knowledge, academic guidance and direction. He has demonstrated how to bring scientific results together in a clear and effective manner. His ever-present enthusiasm has motivated me throughout the most challenging weeks, for which I am extremely grateful.

For the unrivalled selfless donation of time and an admirable level of patience, dedication to providing help with experimental problems, writing, structuring and presenting work throughout the entirety of my PhD, I am incredibly thankful to Graham Rance. His attention to detail has taught me to work at a standard I could not have achieved alone. I can't thank him enough for the many hours he has spent helping with my work. I hope with time to display his level of organisation and dedication in my future endeavours.

The last 3.5 years would not have been the same if it wasn't for everybody in the nanocarbon group, both past and present, who have truly shaped the experience. Tom Chamberlain, Maria Lebedeva, Arron Solomonz, Scott Miners, Rachel Gover, Rob M^{c}Sweeney, Craig Stoppiello, Rhys Lodge, Mehtap Aygun, Bradley Thomas, Max Astle, Julie Watts, Kayleigh Fung, Rosella Mascia, Jack Jordan and all Masters, Erasmus and summer project students.

They have helped in almost every area of analysis, with Rhys Lodge and Craig Stoppiello responsible for the acquisition of many of the TEM images presented in this thesis; Scott Minors and Max Astle have continued to maintain and run the TGA; and all have given valuable help and advice.

The group have provided discussions on everything from the properties of nanotubes to political insight, cooking and climbing tips, to current affairs of the Royal family. I have thoroughly enjoyed working with these friends. From useful information and advice to quirky “traditions” and quotes. Without the “traditions” and entertainment that comes from working with these people my experience would not have been the same, I could not imagine doing a PhD with any other group. “Good.”

I am also very grateful to Mike Fay for his quest for perfect EFTEM images of nanotubes and the clearest EELS spectra and to Ben Pointer-Gleadhill for his time spent helping analyse my samples by ICP-OES.

My thanks must go to Katalin Kamarás, Áron Pekker and Hajnalka Tóháti, from the Hungarian Academy of Sciences, for their fantastic collaboration. Their ideas and analysis, which have helped aid my research, were invaluable.

I must express my gratitude to my family who have continually supported all of my ambitions in life, for their encouragement and support throughout. They are never too busy to give much needed advice and perspective, or provide a retreat to unwind, relax and be incredibly well fed.

The support from my boyfriend Sam has been truly priceless and has made the hardest part of thesis writing manageable. He has shared and celebrated the

successes to make them even better. Thanks for always knowing how to make me laugh (what do you mean, I can be grumpy?).

There are so many people around the department who have helped me throughout my PhD, but Charlotte Clark stands out for helping more than I could ask for, with the creation of gadgets, ideas and inventions to help with my reactions. Even though the chemistry didn't always go to plan, there was always a nifty way to solve any problem.

I could not complete my acknowledgements without mentioning Sue, a valued member of the department, for providing the well-needed cups of tea.

Acronyms

Acronym, abbreviation or symbol	Definition
@	[…] encapsulated within […]
/	[…] attached to the surface of […]
BN	Boron nitride
BNNT	Boron nitride nanotube(s)
BNNS	Boron nitride nanosheets
BT	Benzothiophene
c-BN	Cubic boron nitride
CNT	Carbon nanotube(s)
DBT	Dibenzothiophene
$DBTO_2$	Dibenzothiophene sulfone
4,6-DMDBT	4,6-Dimethyldibenzothiophene
D_{GNF}^{EXT}	Mean internal diameter of the graphitised nanofibre
DMSO	Dimethyl sulfoxide
D_{NT}^{INT}	Mean internal diameter of the nanotubes
D_{NT}^{EXT}	Mean external diameter of the nanotubes
D_{QD}	Mean diameter of the quantum dots
D_{vdW}	Van der Waals diameter
DWNT	Double-walled (carbon) nanotube(s)
EDX	Energy dispersive X-ray (spectroscopy)
E_g	Electronic band gap
GNF	Graphitised nanofiber(s)
h-BN	Hexagonal boron nitride
HPW	$H_3PW_{12}O_{40}$
ICP-OES	Inductively coupled plasma optical emission spectroscopy
I_D:I_G	Intensity ratio of the D and G bands in Raman spectroscopy
L_{NT}	Length of the nanotubes
L_{CNT}	Length of the carbon nanotubes
MB	Methylene blue

MO	Methylene orange
MP-11	Microperoxidase-11
MWNT	Multi-walled (carbon) nanotube(s)
NP	Nanoparticle(s)
NT	Nanotube(s)
ODS	Oxidative desulfurisation
ORR	Oxygen reduction reaction(s)
PDA	Polydopamine
PmPV	poly(m-phenylenevinylene-co-2,5-dioctoxy-p-phenylenevinylene)
PXRD	Powder X-ray diffraction
QD	Quantum dot(s)
Q_e	Equilibrium adsorption
r-BN	Rhombohedral boron nitride
rGO	Reduced graphene oxide
RhB	Rhodamine blue
STEM	Scanning transmission electron microscopy
SWNT	Single-walled (carbon) nanotube(s)
TEM	Transmission electron microscopy
TGA	Thermogravimetric analysis
TGA-MS	Thermogravimetric analysis-mass spectrometry
UV-vis	Ultraviolet-visible spectroscopy
w-BN	Wurtzite boron nitride
wt.%	Weight percent

Contents

Abstract **2**

Publications **3**

Acknowledgements **4**

Acronyms **7**

1. Boron Nitride Allotropes as Catalyst Supports **13**

1.1 Nanoscale allotropes of carbon and boron nitride *19*

1.2 Applications of carbon and boron nitride nanomaterials *23*

1.3 Boron nitride as a nanoparticle supports *24*

1.3.1 Reduction reactions 30

1.3.2 Oxidation reactions 35

1.3.3 Simultaneous oxidation and reduction reactions 47

1.3.4 Cross-coupling reactions 53

1.4 Scope for further investigation *55*

1.5 References *57*

2. Opening and Purification of BNNT **64**

2.1 Introduction *64*

2.2 Aim and Objectives *68*

2.3 Results and Discussion *69*

2.3.1 Analysis of as-received BNNT 69

2.3.2 Opening and purifying BNNT 73

2.3.2.1 Method 1: Oxidation in air 73

2.3.4.2 Method 2: Ball milling 76

2.3.4.3 Method 3: Hydrolysis followed by oxidation in air 78

2.3.4.4 Comparison of opening methods 80

2.3 Conclusions 81

2.4 Experimental 82

2.4.1 Opening and purifying BNNT 83

2.4.1.1 Method 1- Oxidation in air 83

2.4.1.2 Method 2- Ball milling 83

2.4.1.3 Method 3- Hydrolysis followed by oxidation in air 83

2.5 References 84

3. Growth of Carbon Nanotubes inside Boron Nitride Nanotubes by Coalescence of Fullerenes: Towards the World's Smallest Co-axial Cable 86

3.1 Introduction 86

3.2 Aim and Objectives 87

3.3 Results and Discussion 89

3.3.1 Encapsulation of C_{60} into BNNT 89

3.3.2 Forming CNT@BNNT 100

3.3 Conclusions 108

3.4 Experimental 109

3.4.1 Filling BNNT 110

3.4.2 Formation of CNT@BNNT 110

3.4.2.1 Method 1 110

3.4.1.2 Method 2: Increased reaction temperature 110

3.4.1.3 Method 3: Increased reaction time 110

3.4.1.4 Method 4: Repeated filling 111

3.5 References 111

4. Synthesis of Photoactive Nanoparticles inside Nanotubes 114

4.1 Introduction 114

4.2.1 Formation of QD/CNT hybrid materials 117

4.2.2 Scope for further investigation 122

4.2 Aim and Objectives 125

4.3 Results and Discussion 127

4.3.1 The effect of oxidation of nanotubes 127

4.3.2 The effect of nanotube's diameter and internal structure 149

4.3.3 Effect of the container and filling mechanism 154

4.4 Conclusions 167

4.5 Experimental 168

4.5.1 Analysis of 0 h-treated MWNT 171

4.5.2 Oxidation of MWNT 171

4.5.3 CdS/MWNT formation 171

4.5.4 CdS/ 0 h-treated MWNT 172

4.5.5 CdS/1 h-treated MWNT 172

4.5.6 CdS/16 h-treated MWNT 172

4.5.7 CdS/96 h-treated MWNT 173

4.5.8 CdS/SWNT formation 173

4.5.9 CdS/GNF formation 173

4.5.10 CdS@BNNT (solution route) 173

4.5.11 CdS@BNNT (sublimation route) 174

4.6 References 175

5. Photocatalytic Activity of CdS Quantum Dots Attached to Nanotubes 179

5.1 Introduction 179

5.2 Aim and Objectives 184

5.3 Results and discussion 187

5.3.1 Development of probe reaction 191

5.3.2 Method 1: 197

5.3.3 Method 2: 204

5.4 Conclusions 210

5.5 Experimental 212

5.5.1 CdS/MWNT 214

5.5.2 Methylene blue (MB) 214

5.5.3 Calibration curves 215

5.5.4 Adsorption tests 215

5.5.5 Method 1 215

5.5.6 Method 2 216

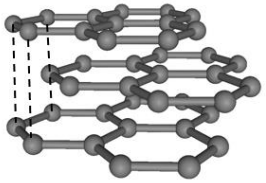
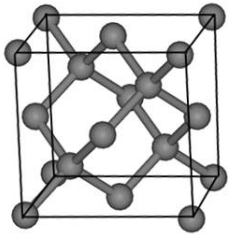
5.6 References 217

6. Concluding Remarks 219

1. Boron Nitride Allotropes as Catalyst Supports

Carbon allotropes are heavily integrated into our everyday lives; the graphite in pencils can be found in every desk and school pencil case, whilst diamond is globally admired for its beauty and made into jewellery. Whilst these materials are both formed of carbon, it is the structural changes at the atomic scale that result in their markedly different properties (Table 1). In graphite, sp^2 hybridised carbon atoms form three bonds with their nearest neighbour within hexagonal sheets, with weak interactions between these sheets, thus allowing the removal of these layers onto a leaf of paper, leaving a pencil mark. Diamond is formed of sp^3 hybridised carbon atoms, with each atom bonded to four others, forming tetrahedral structures in the extended crystal.

Table 1. Structure and properties of carbon allotropes.

Name	Structure	Appearance	Electronic conductivity	Hybridisation	Vickers Hardness /GPa	Density /g cm^{-3}
Graphite		Opaque, metallic lustre [2] 	Conductor	sp^2	*3.9-9.8[1]	2.26[1]
Diamond		Transparent [3] 	Insulator	sp^3	60-100[1]	3.52[1]

*Molded graphite

Yet, much of the general public is unaware that the younger, synthetic analogues of these carbon allotropes even exists. Boron nitride (BN) consists of a 1:1 ratio of boron and nitrogen, is isoelectronic with carbon and can be produced in a variety of allotropes, each possessing their own unique and remarkable properties. These include hexagonal (*h*-BN), rhombohedral (*r*-BN), cubic (*c*-BN) and wurtzite (*w*-BN),[4] some of which share morphologies and configurations analogous to carbon. For example, *h*-BN is related to graphite, forming sheets which can easily slide over each other, whereas *c*-BN is similar to diamond.

BN sheets consist of alternate boron and nitrogen atoms which form hexagons with localised π bonding, a consequence of donation of a lone pair of electrons from the full p_z orbital on nitrogen into the empty p_z orbital on boron (Figure 1).

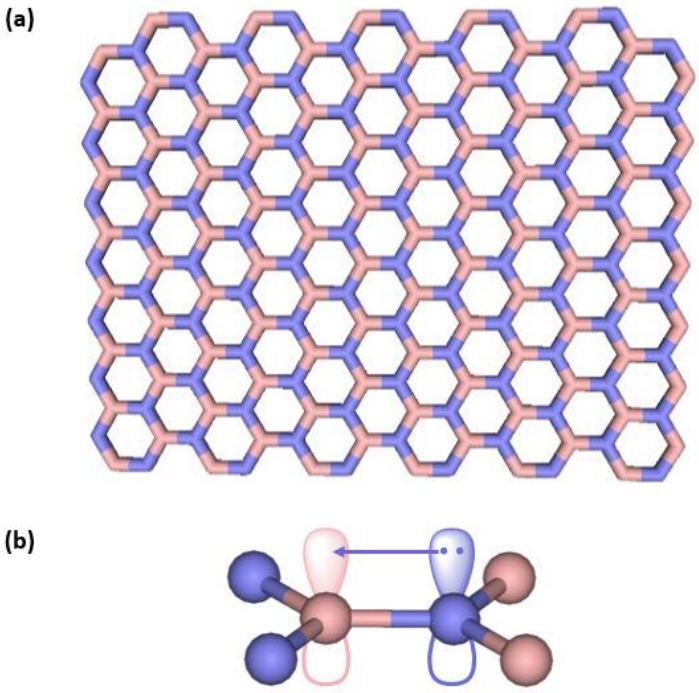


Figure 1. The structure (a) and bonding (b) of boron nitride sheets.

Sheets of boron nitride have been synthesised in layered arrangements, stacking as either *h*-BN or *r*-BN (Figure 2). Both are sp^2-bonded, but with a different layering structure: *h*-BN is the most common and stacks in AA'AA' repeating layers with alternating B and N atoms along the c axis, whereas the rarer *r*-BN is layered in an ABCABC arrangement.[5] Analogous to the better known graphite, *h*-BN is sometimes referred to as "white graphite", a reference to the material's complete transparency to visible light.

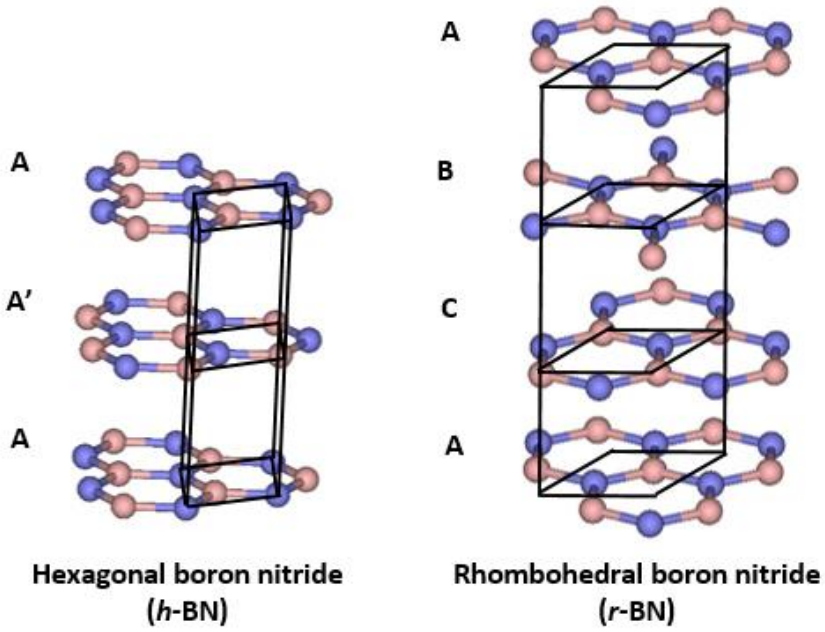


Figure 2. Stacking arrangements of hexagonal and rhombohedral boron nitride.

The π-bonding in BN sheets is much more localised than in graphite, yielding partially ionic characteristics. This minor structural difference between graphite and boron nitride sheets results in contrasting electronic properties. While graphite is metallic (resistivity between 5-15 μΩ·m at room temperature),[6] the reduced electron mean free path in BN sheets renders the material a wide band gap semiconductor (band gap *ca*. 5.5 eV) and thus exhibits insulating behaviour.[7]

The strong B-N bonds (4 eV),[8] comparable to C-C bonds in graphite (3.7 eV),[8] result in very high thermal and chemical stability.[4] Yet, weak (primarily van der Waals)[9] forces between the sheets means the layers are able to slide over each other. Moreover, the interaction within *h*-BN and graphite are similar,[10] resulting in almost identical interlayer distances (*h*-BN = 3.30-3.33 Å,[11-14] graphite = 3.33-3.35 Å).[15-17] This characteristic renders them useful as lubricants and in cosmetic preparations.[7]

Layered structures of BN under high pressure and temperature can transform into polymorphs with more densely packed sp^3-bonding structures, such as *c*-BN and *w*-BN (Figure 3).[5] The cubic structure is more common than the wurtzite crystal, and is appealing to materials scientists as it is an extremely hard material (second only to diamond), with chemical and thermal stability superior to diamond.[4] Consequently, *c*-BN has applications as an abrasive.[4] Wurtzite is a rare, metastable form of BN with astonishing hardness, calculated to be harder than diamond.[18] Unfortunately, large single crystals cannot yet be synthesised at present to test this experimentally. If this material can be prepared, it has applications in cutting, grinding, abrasion or polishing tools as this superabrasive material sharpens itself during cutting.

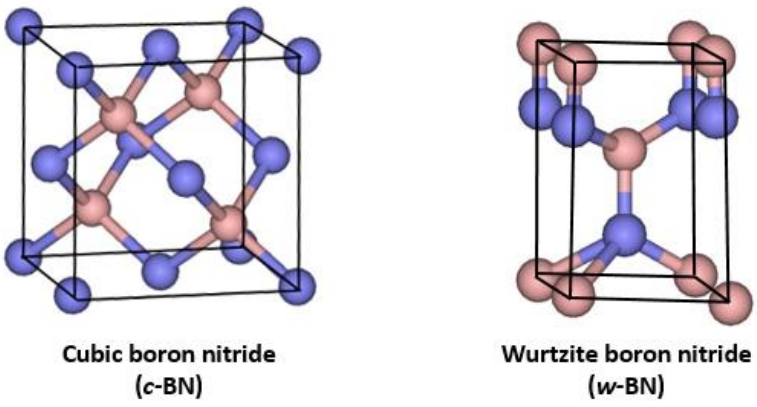
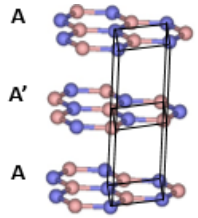
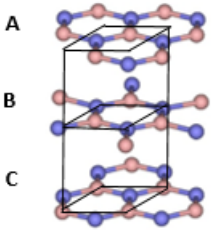
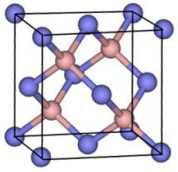
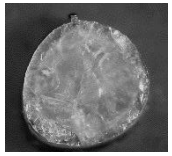
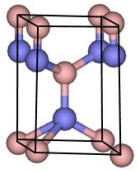


Figure 3. Structures of cubic and wurtzite boron nitride.

Table 2. Structure and properties of boron allotropes.

Name	Structure	Appearance	Electronic conductivity	Hybridisation	Vickers Hardness /GPa	Density /g cm^{-1}
(*h*-BN)		Transparent [25] 	Insulating (wide bandgap semiconductor)	sp^2	24.6*[22]	2.2[19]
(*r*-BN)		Transparent	Insulating (wide bandgap semiconductor)	sp^2	Unavailable	2.25[20]
(*c*-BN)		Transparent** [26] 	Insulating (wide bandgap semiconductor)	sp^3	42.7*[22]	3.45-3.48[21]
(*w*-BN)		Transparent	Insulating (wide bandgap semiconductor)	sp^3	40.7*[22]	3.49[21]

*Theoretical results, no experimental values reported.

** Often coloured due to excess impurities from the catalyst or excess boron or nitrogen.[23, 24]

1.1 Nanoscale allotropes of carbon and boron nitride

The atomic-scale configuration of the allotropes of carbon and boron nitride have a significant impact on the macroscale properties of the bulk materials. However, many more allotropes can be produced on the nanoscale, with their own distinct and interesting properties. For instance, a single sheet of graphite, called graphene, is truly two-dimensional (only a single atom thick) and possesses unique electrical properties, such as very high electron mobility, up to 200 000 cm^{-2} V^{-1} s^{-1} at room temperature,[27, 28] which is ten times higher than the best semiconducting materials.[29]

Conceptually, if a sheet of graphene is rolled up to form a cylinder, the structure forms a one-dimensional carbon nanotube (CNT). Depending on the orientation of the sheet rolling, CNT can therefore form a variety of chiralities (arm-chair, zig-zag or chiral), determined by the circumferential vector C (in terms of unit cell vectors a_1 and a_2 and structural indices (*n*,*m*) (Figure 4), with the properties of the resultant CNT dependent on its chirality. For instance, if *m*-*n* = 3k (where *m* and *n* are structural indices and k is any integer including zero) the CNT is metallic, whereas if *m*-*n* ≠ 3k the nanotube is a semiconductor.[30]

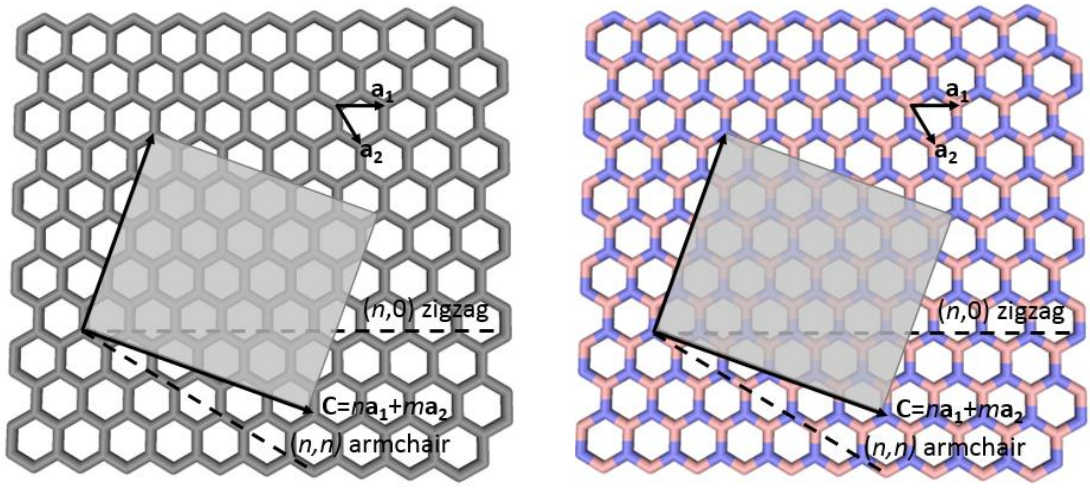
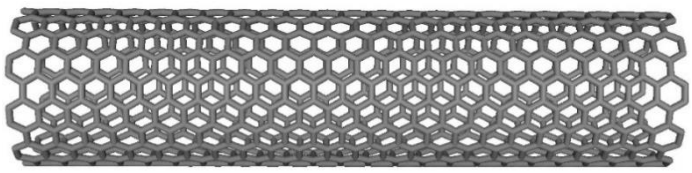


Figure 4. The chirality of the nanotubes is determined as circumferential vector C, in terms of unit cell vectors a_1 and a_2 and structural indices (*n,m*).

While graphene commonly refers to a single layer of graphite, the BN equivalent is often produced as few-layered sheets, referred to in the literature as graphene-like BN, few layered *h*-BN, white graphene or boron nitride nanosheets (BNNS). For consistency this material will be referred to as BNNS hereafter.

Like with CNT, a single sheet of *h*-BN can be conceptually rolled up to form a boron nitride nanotube (BNNT) (Figure 5) with arm-chair, zig-zag and chiral structures possible, analogous to CNT.[31] In this case, however, the properties are independent of the chirality of the nanotube.



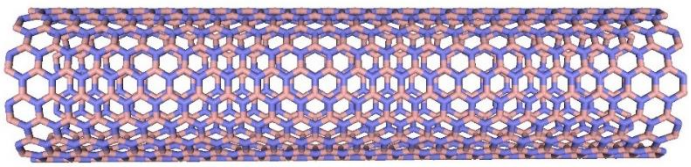
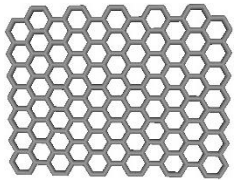
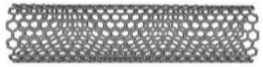
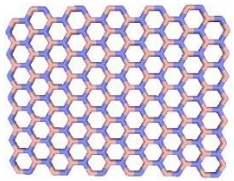


Figure 5. Structure of an armchair carbon nanotube (CNT) and boron nitride nanotubes (BNNT).

In contrast to CNT, pure BNNT are white and completely transparent to visible light. BNNT have a band gap of *ca*. 5.5 eV (independent of their chirality) so are electronically insulating. The thermal properties are also drastically different to CNT, with BNNT being stable to around 950 °C in air,[32] whilst CNT oxidise in the range of 450-500 °C in air (depending primarily on the nanotube's diameter).[32] Both materials have a very high mechanical tensile strength and are chemically inert under common reaction conditions.[7] A summary of the nanostructured forms of carbon and boron nitride and their properties is presented in Table 3.

Table 3. Structure and properties of allotropes of nanostructured carbon and boron nitride, including hybridisation, electronic conductivity, thermal stability, thermal conductivity and Young's modulus.

Composition	Name	Structure	Electronic conductivity	Hybridisation	Thermal stability in air/ °C	Thermal conductivity/ W $m^{-1}K^{-1}$	Young's modulus/ TPa
Carbon	Graphene		Semimetal	sp^2	650-750[44-46]	2000-4000[39-41]	1[33]
Carbon	CNT		Metallic or semiconductor, depending on chirality	sp^2	450-500[32]	300 to >3000[42]	0.27~0.95[34] 0.4-4.15[35]
Boron nitride	BNNS		Insulating (wide band gap semiconductor)	sp^2	700-850[47]	360 (11-layers)[11] 227-280 (9-layers)[43]	0.99 TPa*[36]
Boron nitride	BNNT		Insulating (wide band gap semiconductor) independent of chirality	sp^2	950[32]	*ca*. 180-300[42] **	1.8 ± 0.3[37] 0.81-1.3[38]

*Theoretical result.

**Theoretically predicted to be higher than CNT.[48]

While there are many theoretical studies that appraise the properties and potential applications of BNNT,[49-56] there are significantly fewer experimental studies reported. Techniques which produce BNNT on a large enough scale for use in standard laboratory experiments have not been developed until recently;[57] consequently, BNNT are often produced with a high impurity content, variable diameters and number of walls, all of which are expected to impact the properties of any material based on them.

The first fabrication of BNNT involved arc-discharge between a BN powder-packed hollow tungsten anode and a copper electrode.[58] Various methods have been developed since then, such as: (i) ball milling crystalline boron in a nitrogen atmosphere, followed by heat treatment with NH_3;[59] (ii) LASER ablation,[60] in which a CO_2 LASER is used to obtain multi-walled BNNT from a single crystal of cubic boron nitride, or (iii) chemical vapour deposition (CVD),[61] using the precursor borazine ($B_3N_3H_6$), to form multi-walled BNNT in dense thickets on and in the vicinity of nickel boride catalyst particles at *ca*. 1100 °C.

1.2 Applications of carbon and boron nitride nanomaterials

The applications of carbon nanostructures have been extensively studied and reviewed.[62-64] Graphene and CNT have found uses as field effect transistors,[65-68] sensors,[66-69] transparent conductive films[70, 71] and catalytic supports.[72-74] Many applications of BN are still at their infancy stage, though recent research efforts include drug delivery,[75] hydrogen storage,[76-78] ceramic composites[79] and polymeric composites for electron insulation and packaging.[80]

One of the most widely reported applications of the nanoscale allotropes of carbon are as supports of heterogeneous catalysts.[72-74] Metal nanoparticles are extensively utilised in important chemical transformations as catalysts, aided by their remarkably high surface area and energy leading to high levels of catalytic activity. Yet, the catalytic properties can be further improved upon when supported onto a nanoscale support material, often reducing aggregation, promoting dispersion and thus prolonging the lifetime of the catalyst. Moreover, the composite material can be readily separated from a given reaction mixture often by simple filtration, enhancing recyclability.

Like graphene and CNT, which have been studied in depth as catalytic supports, BN as both nanosheets and nanotubes have several properties in common which are favourable for this application. Namely, good chemical and thermal stability, allowing exposure to a range of reaction conditions. Furthermore, both have an exceptionally high surface area per unit of mass, which is vital for high catalytic activity in the composite material since heterogeneous catalysis occurs at the surface of the catalyst.

1.3 Boron nitride as a nanoparticle supports

Whilst bulk BN catalysts and supports,[81-85] doped BN structures,[86-89] graphene with BN domains,[90] or boron carbon nitride[91, 92] have been shown to exhibit their own catalytic properties, composites of nanoscale BN structures and catalytic nanoparticles are receiving increasing attention from the research community, owing to their ability to readily tailor their specific applications by careful consideration of

the materials used. Consequently, it is predominantly these materials that will be discussed hereafter.

The current range of BN based nanocatalysts, are summarised in the Table 4.

Table 4. Summary of BN-supported catalysts for a variety of reactions, including parameters such as the diameter of both the BN and the nanoparticle (d_{NP}), and the main reported result.

Reaction class	Catalyst	d_{NP}/ nm	Support	BN dimensions	Result	Ref.
Hydrogenation	Pd	4-9	BNNS	3-20 layer sheets, (3-7 nm) Lateral size (4.7 nm)	99% yield and recycled 14 times, shows superiority to commercial Pd/C and Pd/*h*-BN.	[93]
Electrocatalytic reduction of water	Au	*ca*. 30	BNNS	Single to a few layers	Overpotential lowered by *ca*. 320 mV compared to a bare Au electrode.	[94]
Photocatalytic hydrogen production	CdS, CdS/Pt	50	BNNS	Unspecified	BNNS exhibits semiconducting properties due to vacancies and defects. Hydrogen production for Pt/CdS/BNNS was far higher than for CdS/BNNS or CdS alone.	[95]
Reduction of 4-nitrophenol	Ag (tannic acid- ferric ion modified)	*ca*.7	BNNS	Few layers (*ca*. 3 nm)	Faster rate of reaction than graphene/ reduced graphene oxide supported catalysts reported. [100-102]	[96]
Reduction of 4-nitrophenol	Au	8.2 ± 3.7	Polydop-amine (PDA) grafted BNNS	*ca*. 2-2.5 nm (thick) x 240 ± 140 nm (lateral)	PDA-coated Au/BNNS have a higher rate constant (0.005 min^{-1}) than PDA-coated Au (0.004 min^{-1})	[97]
Methanation	Ni	*ca*.9	BN shell	8-12 nm, few layer shell	90.8% conversion for composite, compares to 79.2% without the BN shell.	[98]
Hydrolysis of ammonia borane	Cu	*ca*. 100	BNNS	Unspecified	Lower activation energy for the hydrolysis reaction. Increase in hydrogen generation of Cu/BNNS compared to Cu alone.	[99]

Table 4. ***(continued)***

Reaction class	Catalyst	d_{NP}/ nm	Support	BN dimensions	Result	Ref.
Hydrolysis of ammonia borane	Ni	*ca*. 2-5	BN spheres, sheets	*ca*. 200 nm (spheres), unspecified (sheets)	79.6% conversion for Ni/BN compared to 70.4% conversion for Ni alone.	103
Hydrolysis of ammonia borane	Ni	20-30	BNNS	*ca*. 200 nm thick, *ca*. 30-60 nm	Low activation energy, good recyclability over 5 cycles.	104
Hydrolysis of ammonia borane	CoNi	*ca*. 17	BN shell	10-20 layers	Low activation energy, good recyclability over 5 cycles.	105
Oxidative desulfurisation	WO_x	4.4-5.1	BNNS	Composite < 4 nm thick	99.2% of sulfur is removed and the catalyst could be recycled 5 times, while the removal of sulfur remained above 85%, an improvement upon WO_x alone.	106
Oxidative desulfurisation	$H_3PW_{12}O_{40}$	*ca*. 4-5	BNNS	Few layers	100% sulfur removal achieved, recycled 6 times without noticeable activity decrease.	107
Oxidative desulfurisation	Cu	1	BNNS	Unspecified	Catalytic activity of >97% and can be recycled 10 times with little decrease. Does not require the explosive H_2O_2.	108
Oxidation of lactose	Pd	2-30	*h*-BN	Unspecified	Pd/*h*-BN reached a selectivity of 100% and yield between 14-64%, (depending on catalyst preparation conditions) while Pd/α-Al_2O_3 had less than 100% selectivity, with yield between 8-38%.	109
Oxidation of alcohol	Au	1-8	*h*-BN nano-crystals	Polyhedral, *ca*. 130 nm, layered *h*-BN	Superior conversion (*ca*. 30%) and selectivity (*ca*. 98%) for the oxidation of benzyl alcohol to benzaldehyde compared to unsupported nanoporous gold (conversion 23%, selectivity 98%).	110

Table 4. ***(continued)***

Reaction class	Catalyst	d_{NP}/ nm	Support	BN dimensions	Result	Ref.
Oxidation of CO	Pt	*ca*. 2.5	*h*-BN shell	*ca*. 2.5 nm spherical *h*-BN	100% conversion at 94 °C, whereas Pt NP on C reaches 100% conversion at *ca*. 120 °C	[111]
Oxidation of CO	Pt	5 ± 0.5	BNNS	Few layers	Pt becomes more favourable to O_2 adsorption, alleviating CO poisoning.	[112]
Oxidation of ethanol	Au-Cu	*ca*. 3	*h*-BN sphere	*ca*. 150 nm BN-spheres	92% aldehyde selectivity, whereas SiO_2 supported analogue has 61% selectivity.	[113]
Oxidation of hydrogen	Ni	10-15	*h*-BN shell	*ca*. 8-38	Calculations indicate that the activity of Ni is improved due to the addition of the *h*-BN shell.	[114]
Methane reformation	Ni	3-5	*h*-BN cage	Unspecified	Sintering resistance and maintained activity after 100 hours.	[115]
Enzyme catalysed substrate oxidation	Microper-oxidase-11 (MP-11)/		BNNT	*ca*. 50	Increased rate of substrate oxidation by MP-11 when deposited on BNNT (Au acts purely as a probe)	[116]
Photocatalytic dye degradation	AgI	18-24	BNNS	45-50 nm thickness	Superior photocatalytic activity and improved aqueous stability compared to AgI only. AgI/BNNS electron transfer increases activity.	[117]
Photocatalytic dye degradation	AgI/AgBr	200	BNNS	Few layer	97.4% Rhodamine B and 95% methylene orange degraded in 6 minutes, respectively.	[118]
Photocatalytic dye degradation	Ag_2CrO_4	20	BNNS	Few layers	96.7% Rhodium B degraded in 120 minutes, compared to 75% for Ag_2CrO_4. BNNS decreased the band gap of Ag_2CrO_4.	[119]
Photocatalytic degradation of enrofloxacin	$BiPO_4$	*ca*. 30	BNNS	Few layers	91.5% degradation of antibiotic enrofloxacin in 2 hours, compared to 74.5% degradation by $BiPO_4$ alone.	[120]

Table 4. ***(continued)***

Reaction class	Catalyst	d_{NP}/ nm	Support	BN dimensions	Result	Ref.
Photocatalytic dye degradation	Ag_3PO_4	80-400	BNNS	Few layers	Rate of dye degradation catalysed by BNNS/Ag_3PO_4 is 0.28 min^{-1}, compared to 0.08 min^{-1} for pure Ag_3PO_4.	121
Photocatalytic dye degradation	Ag_3PO_4	*ca*. 200	BNNS	Unspecified	Near complete dye degradation for Ag_3PO_4/BNNS compared to 87.5% dye degradation for Ag_3PO_4.	122
Photocatalytic dye degradation	WO_3	*ca*. 100	BNNS	Few layers	Rate constant for dye degradation increases from 0.22 to 0.63 k h^{-1} for WO_3 alone and WO_3/BNNS repectively.	123
Dye degradation	Au	7-22	BNNS	2.55 nm thick	Kinetic rate constant for dye degradation is much higher for Au/BNNS (0.5206 min^{-1}) than Au (0.0052 min^{-1}) and BNNS (0.0636 min^{-1}).	124
Suzuki-Miyaura coupling	Pd core in Fe shell	1.6	BNNS	Unspecified	Many reactions with high yield, matching or superior to many state of the art Suzuki-Miyaura coupling reaction under milder conditions/ shorter reaction times.	125
3-Component coupling reaction	CuO, Cu(O) or CuS	*ca*.9, 14,>190	BNNS	Few layer	Reduced graphene oxide (rGO) outperformed BNNS as support catalyst (CuO/rGO = 95% yield, CuO/BNNS = 92% yield)	126
Thermal decomposition of ammonium perchlorate	CuO	60-80	BNNS	*ca*. 1.7 nm thick, >200 nm lateral	Decomposition temperature of ammonium perchlorate decreased by around 50 °C.	127

1.3.1 Reduction reactions

Hydrogenation reactions

Palladium is a common catalyst for hydrogenation reactions,[128-130] as hydrogen forms surface hydrides (Pd-H) which can be transferred to chemisorbed substrates (e.g. nitro-containing molecules or alkenes), thus increasing the rate and efficiency of hydrogenation. In the study of Sun *et al*.[93] Pd nanoparticles (4-9 nm) were deposited onto BNNS (3-20 layers) and the application of this composite material in the hydrogenation of nitroaromatics explored (Figure 6). BNNS were chosen as they provide a high surface area to immobilise NP and were produced through the exfoliation of bulk *h*-BN in thionyl sulfide, resulting in *ca*. 1 wt.% of functional groups (NH, OH, Cl) on the BNNS at defect sites. It is these defect sites that the metal-BN interactions are theoretically predicted to interact,[131-133] resulting in the high and even coverage of NP on the BNNS.

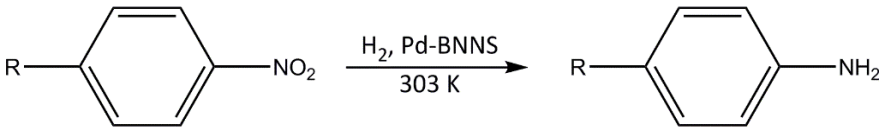


Figure 6. Hydrogenation of nitroaromatics with Pd-BNNS.

The yield of aminoaromatics is >99% for R=Me, $COCH_3$, OH, OCH_3, and 94.3% when R=Cl, within 4 hours (Figure 7) at 4.5 wt.% Pd loading. For the hydrogenation of nitrobenzene, the catalyst was recycled 14 times, with each run completed in the same duration. A parallel reaction was performed using palladium deposited onto bulk *h*-BN (Pd-*h*-BN); however, the catalytic activity was much lower and decreased

upon subsequent cycles. The author attributes these result to the aggregation of Pd when deposited on bulk *h*-BN, rather than nanosheets, due to the lack of functional groups on bulk *h*-BN which anchor Pd in place. However, the small increase in size from 6.6 nm to 8.0 nm for Pd-*h*-BN (calculated from X-ray diffraction using the Debye-Scherrer equation) suggests NP growth through Ostwald ripening, rather than aggregation, decreases the surface area and thus the observed activity of the catalyst.

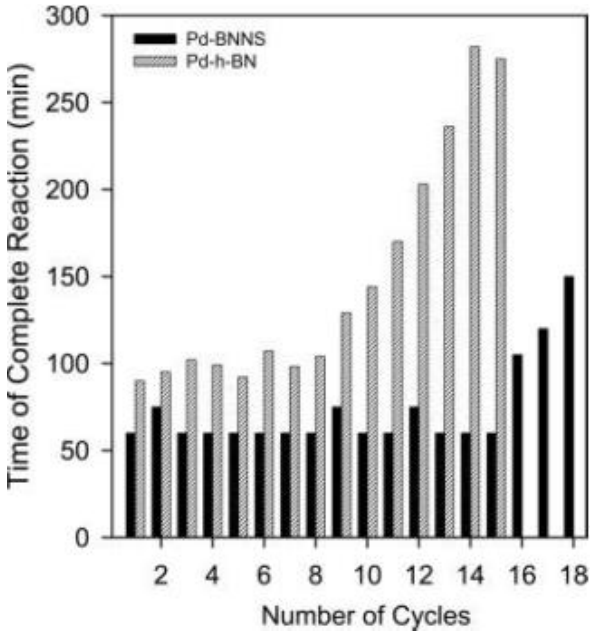


Figure 7. Recyclability of Pd-BNNS and Pd-*h*-BN catalysis for the hydrogenation of nitrobenzene.[93]

BNNS are an effective support for stabilising Pd NP over 15 reaction cycles, thus allowing Pd to remain highly active and well dispersed for effective catalysis. The authors conclude that Pd on BNNS is superior to commercial catalysts (Pd on C); however, no experimental evidence is provided.

Oxygen reduction reactions

Another use for NP on BN is elegantly demonstrated with gold nanoparticles deposited onto BNNS, used to reduce the overpotential of oxygen reduction reactions (ORR) at a gold electrode, a critical barrier to overcome in the production of fuel cells.[134-136] BNNS alone, deposited on gold electrodes lowers the overpotential by 270 mV; however, through increasing Au-BN interactions by depositing Au NP on BNNS this overpotential can be lowered by a further *ca*. 50 mV.[94] It also creates a 4-electron reduction route to water formation (Figure 8). The fraction of water formed is over 50%, compared to a bare Au electrode, or BNNS on a bare Au electrode of 0% and 20% respectively.

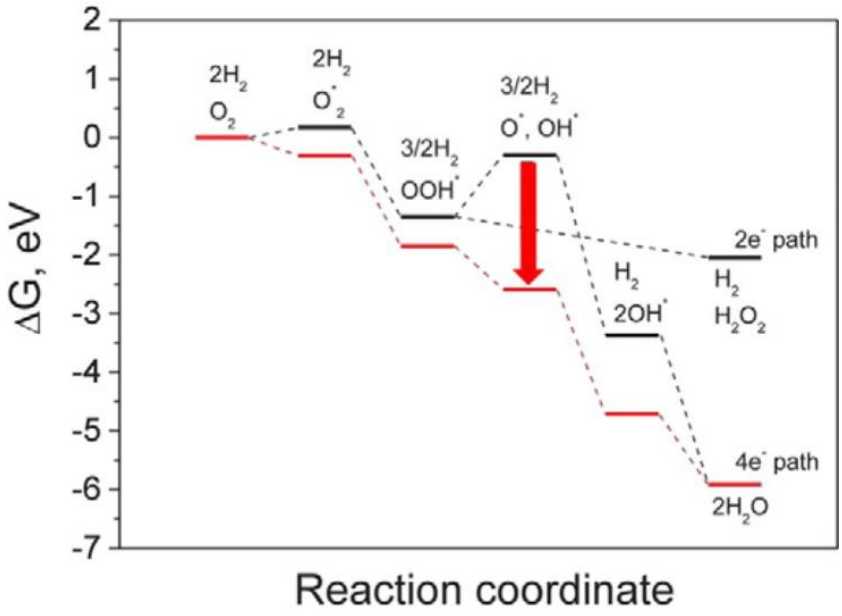


Figure 8. Free energy diagram for ORR at BN monolayer/ Au(111) (black) and Au_8-BN monolayer/ Au(111) (red) electrodes.[94]

Photocatalytic hydrogen production

CdS is effective for capturing visible light and harnessing the photogenerated excitons (electron-hole pairs) to split water.[137-139] However, when grown on BNNS,

photocatalytic performance is improved. Ma *et al*. utilised these properties to fabricate CdS on BNNS for photocatalytic hydrogen production,[95] with the composite providing a higher catalytic surface area, due to many adsorption sites and photocatalytic reaction centres. Moreover, it is reported that the band gap of BNNS can be significantly decreased due to B- or N- vacancies and impurities, leading to semiconducting properties (Table 5).[140,141]

Table 5. Calculated band gap energy for *h*-BN, BN with a nitrogen antisite (B_N), BN with a boron antisite (N_B), carbon substitution in a boron site (C_B), carbon substitution in a nitrogen site (C_N), a boron vacancy (V_B) and a nitrogen vacancy (V_N).[141]

Layer type	$E_{band\ gap}$ (eV)
h-BN	4.75
B_N	1.65
N_B	3.18
C_B	0.90
C_N	3.80
V_B	4.40
V_N	1.68

Under photoirradiation, the number of photogenerated electrons increases as a result of CdS coupling with BNNS. Photoelectrons are produced by both CdS and the imperfections and edges of BNNS, and it is thought that electronic communication between CdS and BNNS occurs. Holes are removed by sacrificial agents, such as Na_2S and Na_2SO_3 and electrons are said to be transferred to the surface of CdS (Figure 9), which in turn enhances the photocatalytic activity. Therefore, BNNS function, not only as a support for CdS, but as an active catalyst itself.

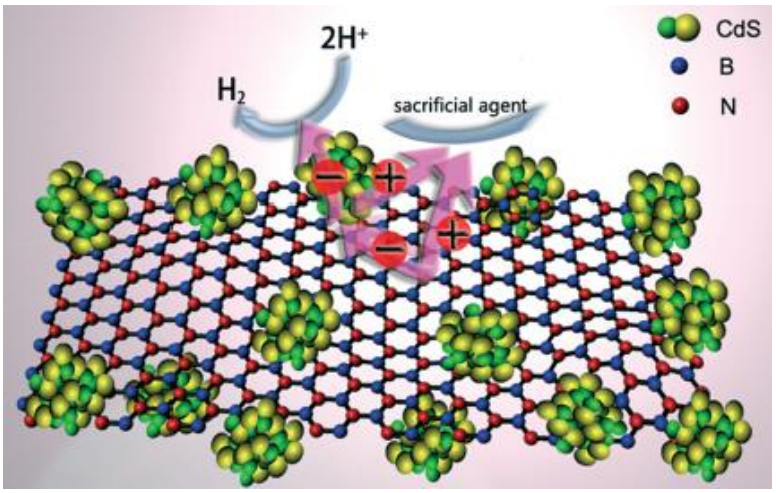


Figure 9. Schematic of the charge separation and transfer in CdS/BNNS.[95]

The amount of hydrogen evolved was significantly higher when Pt was also loaded onto the composite (Pt/CdS/BNNS), attributed to the improved electrical conduction performance. The rate of hydrogen production for this material (5.96 mmol h^{-1} g^{-1}) was significantly higher than CdS nanoparticles alone (0.188 mmol h^{-1} g^{-1}) or CdS/Pt (0.439 mmol h^{-1} g^{-1}) (Figure 10).

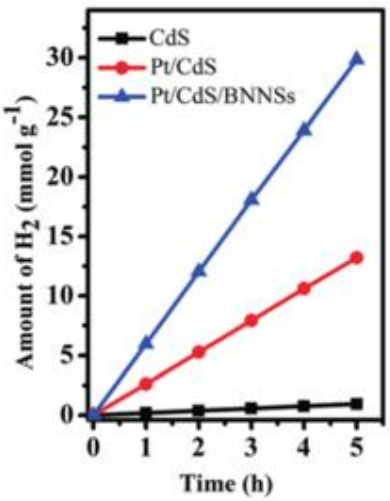


Figure 10. The amount of H_2 evolution of CdS, Pt/CdS and Pt/CdS/BNNS.[95]

Other examples of reduction reactions facilitated by nanoparticles on nanoscale BN supports include the reduction of 4-nitrophenol by both Ag NP on

BNNS[96] and Au NP on Polydopamine (PDA) grafted BNNS,[97] and the hydrogenation of methane catalysed by Ni NP encapsulated within a BN shell.[98] In each of these cases the catalytic activity was enhanced by the addition of a BN support/ shell.

1.3.2 Oxidation reactions

Oxidative desulfurisation

A high percentage of BN supported catalysts target desulfurisation reactions - an important process used to lower the sulfur content in petrol. Tungsten oxide (WO_x) can be used alone as this type of catalyst,[142] but the activity can be markedly improved upon through its deposition onto BN sheets.[106]

Unusually for NP deposited onto BN supports, Wu and coworkers form WO_x NP which are threaded through the *h*-BN plane, rather than deposited onto its surface though an *in situ* synthesis method, in order to improve the dispersion and stability of the NP (Figure 11).

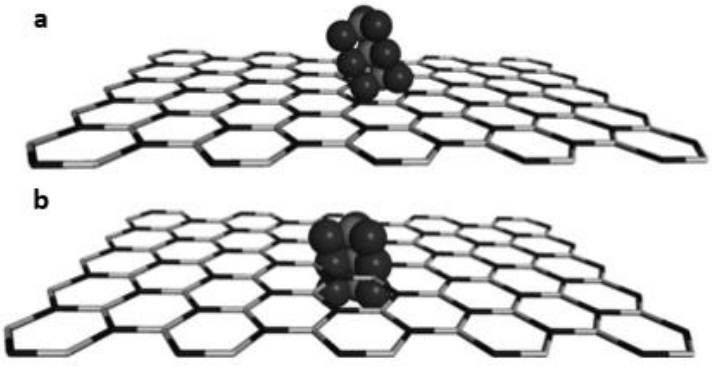


Figure 11. Design of BN sheets with (a) WO_x traditionally supported and (b) WO_x confined.[106]

As the space within a single hexagonal BN ring would not provide enough space for WO_x NP to sit, it is assumed that the displacement of B or N atoms must

occur. However, this is not explicitly specified within the study and it is hard to be sure that the nanoparticles are not simply deposited onto the surface of BNNS.

In the presence of the catalyst and hydrogen peroxide, dibenzothiophene (DBT) is oxidised to yield dibenzothiophene sulfone ($DBTO_2$), thought to be driven by the mechanism shown in Figure 12.

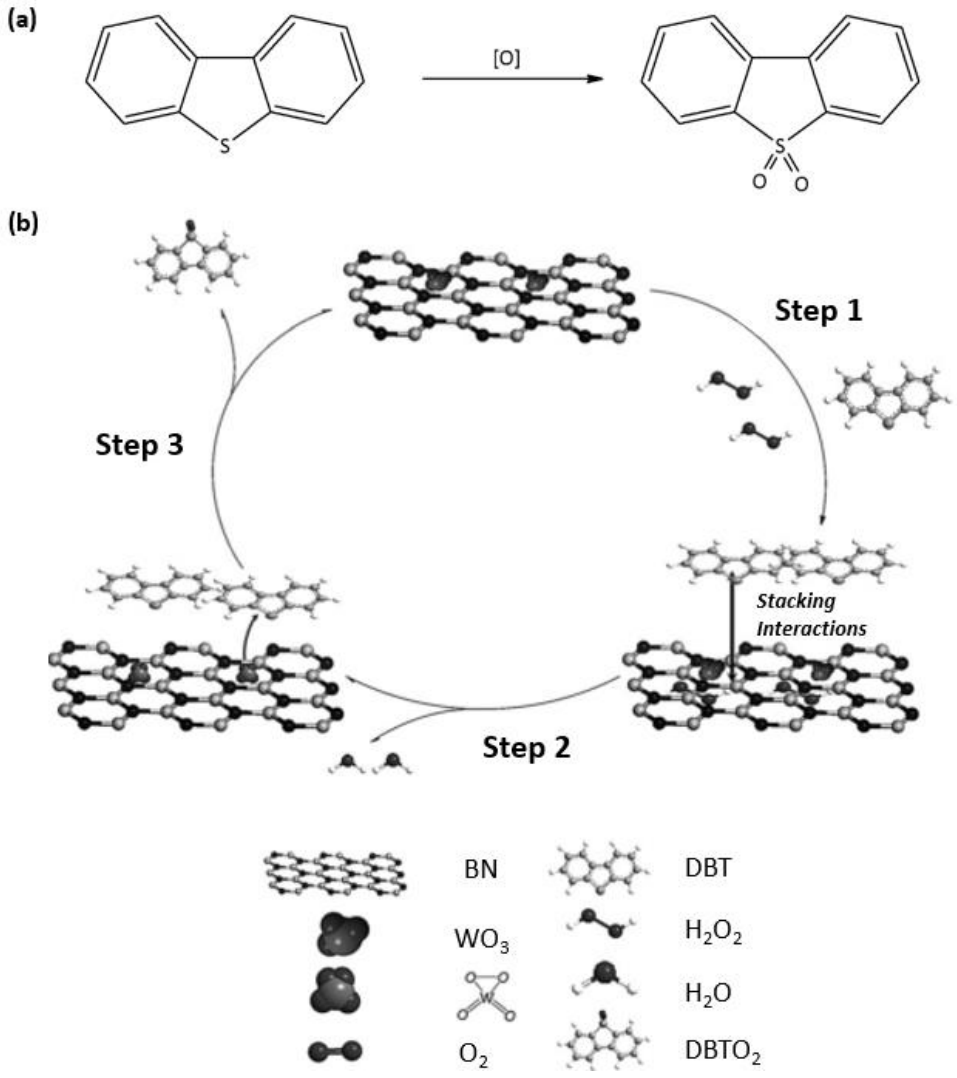


Figure 12. (a) Reaction scheme to show the oxidation of DBT to $DBTO_2$ and (b) the proposed mechanistic pathway for WO_x / BN-catalysed oxidative desulfurisation.[106]

H_2O_2 reacts with WO_x, generating the peroxotungsten intermediate, which then oxidised DBT to $DBTO_2$. Gas chromatography-mass spectrometry (GC-MS) confirms that DBT is adsorbed onto the catalyst and oxidised by WO_x. This high local concentration of DBT around WO_X is thought to be a major contributor to the fast reaction rate, leading to 99.2% of sulfur removal. The catalyst could also be recycled 5 times, with the oxidation of sulfur remaining above 85%. The role of BNNS in this case is both to stabilise the WO_x NP, and to adsorb DBT through stacking interactions, thus increasing its concentration close to the NP.

This catalytic activity is improved upon by Ji and coworkers, who explore a different tungsten containing catalyst supported on BNNS.[107] Heteropoly acids, with a molecular formula of $[XM_{12}O_{40}]^{n-}$ (where $X=P^{5+}$, As^{4+} or Ge^{4+} and $M=Mo^{6+}$ or W^{6+}) show excellent performance as organic catalysts;[143-145] yet their applications are limited by their poor solubility in many solvents. This can be overcome through incorporation into silicon-based materials or metal-organic-frameworks (MOFs).[144, 146-149] However, the limitations of these materials are the poor stability under harsh reaction conditions and high cost/ complex synthesis respectively. Ji and coworkers formed phosphotungstic acid ($H_3PW_{12}O_{40}$, denoted as HPW, representing heteropoly acids) on BN sheets for the desulfurisation of DBT, 4,6-dimethyldibenzothiophene (4,6-DMDBT) and benzothiophene (BT).[107] The desulfurisation of DBT in the presence of hydrogen peroxide is 100%, whereas analogous reactions with BN sheets or HPW only are 40 and 10% respectively. This high activity is attributed to the large surface area of BNNS, providing highly dispersed HPW, which leads to many active sites for DBT and H_2O_2 to adsorb, increasing their proximity and consequent probability of reacting. Complementary orbital arrangement between DBT and BNNS allows strong

adsorption.[150] The transfer of oxygen from H_2O_2 to $[PW_{12}O_{40}]^{3-}$ forms the peroxo species,[151] which oxidises DBT to $DBTO_2$ (Figure 13). This catalyst could be recycled 6 times with the sulfur removal only dropping to 98%.

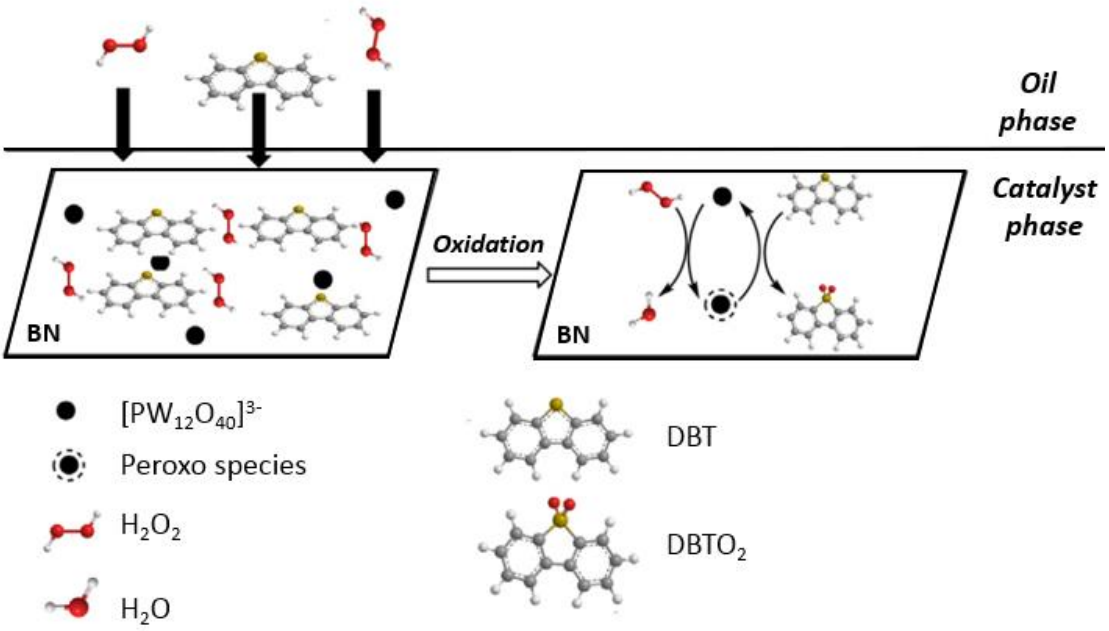


Figure 13. The proposed mechanism of DBT oxidation on HPW/BN.[107]

Again, BN increases the rate of reaction, by not only increasing the dispersion of NP, but through favourable stacking interactions between hexagonal BN layers and the reactant, increasing its concentration on the catalysts surface.

BN as a support often retains its electronically insulating properties, yet, some NP can modify this property. Copper NP, threaded through BNNS have been explored for oxidative desulfurisation (ODS) of 4,6-DMDBT and DBT (Figure 15).[108] The oxygen adsorbs onto BNNS, where the O-O bond can be weakened.[152] As an insulator, the electron mobility in oxidation processes, such as sulfur oxidation, on the surface of BNNS is slow. However, when Cu is incorporated, fast electron transfer between

sulfur (in DBT or 4,6-DMDBT) and adsorbed oxygen is facilitated and the rate of oxidation of sulfur on BNNS improves drastically. Cu NP sit in confined environments, described by the author as micropores, which are formed in the *in situ* synthesis of the hybrid material (Figure 14).



Figure 14. Schematic diagram of Cu/BNNS.[108]

The aerobic oxidation of aromatic sulfur compounds shows an increase in the catalytic activity from 62 to 99% (for DBT) and 63 to 97% (for 4,6-DMDBT) upon the addition of Cu NP, with the composite showing little decrease in activity after recycling 10 times. This method has the advantage of not requiring H_2O_2, a potential explosive. The activity is credited to the raised electron mobility within BN through the incorporation of Cu NP, while the stability is attributed to an improved oxidation resistance of Cu NP when incorporated into BN.

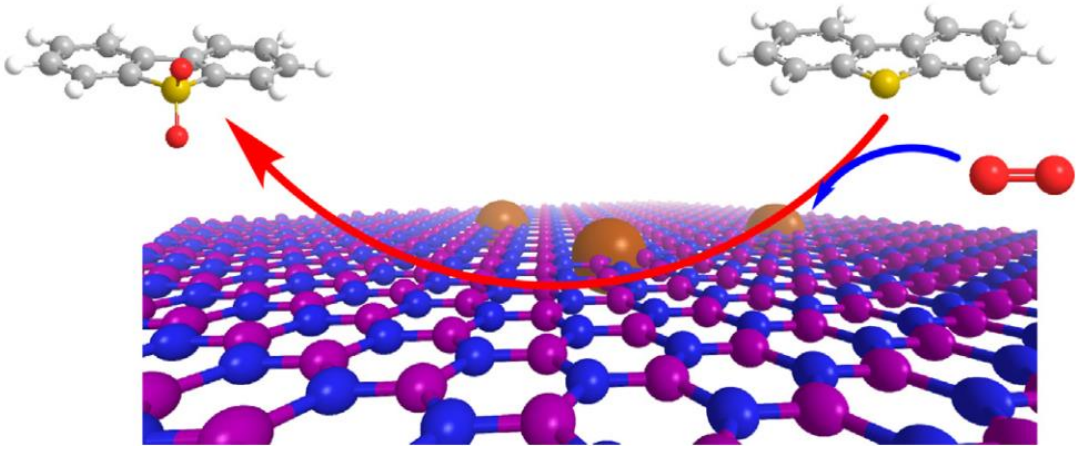


Figure 15. Aerobic oxidation of sulfur compounds over BNNS with confined metallic Cu NP.[108]

Oxidative desulfurisation reactions have also been reported using BNNS alone.[153] High conversion of DBT to $DBTO_2$ of 98.8% has been attributed to high surface area and defect concentration. It is likely that local concentration effects of DBT on nanosheets also contributes to the high conversion, similar to the previous examples. Moreover, BNNS can be recycled 10 times with sulfur removal of more than 90%. BNNS have also been investigated for ODS applications with Brönsted acid ionic liquids.[154]

Oxidation of Lactose

A different type of oxidation reaction uses composites of Pd (2-30 nm) on alumina (Pd/α-Al_2O_3) and *h*-BN (*ca*. 1 µm, Pd/*h*-BN), to catalyse the oxidation of lactose to lactobionic acid (Figure 16).[109] In this case, *h*-BN acts purely as a support for Pd NP, chosen based on its high thermal and chemical stability. The lack of surface functional groups (i.e. hydroxyl groups) are considered to limit side reactions and promote high selectivity, whilst stabilising the metal in its reduced form.

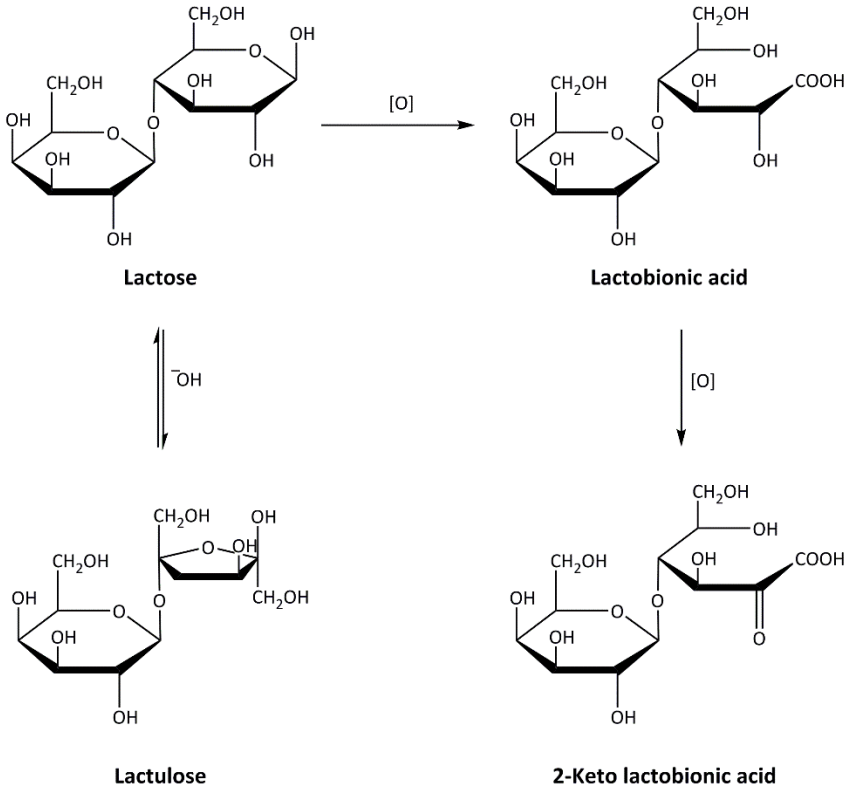


Figure 16. Reaction scheme of the oxidation of lactose to lactobionic acid.[155]

Lactobionic acid is used as an antioxidant or in cosmetics,[156, 157] and a main component of the organ preservation fluids required for transplantation.[158] The by-products lactulose and 2-keto lactobionic acid are often formed during the heterogeneous catalytic oxidation,[155] yet 100% selectivity for the production of lactobionic acid using Pd/*h*-BN was afforded, attributed to the absence of surface functional groups (which could lead to side reactions), small surface area and absence of micropores in *h*-BN and potentially to the particle size (too small can cause overoxidation). The corresponding Pd/α-Al_2O_3 resulted in selectivity below 100% and lower activity (yields between 8-38%, compared to 14-64%, depending on catalyst preparation conditions).

Since *h*-BN is hydrophobic, Meyers *et al*. discovered that by using methanol, instead of water, as a synthesis solvent the sedimentation time of *h*-BN is extended, thus increasing the interactions between the substrate and the Pd precursor [Na_2PdCl_4 or $Pd(OAc)_2(NHEt_2)_2$] and leading to smaller, better dispersed NP on *h*-BN. The composite also proved effective for the oxidation of maltose and glucose, with 100% selectivity in both cases and yields of 43 and 55% of maltobionic acid and gluconic acid respectively.

Oxidation of alcohol

While several catalysts have been formed from composites of NP and BNNS, very few examples are reported for other morphologies. Boron nitride nanocrystals (polyhedral, composed of two hexagons, and twelve side trapezoids, side length 650 nm, thickness *ca*. 130 nm), with layered hexagonal BN structure, have been synthesised by Wang *et al*.[110] When gold NP (1-8 nm) are deposited onto their surface they prove to be effective catalysts for the selective oxidation of benzyl alcohol to benzaldehyde in air.[110] The reaction scheme is shown below (Figure 17).

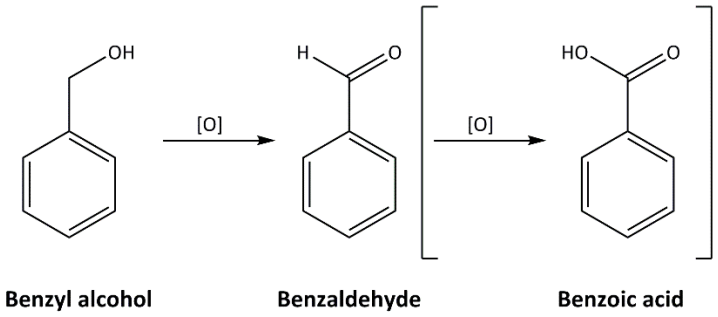


Figure 17. Oxidation of benzyl alcohol to benzaldehyde, with over-oxidation leading to the formation of benzoic acid.

Selective oxidation of alcohols is essential for the production of fine chemicals. The conversion and selectivity is reported as 30% and 98% respectively, somewhat better than analogous reactions using unsupported nanoporous pure gold (23% conversion and 98% selectivity),[159] and double the conversion of BN nanocrystals alone (15% conversion and 99% selectivity).[160] The author attributes these positive results to the high thermal conductivity and selectivity of BN nanocrystals, along with exposed {102} planes (on account of other exposed facets being important features for catalysis in Co_3O_4 nanorods[161] and efforts towards the synthesis of nanocrystals with different geometries and exposed facets).[162] Gold NP are recognised for their impressive selectivity and conversion of benzyl alcohol to benzaldehyde in isolation[159] and when supported on nanoscale structures.[163] Wang *et al*. do not claim to know the mechanism by which BN nanocrystals improve the rate and selectivity and therefore cannot distinguish whether BN functions as a support for Au NP or plays an active role in catalysis. Yet considering the properties of *h*-BN, it is plausible that favourable stacking interactions between benzyl alcohol and BN nanocrystals, along with oxygen activation from favourable *h*-BN-O_2 interactions increase the local concentration and reactivity of the reactants respectively, increasing conversion.

Oxidation of CO

A range of unusual structures have been explored for catalysis, with BN formed as spheres and cages, which can act as a protective barrier or modify the NP chemical properties and electronic structure after encapsulation.[105, 111, 114, 115] A rather unconventional NP/BN structure has been formed by Sun *et al*. who coated Pt

NP with ammonia borane, then heated in the presence of ammonia to yield catalysts targeted at CO oxidation reactions (Figure 18).[111]

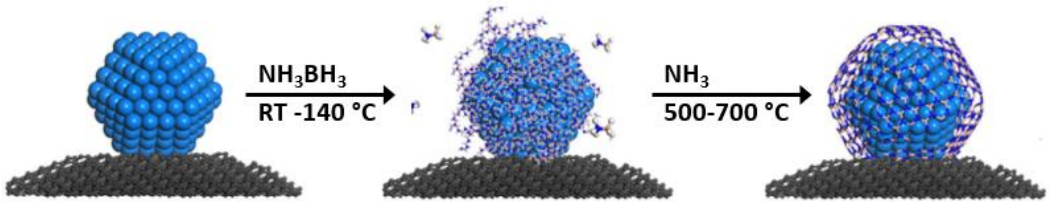


Figure 18. Schematic of the preparation of Pt@*h*-BN.[111]

Small molecules can permeate the BN shell to access the active metal core, hence CO and O_2 were able to intercalate with the BN layers and adsorb onto the surface of platinum. CO adsorption is weakened by the shell, which alleviates CO contamination promoting CO oxidation and resulted in 100% CO conversion at 94 °C, while the same conversion was not achieved until *ca*. 120 °C for Pt NP supported on carbon. The BN shell acts as a protective layer for Pt under harsh reaction conditions, such as preventing sintering at high temperatures (Figure 19).

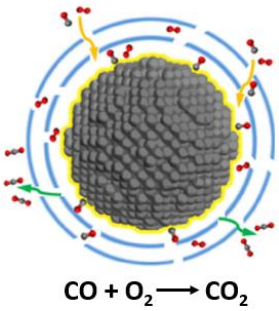


Figure 19. Reactions for the core-shell nanocatalyst, in which most of the metal-core surface is accessible to the reactants.[111]

In this example, the thermally and chemically stable shell acts as a shield to protect the encapsulated Pt NP and does not play a part in the catalytic mechanism. Bao and coworkers use the same approach for methanation reactions using Ni/BN

core-shell catalysts.[98] CO oxidation reactions have also been catalysed by Pt/BNNS composites, where Pt NP interact strongly with vacancies on BNNS for improved rates of reaction.[112] Interestingly, calculations indicate the reaction will be catalysed by single Co atoms embedded into the boron vacancies of BNNS.[164]

Oxidation of ethanol to acetaldehyde

Gold-copper (*ca*. 3 nm) catalysts have been incorporated into BN "nanospheres" (Au-Cu/BN-sphere) and work synergistically for the selective oxidation of ethanol to acetaldehyde (Figure 20).[113]

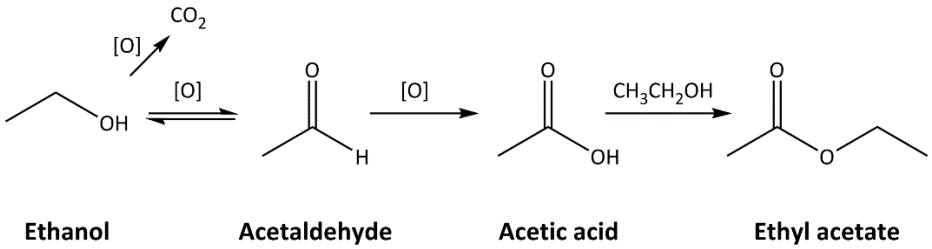


Figure 20. Oxidation of ethanol to acetaldehyde, with possible by-products including CO_2, acetic acid and ethyl acetate.

Cu_xO are largely responsible for O-H cleavage through activating molecular oxygen,[165] to form O^{2-} or O^-, while Au species provide a site for the notoriously difficult C-H cleavage,[166] when in close proximity to oxygen. Thus Au-Cu/BN outperforms Au/BN-sphere and Cu/BN-sphere (Figure 21). The BN support enables a high NP dispersion, facilitating higher conversion when using Au-Cu/BN compared to Au and Cu on SiO_2 (Au-Cu/SiO_2), a more traditional catalyst.[167]

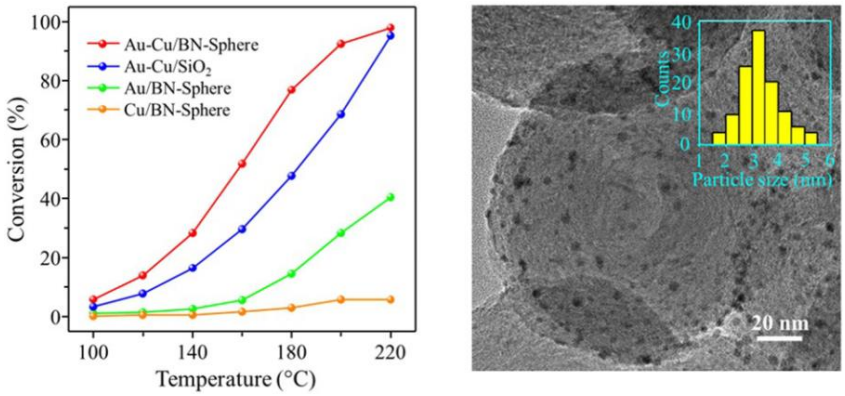


Figure 21. The effect of temperature on the aerobic oxidation of ethanol across a range of catalysts (b) TEM image of Au-Cu/BN-spheres. The larger, light areas are BN-spheres and the smaller, darker circles are Au-Cu NP.[113]

Acetaldehyde is found to interact less strongly with Au-Cu/BN than Au-Cu/SiO_2. Weaker interactions minimise the adsorption of acetaldehyde onto metal sites and thus prevents secondary reactions which form by-products. Therefore, Au-Cu/BN increase the selectivity of acetaldehyde (92%, compared to 61% for Au-Cu/SiO_2) at low reaction temperatures. Additionally, the high dispersion of NP strongly interacts with the BN support, creating a highly stable catalyst. Even after an 80 h reaction, the selectivity remained at *ca*. 93%, while conversion only dropped from 80 to 74%.

These BN-spheres demonstrate dual functionality: they behave as a strong support for Au-Cu NP and also modify the strength of substrate-metal interactions to minimise by-product formation.

Other oxidation reactions

Enzyme catalysed substrate oxidation reactions have been catalysed by microperoxidase-11 (MP-11) attached to Au NP deposited onto BNNT.[116] An

increased rate of substrate oxidation is observed when MP-11 is deposited on BNNT, in this case the Au NP act purely as probes.

Other examples of a NP/BN catalysed oxidation reactions reported recently include the oxidation of hydrogen catalysed by Ni NP within *h*-BN shells[114] and methane reformation catalysed by Ni NP within *h*-BN cages.[115] All show favourable catalytic properties resulting from the BN support, such as improved activation energy of the reaction,[114] high NP stability against sintering from a BN protective shell,[115] or a reduced decomposition temperature.[127]

1.3.3 Simultaneous oxidation and reduction reactions

Photocatalytic dye degradation

Silver iodide has been reported to show good photocatalytic performance for the degradation of organic pollutants under visible light irradiation.[168] Choi *et al*. formed AgI NP on BNNS to improve the visible light degradation of Rhodamine B (RhB).[117] A significant improvement in photocatalytic activity was determined, attributed to the synergistic effect of AgI with BNNS. For instance, the composites are hydrophobic with a high surface area and a strong adsorption ability for RhB. The dispersion of AgI NP is improved when attached to BNNS, therefore the accessible surface area and number of active sites of the NP is increased.

Pure AgI is unstable in light due to low aqueous solubility and susceptibility to photocorrosion, so the recyclability for photocatalytic reactions is often poor. After five cycles, only 25% RhB is degraded. Yet, if the adsorption onto insoluble BNNS is strong, as in this reported case, AgI remain stable in aqueous solution. After the same

number of cycles 87.8% degradation efficiency was achieved (Figure 22). Thus, BNNS are an effective support for stabilising AgI NP.

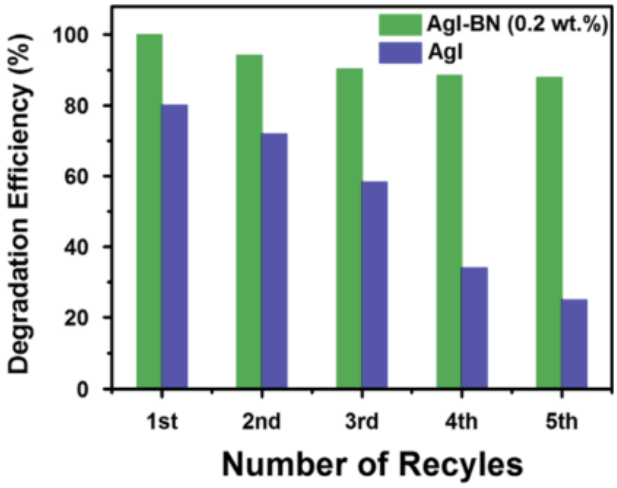


Figure 22. Recyclability of AgI-BN compared to AgI for the degradation of RhB under solar light.

In addition to the high stability of AgI NP, similar to the results concluded by Ma *et al*.,[95] the high photocatalytic activity of the composite is attributed to the electron transfer between the NP and BNNS, increasing the charge separation, transportation and efficiency. Consequently, the photogenerated hole is also more available to oxidise OH^- (since $H_2O \rightarrow H^+ + OH^-$) to $OH^\bullet$. Hence, BNNS play an active role in the photocatalytic reaction.

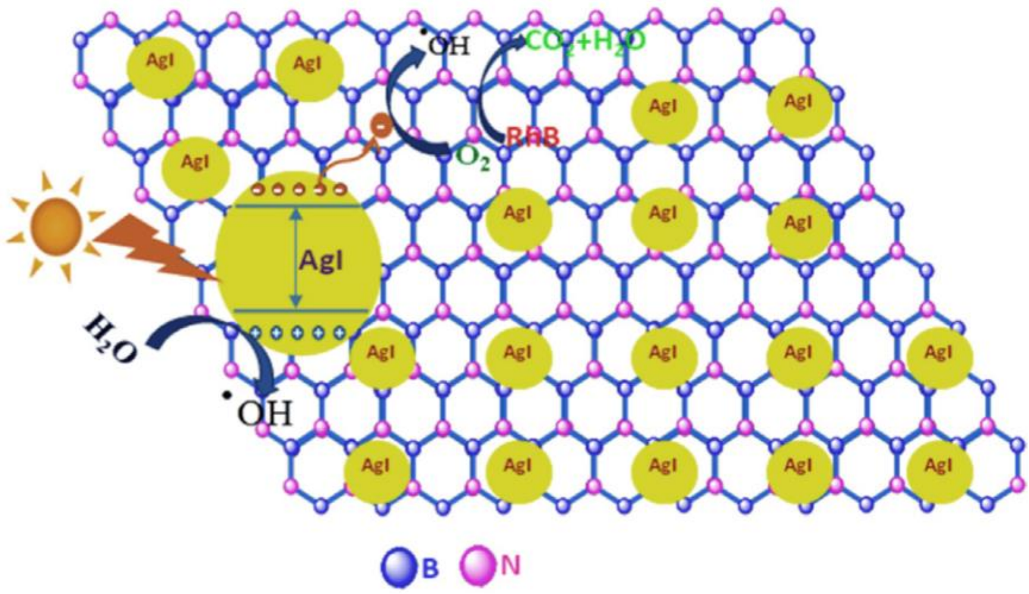


Figure 23. Schematic of the flow of photo-induced electrons in the AgI-BNNS composite under simulated solar light.[117]

This material was also used to catalyse the reduction of 4-nitrophenol to 4-aminophenol; no reaction was observed without the catalyst present.

Photocatalytic reactions have also been carried out using "navy bean" shaped AgI/AgBr nanoparticles on BNNS, resulting in the degradation of RhB and methylene orange (MO).[118] The photocatalyst degrades at 97.4% RhB and 95.0% MO in 6 minutes, compared to 51.1% RhB and 55.6% MO for AgI/AgBr navy beans only. Furthermore, there is little decrease in activity over 5 cycles.

A possible mechanism involves the electron transfer of photoexcited electrons from AgI, through AgBr, to the BNNS to reduce O_2 to $O_2^{\bullet -}$ which can then degrade organic dyes, with photogenerated holes also acting to degrade RhB (Figure 24).

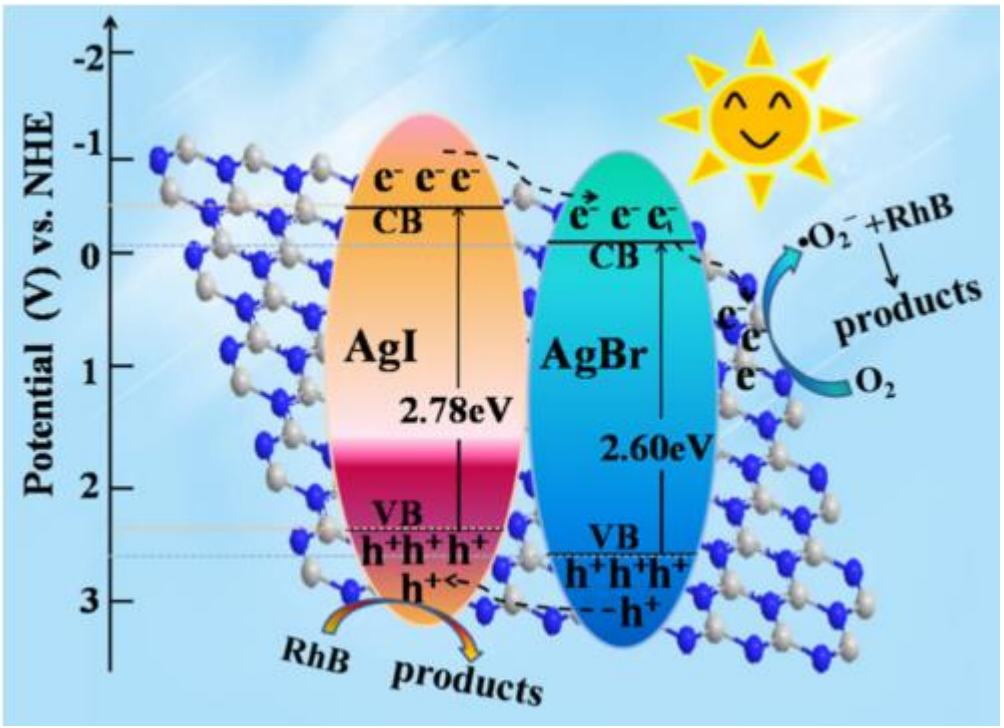


Figure 24. The possible photocatalytic mechanism of AgI/AgBr/BNNS for the degradation of organic dyes under visible light irradiation.[118]

In this instance, the role of the BNNS is not to stabilise the AgI/AgBr navy beans, rather to accept electrons from AgI/AgBr and thus prevent electron-hole recombination.

Similarly, photoactive Ag_2CrO_4 NP deposited onto BNNS increased the degradation of RhB.[119] Composites degraded 96.7% of the dye in 120 minutes compared to 75% degradation for NP alone. The principal role of the BNNS is to accept photoexcited electron from Ag_2CrO_4 NP, preventing electron-hole recombination and forming active species $O_2^{\bullet-}$ and $OH^{\bullet}$ for dye degradation (Figure 25).

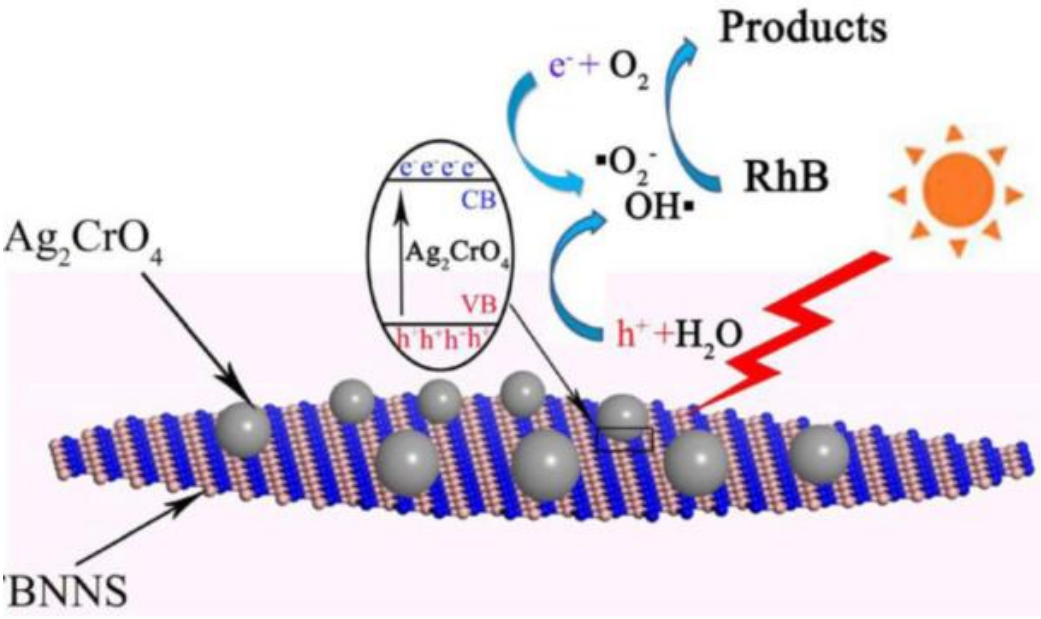


Figure 25. The possible photocatalytic mechanism of Ag_2CrO_4/ BNNS for the degradation of RhB under visible light irradiation.[119]

It is also shown from UV-vis diffuse reflectance spectroscopy that the band gap of the NP decreases from 1.64 to 1.60 eV when the NP are deposited onto BNNS. Although no explanation is provided, it is possible that particle growth could be the cause of this.

Similar behaviour has been observed using nanoparticles of $BiPO_4$,[120] Ag_3PO_4,[121, 122] Au,[124] and WO_3[123] supported on nanoscale BN.

Hydrogen production through hydrolysis of ammonia borane

BN supports have also proven useful for hydrolysis. For example, copper on BNNS drastically increases the rate of reaction, with the mass of hydrogen/ mass of ammonia borane increasing to *ca*. 2.9 for Cu on BNNS in the first hour of reaction, from *ca*. 1 for unsupported Cu NP.[99] The result is attributed to the highly dispersed Cu NP on BNNS. Additionally, the activation energy of the reaction is low for

Cu/BNNS, measured at around 23.8 kJ mol^{-1}, compared to other reported catalysts, including zeolite confined copper nanoclusters (51.8 kJ mol^{-1}),[169] Cu/reduced graphene oxide (38.2 kJ mol^{-1})[170] and CuCO/C (51.9 kJ mol^{-1}),[171] and close to that of some Pt-based catalysts.[172, 173] The predicted mechanism is shown in Figure 26.

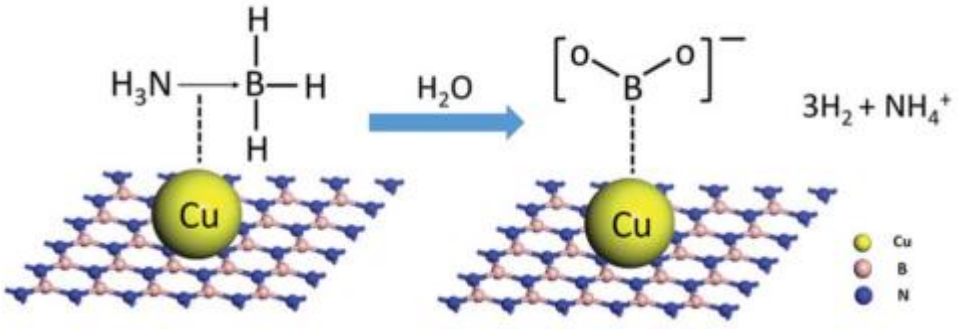


Figure 26. Predicted mechanism for the hydrolysis of ammonia borane catalysed by Cu/BNNS.[99]

Similar catalysts have also been targeted for hydrogen production from the hydrolysis of ammonia borane, including Ni nanoparticles supported by BN nanospheres and sheets[103, 104] and CoNi NP encapsulated within BN shells.[105] Additionally, reversible hydrogen production/removal has been investigated using $LiBH_4$/BNNS, with BNNS reducing the temperature of dehydrogenation of $LiBH_4$ to 175 °C and the peak temperature of hydrogen release reduced by 80 °C compared to pre-milled $LiBH_4$.[174]

1.3.4 Cross-coupling reactions

Suzuki-Miyaura reactions

Another example of BNNS composites as effective catalysts is demonstrated by Fu and coworkers, who use Pd-Fe core-shell NP on BNNS to catalyse a range of Suzuki-Miyaura reactions (Figure 27).[125]

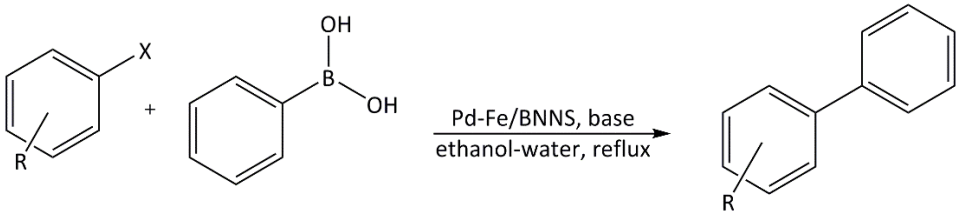


Figure 27. Suzuki-Miyaura coupling reactions of bromo- or iodo- aromatic molecules with boronic acids, where X=Br or I and R= H, $COCH_3$, COH, NO_2, OCH_3, NH_2 or OH.

The material showed promising results, for example, greater than 90% yield was achieved in 30 minutes for the coupling of bromobenzene and phenylboronic acid, whereas the BNNS alone showed poor or no yield. Over 6 cycles the average yield was above 90% for the coupling of bromobenzene with phenylboronic acid, demonstrating effective recyclability. In contrast to many Suzuki-Miyaura reactions, benign solvents are used and no special conditions (inert gas, surfactants, or specific ligands) are employed. The low Pd content and short reaction times (i.e. 10 minutes for iodobenzene) still enables equivalent or superior catalytic activity to state-of-the-art Suzuki-Miyaura reactions.[175, 176]

As a control, reduced graphene oxide (rGO) was used instead of the BNNS. This proved to be drastically less effective under the same conditions (the yield for

bromobenzene-phenylboronic acid reacting pairs was 64% for Pd-Fe/rGO, in comparison to 99% for Pd-Fe/BNNS).

The strong metal-BNNS interactions are accredited for the high recyclability of the catalyst. Yet, the BNNS clearly function as more than just a support for the NP. The full mechanism and synergistic effects of the material is not fully understood at present but clearly provides an advantage over analogous materials. It is likely that the combination of NP stabilisation and high dispersion are responsible for the effective catalysis.

3-Compondent cross-coupling reactions

3-Component coupling reactions have been catalysed by CuO, Cu(O) and CuS on few-layered BNNS (Figure 28),[126] however, rGO outperformed BNNS as support catalyst (CuO/rGO = 95% yield, CuO/BNNS = 92% yield). The result is accredited to enhanced interactions between CuO and rGO, compared to BNNS, resulting in a uniform distribution of small CuO NP.

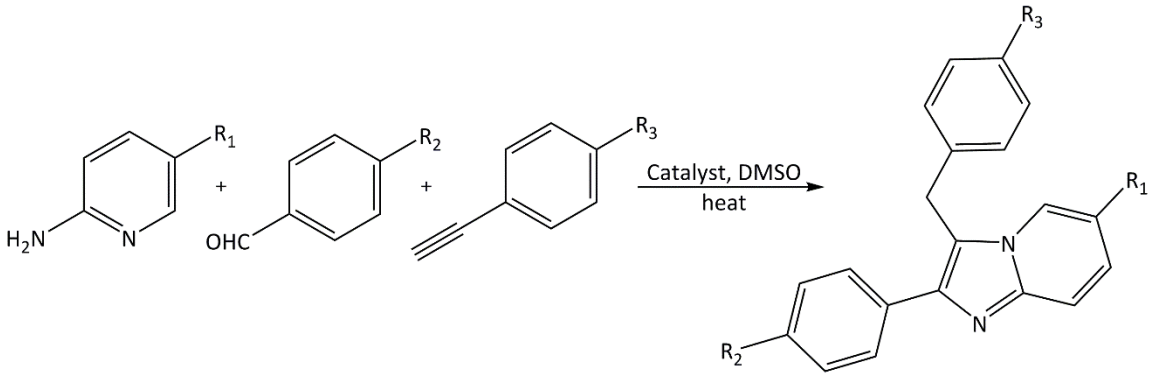


Figure 28. 3-Component coupling reaction where R_1, R_2 = H or Me and R_2 = Cl or H.

1.4 Scope for further investigation

It is clear that allotropes of nanoscale BN are powerful components for the future of catalysis. Through the incorporation of different nanoparticles/ metals, they can be targeted to almost any heterogeneous catalytic application, proving superior to many existing catalyst. Their affinity for stabilising nanoparticles increases the dispersion and number of accessible catalytic centres. Although the interaction energy of NP with *h*-BN is unknown, surprisingly, the binding energy of cobalt adatoms onto *h*-BN (1.03 eV) is calculated to be weaker than graphene (1.60 eV), due to the increased availability of low-energy electronic states in graphite, resulting in charge transfer and more efficient interactions.[177] This is surprising considering the increased interaction energies of NP on BNNS discussed earlier. Yet, the presence of defects significantly increases the adsorption energy, as calculated through simulations of Fe nanoparticles on *h*-BNNS with B- or N- vacancies.[178] In the case of BNNS, the electronically insulating properties of bulk BN are altered as the size reduces, and is considered to become semiconducting due to defects and imperfections.[140, 141] Then, under visible light irradiation, BNNS are thought to enhance the number of photoelectrons generated and transferred to the NP, thus changing the catalytic mechanism.[117, 95]

In most of the catalytic materials described above, nanoparticles are either deposited onto the surface,[93-95, 109, 110, 117] or confined within the plane of *h*-BN.[106, 108] The elegant alternative of encapsulating nanoparticles inside hollow BN nanostructures has not been widely explored, yet Pt encapsulated within *h*-BN formed by Sun and coworkers,[111] and Au-Cu/BN-sphere formed by Wang *et al*.[55] to

name just two examples, have shown to be beneficial for stabilising the confined nanoparticles against harsh reaction conditions.[111] This increased stability is analogous to the encapsulation of metals inside the more established carbon nanotube-based nanoreactors.[179, 180]

The confinement of molecules inside nanocontainers allows for the properties and reactivity to be studied.[181-185] By analogy, metal catalyst particles can be encapsulated within the nanotubes and the catalytic performance probed. The catalyst is thus stabilised by the nanotube and positioned close to a high concentration of precursor molecules, and can additionally be modified by nanotube-metal interactions.[72, 180, 186, 187]

To date, boron nitride nanotubes have not been commonly reported as supports for metal nanoparticles aimed at catalysis applications. This is somewhat surprising given that they have many appealing properties, such as strength,[38] chemical[7] and thermal stability,[32] with the additional benefit of being hollow cylindrical structures, predicted to behave as nano-test-tubes to confine and template chemical reactions.[188]

The simple explanation for the current limited reports on these types of materials is that the essential methods of opening and filling boron nitride nanotubes is underexplored, with only a select number of research groups focusing their attention on solving this problem.[189-191] Methods for filling BNNT sometimes requires expensive, specialised equipment so the topic remains a niche research area. However, the confinement of molecules and nanoparticles inside BNNT may help to understand important molecular transformations in confined spaces and thus further exploration of these materials is critically required.

1.5 References

1. K. Miyoshi, *Solid Lubrication Fundamentals and Applications*, CRC Press, 2001.
2. Investor inter, https://investorintel.com/sectors/technology-metals/technology-metals-intel/graphite-every-resource-investor-needs-know/, (accessed 04/08/17).
3. Inhabitat, http://inhabitat.com/new-man-made-diamonds-turn-nuclear-waste-into-long-lasting-batteries/, (accessed 04/08/17).
4. T. E. Warner, *Synthesis, Properties and Mineralogy of Important Inorganic Materials*, Wiley, Somerset, 2011.
5. W. J. Zhang, Y. M. Chong, I. Bello and S. T. Lee, *J. Phys. D: Appl. Phys.*, 2007, **40**, 6159.
6. P. Mukhopadhyay and R. K. Gupta, *Graphite, Graphene, and Their Polymer Nanocomposites*, CRC Press, Boca Raton, United States, 2012.
7. Y. Chen, *Nanotubes and Nanosheets*, CRC Press, Baton Rouge, United States, 2015.
8. X.-F. Jiang, Q. Weng, X.-B. Wang, X. Li, J. Zhang, D. Golberg and Y. Bando, *J. Mater. Sci. Technol.*, 2015, **31**, 589.
9. N. Marom, J. Bernstein, J. Garel, A. Tkatchenko, E. Joselevich, L. Kronik and O. Hod, *Phys. Rev. Lett.*, 2010, **105**, 046801.
10. O. Hod, *J. Chem. Theory Comput.*, 2012, **8**, 1360.
11. Y. M. Shi, C. Hamsen, X. T. Jia, K. K. Kim, A. Reina, M. Hofmann, A. L. Hsu, K. Zhang, H. N. Li, Z. Y. Juang, M. S. Dresselhaus, L. J. Li and J. Kong, *Nano Lett.*, 2010, **10**, 4134.
12. R. S. Pease, *Acta Crystallogr.*, 1952, **5**, 356.
13. V. L. Solozhenko, G. Will and F. Elf, *Solid State Commun.*, 1995, **96**, 1.
14. W. Paszkowicz, J. B. Pelka, M. Knapp, T. Szyszko and S. Podsiadlo, *Appl. Phys. A*, 2002, **75**, 431.
15. J. D. Bernal, *P. Roy. Soc. Lond. A Mat.*, 1924, **106**, 749.
16. Y. Baskin and L. Meyer, *Phys. Rev.*, 1955, **100**, 544.
17. D. D. L. Chung, *J. Mater. Sci.*, 2002, **37**, 1475.
18. Z. C. Pan, H. Sun, Y. Zhang and C. F. Chen, *Phys. Rev. Lett.*, 2009, **102**, 055503.
19. M. G. Nicholas, D. A. Mortimer, L. M. Jones and R. M. Crispin, *J. Mater. Sci.*, 1990, **25**, 2679.
20. Sinyo Nitride Materials, http://www.nitridematerial.com/info/structure-and-properties-of-boron-nitride-3019069.html, (accessed 08/08/17).
21. G. E. Spriggs, *Materials · Powder Metallurgy Data. Refractory, Hard and Intermetallic Materials*, Springer Berlin Heidelberg, 2002.
22. M. I. Petrescu, *Diamond Relat. Mater.*, 2004, **13**, 1848.
23. Y. Du, Z. Su, D. Yang, X. Yang, X. Ji, X. Gong and T. Zhang, *Mater. Lett.*, 2007, **61**, 3409.
24. X. R. Ji and X. H. Yang, *Chin. Phys. Lett.*, 2012, **29**, 038101.
25. hq graphene, http://www.hqgraphene.com/h-BN.php, (accessed 04/08/17).
26. Wired, https://www.wired.com/2013/01/nanotwinned-cubic-boron-nitride/, (accessed 04/08/17).

27. K. I. Bolotin, K. J. Sikes, Z. Jiang, M. Klima, G. Fudenberg, J. Hone, P. Kim and H. L. Stormer, *Solid State Commun.*, 2008, **146**, 351.
28. X. Du, I. Skachko, A. Barker and E. Y. Andrei, *Nat. Nanotechnol.*, 2008, **3**, 491.
29. P. Avouris, *Nano Lett.*, 2010, **10**, 4285.
30. E. Joselevich, *Chemphyschem*, 2004, **5**, 619.
31. D. Golberg, Y. Bando, Y. Huang, T. Terao, M. Mitome, C. C. Tang and C. Y. Zhi, *ACS Nano*, 2010, **4**, 2979.
32. D. Golberg, Y. Bando, K. Kurashima and T. Sato, *Scripta Mater.*, 2001, **44**, 1561.
33. C. Lee, X. Wei, J. W. Kysar and J. Hone, *Science*, 2008, **321**, 385.
34. J. N. Coleman, U. Khan and Y. K. Gun'ko, *Adv. Mater.*, 2006, **18**, 689.
35. M. M. J. Treacy, T. W. Ebbesen and J. M. Gibson, *Nature*, 1996, **381**, 678.
36. M. Q. Le, *Int. J. Mech. Mater. Des.*, 2015, **11**, 15.
37. A. E. Tanur, J. Wang, A. L. M. Reddy, D. N. Lamont, Y. K. Yap and G. C. Walker, *J. Phys. Chem. B*, 2013, **117**, 4618.
38. X. L. Wei, M. S. Wang, Y. Bando and D. Golberg, *Adv. Mater.*, 2010, **22**, 4895.
39. S. S. Chen, A. L. Moore, W. W. Cai, J. W. Suk, J. H. An, C. Mishra, C. Amos, C. W. Magnuson, J. Y. Kang, L. Shi and R. S. Ruoff, *ACS Nano*, 2011, **5**, 321.
40. A. A. Balandin, *Nat. Mater.*, 2011, **10**, 569.
41. S. S. Chen, Q. Z. Wu, C. Mishra, J. Y. Kang, H. J. Zhang, K. J. Cho, W. W. Cai, A. A. Balandin and R. S. Ruoff, *Nat. Mater.*, 2012, **11**, 203.
42. C. W. Chang, A. M. Fennimore, A. Afanasiev, D. Okawa, T. Ikuno, H. Garcia, D. Li, A. Majumdar and A. Zettl, *Phys. Rev. Lett.*, 2006, **97**, 085901.
43. H. Zhou, J. Zhu, Z. Liu, Z. Yan, X. Fan, J. Lin, G. Wang, Q. Yan, T. Yu, P. M. Ajayan and J. M. Tour, *Nano Res.*, 2014, **7**, 1232.
44. J. Y. Wang, J. L. Huang, R. Yan, F. X. Wang, W. G. Cheng, Q. G. Guo and J. Z. Wang, *J. Mater. Chem. A*, 2015, **3**, 3144.
45. M. Ara, K. Wadumesthrige, T. J. Meng, S. O. Salley and K. Y. S. Ng, *RSC Adv.*, 2014, **4**, 20540.
46. Y. Wimalasiri, R. Fan, X. S. Zhao and L. Zou, *Electrochim. Acta*, 2014, **134**, 127.
47. L. H. Li, J. Cervenka, K. Watanabe, T. Taniguchi and Y. Chen, *ACS Nano*, 2014, **8**, 1457.
48. Y. Xiao, X. H. Yan, J. X. Cao, J. W. Ding, Y. L. Mao and J. Xiang, *Phys. Rev. B: Condens. Matter*, 2004, **69**, 205415.
49. H. F. Bettinger, T. Dumitrica, G. E. Scuseria and B. I. Yakobson, *Phys. Rev. B: Condens. Matter*, 2002, **65**, 041406.
50. B. Akdim, R. Pachter, X. F. Duan and W. W. Adams, *Phys. Rev. B: Condens. Matter*, 2003, **67**, 8.
51. J. X. Zhao and Y. H. Ding, *J. Phys. Chem. C*, 2008, **112**, 20206.
52. M. El Khalifi, E. Duverger, T. Gharbi, H. Boulahdour and F. Picaud, *Phys. Chem. Chem. Phys.*, 2015, **17**, 30057.
53. T. A. Hilder and J. M. Hill, *Micro & Nano Letters*, 2008, **3**, 18.
54. R. Chowdhury and S. Adhikari, *Ieee Trans. Nanotechnol.*, 2011, **10**, 659.
55. G. C. Loh and D. Baillargeat, *J. Appl. Phys.*, 2013, **114**, 183502.
56. Z. G. Wang, Z. Li and D. M. Cheng, *Eur. Phys. J. Appl. Phys.*, 2009, **46**, 20601.
57. C. Zhi, Y. Bando, C. Tang and D. Golberg, *Mat. Sci. Eng. R.*, 2010, **70**, 92.
58. N. G. Chopra, R. J. Luyken, K. Cherrey, V. H. Crespi, M. L. Cohen, S. G. Louie and A. Zettl, *Science*, 1995, **269**, 966.

59. J. Kim, S. Lee, Y. R. Uhm, J. Jun, C. K. Rhee and G. M. Kim, *Acta Mater.*, 2011, **59**, 2807.
60. D. Golberg, Y. Bando, M. Eremets, K. Takemura, K. Kurashima and H. Yusa, *Appl. Phys. Lett.*, 1996, **69**, 2045.
61. O. R. Lourie, C. R. Jones, B. M. Bartlett, P. C. Gibbons, R. S. Ruoff and W. E. Buhro, *Chem. Mater.*, 2000, **12**, 1808.
62. Q. Zhang, *Carbon Nanotubes and Their Applications*, Pan Stanford, 2012.
63. J. H. Warner, F. Schaffel, M. Rummeli and A. Bachmatiuk, *Graphene: Fundamentals and Emergent Applications*, Elsevier, Oxford, UK, 2013.
64. D. M. Guldi and N. Martín, *Carbon Nanotubes and Related Structures: Synthesis, Characterization, Functionalization, and Applications*, Wiley, 2010.
65. D. Reddy, L. F. Register, G. D. Carpenter and S. K. Banerjee, *J. Phys. D: Appl. Phys.*, 2011, **44**, 313001.
66. Y. Zhu, S. Murali, W. Cai, X. Li, J. W. Suk, J. R. Potts and R. S. Ruoff, *Adv. Mater.*, 2010, **22**, 3906.
67. H. J. Dai, *Accounts Chem. Res.*, 2002, **35**, 1035.
68. A. Maiti, *Comput. Model. Eng. Sci.*, 2002, **3**, 589.
69. E. W. Hill, A. Vijayaragahvan and K. Novoselov, *IEEE Sens. J.*, 2011, **11**, 3161.
70. J. J. Tang, F. Di, X. Xu, Y. H. Xiao and J. F. Che, *Prog. Chem.*, 2012, **24**, 501.
71. Z. C. Wu, Z. H. Chen, X. Du, J. M. Logan, J. Sippel, M. Nikolou, K. Kamaras, J. R. Reynolds, D. B. Tanner, A. F. Hebard and A. G. Rinzler, *Science*, 2004, **305**, 1273.
72. S. A. Miners, G. A. Rance and A. N. Khlobystov, *Chem. Soc. Rev.*, 2016, **45**, 4727.
73. R. F. Nie, J. H. Wang, L. N. Wang, Y. Qin, P. Chen and Z. Y. Hou, *Carbon*, 2012, **50**, 586.
74. E. Antolini, *Appl. Catal. B-Environ.*, 2012, **123**, 52.
75. G. Ciofani, *Expert Opin. Drug Deliv.*, 2010, **7**, 889.
76. X. Chen, X. P. Gao, H. Zhang, Z. Zhou, W. K. Hu, G. L. Pang, H. Y. Zhu, T. Y. Yan and D. Y. Song, *J. Phys. Chem. B*, 2005, **109**, 11525.
77. S. H. Jhi and Y. K. Kwon, *Phys. Rev. B: Condens. Matter*, 2004, **69**, 245407.
78. W. W. Lei, H. Zhang, Y. Wu, B. Zhang, D. Liu, S. Qin, Z. W. Liu, L. M. Liu, Y. M. Ma and Y. Chen, *Nano Energy*, 2014, **6**, 219.
79. A. P. Garshin, *Refract. Ind. Ceram.*, 2009, **50**, 363.
80. C. Y. Zhi, Y. Bando, T. Terao, C. C. Tang, H. Kuwahara and D. Golberg, *Adv. Funct. Mater.*, 2009, **19**, 1857.
81. J. Li, H. Jia, Y. Ding, H. Luo, S. Abbas, Z. Liu, L. Hu and C. Tang, *Nanotechnology*, 2015, **26**.
82. T. M. Tran-Thuy, C. C. Chen and S. D. Lin, *ACS Catal.*, 2017, **7**, 4304.
83. J. M. Venegas, J. T. Grant, W. P. McDermott, S. P. Burt, J. Micka, C. A. Carrero and I. Hermans, *ChemCatChem*, 2017, **9**, 2118.
84. J. Schnee, A. Eggermont and E. M. Gaigneaux, *ACS Catal.*, 2017, **7**, 4011.
85. L. Shi, D. Wang, W. Song, D. Shao, W. P. Zhang and A. H. Lu, *ChemCatChem*, 2017, **9**, 1720.
86. C. J. Huang, C. Chen, M. W. Zhang, L. H. Lin, X. X. Ye, S. Lin, M. Antonietti and X. C. Wang, *Nat. Commun.*, 2015, **6**, 7698.

87. Z. Lu, P. Lv, Z. Yang, S. Li, D. Ma and R. Wu, *Phys. Chem. Chem. Phys.*, 2017, **19**, 16795.
88. F. Guo, P. Yang, Z. Pan, X. N. Cao, Z. Xie and X. Wang, *Angew. Chem. Int. Ed.*, 2017, **56**, 8231.
89. M. D. Esrafili and P. Nematollahi, *Synthetic Metals*, 2017, **226**, 129.
90. M. Li, Y. Wang, P. Tang, N. Xie, Y. Zhao, X. Liu, G. Hu, J. Xie, Y. Zhao, J. Tang, T. Zhang and D. Ma, *Chem. Mater.*, 2017, **29**, 2769.
91. J. Wang, J. Hao, D. Liu, S. Qin, D. Portehault, Y. Li, Y. Chen and W. Lei, *ACS Energy Lett.*, 2017, **2**, 306.
92. T. Balakrishnan, K. U. V. Kiran, S. M. Kumar, A. Raju, S. A. Kumar and S. Mayavan, *J. Environ. Chem. Eng.*, 2017, **5**, 564.
93. W. L. Sun, Y. Meng, Q. R. Fu, F. Wang, G. J. Wang, W. H. Gao, X. C. Huang and F. S. Lu, *ACS Appl. Mater. Interfaces*, 2016, **8**, 9881.
94. G. Elumalai, H. Noguchi, A. Lyalin, T. Taketsugu and K. Uosaki, *Electrochem. Commun.*, 2016, **66**, 53.
95. F. K. Ma, G. Zhao, C. Li, T. L. Wang, Y. Z. Wu, J. X. Lv, Y. Y. Zhong and X. P. Hao, *CrystEngComm.*, 2016, **18**, 631.
96. H. Shen, C. T. Duan, J. Guo, N. Zhao and J. Xu, *J. Mater. Chem. A*, 2015, **3**, 16663.
97. A. K. Roy, S. Y. Park and I. In, *Nanotechnology*, 2015, **26**, 105601.
98. L. J. Gao, Q. Fu, M. M. Wei, Y. F. Zhu, Q. Liu, E. Crumlin, Z. Liu and X. H. Bao, *ACS Catal.*, 2016, **6**, 6814.
99. X. Qiu, X. Wu, Y. Wu, Q. Liu and C. Huang, *RSC Adv.*, 2016, **6**, 106211.
100. E. K. Jeon, E. Seo, E. Lee, W. Lee, M. K. Um and B. S. Kim, *Chem. Commun.*, 2013, **49**, 3392.
101. J. Luo, N. Zhang, R. Liu and X. Y. Liu, *RSC Adv.*, 2014, **4**, 64816.
102. M. Ayan-Varela, M. J. Fernandez-Merino, J. I. Paredes, S. Villar-Rodil, C. Fernandez-Sanchez, L. Guardia, A. Martinez-Alonso and J. M. D. Tascon, *J. Mater. Chem. A*, 2014, **2**, 7295.
103. X. J. Yang, L. L. Li, W. L. Sang, J. L. Zhao, X. X. Wang, C. Yu, X. H. Zhang and C. C. Tang, *J. Alloys Compd.*, 2017, **693**, 642.
104. Y. W. Wu, X. Wu, Q. W. Liu, C. J. Huang and X. Q. Qiu, *Int. J. Hydrogen Energy*, 2017, **42**, 16003.
105. D. Fan, X. Lv, J. Feng, S. Zhang, J. Bai, R. Lu and J. Liu, *Int. J. Hydrogen Energy*, 2017, **42**, 11312.
106. P. W. Wu, W. S. Zhu, A. M. Wei, B. L. Dai, Y. H. Chao, C. F. Li, H. M. Li and S. Dai, *Chem. Eur. J.*, 2015, **21**, 15421.
107. H. Y. Ji, J. Sun, P. W. Wu, B. L. Dai, Y. H. Chao, M. Zhang, W. Jiang, W. S. Zhu and H. M. Li, *J. Mol. Catal. A: Chem.*, 2016, **423**, 207.
108. P. W. Wu, W. S. Zhu, B. L. Dai, Y. H. Chao, C. F. Li, H. P. Li, M. Zhang, W. Jiang and H. M. Li, *Chem. Eng. J.*, 2016, **301**, 123.
109. N. Meyer, K. Bekaert, D. Pirson, M. Devillers and S. Hermans, *Catal. Commun.*, 2012, **29**, 170.
110. L. C. Wang, L. L. Shen, X. H. Xu, L. Q. Xu and Y. T. Qian, *RSC Adv.*, 2012, **2**, 10689.
111. M. M. Sun, Q. Fu, L. J. Gao, Y. P. Zheng, Y. Y. Li, M. S. Chen and X. H. Bao, *Nano Res.*, 2017, **10**, 1403.

112. W. Zhu, Z. Wu, G. S. Foo, X. Gao, M. Zhou, B. Liu, G. M. Veith, P. Wu, K. L. Browning, H. N. Lee, H. Li, S. Dai and H. Zhu, *Nat. Commun.*, 2017, **8**, 15291.
113. Y. Wang, L. Shi, W. D. Lu, Q. Sun, Z. F. Wang, C. Y. Zhi and A. H. Lu, *ChemCatChem*, 2017, **9**, 1363.
114. L. J. Gao, Y. Wang, H. B. Li, Q. H. Li, N. Ta, L. Zhuang, Q. Fu and X. H. Bao, *Chem. Sci.*, 2017, **8**, 5728.
115. Y. Cao, M. Lu, J. Fang, L. Shi and D. Zhang, *Chem. Commun.*, 2017, **53**, 7549.
116. R. Q. Li, J. Q. Liu, L. H. Li, H. B. Wang, Z. Q. Weng, S. K. H. Lam, A. J. Du, Y. Chen, C. J. Barrow and W. R. Yang, *Chem. Commun.*, 2014, **50**, 225.
117. J. Choi, D. A. Reddy and T. K. Kim, *Ceram. Int.*, 2015, **41**, 13793.
118. W. Wu, X. M. Lv, J. X. Wang and J. M. Xie, *J. Colloid Interface Sci.*, 2017, **496**, 434.
119. X. F. Wu, Z. H. Zhao, Y. Sun, H. Li, C. X. Zhang, Y. J. Wang, Y. Liu, Y. D. Wang, X. Y. Yang and X. D. Gong, *J. Nanopart. Res.*, 2017, **19**, 193.
120. Z. Chen, X. Chen, J. Di, Y. Liu, S. Yin, J. Xia and H. Li, *J. Colloid Interface Sci.*, 2017, **492**, 51.
121. Y. Song, H. Xu, C. Wang, J. Chen, J. Yan, Y. Xu, Y. Li, C. Liu, H. Li and Y. Lei, *RSC Adv.*, 2014, **4**, 56853.
122. C. S. Zhu, J. T. Zheng, L. Y. Fang, P. Hu, Y. K. Liu, X. Q. Cao and M. B. Wu, *J. Mol. Catal. A: Chem.*, 2016, **424**, 135.
123. H. Xu, L. Liu, Y. Song, L. Huang, Y. Li, Z. Chen, Q. Zhang and H. Li, *J. Alloys Compd.*, 2016, **660**, 48.
124. L. Fu, G. Chen, N. Jiang, J. Yu, C. T. Lin and A. Yu, *J. Mater. Chem. A*, 2016, **4**, 19107.
125. Q. R. Fu, Y. Meng, Z. L. Fang, Q. Q. Hu, L. Xu, W. H. Gao, X. C. Huang, Q. Xue, Y. P. Sun and F. S. Lu, *ACS Appl. Mater. Interfaces*, 2017, **9**, 2469.
126. N. Hussain, P. Gogoi, M. R. Das, P. Sengupta, V. E. Fedorov, I. P. Asanov, M. N. Kozlova and S. B. Artemkina, *Appl. Catal. A-Gen.*, 2017, **542**, 368.
127. S. Paulose, R. Raghavan and B. K. George, *J. Colloid Interface Sci.*, 2017, **494**, 64.
128. Y. Monguchi and H. Sajiki, *Kobunshi Ronbunshu*, 2011, **68**, 232.
129. C. M. Pradier, M. Mazina, Y. Berthier and J. Oudar, *J. Mol. Catal.*, 1994, **89**, 211.
130. G. Vile, D. Albani, M. Nachtegaal, Z. Chen, D. Dontsova, M. Antonietti, N. Lopez and J. Perez-Ramirez, *Angew. Chem. Int. Ed.*, 2015, **54**, 11265.
131. M. Gao, A. Lyalin and T. Taketsugu, *J. Phys. Chem. C*, 2012, **116**, 9054.
132. M. Gao, A. Lyalin and T. Taketsugu, *Int. J. Quantum Chem.*, 2013, **113**, 443.
133. S. Lin, X. Ye, R. S. Johnson and H. Guo, *J. Phys. Chem. C*, 2013, **117**, 17319.
134. F. Colmati, E. Antolini and E. R. Gonzalez, *J. Power Sources*, 2006, **157**, 98.
135. M. Winter and R. J. Brodd, *Chem. Rev.*, 2004, **104**, 4245.
136. M. H. Shao, K. Sasaki and R. R. Adzic, *J. Am. Chem. Soc.*, 2006, **128**, 3526.
137. Y. Li, L. Tang, S. Peng, Z. Li and G. Lu, *CrystEngComm.*, 2012, **14**, 6974.
138. N. Z. Bao, L. M. Shen, T. Takata and K. Domen, *Chem. Mater.*, 2008, **20**, 110.
139. J. Xu, L. Wang and X. J. Cao, *Chem. Eng. J.*, 2016, **283**, 816.
140. H. B. Zeng, C. Y. Zhi, Z. H. Zhang, X. L. Wei, X. B. Wang, W. L. Guo, Y. Bando and D. Golberg, *Nano Lett.*, 2010, **10**, 5049.

141. S. Azevedo, J. R. Kaschny, C. M. C. de Castilho and F. D. Mota, *Eur. Phys. J. B*, 2009, **67**, 507.
142. J. He, H. Liu, B. Xu and X. Wang, *Small*, 2015, **11**, 1144.
143. M. Kooti and E. Nasiri, *J. Mol. Catal. A: Chem.*, 2015, **406**, 168.
144. L. H. Wee, F. Bonino, C. Lamberti, S. Bordiga and J. A. Martens, *Green Chem.*, 2014, **16**, 1351.
145. W. S. Zhu, W. L. Huang, H. M. Li, M. Zhang, W. Jiang, G. Y. Chen and C. R. Han, *Fuel Process. Technol.*, 2011, **92**, 1842.
146. L. Bromberg and T. A. Hatton, *ACS Appl. Mater. Interfaces*, 2011, **3**, 4756.
147. N. R. Shiju, A. H. Alberts, S. Khalid, D. R. Brown and G. Rothenberg, *Angew. Chem. Int. Ed.*, 2011, **50**, 9615.
148. E. V. Ramos-Fernandez, C. Pieters, B. van der Linden, J. Juan-Alcaniz, P. Serra-Crespo, M. Verhoeven, H. Niemantsverdriet, J. Gascon and F. Kapteijn, *J. Catal.*, 2012, **289**, 42.
149. J. Zeng and S. P. Jiang, *J. Phys. Chem. C*, 2011, **115**, 11854.
150. J. Xiong, W. S. Zhu, H. P. Li, W. J. Ding, Y. H. Chao, P. W. Wu, S. H. Xun, M. Zhang and H. M. Li, *Green Chem.*, 2015, **17**, 1647.
151. W. S. Zhu, Y. X. Ding, H. M. Li, J. Qin, Y. H. Chao, J. Xiong, Y. H. Xu and H. Liu, *RSC Adv.*, 2013, **3**, 3893.
152. A. Lyalin, A. Nakayama, K. Uosaki and T. Taketsugu, *J. Phys. Chem. C*, 2013, **117**, 21359.
153. P. Wu, W. Zhu, Y. Chao, J. Zhang, P. Zhang, H. Zhu, C. Li, Z. Chen, H. Li and S. Dai, *Chem. Commun.*, 2016, **52**, 144.
154. P. W. Wu, B. L. Dai, Y. H. Chao, Y. C. Wu, W. Jiang, C. F. Li, W. S. Zhu and H. M. Li, *Molecular Catalysis*, 2017, **436**, 53.
155. L. F. Gutierrez, S. Hamoudi and K. Belkacemi, *Int. Dairy J.*, 2012, **26**, 103.
156. S. Karski, I. Witonska and J. Goluchowska, *J. Mol. Catal. A: Chem.*, 2006, **245**, 225.
157. A. V. Tokarev, E. V. Murzina, J. Kuusisto, J. P. Mikkola, K. Eranen and D. Y. Murzin, *J. Mol. Catal. A: Chem.*, 2006, **255**, 199.
158. J. H. Southard and F. O. Belzer, *Annu. Rev. Med.*, 1995, **46**, 235.
159. D. Q. Han, T. T. Xu, J. X. Su, X. H. Xu and Y. Ding, *ChemCatChem*, 2010, **2**, 383.
160. Y. X. Zhang, L. Q. Xu, B. Tang and Z. W. Li, *Catal. Sci. Tech.*, 2013, **3**, 222.
161. X. W. Xie, Y. Li, Z. Q. Liu, M. Haruta and W. J. Shen, *Nature*, 2009, **458**, 746.
162. J. Z. Yin, Z. N. Yu, F. Gao, J. J. Wang, H. A. Pang and Q. Y. Lu, *Angew. Chem. Int. Ed.*, 2010, **49**, 6328.
163. J. J. Zhu, S. A. C. Carabineiro, D. Shan, J. L. Faria, Y. J. Zhu and J. L. Figueiredo, *J. Catal.*, 2010, **274**, 207.
164. Z. Lu, P. Lv, Y. Liang, D. Ma, Y. Zhang, W. Zhang, X. Yang and Z. Yang, *Phys. Chem. Chem. Phys.*, 2016, **18**, 21865.
165. X. Y. Liu, A. Q. Wang, L. Li, T. Zhang, C. Y. Mou and J. F. Lee, *J. Catal.*, 2011, **278**, 288.
166. J. C. Bauer, G. M. Veith, L. F. Allard, Y. Oyola, S. H. Overbury and S. Dai, *ACS Catal.*, 2012, **2**, 2537.
167. N. F. Zheng and G. D. Stucky, *J. Am. Chem. Soc.*, 2006, **128**, 14278.
168. K. Vignesh, A. Suganthi, B. K. Min, M. Rajarajan and M. Kang, *RSC Adv.*, 2015, **5**, 576.

169. M. Zahmakiran, F. Durap and S. Ozkar, *Int. J. Hydrogen Energy*, 2010, **35**, 187.
170. Y. Yang, Z.-H. Lu, Y. Hu, Z. Zhang, W. Shi, X. Chen and T. Wang, *RSC Adv.*, 2014, **4**, 13749.
171. A. Bulut, M. Yurderi, I. E. Ertas, M. Celebi, M. Kaya and M. Zahmakiran, *Appl. Catal. B-Environ.*, 2016, **180**, 121.
172. M. Chandra and Q. Xu, *J. Power Sources*, 2007, **168**, 135.
173. W. Chen, J. Ji, X. Feng, X. Duan, G. Qian, P. Li, X. Zhou, D. Chen and W. Yuan, *J. Am. Chem. Soc.*, 2014, **136**, 16736.
174. J. Y. Zhu, H. Wang, W. T. Cai, J. W. Liu, L. Z. Ouyang and M. Zhu, *Int. J. Hydrogen Energy*, 2017, **42**, 15790.
175. S. Handa, Y. Wang, F. Gallou and B. H. Lipshutz, *Science*, 2015, **349**, 1087.
176. M. Gholinejad, M. Razeghi, A. Ghaderi and P. Biji, *Catal. Sci. Tech.*, 2016, **6**, 3117.
177. O. V. Yazyev and A. Pasquarello, *Phys. Rev. B: Condens. Matter*, 2010, **82**, 045407.
178. S. Lin, J. Huang and X. X. Ye, *Appl. Surf. Sci.*, 2014, **320**, 237.
179. G. A. Rance, W. A. Solomonsz and A. N. Khlobystov, *Chem. Commun.*, 2013, **49**, 1067.
180. S. J. Guo, X. L. Pan, H. L. Gao, Z. Q. Yang, J. J. Zhao and X. H. Bao, *Chem. Eur. J.*, 2010, **16**, 5379.
181. B. W. Smith, M. Monthioux and D. E. Luzzi, *Nature*, 1998, **396**, 323.
182. T. Okazaki, Y. Iizumi, S. Okubo, H. Kataura, Z. Liu, K. Suenaga, Y. Tahara, M. Yudasaka, S. Okada and S. Iijima, *Angew. Chem. Int. Ed.*, 2011, **50**, 4853.
183. B. Botka, M. E. Fuestoes, H. M. Tohati, K. Nemeth, G. Klupp, Z. Szekrenyes, D. Kocsis, M. Utczas, E. Szekely, T. Vaczi, G. Tarczay, R. Hackl, T. W. Chamberlain, A. N. Khlobystov and K. Kamaras, *Small*, 2014, **10**, 1369.
184. Y. K. Chen, A. Chu, J. Cook, M. L. H. Green, P. J. F. Harris, R. Heesom, M. Humphries, J. Sloan, S. C. Tsang and J. F. C. Turner, *J. Mater. Chem.*, 1997, **7**, 545.
185. J. Sloan, J. Hammer, M. Zwiefka-Sibley and M. L. H. Green, *Chem. Commun.*, 1998, **0**, 347.
186. W. Chen, Z. Fan, X. Pan and X. Bao, *J. Am. Chem. Soc.*, 2008, **130**, 9414.
187. D. Deng, L. Yu, X. Chen, G. Wang, L. Jin, X. Pan, J. Deng, G. Sun and X. Bao, *Angew. Chem. Int. Ed.*, 2013, **52**, 371.
188. A. N. Khlobystov, *ACS Nano*, 2011, **5**, 9306.
189. Y. Liao, Z. Chen, J. W. Connell, C. C. Fay, C. Park, J. W. Kim and Y. Lin, *Adv. Funct. Mater.*, 2014, **24**, 4497.
190. C. Y. Zhi, Y. Bando, C. C. Tang, S. Honda, K. Sato, H. Kuwahara and D. Golberg, *J. Phys. Chem. B*, 2006, **110**, 1525.
191. H. Chen, Y. Chen, J. Yu and J. S. Williams, *Chem. Phys. Lett.*, 2006, **425**, 315.

2. Opening and Purification of BNNT

2.1 Introduction

Carbon nanotubes (CNT) – often described as the world's smallest test tube – behave as excellent nanoscale containers for molecules,[1-3] metals[4-6] and metal halides,[7] where the spontaneous encapsulation is driven by van der Waals forces that stabilise the confined guest-species in the internal channel of the host-nanotube.[8] Moreover, a good geometric fit between the critical dimensions of the encapsulated guest and the internal dimensions of the host can result in van der Waals forces that are sufficiently high that insertion is irreversible. This effective nanoscale confinement permits the study of the structure,[9, 10] motion[11] and dynamics[12, 13] of individual molecules.

Whilst less well explored relative to CNT, boron nitride nanotubes (BNNT) represent a remarkable class of one-dimensional nanoscale containers for metals,[14-19] metal halides[20, 21] and molecules, such as C_{60}.[22] Yet, the significant difference in chemical properties between BNNT and CNT, such as the polarity of interatomic bonding, delocalisation of π electrons and polarizability, are likely to affect the structure and properties of the encapsulated guest materials. The lack of literature reported for the filling of BNNT means that many of these important questions remain unanswered.

A fundamental requirement for the transfer of any guest-species into the inner cavity of a host-nanotube is the presence of accessible holes through which the guests can pass. At present, there are no established methods to reliably and

reproducibly open BNNT. Moreover, as-prepared BNNT often contain a variety of impurities, such as elemental boron, *h*-BN and amorphous particles, which can inhibit the access of guest-molecules to the internal channel of BNNT and preclude a complete understanding of physicochemical properties of BNNT in host-guest systems. Together, these represent major barriers restricting the advancement of BNNT as nanocontainers and nanoreactors.

Whilst the opening and purification of CNT has been refined over the years, with methods including ball milling[23] and high temperature oxidation in air,[5] these approaches are potentially not directly transferable to BNNT owing to differences in the fundamental chemical reactivity of CNT and BNNT. Nevertheless, several possible strategies for the selective opening and purification of BNNT have been explored.

The surfactant purification approach utilises surface-active agents, or surfactants, to control the interfacial tension of the various components present in a raw, unprocessed BNNT sample and thus enables the selective removal of impurities. Chunyi Zhi *et al*. have reported an effective method for the removal of BN particles and fibres with large diameters from BNNT utilising π-π interactions between poly(m-phenylenevinylene-co-2,5-dioctoxy-p-phenylenevinylene) (PmPV) and BNNT to selectively wrap and solubilise the nanotubes.[24] PmPV tends to coiling and form helical structures, believed to easily wrap around the nanotube. Sonication of wrapped BNNT makes them soluble. The mixture is then centrifuged, and the insoluble impurities are removed. However, this approach is not effective for opening BNNT or removing any impurities encapsulated within the internal channel.

BNNT are extremely chemically robust nanoscale structures and so highly reactive species are typically required to covalently modify the exterior surface. For

example, sonication of BNNT in aqueous ammonia solution has been reported as an effective route towards the modification of the surface functionality.[25] Analogous to the high temperature treatment of CNT in air, this procedure can both selectively remove the end-caps and reduce the mean length of BNNT. In this approach, the lone pair of electrons on the N atom of the ammonia molecules interact with the empty p_z orbital of B in the as-received BNNT (Figure 29), activating B-N bonds towards hydrolysis and causing the corrosion, thinning and removal of the BNNT end-caps.

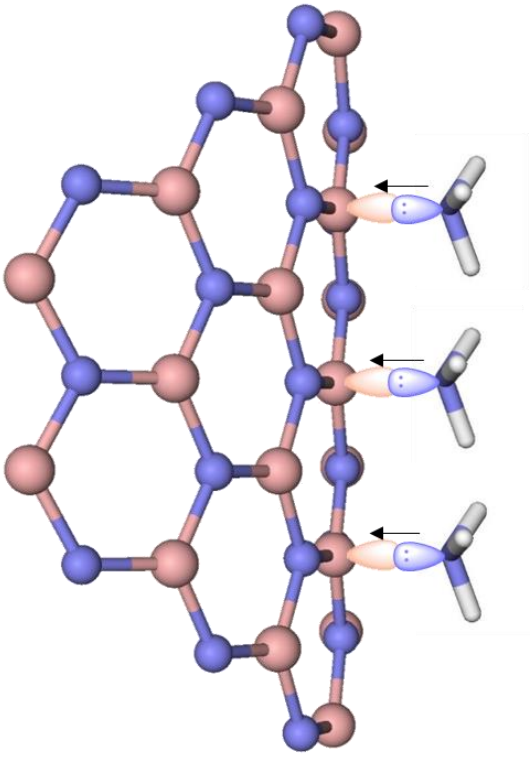


Figure 29. Schematic to show the bonding between boron nitride nanotubes and ammonia molecules. A pair of electrons are donated from the sp^3 orbital of nitrogen in ammonia to the p_z orbital of boron in the boron nitride nanotubes. Purple atoms represent nitrogen, pink represent boron and white represents hydrogen.

The interaction of multiple ammonium molecules may significantly weaken the B-N bonds and make them much more susceptible to sonication-assisted

hydrolysis.[25] The end-caps typically contain strained four- or eight- membered rings,[26, 27] making them more reactive towards water molecules than the less strained six-membered rings forming the sidewalls and thus are selectively removed. The resultant BNNT are terminated with either ammonia, or hydroxyl groups as a result of hydrolysis, causing them to be more hydrophilic and dispersible in water.

A simple method to remove fine boron nitride particles, described by Chen *et al.*,[28] involves heating the raw BNNT sample at 800 ˚C for 1 h and results in the selective oxidation of most of the fine boron nitride particles present, whilst preserving the structure of thin BNNT. It was reported that heating at 750 ˚C partially oxidised boron nitride particles, whereas heating at 850 ˚C resulted in the undesired damage to some of the nanotubes. After oxidation, the formed boron oxide (B_2O_3) can simply be washed away with hot water and the pure BNNT collected by filtration.

A range of approaches are reported for opening and purifying BNNT, yet no one particular method stands out or has become established, and there are a number of limitations to all of the methods reported. By understanding the chemical behaviour of BNNT, it is likely that heating will oxidise the entire surface of the BNNT, adding material to the outer walls, instead of removing the caps. Methods like sonication assisted hydrolysis could severely damage the nanotubes. The removal of impurities from surfactant wrapped BNNT, while reported to be successful for longer BNNT, may not be as effective for shorter/ opened BNNT. Other methods which have not been attempted for opening and/or purifying BNNT could prove to be even more successful than those reported. For instance, ball-milling has not been explored for opening BNNT, yet has the potential to be a clean method of opening BNNT through

physically breaking the nanotubes. A range of methods must therefore be evaluated to determine the most desirable technique.

2.2 Aim and Objectives

In order to produce BNNT which are suitable for filling with guest molecules and nanoparticles, the principle challenge is to selectively remove the end-caps and remove any impurities which could block the cavity. The aim of this study is therefore to explore a range of different methods of opening and purifying BNNT. Three methods will be appraised herein: oxidation in air (Method 1), ball milling (Method 2) and hydrolysis, followed by oxidation in air (Method 3). These methods were chosen owing to their reported success for the effective opening of either BNNT or CNT. For systematic comparisons, a common batch of BNNT is necessary and therefore BNNT synthesised by the pressurised vapour/condenser (PVC) method and sourced from www.bnnt.com – the only current commercial supplier of BNNT at the time of writing – will be used throughout this study.

To evaluate the success of these methods, the reduction in length and the percentage of open nanotubes was appraised using statistical analysis of transmission electron microscopy (TEM) images. This technique is used to directly observe nanomaterials and can be used to assess the structure of the BNNT. An electron gun is used to generate electrons, which are accelerated towards an anode, through a condenser lens and focused upon a sample. Elastically scattered electrons pass through a variety of lenses to reach a detector and generate an image. A typical resolution of 0.2 nm is achieved.

The purity of the sample was evaluated by attaining the B:N elemental ratio from energy dispersive X-ray (EDX) spectroscopy. In this technique, electrons in the sample are excited under an electron beam, leading to the release of an X-ray, characteristic of the elements. The relative intensities corresponding to each element can then be used to calculate the relative atomic percentages and thus the stoichiometry/ composition of the appraised material. An ideal, impurity-free sample of BNNT should comprise an elemental ratio of 1:1. The procedure judged to be the most successful was applied to BNNT for all further work in this thesis.

2.3 Results and Discussion

2.3.1 Analysis of as-received BNNT

In order to determine the nanoscale structure and purity of the as-received BNNT product, samples were initially analysed by a range of spectroscopy and microscopy approaches. Simple visual inspection of the solid implied that non-BNNT impurities were present, with the grey colouration consistent with the inclusion of elemental boron in the supplied fluffy powder. To examine the structure of the as-received material Raman and IR spectroscopies and powder X-ray diffraction (PXRD) were employed (Figure 30). In Raman spectroscopy, a photon of a fixed energy interacts with the material, and the change in energy of the scattered photon is detected as the Raman shift. Information about molecular vibrations, phonons and other processes in the material can then be obtained, providing insight into the structure of the material. In IR spectroscopy, infrared radiation interacts with the material causing stretching and bending modes. The absorbance of IR light by the

sample provides information about these modes and thus the nature of the material. PXRD involves irradiating the sample with X-rays, which may then be diffracted, depending on the incident angle, to reach a detector. The technique works by scanning through a range of angles and detecting where diffraction has occurs, to provide information about the atomic spacing in the material.

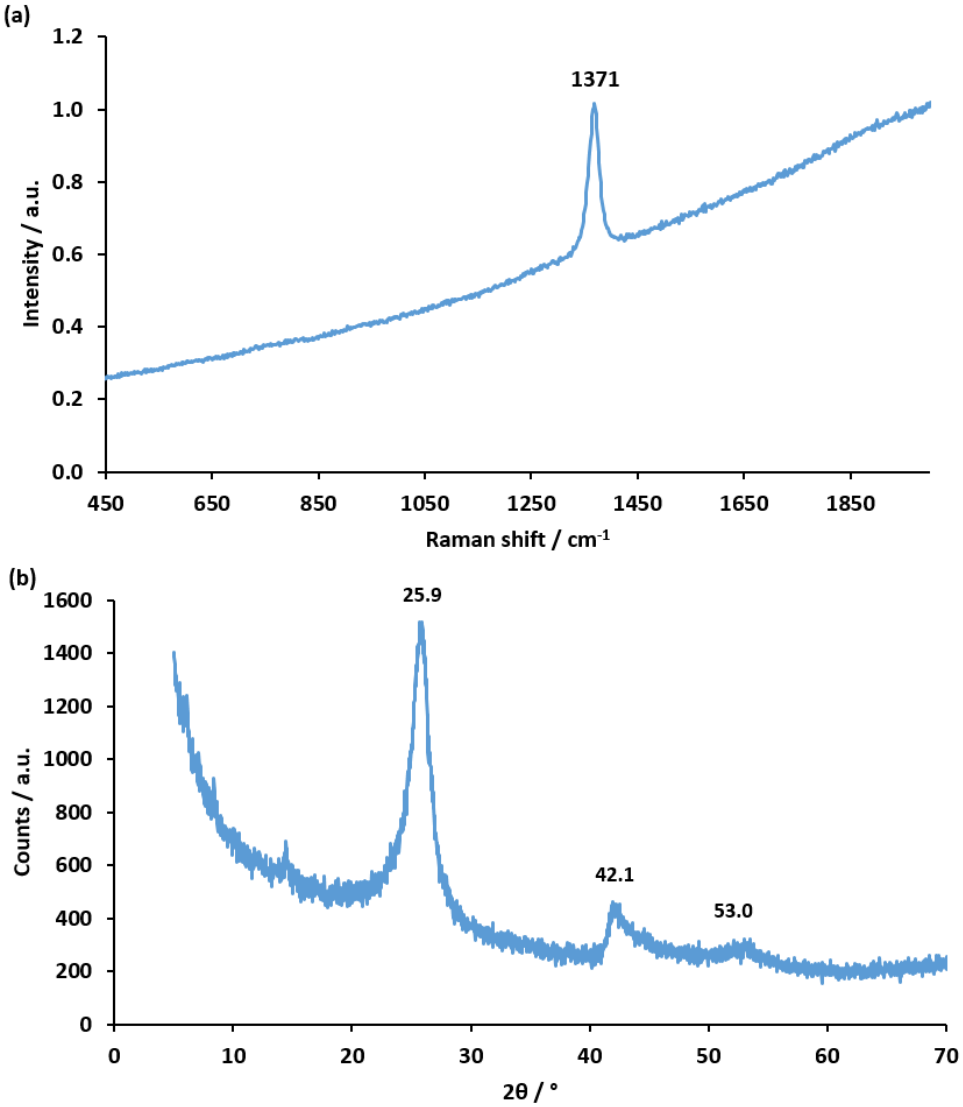


Figure 30. (a) The UV Raman spectrum of as-received BNNT shows the characteristic peak at 1371 cm^{-1} which corresponds to a B-N stretching vibrational mode of E_{2g} symmetry in hexagonal boron nitride (*h*-BN). (b) Powder X-ray diffraction (PXRD) analysis shows peaks at 25.9, 42.1 and 53.0˚ corresponding to the (002), (100) and (004) planes of BNNT.

2. Opening and Purification of BNNT

In the UV Raman spectrum (λ_{ex} = 355 nm) only one peak was observed at 1371 cm^{-1} which correlates well with the B-N stretching vibrational mode of E_{2g} symmetry in *h*-BN. This was confirmed by IR spectroscopy (data not shown), where peaks at 1363 and 802 cm^{-1} corresponding to v_{BN} in-plane (ip) stretch and BN out-of-plane (oop) buckling mode in BNNT respectively were noted. Moreover, strong luminescence observed in the UV Raman spectrum, contributing to a non-zero baseline, confirmed the presence of non-BNNT impurities.[29] The three features in the PXRD spectrum of as-received BNNT at 25.9, 42.1 and 53.0˚ were identified as the (002), (100) and (004) planes of BNNT.[30, 31] No further features were present, suggesting that any impurities present in the sample were amorphous.

As neither spectroscopy nor diffraction approaches enabled definitive identification of the structure and purity of the as-produced BNNT material, a small sample was dispersed in methanol and deposited on lacy carbon films supported on a copper grids and analysed by TEM (Figure 31).

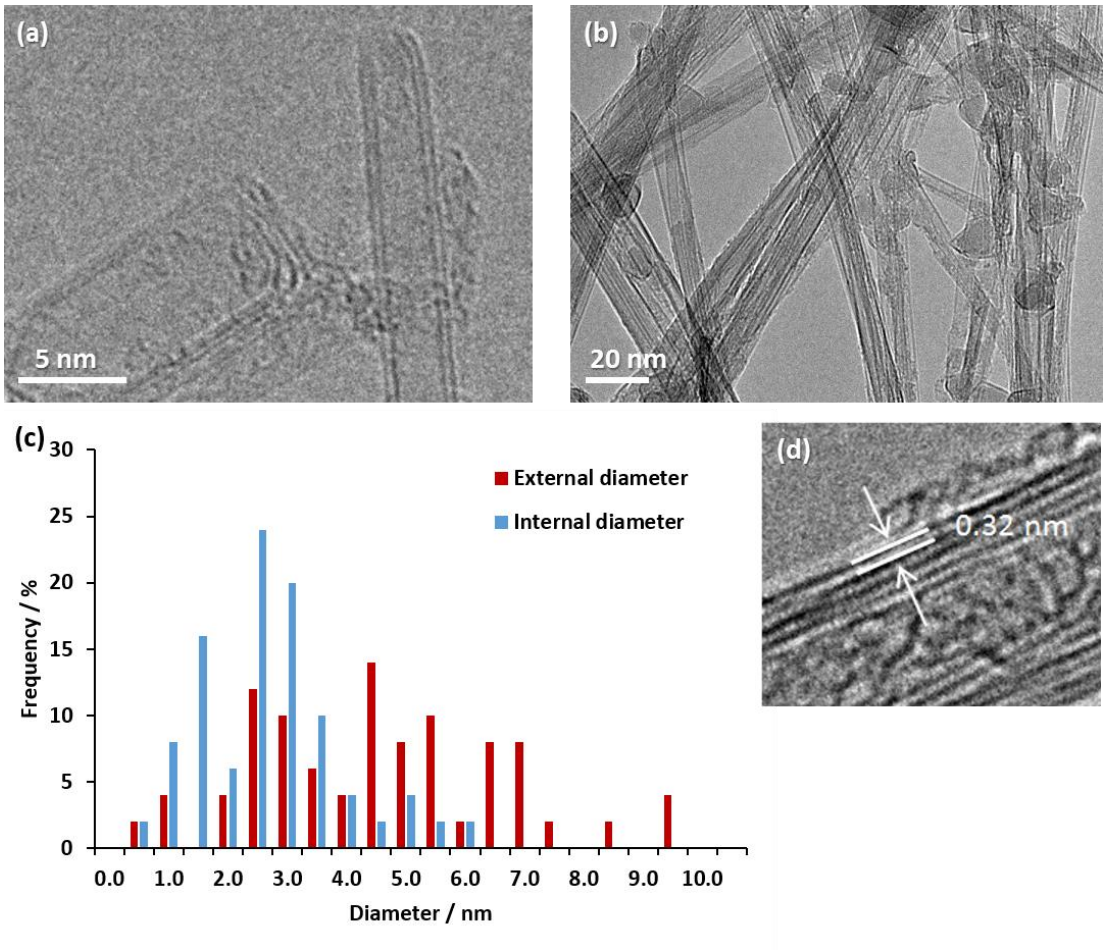


Figure 31. TEM analysis showing (a) the closed termini of BNNT and (b) the broad range of BNNT diameters and boron impurities present. A measured d-spacing of 0.34 nm (d) is consistent with the (0002) lattice plane in hexagonal boron nitride. (c) Statistical analysis of multiple micrographs revealed that the mean internal and external diameters of BNNT were 2.45 ± 1.19 and 4.32 ± 2.09 nm respectively, the number of walls ranged between 1 and 5 (with 2 or 3 the most common) and the mean length was greater than 200 µm.

TEM observations indicated that nanotubes were extremely long (L_{NT} > 200 µm) and whilst the internal diameter of BNNT (d_{NT}^{INT} = 2.45 ± 1.19 nm) was large enough to accommodate the majority of small molecules, e.g. C_{60} has a van der Waals diameter of 1.0 nm, most nanotubes were capped and possessed a moderate amount of boron-containing impurities which would prohibit the transport of C_{60} into the inner channel. Furthermore, EDX spectroscopy was used to appraise the composition of the material (Figure 32).

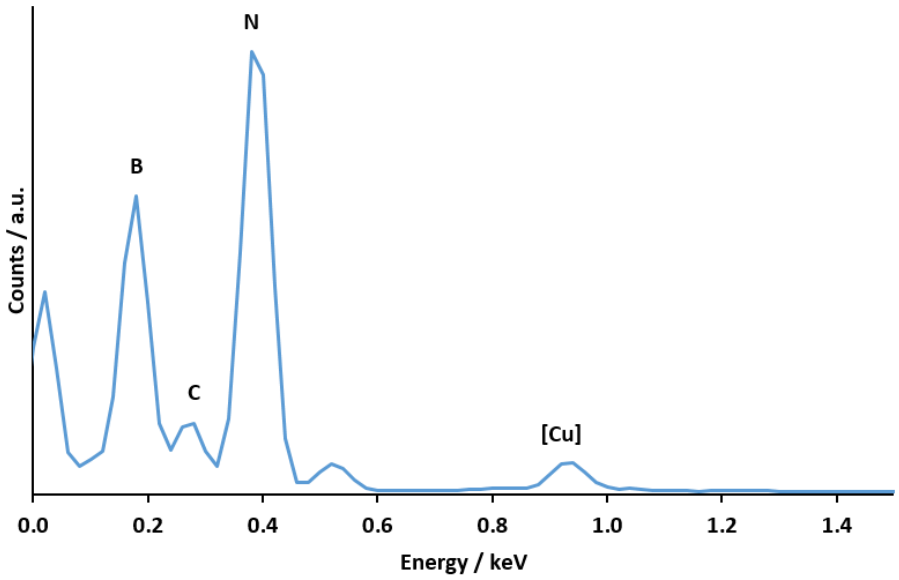


Figure 32. Energy dispersive X-ray (EDX) analysis indicates that the ratio of B:N is 61:39, confirming the presence of elemental boron as an impurity. Copper and carbon are detected from the TEM grid.

From this analysis, a significant excess of boron relative to nitrogen (B:N is 61:39) was observed and thus an effective method for opening and purification of BNNT was critically required.

2.3.2 Opening and purifying BNNT

2.3.2.1 Method 1: Oxidation in air

The first method employed for the opening and purification of BNNT involved heating the as-received material from room temperature to 800 ˚C at 10 ˚C min^{-1} in air and then maintaining at 800 ˚C for 60 min. This experiment was conducted inside a thermogravimetric analyser, in order that the thermal properties could be appraised, whilst simultaneously producing a purified BNNT material (Figure 33). The

initial grey, fluffy BNNT turned white and brittle after heating, qualitatively indicating the removal of impurities of elemental boron. The yield of 4.13 mg, compared to the starting mass of 3.86 mg, shows the gain in material through this method, rather than simply removing impurities and opening the caps.

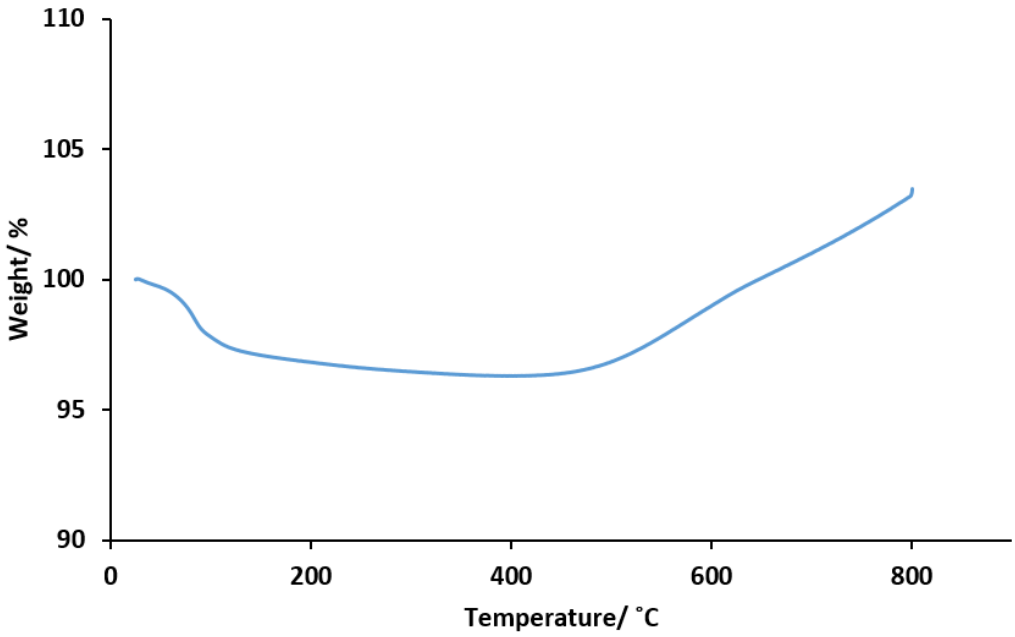


Figure 33. Thermogravimetric analysis (TGA) of BNNT, highlighting the excellent thermal stability of BNNT in air. The small increase in mass above 500˚C is caused by oxidation of boron ($B + O_2 \rightarrow B_2O_3$) and boron nitride ($BN + O_2 \rightarrow B_2O_3 + NO + NO_2$) in the presence of atmospheric oxygen.

It is important to note that this experiment highlights the excellent thermal stability of BNNT, as no mass loss was observed across the entire heating range. This contrasts with CNT, which combust at elevated temperatures (300-800 °C) in the presence of oxygen, resulting in a mass loss associated with the formation of carbon dioxide.

A mass loss at approximately 100 ˚C was observed, attributed to the evaporation of associated water. Above 500 ˚C, a mass gain of 10% was noted,

associated with the oxidation of boron (as impurities, Equation 1) and boron nitride (from impurities and the nanotubes themselves, Equation 2).

$$\mathbf{B + O_2 \rightarrow B_2O_3\ (600 - 1100\ °C)}\ ^{32} \qquad \mathbf{(1)}$$

$$\mathbf{BN + O_2 \rightarrow B_2O_3 + NO + NO_2\ \ (760 - 860\ °C^*)} \qquad \mathbf{(2)}$$

* *ca*. 760 – 860 °C* for amorphous BN nanoparticles, *ca*. 860 – 1000 °C for bulk BN.[33]

The formation of boron oxide was confirmed by IR spectroscopy analysis of the sample after heating in air (data not shown). It was found that in addition to peaks at 1373 and 801 cm^{-1}, corresponding to known BN stretching and buckling modes in BNNT, new peaks at 3205 cm^{-1} (ν_{OH} stretch in B-OH), 1438 cm^{-1} (ν_{BO} stretch) and 1196 cm^{-1} (ν_{BOH} ip stretch) were observed. Whilst only the vibrational mode at 1438 cm^{-1} could be directly attributed to B_2O_3, it is known that when exposed to water, boron oxide reacts to form boric acid (Equation 3) and as such all other peaks are associated with formation of this further product.

$$\mathbf{B_2O_3 + 3H_2O \rightarrow 2B(OH)_3} \qquad \mathbf{(3)}$$

To probe the nanoscale structure of the resultant material, TEM was performed (Figure 34).

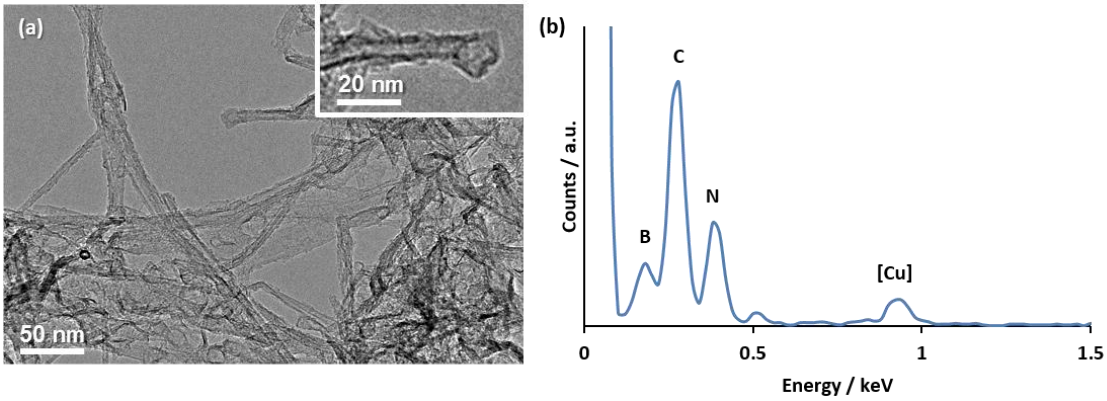


Figure 34. (a) TEM analysis of BNNT heated to 800 ˚C in air indicates that the termini remain closed, with no discernible reduction in length observed. (b) EDX analysis shows the ratio of B:N to be 87:13, consistent with the loss of boron nitride due to the formation of boron oxide under these conditions.

Analysis of the material subsequent to heating to 800 ˚C in air using TEM shows that this procedure is ineffective at opening BNNT as most of the nanotubes (>99%) remained closed with no significant change in the length measured (L_{NT} > 200 µm). Furthermore, many nanotubes appeared to be passivated with an amorphous coating, the composition of which was likely to be boron oxide, consistent with the IR spectroscopy observations and the noted decrease in the nitrogen content determined by EDX spectroscopy (B:N is 87:13) as boron nitride reacts with molecular oxygen at elevated temperatures to form B_2O_3.

2.3.4.2 Method 2: Ball milling

The second method explored involved ball milling, which subjects the nanotubes to high energy collisions from the ball and has proved a useful method for opening CNT.[23] In order to evaluate the transferability of this method, BNNT were loaded in a hardened steel jar equipped with a hardened steel ball and milled at 10 Hz for 90 min. The compressed grey solid was subsequently analysed by TEM and EDX

(Figure 35) to investigate if the nanotubes had been opened and if there was any noticeable change in the impurities present. No change in mass occurred since only mechanical deformations took place.

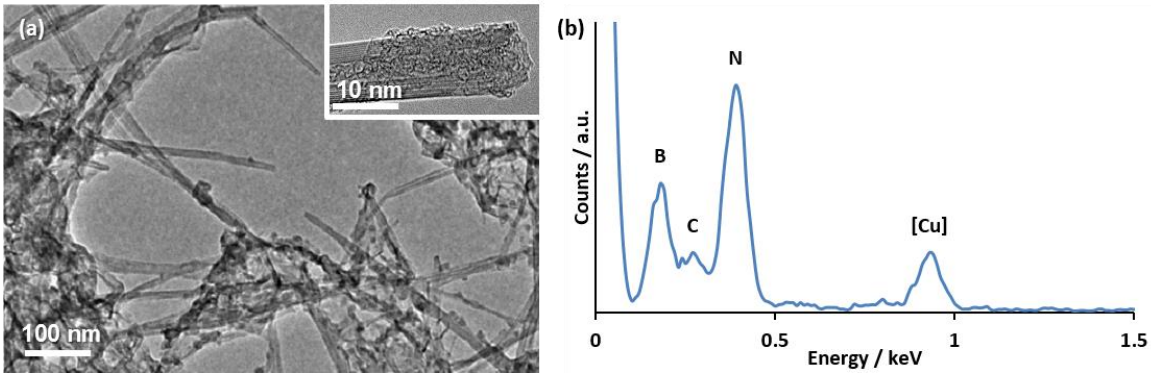


Figure 35. (a) TEM analysis of BNNT subjected to ball milling indicates that the afforded BNNT were largely open (80%) and significantly shorter (mean length is 1.98 ± 0.78 µm) than the as-received material. (b) EDX analysis shows the ratio of B:N to be 57:43.

TEM analysis indicated that around 80% of the BNNT were opened and appeared to have been significantly shortened (L_{NT} = 1.98 ± 0.78 µm). Shortening of the nanotubes is an attractive result, since transport resistance of molecules within the internal volume may be dependent on the length of the cylindrical container. An amorphous material, presumed to be boron or boron nitride, appeared to be coating and blocking some of the nanotubes which may lead to further difficulties when attempting to fill the nanotubes at a later stage. The observed decrease in the boron to nitrogen ratio (from 61:39 to 57:43 after ball milling) was unexpected as no mechanism of purification was provided utilising this approach. Thus this apparent difference in composition is more likely to reflect the inhomogeneity of the appraised sample.

2.3.4.3 Method 3: Hydrolysis followed by oxidation in air

The final method appraised in this study involved the dispersion of as-received BNNT in an aqueous solution of ammonium hydroxide using tip ultrasonication. The duration of tip ultrasonication was varied, where t = 4, 10 or 24 h, to enable the optimum treatment time to be identified. Extended exposure is likely to completely destroy the nanotubes structure, while too short a treatment may not open and shorten the BNNT. Changes to the surface functionality of BNNT during this treatment was evident in changes to the extent of suspended material. The initial clumps of grey and fluffy solid floated on the surface due to the high hydrophobicity of the material; however, as the sonication treatment proceeded, increasing amounts of the nanotubes became dispersed as ammonia reacted and the surface of the nanotubes became more hydrophilic. Any visible clumps of BNNT which had not dispersed were discarded and the resultant suspended grey/brown solid was collected by filtration and washed with deionised water. The collected solid was next heated to 800 ˚C to oxidise boron impurities and boron nitride nanoparticles.[28] The resulting BNNT were extracted into hot (*ca*. 90 ˚C) deionised water to remove water soluble B_2O_3 that formed during heating, washed with further hot water, collected by filtration and analysed by TEM and EDX spectroscopy (Figure 36). A reduction in mass from 100 mg to 52 mg (4 h-treated BNNT) was indicative of the removal of impurities, opening and/or shortening of BNNT.

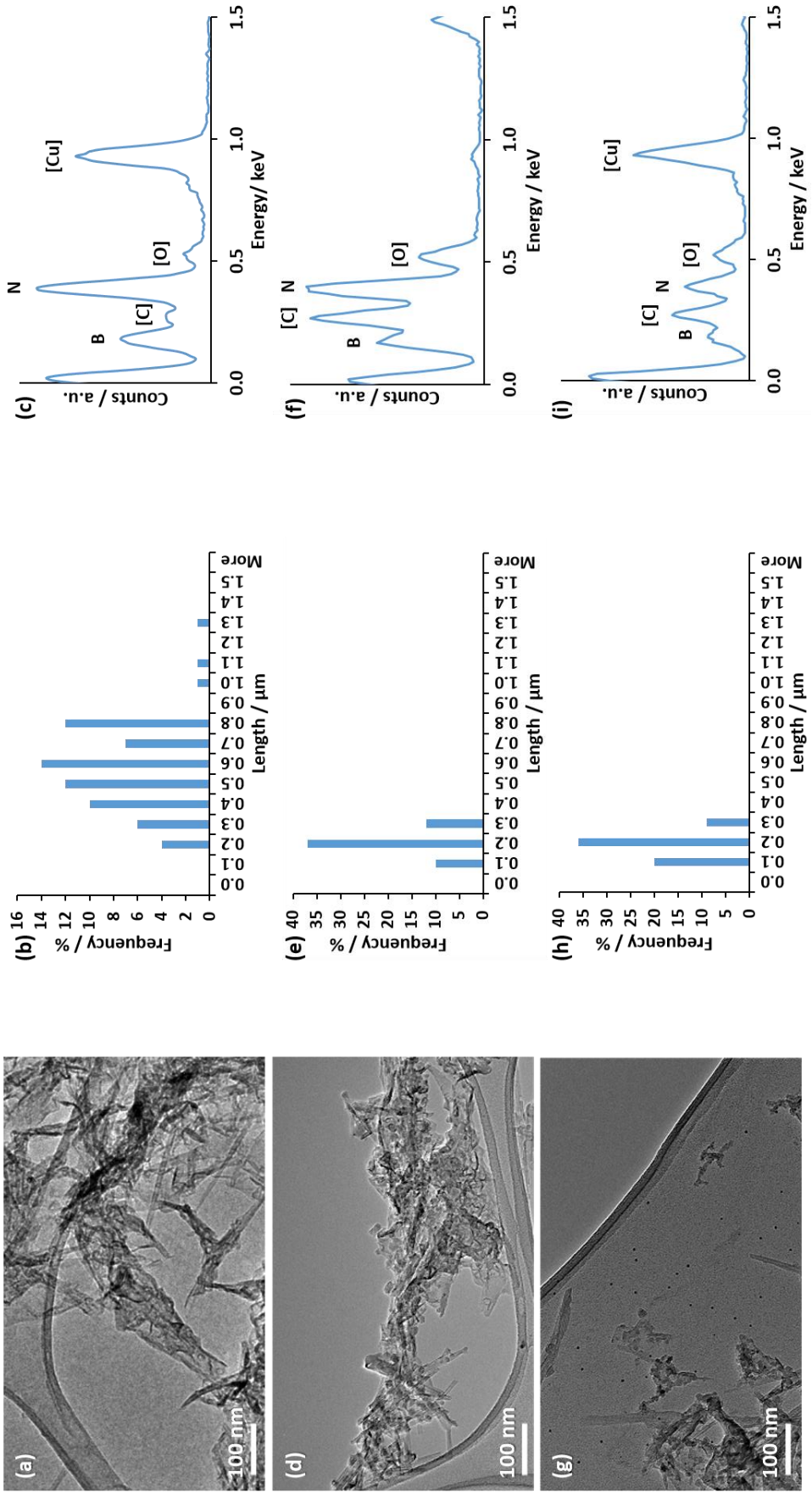


Figure 36. TEM/EDX analysis of BNNT purified by (a) 4, (d) 10 and (g) 24 h sonication in aqueous ammonium hydroxide solution, followed by oxidation in air, indicate that this method is effective for the removal of the nanotube endcaps, resulting in a reduction of the mean nanotube length (b, e and h respectively) and removing the boron-containing impurities (c, f and i respectively).

Statistical analysis of TEM images confirmed that a very high proportion of nanotube were open subsequent to this procedure (>80% independent of reaction time). Furthermore, a drastic reduction in the mean BNNT length was observed, with longer reaction times confirming greater reductions in nanotube length (L_{NT} = 0.55 ± 0.72, 0.16 ± 0.05 and 0.14 ± 0.06 μm for t = 4, 10 and 24 h respectively). Moreover, the purity of the samples, as determined by EDX spectroscopy, was greatly improved, approaching the ideal boron to nitrogen ratio of 50:50 (i.e. 1:1) in all cases. It is important to note, however, that as 4 h sonic treatment was sufficient to open, shorten and purify BNNT, extended sonication is not required and may potentially facilitate further damage to the nanotube sidewall structure.

2.3.4.4 Comparison of opening methods

The comparative success of the appraised methods are presented (Table 6) and highlight a significant amount of variation in the nanotube length, percentage of open nanotubes and purities as a function of the specific method applied.

Table 6. Comparison of methods for opening and purifying BNNT.

Method	Conditions	L_{NT} / µm [a]	% open [a]	B : N [b]
-	as-received	> 200	< 1	61 : 39
1	oxidation in air (800 ˚C, 1 h)	> 200	< 1	87 : 13
2	ball milling (10 Hz, 90 min)	1.98 ± 0.78	80	57 : 43
3a	hydrolysis (4 h), oxidation in air (800 ˚C, 1 h)	0.55 ± 0.22	83	51 : 49
3b	hydrolysis (10 h), oxidation in air (800 ˚C, 1 h)	0.16 ± 0.05	81	55 : 45
3c	hydrolysis (24 h), oxidation in air (800 ˚C, 1 h)	0.14 ± 0.06	88	55 : 45

[a] Determined by statistical analysis of TEM images. [b] Determined by EDX spectroscopy.

From this, it is evident that hydrolysis for 4 h, followed by high temperature oxidation in air (Method 3a) represents the ideal method for opening and purification of BNNT as it results in a significant reduction in the mean nanotube length from over 200 µm to 0.55 ± 0.22 µm, with a significant proportion of the nanotube tips removed (83%), which are generally free of the boron impurities.

2.3 Conclusions

A range of procedures for the opening, shortening and purification of BNNT have been appraised to test which strategy results in the most suitable BNNT host-material for filling with guest molecules and nanoparticles.

Through a combination of microscopy and spectroscopy approaches it was determined that oxidation in air (Method 1) is largely ineffective for opening and purifying BNNT (less than 1% of nanotubes were open) and is undoubtedly the least useful method of those explored. A marginal improvement was observed using ball

milling (Method 2) which resulted a high percentage of open BNNT (80%) and a moderate reduction in the amount of boron-containing impurities (B:N is 57:43). However, the combined method of hydrolysis followed by high temperature oxidation in air (Method 3) produced the most suitable material for filling with guest species as BNNT treated under these conditions were significantly shorter, mostly open and had fewer impurities. Moreover, it was found that 4 h of tip sonication during the initial hydrolysis step was sufficient to affect these improvements in structure (L_{NT} = 0.55 ± 0.22 μm,% of open tubes = 83) and purity (B:N is 51:49), whilst inhibiting the introduction of surface disorder and maintaining the tubular morphology of BNNT. Consequently, this method is the sole method that will be used for opening and purifying BNNT in subsequent chapters.

2.4 Experimental

All common reagents and solvents were purchased from Sigma-Aldrich, UK and used without further purification unless stated otherwise. Water was purified (> 18.0 MΩ cm) using a Barnstead NANOpure II system. BNNT were purchased from BNNT LLC, produced using the high temperature high pressure method. TEM imaging was performed using a JEOL 2100F TEM (field emission gun source, information limit < 0.19 nm) at 100 kV at room temperature. EDX spectra were recorded using an Oxford Instruments 30mm^2 Si(Li) detector or an Oxford Instruments x-Max 80 SDD running on an INCA microanalysis system. Samples for TEM EDX were typically prepared by casting several drops of a suspension of nanotubes onto copper-grid mounted “lacy” carbon films. Raman spectroscopy was conducted using a laser wavelength of 355 nm. IR spectroscopy was performed using a Bruker IFS 66v FTIR

spectrometer, using KBr pellets at room temperature. Thermogravimetric analysis (TGA) was performed using a TA Instruments SDT Q600 under a flow of air at a heating rate of 10 °C min^{-1} from room temperature to 1000 °C. Powder X-Ray diffraction measurements were performed on a PANalytical X'Pert PRO diffractometer equipped with a Cu Kα radiation source (λ = 1.5418 Å) in Bragg-Brentano geometry using a Si zero-background holder.

2.4.1 Opening and purifying BNNT

2.4.1.1 Method 1- Oxidation in air

As-received BNNT (3.86 mg) were heated from room temperature to 800 ˚C at 10 ˚C min^{-1} in air and then held at 800 ˚C for 60 min. The initial grey, fluffy BNNT turned white and brittle after heating. Mass = 4.12 mg.

2.4.1.2 Method 2- Ball milling

As-received BNNT (5.05 mg) were loaded in a hardened steel jar (1.5 mL capacity) equipped with a hardened steel ball (10 mm diameter) and milled (10 Hz, Retsch Mixer Mill MM400) for 90 min at room temperature. Mass = 4.35 mg.

2.4.1.3 Method 3- Hydrolysis followed by oxidation in air

To as-received BNNT (100 mg) was added an aqueous solution of ammonium hydroxide (200 mL, 10% in water) and the suspension homogenised by tip ultrasonication (20 kHz, 130 W Sonics Vibracell CPX150 ultrasonic processor) for 4,

10 or 24 hr at room temperature. Any visible clumps of BNNT which had not dispersed were discarded. The resultant suspended grey/brown solid was collected by vacuum filtration (0.2 µm PTFE membrane) and washed with deionised water (20 mL). This was further heated at 800 ˚C for 1 hr in air, washed with hot (*ca*. 90 ˚C) deionised water (*ca*. 500 mL) and collected by vacuum filtration (0.2 µm PTFE membrane). Mass = 52 mg.

2.5 References

1. B. W. Smith, M. Monthioux and D. E. Luzzi, *Nature*, 1998, **396**, 323.
2. T. Okazaki, Y. Iizumi, S. Okubo, H. Kataura, Z. Liu, K. Suenaga, Y. Tahara, M. Yudasaka, S. Okada and S. Iijima, *Angew. Chem. Int. Ed.*, 2011, **50**, 4853.
3. B. Botka, M. E. Fuestoes, H. M. Tohati, K. Nemeth, G. Klupp, Z. Szekrenyes, D. Kocsis, M. Utczas, E. Szekely, T. Vaczi, G. Tarczay, R. Hackl, T. W. Chamberlain, A. N. Khlobystov and K. Kamaras, *Small*, 2014, **10**, 1369.
4. Y. K. Chen, A. Chu, J. Cook, M. L. H. Green, P. J. F. Harris, R. Heesom, M. Humphries, J. Sloan, S. C. Tsang and J. F. C. Turner, *J. Mater. Chem.*, 1997, **7**, 545.
5. P. M. Ajayan, T. W. Ebbesen, T. Ichihashi, S. Iijima, K. Tanigaki and H. Hiura, *Nature*, 1993, **362**, 522.
6. E. Dujardin, T. W. Ebbesen, H. Hiura and K. Tanigaki, *Science*, 1994, **265**, 1850.
7. J. Sloan, J. Hammer, M. Zwiefka-Sibley and M. L. H. Green, *Chem. Commun.*, 1998, **0**, 347.
8. Y. J. Dappe, *J. Phys. D: Appl. Phys.*, 2014, **47**, 083001.
9. A. N. Khlobystov, D. A. Britz, A. Ardavan and G. A. D. Briggs, *Phys. Rev. Lett.*, 2004, **92**, 245507.
10. D. A. Britz, A. N. Khlobystov, K. Porfyrakis, A. Ardavan and G. A. D. Briggs, *Chem. Commun.*, 2005, 37.
11. A. Botos, J. Biskupek, T. W. Chamberlain, G. A. Rance, C. T. Stoppiello, J. Sloan, Z. Liu, K. Suenaga, U. Kaiser and A. N. Khlobystov, *J. Am. Chem. Soc.*, 2016, **138**, 8175.
12. V. V. Chaban and O. V. Prezhdo, *ACS Nano*, 2011, **5**, 5647.
13. S. Campestrini, C. Corvaja, M. De Nardi, C. Ducati, L. Franco, M. Maggini, M. Meneghetti, E. Menna and G. Ruaro, *Small*, 2008, **4**, 350.
14. D. Golberg, Y. Bando, M. Mitome, K. Fushimi and C. C. Tang, *Acta Mater.*, 2004, **52**, 3295.
15. W. Q. Han, P. Redlich, F. Ernst and M. Ruhle, *Appl. Phys. Lett.*, 1999, **75**, 1875.
16. W. Q. Han and A. Zettl, *Appl. Phys. Lett.*, 2002, **81**, 5051.
17. Y. Bando, K. Ogawa and D. Golberg, *Chem. Phys. Lett.*, 2001, **347**, 349.

18. F. F. Xu, Y. Bando, D. Golberg, M. Hasegawa and M. Mitome, *Acta Mater.*, 2004, **52**, 601.
19. D. Golberg, F. F. Xu and Y. Bando, *Appl. Phys. A*, 2003, **76**, 479.
20. W. Q. Han, C. W. Chang and A. Zettl, *Nano Lett.*, 2004, **4**, 1355.
21. T. Pham, A. Fathalizadeh, B. Shevitski, S. Turner, S. Aloni and A. Zettl, *Nano Lett.*, 2016, **16**, 320.
22. A. Zettl, *Science*, 2003, **300**, 467.
23. Á. Kukovecz, T. Kanyó, Z. Kónya and I. Kiricsi, *Carbon*, 2005, **43**, 994.
24. C. Y. Zhi, Y. Bando, C. C. Tang, S. Honda, K. Sato, H. Kuwahara and D. Golberg, *J. Phys. Chem. B*, 2006, **110**, 1525.
25. Y. Liao, Z. Chen, J. W. Connell, C. C. Fay, C. Park, J.-W. Kim and Y. Lin, *Adv. Funct. Mater.*, 2014, **24**, 4497.
26. D. Golberg, Y. Bando, Y. Huang, T. Terao, M. Mitome, C. C. Tang and C. Y. Zhi, *ACS Nano*, 2010, **4**, 2979.
27. D. Golberg, Y. Bando, C. Tang and C. Zhi, *Adv. Mater.*, 2007, **19**, 2413.
28. H. Chen, Y. Chen, J. Yu and J. S. Williams, *Chem. Phys. Lett.*, 2006, **425**, 315.
29. B. Fakrach, A. Rahmani, H. Chadli, K. Sbai and J. L. Sauvajol, *Physica E*, 2009, **41**, 1800.
30. S. Kalay, Z. Yilmaz and M. Culha, *Beilstein J. Nanotechnol.*, 2013, **4**, 843.
31. C. Zhi, *J. Phys. Chem. B*, 2006, **110**, 8548.
32. H. F. Rizzo, in *Boron Synthesis, Structure, and Properties: Proceedings of the Conference on Boron*, eds. J. A. Kohn, W. F. Nye and G. K. Gaulé, Springer US, Boston, MA, 1960, pp. 175.
33. N. Kostoglou, J. Lukovic, B. Babic, B. Matovic, D. Photiou, G. Constantinides, K. Polychronopoulou, V. Ryzhkov, B. Grossmann, C. Mitterer and C. Rebholz, *Mater. Des.*, 2016, **110**, 540.

3. Growth of Carbon Nanotubes inside Boron Nitride Nanotubes by Coalescence of Fullerenes: Towards the World's Smallest Co-axial Cable

3.1 Introduction

The effective nanoscale confinement of guest-species inside host-nanotubes creates an interesting opportunity to study of the structure,[1, 2] motion[3] and dynamics[4, 5] of the confined guest. Furthermore, the extreme spatial confinement in nanotubes allows us to probe the kinetics and pathways of chemical reactions and processes at the nanoscale, including the formation of one-dimensional materials templated by the internal channel of the host-nanotube.[6, 7, 8] The simplest and most widely studied confined transformation in single-walled carbon nanotubes (SWCNT) is the conversion of C_{60}@SWCNT, so-called 'peapods', into double-walled carbon nanotubes (DWCNT) *via* the thermally activated polymerisation and coalescence of guest-fullerenes to an internal carbon nanotube.[7,9] Numerous more complex processes have also been observed inside nanotubes, such as unusual oligomerisation and polymerisation reactions,[2, 10, 11] the growth of graphene nanoribbons,[12-14] and the formation of molecular nanodiamonds[8] from encapsulated fullerenes and organic molecules respectively. As such, chemical reactions inside carbon nanotubes open up new avenues for the synthesis of nanoscale materials with unique structures and functional properties inaccessible by other means.

BNNT are a more recently discovered and comparatively underexplored alternative to CNT as nanocontainers and nanoreactors. Like CNT, the encapsulation of guest-species into BNNT is modulated by ubiquitous van der Waals forces between

host and guest.[15] Yet, as the polarity of interatomic bonding, delocalisation of π electrons and polarisability differs significantly between CNT and BNNT, the extent to which these properties can influence the interactions between BNNT and molecules are at present not fully understood. Moreover, experimental studies on the structure, motion and dynamics of molecules in BNNT are still extremely limited, with rare examples being the formation of metal particles from metal halides[16] and the preparation of graphene nanoribbons from coronene.[17]

3.2 Aim and Objectives

The aim of this study is to make the first important steps towards establishing BNNT as a nanoreactors through the polymerisation and coalescence of C_{60} (Figure 37). This is a classical model reaction in CNT and thus provides an effective test reaction for BNNT as nanoreactors.

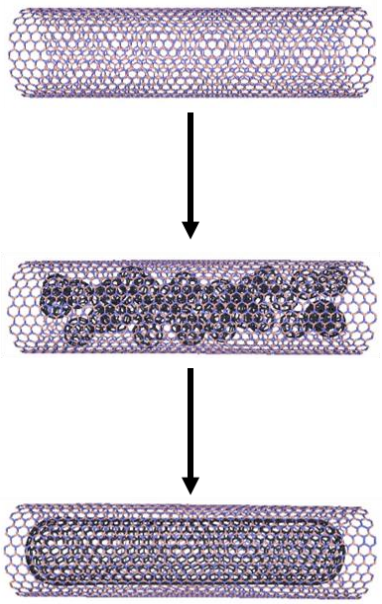


Figure 37. Schematic representation of the filling of BNNT with C_{60} followed by the formation of CNT inside BNNT.

The first objective is to fill BNNT with C_{60} and study the structure of the confined guest-molecules inside the nanotubes. This will involve careful analysis by TEM, where C_{60} is observed as distinctive dark circles between the long parallel lines that comprise the sidewalls of the nanotube, to appraise the stacking arrangements and molecular spacing. The filling yield will be evaluated through comparative techniques such as UV-vis and IR spectroscopies, which measure transitions between electronic and vibrational levels respectively, and the interactions between C_{60} and BNNT carefully examined using variable temperature analysis.

The second objective is to heat C_{60}@BNNT at elevated temperatures in vacuum in order to form an encapsulated CNT (CNT@BNNT). The formation method of this novel material will be optimised by variation of reaction time and temperature, to maximise the yield of the confined CNT. Finally, this material will be thoroughly characterised to probe its structure and physicochemical properties and thus discern the ability of BNNT to act as an effective template of one-dimensional nanostructures, in this case leading to the formation of CNT@BNNT, where an electrically conducting CNT is embedded within an insulating BNNT. Such a nanostructure – the world's smallest co-axial cable – is predicted to have a wealth of unique functional properties for applications in nanoelectronics and sensing devices.[18-20]

3.3 Results and Discussion

3.3.1 Encapsulation of C_{60} into BNNT

The internal diameter of BNNT (d_{NT}^{INT} = 2.45 ± 1.19 nm) is large enough to accommodate C_{60}, which has a van der Waals diameter of 1.0 nm. The BNNT were opened and purified through sonication assisted hydrolysis, followed by oxidation in air, as described in Chapter 2, providing a route for C_{60} into the BNNT cavity. The encapsulation of C_{60} into BNNT was carried out at 600 °C in vacuum which was based on an effective method for the preparation of C_{60}@CNT.[1] The encapsulation of C_{60} into CNT is known to be a highly exothermic and generally irreversible process (up to 3 eV per C_{60}, depending on the specific van der Waals contact area between the convex external surface of C_{60} and the concave internal surface of the CNT channel),[21, 22] in which adsorbed C_{60} migrates along the surface of the CNT before entering at the termini and at accessible defect sites along the sidewall. Provided the CNT diameter is large enough to accommodate C_{60} molecules (0.6 nm wider than the diameter of the guest molecule), the CNT will be completely filled.[23-25] Whilst the encapsulation of C_{60} into BNNT has been reported,[26] no experimental studies to date report the energy of encapsulation of C_{60} into BNNT. However, the calculated energy of adsorption for C_{60} onto graphene (0.85 eV) is comparable to C_{60} onto hexagonal boron nitride sheets (0.83 eV),[22] suggesting similar interactions for C_{60}@BNNT and C_{60}@CNT.[27] Moreover, the calculated energy for encapsulation into CNT and BNNT suggests that the energy gain for the insertion of C_{60} into BNNT (C_{60}@(10, 10)BNNT ΔE = 4.38 eV) may surpass that of the CNT analogue (C_{60}@(10, 10)CNT ΔE = 3.02 eV).[15]

TEM imaging confirmed the filling of BNNT under our conditions (Figure 38). Similarly to CNT with internal diameters matching the van der Waals diameter of C_{60}, the guest-molecules of C_{60} confined within narrow BNNT lined up in a single-chain, with separations of *ca*. 0.3 nm between the neighbouring fullerenes and between the fullerene and the internal walls of BNNT (Figure 38 (a)). The inter-fullerene distance was *ca*. 0.9-1.0 nm (depending on the diameter of the host-nanotube), consistent with a previous study of C_{60} in BNNT[26] and the minimum separation in the bulk fcc-crystal (1.0 nm)[28, 29] and slightly smaller than in SWCNT (1.1 nm)[23] as a result of tighter packing arrangements. These measurements indicate that the nature of C_{60}-BNNT interactions is similar to that of C_{60}-CNT interactions.

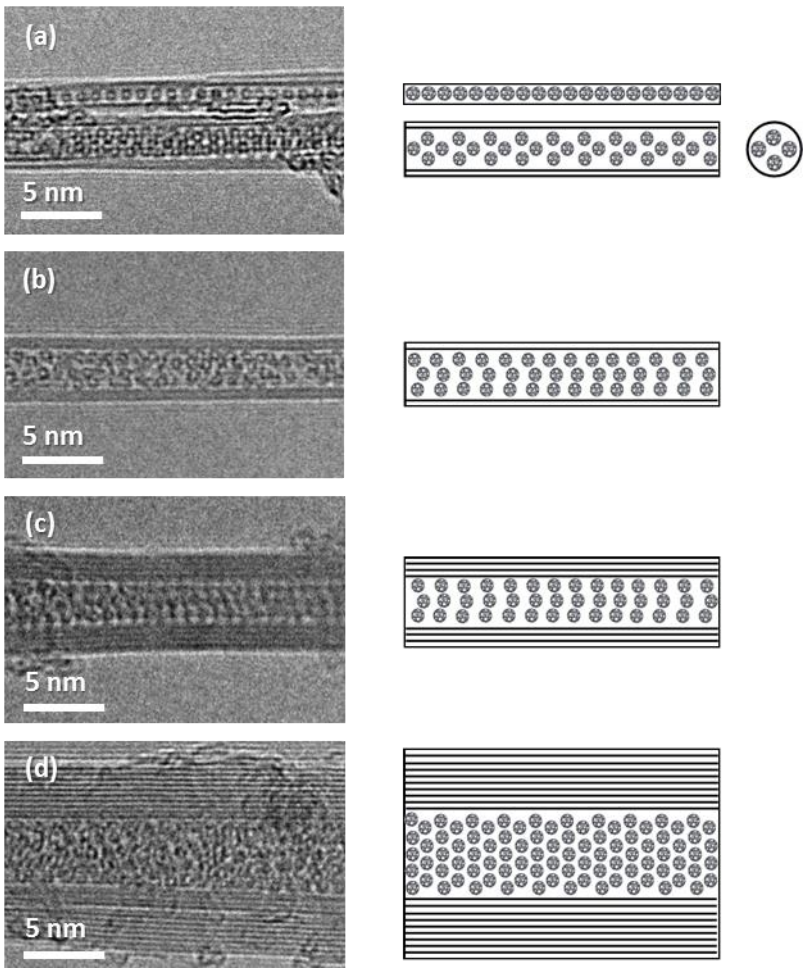


Figure 38. TEM images and schematic representation of C_{60}@BNNT demonstrating the dependence of the stacking arrangement of C_{60} on the internal diameter of the respective BNNT: (a) 1.2 nm (top), 2.1 nm (bottom), (b) 2.4-2.6 nm, (c) *ca*. 2.6 nm and (d) 4.4-5.2 nm. The stacking arrangements are assigned to (a) linear (top), two layer phase (bottom), (b) helical, (c) helical and (d) amorphous.

In wider BNNT, fullerenes adjusted their positions to maximise the interactions with the host-nanotube and to fill the cylindrical cavity in the most efficient way (Figure 38 (b-d) and Figure 39), which is analogous to the behaviour of C_{60} in wider CNT.[23] This formed packing patterns of C_{60} which were clearly ordered in some cases (Figure 38 (a) and (c)), but more disordered in others (Figure 38 (b) and (d)). For example, there was no real packing order in the very large BNNT in Figure 38

(d) possibly due to the wide, yet variable, diameter of BNNT in this instance. Figure 38 (c) appears to show a corkscrew arrangement of C_{60} inside the BNNT with an internal diameter of 2.6 nm which agrees with previous studies of C_{60} in BNNT,[26] but some other corkscrew packing patterns, such as in Figure 38 (b) appear to be discontinuous along the length of the nanotube, possibly due to the non-uniform diameter of the host-BNNT. Non-helical packing patterns were also present (Figure 38 (a)), such as the two-molecule layer phase inside a 2.1 nm diameter BNNT, narrower than that described for C_{60} inside a *ca*. 2.6 nm DWCNT.[23] Statistical analysis of multiple electron micrographs indicated that around 25% of the BNNT were completely filled.

Complimentary to TEM, the sample was further analysed by electron energy loss spectroscopy (EELS) and energy-filtered TEM (EFTEM) imaging, which maps the location of each element within the hybrid nanomaterial (Figure 39).

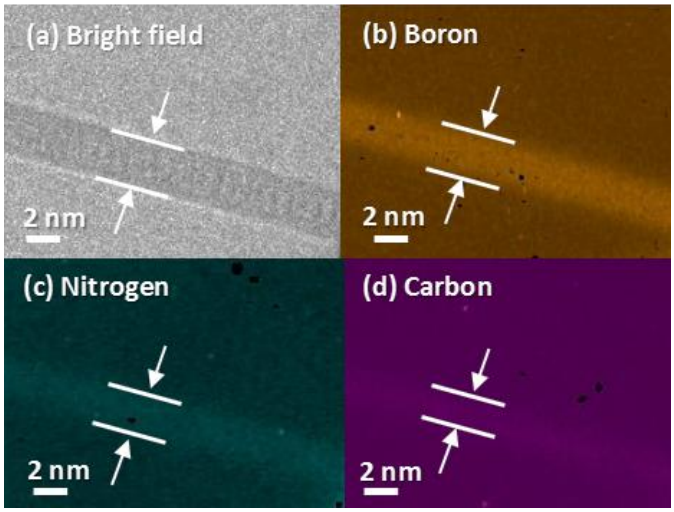


Figure 39 (a) Bright field and (b-d) energy filtered TEM images of a BNNT. The line widths are as follows: bright field=3.3 nm, boron=3.3 nm, nitrogen=3.2 nm and carbon=2.2 nm. This analysis confirmed the encapsulation of C_{60} within BNNT.

The linear contrast identifying the location of carbon (2.2 nm wide) was much narrower than that of boron (3.3 nm), and nitrogen (3.2 nm), consistent with the confinement of C_{60} within the internal channel, with no fullerene attached to the outer walls of the BNNT observed.

TGA was performed to probe the composition of the material (Figure 40). A weight loss between 360 and 600 °C was clearly observed and is the result of the oxidation of carbon (as C_{60}) in air to form carbon dioxide. Whilst TGA can in principle be used to approximate the filling of C_{60} in BNNT (8.5% by mass in this instance), it is important to note that it is likely that larger nanotubes, with lower host-guest contact area and hence weaker van der Waals interactions between the fullerene and the BNNT, would not retain all of the C_{60} molecules inside the nanotube upon heating and as such the observed value of 8.5% loading was not representative of the sample as a whole.

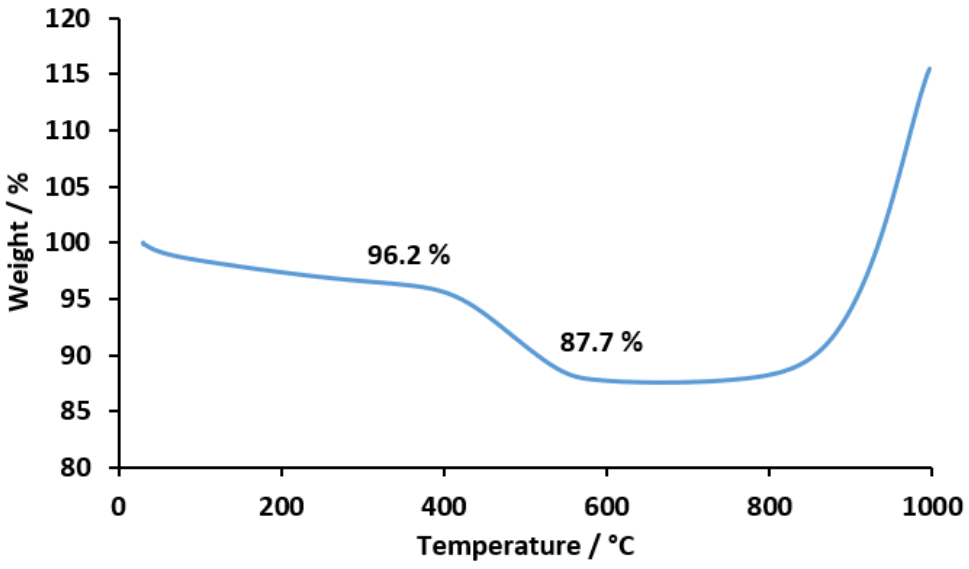


Figure 40. TGA of C_{60}@BNNT indicates a weight loss of 8.5% between 360 and 600 °C consistent with the oxidation of carbon within BNNT.

To further probe the efficiency of encapsulation of C_{60} in BNNT, IR and UV-vis spectroscopies were performed (Figure 41). Being electrically insulating and optically transparent, BNNT should allow the vibrations of guest-molecules to be directly analysed by IR spectroscopy, unlike CNT that have often hindered such analysis.[30] Indeed, the IR spectrum of toluene-washed C_{60}@BNNT (Figure 41 (a)) contained prominent bands at 803 and 1375 cm^{-1} corresponding to the out-of-plane radial buckling (R) mode and the in-plane stretching modes of *h*-BN in BNNT respectively,[31] [32] as well as weak features at 527, 576 and 1183 cm^{-1} consistent with known vibrational modes of $T_{1u}(1)$, $T_{1u}(2)$ and $T_{1u}(3)$ symmetry in C_{60}.[33] Through correlation of the dependence of the absorbance intensity at 527 cm^{-1} ($T_{1u}(1)$) with the mass of C_{60} (Figures 3 (b) and (c)), the quantity of C_{60} in C_{60}@BNNT was found to be *ca*. 29 wt.%. Corresponding UV-vis spectroscopy analysis (Figure 41 (d-f)) indicated that the amount of C_{60} extracted from C_{60}@BNNT through extensive sonication in toluene was *ca*. 37%.

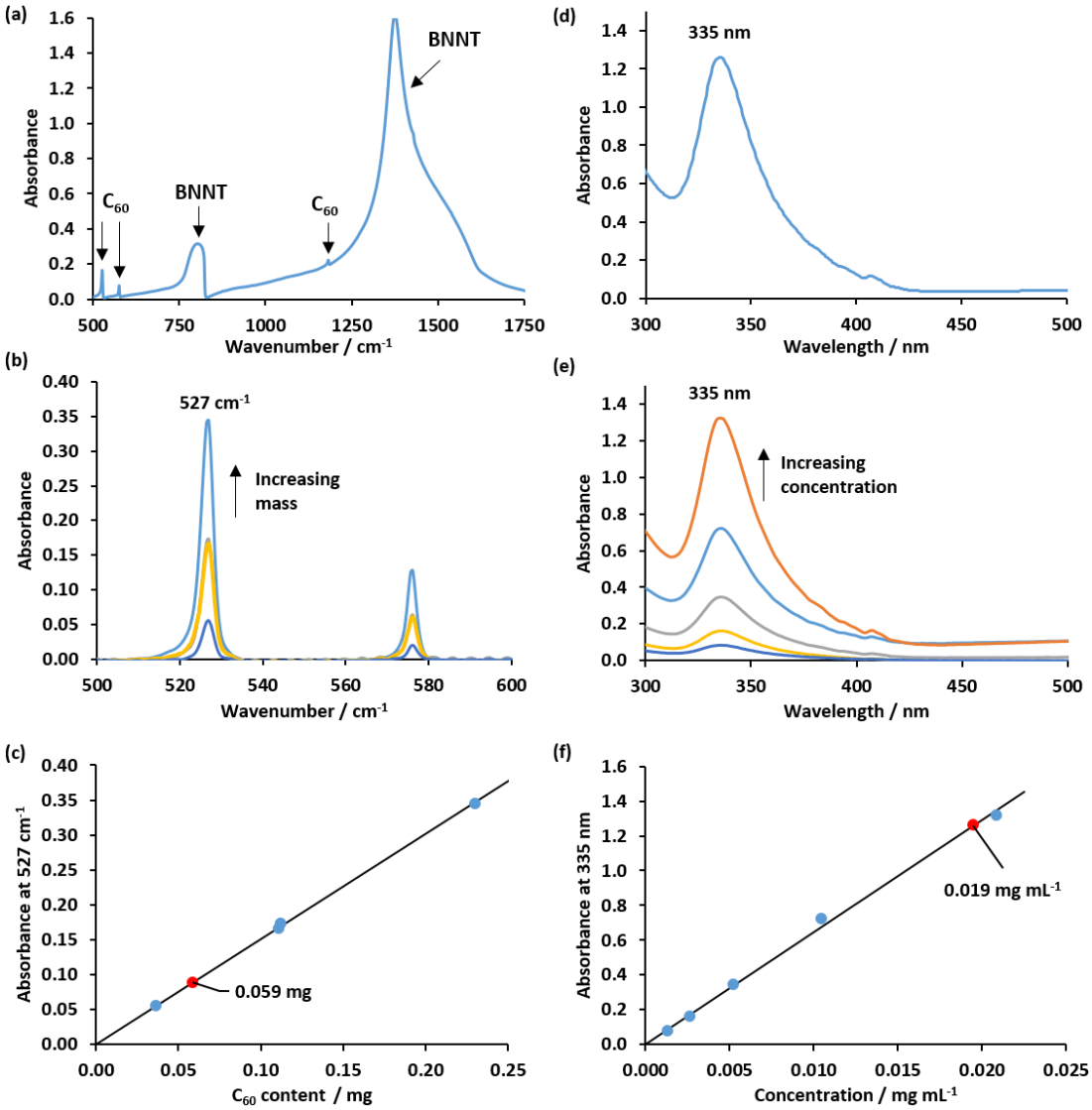


Figure 41. (a) IR spectrum of C_{60}@BNNT. (b) Baseline-corrected IR spectra of C_{60} with varying C_{60} content (0.036, 0.111, 0.112 and 0.230 mg) in potassium bromide (265 mg) used to construct the calibration curve (c) which correlates the intensity of the absorbance at 527 cm^{-1} ($T_{1u}(1)$) with C_{60} content. The amount of C_{60} in C_{60}@BNNT using this method was found to be 0.059 mg in 0.260 mg (mass ratio ca. 29%). y=1.509x, R^2=1.000, standard error = 0.01. (d) UV-vis spectrum of C_{60} extracted from C_{60}@BNNT through extensive sonication in toluene (4 mL). (e) UV-vis spectra of C_{60} at a variety of concentrations in toluene (0.0013, 0.0026, 0.0052, 0.0104 and 0.0208 mg mL^{-1}) used to produce the calibration curve (f) which correlates the intensity of the absorbance at 335 nm with the concentration of C_{60} in toluene. The amount of C_{60} extracted from C_{60}@BNNT using this method was found to be 0.019 mg in 0.07 mg (mass ratio *ca*. 37%). y=64.7x, R^2=0.998, standard error=1.15.

It is important to note that both the IR spectroscopy method, where C_{60} remained within the internal channel of BNNT during analysis, and the UV-vis spectroscopy approach, where C_{60} was removed, gave approximately the same

loading of C_{60} in BNNT as was observed by TEM analysis. Moreover, comparison of the spectroscopy approaches confirms that C_{60} can be effectively and fully removed from within BNNT by excessive sonication in organic solvent (toluene), a feat that cannot be achieved from within CNT. This suggests that the host-guest interactions in C_{60}@BNNT are likely to be weaker than in C_{60}@CNT; however, the poor host-guest fit (the van der Waals diameter of C_{60} of 1.0 nm is smaller than the mean internal diameter of BNNT of 2.45 ± 1.19 nm) precludes a large number of C_{60}-BNNT contacts and as such the encapsulated fullerenes could be solvated in a manner analogous to that observed in the bulk fcc-crystal. This observation also indicates that caution has to be exercised when purifying the products: repeated rinsing with toluene should be used for removing C_{60} molecules from the surface but sonication should be avoided as it results in emptying of the BNNT.

Temperature dependent IR spectroscopy was used to identify the different vibrational modes of guest-molecules of C_{60} inside BNNT as orientational order develops with lowering temperature (Figure 42).

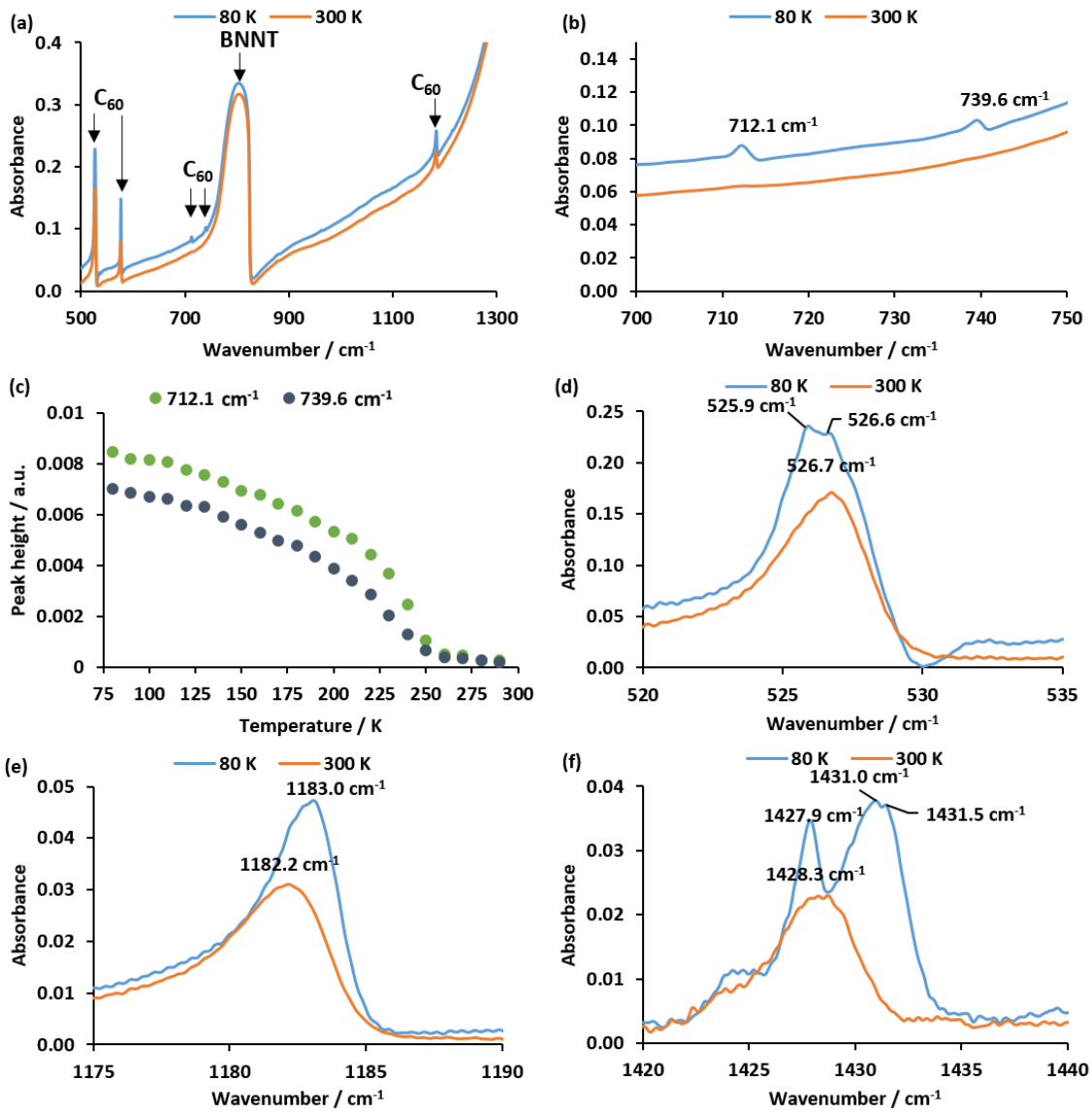


Figure 42. High resolution IR spectra of C_{60}@BNNT at 80 and 300 K in the range 500-1300 cm^{-1} (a) and 700-750 cm^{-1} (b). The height of the peaks at 712.1 and 739.6 cm^{-1} (H_u) vary as a function of temperature (c). The band at 526.7 cm^{-1} ($T_{1u}(1)$) increases in intensity and splits into two peaks at 525.9 and 526.6 cm^{-1} (d), the band intensity at 1182.2 cm^{-1} ($T_{1u}(3)$) increases and shifts to higher energy (e) and the band at 1428.3 cm^{-1} ($G_u/T_{1u}(4)$) splits into three bands when cooled from 300 K to 80 K.

At 300 K, the spectrum of C_{60} in C_{60}@BNNT contained only the four IR-active T_{1u} modes of the icosahedral C_{60} molecule. As the temperature decreased below the orientational phase transition temperature the molecular rotation was restricted leading to a symmetry lowering as the molecules had to adjust to the crystal

structure. This resulted in splitting of the triply degenerate T_{1u} modes and the appearance of previously IR-inactive new modes (Figure 42 (a)). The new bands at 712.1 and 739.6 cm^{-1} (Figure 42 (b)), assigned to H_u symmetry,[34] increased in intensity with decreasing temperature (Figure 42 (c)). The temperature where they appeared was around 250 K, exactly where the orientational phase transition occurs in fcc C_{60}.[54] Splitting of the T_{1u} modes, such as the 526.7 cm^{-1} band ($T_{1u}(1)$) becoming two at 525.9 cm^{-1} and 526.6 cm^{-1} (Figure 42 (d)) and the 1428.3 cm^{-1} band ($G_u/T_{1u}(4)$) splitting into three bands at 1427.9, 1431.0 and 1431.5 cm^{-1} (Figure 42 (f)), along with the lack of splitting of the $T_{1u}(3)$ mode (Figure 42 (e)), are also consistent with earlier observations in the bulk fcc crystal.[59] This temperature-dependent behaviour suggests that C_{60} molecules are in a similar environment when encapsulated in the BNNT. Vibrational spectroscopy, however, reflects short-range rather than long-range order: the lowering of symmetry indicates that the molecular rotation had stopped due to interactions with neighbouring fullerenes. The orientational transition temperature is determined by the intermolecular distance[35] rather than the long-range crystal structure; so long as the intermolecular distance is similar, these results can be reconciled with any arrangement shown in Figure 38.

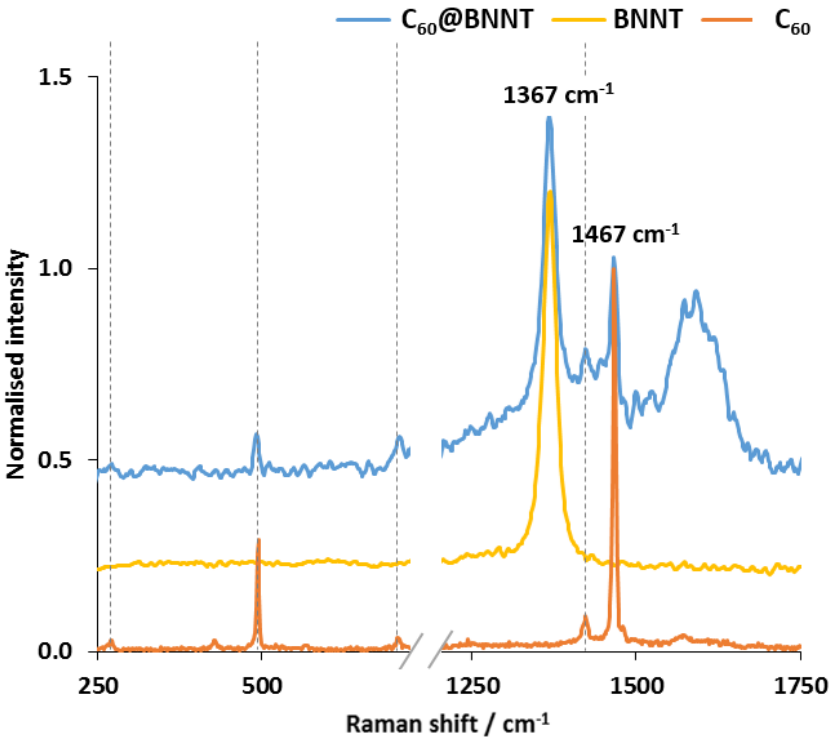


Figure 43. UV Raman spectra of BNNT, C_{60} and C_{60}@BNNT at room temperature (λ_{ex} = 355 nm is required due to the onset of significant luminescence using alternate visible excitation). The presence of C_{60} is evident in the spectra of the filled tubes. The broad band centred at *ca*. 1600 cm^{-1} in the Raman spectrum of C_{60}@BNNT corresponds to the G band of a graphitic nanostructure – most likely a carbon nanotube – that is formed through either thermal or photochemical decomposition of C_{60} under the conditions of spectral acquisition.

The presence of C_{60} was further confirmed by Raman spectroscopy (Figure 43). Five of the ten Raman-active modes[36] could be clearly identified in the Raman spectrum of C_{60}@BNNT. This is regarded as sufficient, as the remaining modes have small intensity. It is important to note that in these experiments encapsulation did not cause a measurable shift in the frequency of C_{60} vibrational modes, unlike what has been reported for C_{60} in narrow-diameter carbon nanotube peapods.[37] Such an unshifted C_{60} Raman line has been observed in carbon nanotube peapods with a large mean diameter and a broad diameter distribution, similar to our BNNT.[38]

3.3.2 Forming CNT@BNNT

The polymerisation and coalescence of guest C_{60} molecules into a CNT inside the host-BNNT offers an exciting opportunity to form a conducting nanowire inside an insulating BNNT. Previous attempts to fabricate CNT@BNNT have been made by other routes, such as the coating of CNT with boron nitride.[39-46] However, the formation of CNT within pre-formed BNNT would be more desirable because the structure of the outer insulating nanotube is well-defined and easier to control with uniform coverage of BN. Furthermore, this approach also permits the formation of very narrow SWCNT in BNNT, a nanostructure with favourable properties in chemical sensing.[47] One specific example of forming CNT@BNNT involved the electron irradiation of amorphous carbon inside BNNT,[48] though the inherent nature of this method is not scalable.

Previous studies on the thermal transformations of C_{60}@CNT suggest that confined C_{60} molecules begin to coalesce at *ca*. 800 ˚C inside a CNT[9] and at 1200 ˚C most of the C_{60} has rearranged to form an internal CNT within the host-CNT.[49] The templating effects of the host-CNT were shown to be important in the CNT formation, as the diameter of the inner CNT is dependent on the outer nanotube and completely independent of the size of C_{60}.[9] In this study, C_{60}@BNNT was heated at 1200 °C for 6 h under argon to stimulate the polymerisation and coalescence processes (Method 1), similar to those well-documented for C_{60}@CNT, and the resulting material analysed by TEM (Figure 44). It is important to note that during the heating process, C_{60} desorbs from within the wider (>2 nm diameter) BNNT, and as such CNT are only

formed in narrow BNNT, consistent with the previously reported desorption of C_{60} from wider CNT.[50]

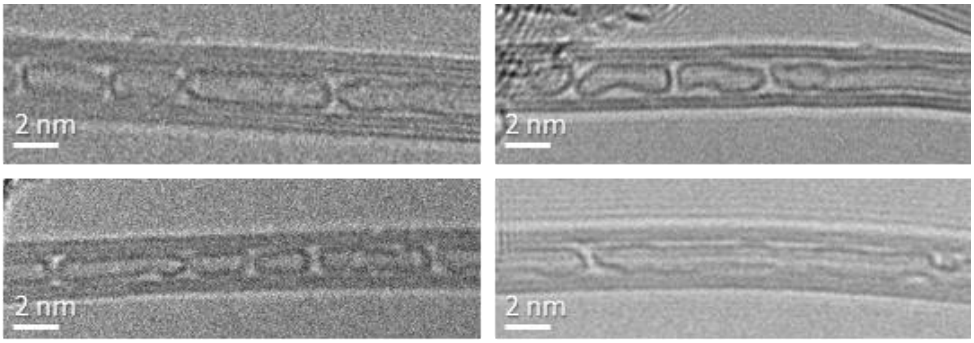


Figure 44. Bright field TEM images of CNT@BNNT formed by heating C_{60}@BNNT at 1200 °C for 6 h.

TEM imaging of C_{60}@BNNT after heating at 1200 °C for 6 h revealed that most molecules have undergone coalescence to tubular structures with mean diameters of 1.1 ± 0.2 nm and lengths of 4.3 ± 2.9 nm, with a modal van der Waals separation of *ca*. 0.34 nm between the CNT and BNNT.

In an attempt to enhance the length and structural ordering of the confined carbon nanotube, a series of additional experiments were conducted. The first involved increasing the reaction temperature from 1200 to 1400 ˚C (Method 2- Figure 45). The second explored the effect of reaction time by increasing the duration of heating at 1200 ˚C from 6 to 10 h (Method 3- Figure 46). The final modification involved refilling the CNT@BNNT produced by thermal decomposition of C_{60}@BNNT at 1200 ˚C for 6 h with further C_{60} and then repeating the heating step (1200 ˚C for 6 h) in an attempt to increase the amount of carbon available to produce the encapsulated CNT (Method 4- Figure 47). The extent of nanotube filling and the

length of the afforded CNT was then correlated with experimental conditions (Table 1).

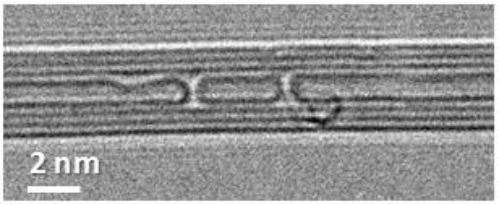


Figure 45. TEM of single-walled carbon nanotubes formed inside a triple-walled BNNT from C_{60}@BNNT when heated at 1400 ˚C for 6 h (Method 2).



Figure 46. TEM of single-walled carbon nanotubes formed inside a double-walled BNNT from C_{60}@BNNT when heated at 1200 ˚C for 10 h (Method 3).

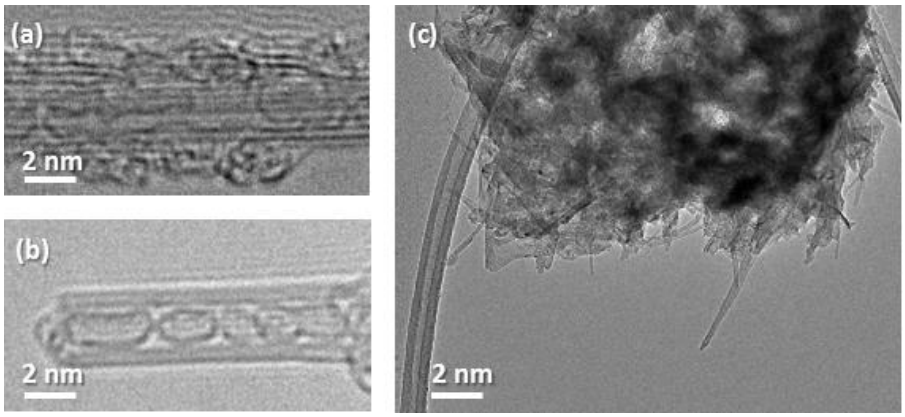


Figure 47. TEM of single-walled carbon nanotubes formed inside BNNT (Method 4). The newly formed carbon nanotubes (a,b) are of similar length to those produced in the original single filling procedure. The additional carbon added appears to coat the exterior of BNNT as an amorphous layer €.

Table 7. Comparison of the methods used to form CNT@BNNT from C_{60}@BNNT.

Method	Conditions	Filling / %	L_{CNT} / nm
1	Heat C_{60}@BNNT at 1200 °C for 6 h	ca. 25	4.3 ± 2.9
2	Heat C_{60}@BNNT at 1400 °C for 6 h	ca. 25	4.2 ± 2.5
3	Heat C_{60}@BNNT at 1200 °C for 10 h	ca. 25	4.5 ± 2.7
4	Heat C_{60}@BNNT at 1200 °C for 6 h, repeat C_{60} filling then heat C_{60}@BNNT at 1200 °C for 6 h	> 25	3.8 ± 2.6

It is evident from thorough statistical analysis of TEM images that none of these additional experiments were effective for increasing the length of the confined CNT and as such only CNT@BNNT materials produced by Method 1 were explored further.

To confirm that the cylindrical structures observed in the TEM images of CNT@BNNT were in fact carbon nanotubes encapsulated in boron nitride nanotubes, the sample was analysed by EELS and EFTEM imaging (Figure 48).

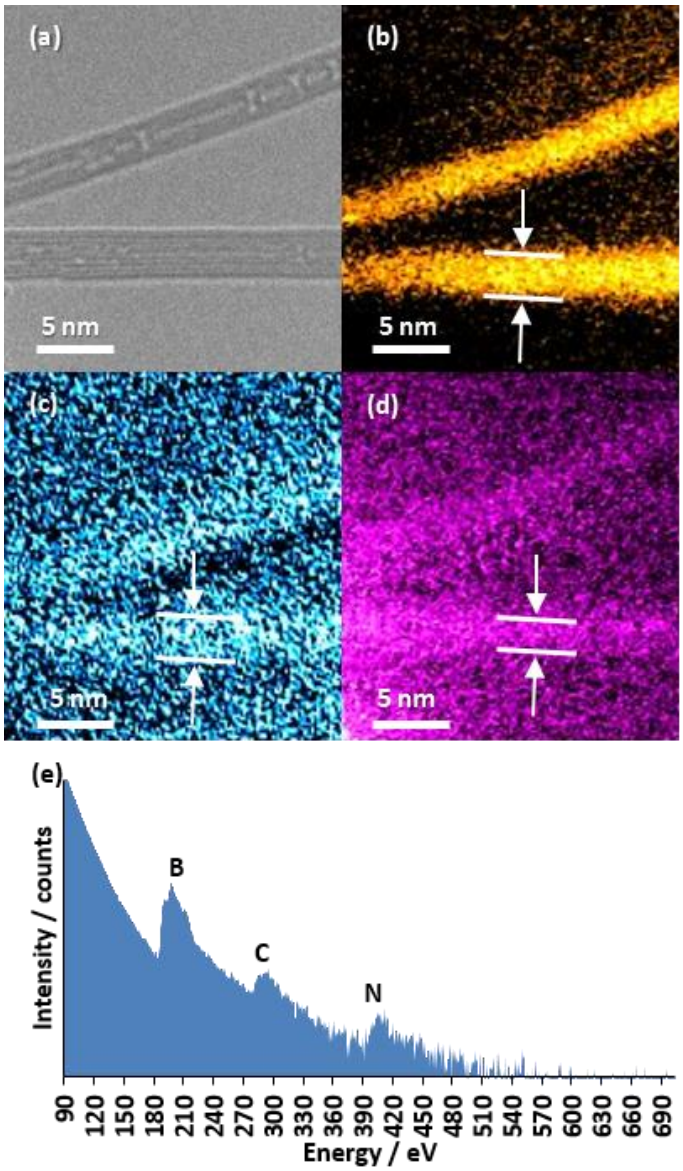


Figure 48. (a) Bright field TEM image of CNT@BNNT produced by heating C_{60}@BNNT. EELS EFTEM elemental maps showing the distributions of boron (b), nitrogen (c) and carbon (d) in the same nanotube. Line widths for boron, carbon and nitrogen are 3.9, 3.2 and 3.9 nm respectively. € A representative electron energy loss spectrum of CNT@BNNT.

The linear contrast showing the location of carbon in the CNT@BNNT structure was visibly narrower (3.2 nm) than those attained for boron (3.9 nm) and nitrogen (3.9 nm), providing further evidence that the structures were indeed CNT embedded within BNNT. Since BNNT are electrical insulators, charge induced by the e-beam during TEM analysis built up and could not be removed from the sample. This

caused the BNNT to move around, thus blurring EFTEM images during the data acquisition, such as in the case of upper CNT@BNNT in Figure 48 which appeared broader as a result. The bottom nanotube in Figure 48, however, was fixed firmly at both ends on the TEM grid, restricting the movement and producing clearer elemental maps. It is also worth noting that with B:N = 1:1, the nitrogen signal appears much weaker than the boron signal, as the relationship between core-loss intensity and energy is approximately that of an inverse power law.[51]

To further probe the composition of the afforded CNT@BNNT material, TGA was performed. This analysis indicates a clear reduction in the carbon content of the material by a factor of 4, from 8.5% of C in C_{60}@BNNT before heating (Figure 40) to around 2.4% after (Figure 49) commensurate with the expected loss of C_{60} from within wider BNNT during the high temperature treatment.

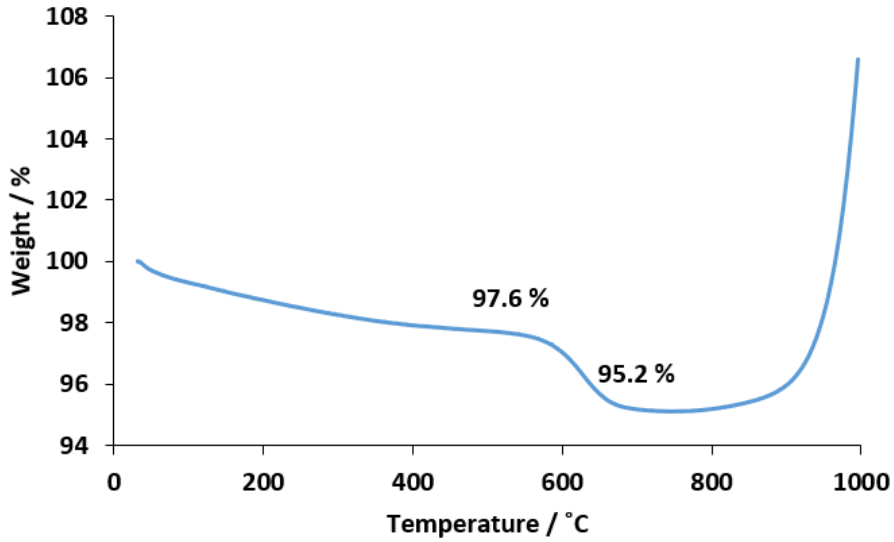


Figure 49. TGA of CNT@BNNT indicates a weight loss of 2.4% between 530 and 700 °C consistent with the oxidation of carbon nanotubes within BNNT. This carbon loading is approximately four times lower than in C_{60}@BNNT, consistent with the loss of C_{60} from the internal channel of BNNT during the high temperature treatment.

The Raman spectrum of C_{60}@BNNT showed clear changes on annealing (Figure 50): the C_{60} modes disappeared and those of carbon nanotubes were observed, namely the D and G modes at *ca*. 1350 and *ca*. 1600 cm^{-1} respectively. The growth of inner nanotubes proves that the majority of C_{60} molecules were encapsulated.

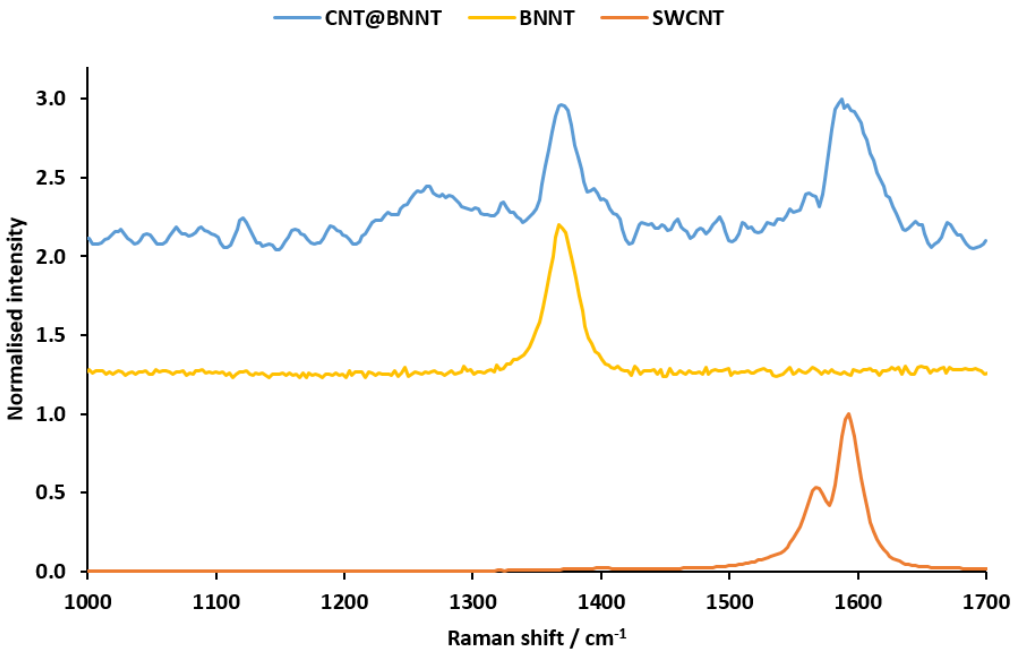


Figure 50. Raman spectra of BNNT and C_{60}@BNNT annealed at 1200 °C (forming CNT@BNNT) collected using 355 nm excitation. The two new bands in the annealed sample are assigned to carbon nanotube modes: the D mode – a ring breathing vibrational mode of A_{1g} symmetry in a disordered graphitic lattice that is activated by the presence of a defect – at around 1300 cm^{-1} and the G mode – a stretching mode of E_{2g} symmetry, present in all graphitic nanostructures (see for example the spectrum of SWCNT) – at around 1600 cm^{-1}. The presence and high intensity of the D band (relative to the G band) in the Raman spectrum of CNT@BNNT indicates a high level of structural disorder within the graphitic lattice that comprises the internal carbon nanotube.

UV-vis spectroscopy was used as a tool to understand the size of the electronic band gap of the new material CNT@BNNT (Figure 51).

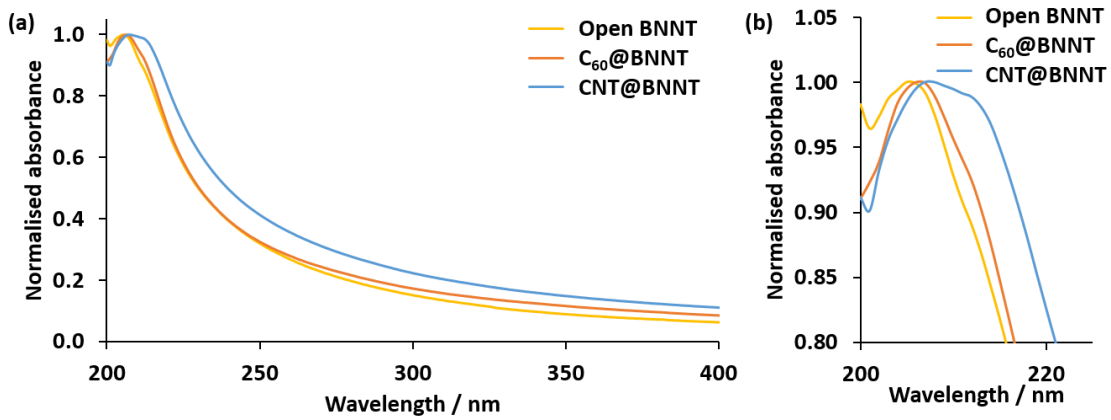


Figure 51. (a) UV-vis spectra of open and purified BNNT, C_{60}@BNNT and CNT@BNNT. The determined band gaps are 6.04 eV (205.3 nm) for open and purified BNNT, 6.00 eV (206.5 nm) for C_{60}@BNNT and 5.98 eV (207.4 nm) for CNT@BNNT. A shoulder at 212 nm in the spectrum of CNT@BNNT (b) is consistent with the π-π* absorption of a narrow SWCNT.

The absorption maximum shifted to a higher wavelength as the BNNT was opened and purified, filled with C_{60} and then finally transformed into CNT@BNNT. For CNT@BNNT, the electronic structures of the BNNT and CNT in the composite was predicted to change when compared to the pristine nanotube analogues due to the stretching of C-C bonds and compression of B-N bonds,[52] explaining our measured change in the band gap of BNNT when the CNT was encapsulted. However, the BNNT would remain insulating and the CNT core would be electonically conducting.[52] The most significant result from the UV-vis spectroscopy measurements was that the absorption band of CNT@BNNT was significantly broader than for any other samples and had a distinct shoulder at 212 nm (Figure 51 (b)), corresponding to the π – π* excitation of a single-walled carbon nanotube with a diameter of 0.90 nm.[53] This value is consistent with the diameter of a carbon nanotube formed from C_{60} inside BNNT measured in TEM images of CNT@BNNT (0.9-1.2 nm at the widest point, with narrow parts of as small as 0.4 nm).

3.3 Conclusions

Boron nitride nanotubes have been demonstrated as effective nanoscale containers and reactors for molecules of fullerene C_{60} which can be inserted into BNNT from the gas phase to form ordered quasi-one-dimensional arrays. The packing arrangement of fullerenes in C_{60}@BNNT was shown to be different to the packing of C_{60} in the bulk crystal and highly dependent on the internal diameter of the host-nanotube, but IR spectroscopy analysis of the guest-molecules suggest that the dynamic behaviour and temperature-controlled phase transitions of C_{60} in BNNT are the same as in the bulk fullerene crystal. The thermal treatment of C_{60}@BNNT at 1200 °C in argon triggers drastic transformations of the guest-molecule which polymerise and coalesce into carbon nanotubes inside boron nitride nanotubes thus forming a hybrid nanostructure CNT@BNNT, as confirmed by high resolution bright field TEM imaging and EELS EFTEM elemental mapping of individual CNT@BNNT structures, which clearly indicate that B and N comprise the shell and C is located in the core of this hybrid nanostructure. Furthermore, UV-vis absorption spectroscopy indicates a new optical transition in CNT@BNNT material (absent in BNNT or C_{60}@BNNT) suggesting that the average diameter of the guest carbon nanotube is *ca*. 0.9 nm which correlates well with that measured by TEM. Overall, the concentric structure CNT@BNNT with insulating BNNT as the outer shell, and conducting CNT as the inner core, represents an excellent candidate material for nanoscale coaxial cables which are required for several electronic and sensing applications. This method of carbon nanotube growth from molecules, directly inside BNNT builds on the concept of nanoreactors developed for carbon nanotubes, and provides the first

scalable method for the controlled growth of conducting nanotubes inside insulating nanotubes.

3.4 Experimental

All common reagents and solvents were purchased from Sigma-Aldrich, UK and used without further purification unless stated otherwise. Water was purified (> 18.0 MΩ cm) using a Barnstead NANOpure II system. TEM imaging was performed using a JEOL 2100F TEM (field emission gun source, information limit < 0.19 nm) at 100 kV at room temperature. EEL spectra were acquired using a Gatan Tridiem energy filter from regions defined by the selected area aperture to exclude any contribution from the supporting carbon film. Acquisition parameters were a 2 mm spectrometer aperture, with a dispersion of 0.3 eV/pixel. EDX spectra were recorded using an Oxford Instruments 30mm^2 Si(Li) detector or an Oxford Instruments x-Max 80 SDD running on an INCA microanalysis system. Samples for TEM, EELS and EDX were typically prepared by casting several drops of a suspension of nanotubes onto copper-grid mounted “lacy” carbon films. Raman spectroscopy was conducted using a laser wavelength of 355 nm. FTIR spectroscopy was performed on a Bruker IFS66v spectrometer using the KBr pellet technique. UV-vis spectroscopy was performed by an Ocean Optics QE65000 spectrometer or Perkin-Elmer Lambda 25 UV-vis spectrometer. Thermogravimetric analysis (TGA) was performed using a TA Instruments SDT Q600 under a flow of air at a heating rate of 10 °C min^{-1} from room temperature to 1000°C. Powder X-Ray diffraction measurements were performed on a PANalytical X’Pert PRO diffractometer equipped with a Cu Kα radiation source (λ = 1.5418 Å) in Bragg-Brentano geometry using a Si zero-background holder.

3.4.1 Filling BNNT

Open and purified BNNT (as reported in Chapter 2, 10 mg) and C_{60}-fullerene (10 mg, SES Research) were sealed under vacuum (10^{-5} mbar) in a Pyrex tube and heated at 600 ˚C for 20 h. The solid was collected by vacuum filtration (0.2 µm PTFE membrane) and washed extensively with toluene until the filtrate became colourless. Mass = 8.2 mg.

3.4.2 Formation of CNT@BNNT

3.4.2.1 Method 1

C_{60}@BNNT (9.0 mg) was sealed under Ar (0.7 bar) in a quartz ampoule and heated at 1200 ˚C for 6 h. Mass = 7.1 mg.

3.4.1.2 Method 2: Increased reaction temperature

C_{60}@BNNT (5.0 mg) was sealed under Ar (0.7 bar) in a quartz ampoule and heated at 1400 ˚C for 6 h. Mass = 4.0 mg.

3.4.1.3 Method 3: Increased reaction time

C_{60}@BNNT (5.0 mg) was sealed under Ar (0.7 bar) in a quartz ampoule and heated at 1200 ˚C for 10 h. Mass = 4.0 mg.

3.4.1.4 Method 4: Repeated filling

C_{60}@BNNT (5.0 mg) was sealed under Ar (0.7 bar) in a quartz ampoule and heated at 1200 ˚C for 6 h. The sample (3.0 mg) was then sealed with C_{60}-fullerene (3.0 mg) in a quartz tube under vacuum (10^{-5} mbar) and heated at 600˚C for 16 h, then sealed under Ar (0.7 bar) at 1200˚C for 6 h. Mass = 2.0 mg.

3.5 References

1. A. N. Khlobystov, D. A. Britz, A. Ardavan and G. A. D. Briggs, *Phys. Rev. Lett.*, 2004, **92**, 245507.
2. D. A. Britz, A. N. Khlobystov, K. Porfyrakis, A. Ardavan and G. A. D. Briggs, *Chem. Commun.*, 2005, 37.
3. A. Botos, J. Biskupek, T. W. Chamberlain, G. A. Rance, C. T. Stoppiello, J. Sloan, Z. Liu, K. Suenaga, U. Kaiser and A. N. Khlobystov, *J. Am. Chem. Soc.*, 2016, **138**, 8175.
4. V. V. Chaban and O. V. Prezhdo, *ACS Nano*, 2011, **5**, 5647.
5. S. Campestrini, C. Corvaja, M. De Nardi, C. Ducati, L. Franco, M. Maggini, M. Meneghetti, E. Menna and G. Ruaro, *Small*, 2008, **4**, 350.
6. B. Botka, M. E. Fuestoes, H. M. Tohati, K. Nemeth, G. Klupp, Z. Szekrenyes, D. Kocsis, M. Utczas, E. Szekely, T. Vaczi, G. Tarczay, R. Hackl, T. W. Chamberlain, A. N. Khlobystov and K. Kamaras, *Small*, 2014, **10**, 1369.
7. H. E. Lim, Y. Miyata, R. Kitaura, Y. Nishimura, Y. Nishimoto, S. Irle, J. H. Warner, H. Kataura and H. Shinohara, *Nat. Commun.*, 2013, **4**, 2548.
8. Y. Nakanishi, H. Omachi, N. A. Fokina, P. R. Schreiner, R. Kitaura, J. E. P. Dahl, R. M. K. Carlson and H. Shinohara, *Angew. Chem. Int. Ed.*, 2015, **54**, 10802.
9. S. Bandow, M. Takizawa, K. Hirahara, M. Yudasaka and S. Iijima, *Chem. Phys. Lett.*, 2001, **337**, 48.
10. G. Pagona, G. Rotas, A. N. Khlobystov, T. W. Chamberlain, K. Porfyrakis and N. Tagmatarchis, *J. Am. Chem. Soc.*, 2008, **130**, 6062.
11. C. S. Allen, Y. Ito, A. W. Robertson, H. Shinohara and J. H. Warner, *ACS Nano*, 2011, **5**, 10084.
12. A. Chuvilin, E. Bichoutskaia, M. C. Gimenez-Lopez, T. W. Chamberlain, G. A. Rance, N. Kuganathan, J. Biskupek, U. Kaiser and A. N. Khlobystov, *Nat. Mater.*, 2011, **10**, 687.
13. A. V. Talyzin, I. V. Anoshkin, A. V. Krasheninnikov, R. M. Nieminen, A. G. Nasibulin, H. Jiang and E. I. Kauppinen, *Nano Lett.*, 2011, **11**, 4352.
14. A. I. Chernov, P. V. Fedotov, A. V. Talyzin, I. S. Lopez, I. V. Anoshkin, A. G. Nasibulin, E. I. Kauppinen and E. D. Obraztsova, *ACS Nano*, 2013, **7**, 6346.

15. J. W. Kang and H. J. Hwang, *J. Phys. Condens. Matter.*, 2004, **16**, 3901.
16. T. Pham, A. Fathalizadeh, B. Shevitski, S. Turner, S. Aloni and A. Zettl, *Nano Lett.*, 2016, **16**, 320.
17. H. R. Barzegar, T. Pham, A. V. Talyzin and A. Zettl, *Phys. Status Solidi B*, 2016, **253**, 2377.
18. J. S. Wang, C. H. Lee and Y. K. Yap, *Nanoscale*, 2010, **2**, 2028.
19. P. Singla, N. Goel, V. Kumar and S. Singhal, *Ceram. Int.*, 2015, **41**, 10565.
20. Q. Weng, X. Wang, X. Wang, Y. Bando and D. Golberg, *Chem. Soc. Rev.*, 2016, **45**, 3989.
21. L. A. Girifalco, M. Hodak and R. S. Lee, *Phys. Rev. B: Condens. Matter*, 2000, **62**, 13104.
22. H. Ulbricht, G. Moos and T. Hertel, *Phys. Rev. Lett.*, 2003, **90**, 095501.
23. A. N. Khlobystov, D. A. Britz, A. Ardavan and G. A. D. Briggs, *Phys. Rev. Lett.*, 2004, **92**.
24. K. S. Troche, V. R. Coluci, S. F. Braga, D. D. Chinellato, F. Sato, S. B. Legoas, R. Rurali and D. S. Galvao, *Nano Lett.*, 2005, **5**, 349.
25. J. H. Warner, Y. Ito, M. Zaka, L. Ge, T. Akachi, H. Okimoto, K. Porfyrakis, A. A. R. Watt, H. Shinohara and G. A. D. Briggs, *Nano Lett.*, 2008, **8**, 2328.
26. A. Zettl, *Science*, 2003, **300**, 467.
27. K. Berland and P. Hyldgaard, *Phys. Rev. B: Condens. Matter*, 2013, **87**.
28. P. A. Heiney, J. E. Fischer, A. R. McGhie, W. J. Romanow, A. M. Denenstein, J. P. McCauley, A. B. Smith and D. E. Cox, *Phys. Rev. Lett.*, 1991, **66**, 2911.
29. P. A. Heiney, *J. Phys. Chem. Solids*, 1992, **53**, 1333.
30. A. Pekker, G. Nemeth, A. Botos, H. M. Tohati, F. Borondics, Z. Osvath, L. P. Biro, K. Walker, A. N. Khlobystov and K. Kamaras, *Phys. Status Solidi B*, 2016, **253**, 2457.
31. B. Fakrach, A. Rahmani, H. Chadli, K. Sbai, M. Bentaleb, J. L. Bantignies and J. L. Sauvajol, *Phys. Rev. B: Condens. Matter*, 2012, **85**, 115437.
32. C. H. Lee, M. Xie, V. Kayastha, J. Wang and Y. K. Yap, *Chem. Mater.*, 2010, **22**, 1782.
33. K. Kamaras, L. Akselrod, S. Roth, A. Mittelbach, W. Honle and H. G. Vonschnering, *Chem. Phys. Lett.*, 1993, **214**, 338.
34. R. A. Jishi, R. M. Mirie and M. S. Dresselhaus, *Phys. Rev. B: Condens. Matter*, 1992, **45**, 13685.
35. S. Pekker, E. Kovats, G. Oszlanyi, G. Benyei, G. Klupp, G. Bortel, I. Jalsovszky, E. Jakab, F. Borondics, K. Kamaras, M. Bokor, G. Kriza, K. Tompa and G. Faigel, *Nat. Mater.*, 2005, **4**, 764.
36. D. S. Bethune, G. Meijer, W. C. Tang, H. J. Rosen, W. G. Golden, H. Seki, C. A. Brown and M. S. Devries, *Chem. Phys. Lett.*, 1991, **179**, 181.
37. R. Pfeiffer, H. Kuzmany, T. Pichler, H. Kataura, Y. Achiba, M. Melle-Franco and F. Zerbetto, *Phys. Rev. B: Condens. Matter*, 2004, **69**, 035404.
38. F. Simon, H. Peterlik, R. Pfeiffer, J. Bernardi and H. Kuzmany, *Chem. Phys. Lett.*, 2007, **445**, 288.
39. L. Jing, R. Y. Tay, H. Li, S. H. Tsang, J. Huang, D. Tan, B. Zhang, E. H. T. Teo and A. I. Y. Tok, *Nanoscale*, 2016, **8**, 11114.
40. C. Y. Su, Z. Y. Juang, Y. L. Chen, K. C. Leou and C. H. Tsai, *Diamond Relat. Mater.*, 2007, **16**, 1393.

41. Y. Morihisa, C. Kimura, M. Yukawa, H. Aoki, T. Kobayashi, S. Hayashi, S. Akita, Y. Nakayama and T. Sugino, *J. Vac. Sci. Technol.*, 2008, **26**, 872.
42. M. Mohai, I. Mohai, Z. Sebestyen, A. Gergely, P. Nemeth and J. Szepvolgyi, *Surf. Interface Anal.*, 2010, **42**, 1148.
43. Y. Joo Jeong and M. F. Islam, *Nanoscale*, 2015, **7**, 12888.
44. X. Yang, Z. Li, F. He, M. Liu, B. Bai, W. Liu, X. Qiu, H. Zhou, C. Li and Q. Dai, *Small*, 2015, **11**, 3710.
45. W. L. Wang, J. Q. Bi, W. X. Sun, H. L. Zhu, J. J. Xu, M. T. Zhao and Y. J. Bai, *Mater. Chem. Phys.*, 2010, **122**, 129.
46. L. L. Chen, H. H. Ye and Y. Gogotsi, *J. Am. Ceram. Soc.*, 2004, **87**, 147.
47. D. R. Kauffman and A. Star, *Angew. Chem. Int. Ed.*, 2008, **47**, 6550.
48. R. Arenal and A. Lopez-Bezanilla, *ACS Nano*, 2014, **8**, 8419.
49. B. W. Smith and D. E. Luzzi, *Chem. Phys. Lett.*, 2000, **321**, 169.
50. R. Pfeiffer, M. Holzweber, H. Peterlik, H. Kuzmany, Z. Liu, K. Suenaga and H. Kataura, *Nano Lett.*, 2007, **7**, 2428.
51. R. F. Egerton, *Rep. Prog. Phys.*, 2009, **72**, 016502.
52. Z. H. Zhang, W. L. Guo and G. A. Tai, *Appl. Phys. Lett.*, 2007, **90**, 133103.
53. G. A. Rance, D. H. Marsh, R. J. Nicholas and A. N. Khlobystov, *Chem. Phys. Lett.*, 2010, **493**, 19.

4. Synthesis of Photoactive Nanoparticles inside Nanotubes

4.1 Introduction

There are many remarkable materials that harness light to drive processes or reactions. Nature has evolved extraordinary molecules for this purpose, namely, chlorophyll which absorbs sunlight, resulting in energy harvesting for plants. Chemists have synthesised fascinating molecules, and more recently nanoparticles (NP), that are able to capture light as a form of cheap, clean and renewable energy. Light energy can then be converted into a whole range of desired forms for specific processes.

For instance, molecular sensors have been developed which absorb sunlight and produce electricity in dye sensitised solar cells.[1] Recently, nanoparticles have been explored in more depth owing to their unusual and extraordinary size-dependent properties.[2] With dimensions of 1-100 nm, NP bridge the gap between bulk materials and molecular structures. Quantum dots (QD) are a remarkable class of semiconducting nanoparticles which possess size-tuneable band gaps, in which the absorption and emission wavelengths can be tailored to suit the desired function.[2] When photons are absorbed by QD, an electron can be excited from the valence band to the conduction band, producing an electron hole pair, called an exciton (Figure 52).

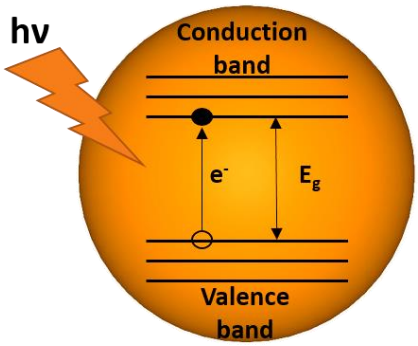


Figure 52. Mechanism of exciton formation in a QD. Absorption of a photon leading to excitation of an electron from the valence band to the conduction band, across the electronic band gap (E_g), to form an electron-hole pair (exciton).[3]

The electron and hole can recombine radiatively, emitting a photon at lower energy than the incident photon, as fluorescence. The energy of the photon emitted by fluorescence correlates with the bandgap, and hence diameter (or radius), of the QD,[4, 5] as shown in Equation 1; Equation of Brus, where E_g is the band gap of the bulk material, $\hbar$ is the reduced Plank's constant, r the radius of spherical nanocrystals, e is the charge of the electron, ε is the semiconductor dielectric constant, m_e and m_h are effective masses of the electron and holes respectively.

$$E = E_g + \hbar^2\pi^2/2r^2\,(1/m_e + 1/m_h) - 1.8e^2/\varepsilon r \qquad (1)$$

This fluorescence can be incredibly useful for applications, such as biological labelling, although a significantly more attractive use is to prevent recombination of the electron-hole pair. Photogenerated electrons and holes can be transferred to another material where they can then be utilised to generate a current or instigate a chemical reaction.[6-10] A high ratio of excited electrons can be generated from the

absorbed photons, so QD have understandably attracted attention for potential applications in solar cells[11] and hydrogen production.[12]

In order to modulate the properties of QD, by preventing excitons recombining through fluorescence, research effort has focused on depositing them on various substrates. For instance, carbon nanotube (CNT) supports can stabilise the QD and together form an exciting new hybrid structure.[13]

CNT are extended cylinders of sp^2 hybridised carbon, with attractive chemical, optical, mechanical and electrical properties.[13] CNT can be functionalised on the surface, yet remain chemically inert under many harsh chemical environments.[13] The unique structure of CNT provides ballistic conduction, with resistance independent of the nanotubes length.[14] This can provide an exceptional pathway for stabilising and transporting electrons. Strong dependence of the CNT properties on the structure of the CNT means that by carefully selecting the diameter, length, number of walls and chirality of the CNT, the functionality can be tailored.

The CNT represent a suitable nucleation site for controlled growth of nanoparticles in the absence of a stabiliser, while the high surface area of CNT allows high QD coverage. Furthermore, the high electron-storage capacity of CNT allows many photoexcited electrons, generated from QD, to be stabilised effectively. The long-range π electronic conjugation of CNT can successfully accept electrons from QD and transport them away from the QD to prevent recombination. Thereafter, electrons can then be utilised for further reactions or electronic applications. Hence, these incredible hybrids are directed at applications such as hydrogen production,[12, 15] dye degradation for water purification,[16] electrochemical sensors,[17] and optoelectronic devices.[18] Through careful and effective assembly of

these hybrid structure, the interesting and unusual electrochemical properties can be utilised further to yield hybrid materials with new and unexpected properties.

4.2.1 Formation of QD/CNT hybrid materials

A wide range of interesting hybrid structures have been prepared using different nanotubes, QD and synthetic approaches, yielding composite materials comprising QD of different size, shape and density on CNT, and harnessing different fundamental interactions to drive their self-assembly (Table 8).

Table 8. Summary of formation of QD on CNT, including parameters such as type of CNT and external diameter (D_{NT}^{EXT}/ nm), QD species and diameter (D_{QD}/ nm) and the interactions involved in hybrid formation.

Ref.	*In Situ*/ *Ex Situ*	Nanotube/QD Interactions	QD	D_{QD}/nm	CNT	Functionalisation to CNT	D_{NT}^{EXT}/nm
12	*In situ*	Electrostatic interactions between CNT-COO^- and Cd^{2+}	CdS	Clusters (50 nm)	MWNT	As-received, carboxylic acid functionalised through oxidation with O_2 or HCl/ HNO_3	*ca*. 20-40
19	*In situ*	Electrostatic interactions between CNT-COO^- and Pb^{2+}	PbS	6-10	SWNT	Carboxylic acid functionalised	*ca*.10
6	*In situ*	Electrostatic interactions between (capped CNT)Br^- and Cd^{2+}	CdS	6-9	SWNT	Tetraoctylammonium bromide (TOAB)	*ca*. 7
20	*In situ*	Electrostatic interactions between polymer-SO_3^- and Cd^{2+}	CdS	5-20	MWNT	Block copolymer wrapped	20-30
21	*In situ*	Electrostatic interactions between polymer-SO_3^- and Cd^{2+}	CdS	5-20	MWNT	Block copolymer wrapped	20-30
22	*In situ*	Electrostatic interactions between CNT-COO^- and Cd^{2+}	CdS	*ca*. 8	MWNT	Carboxylic acid functionalised	*ca*. 20
23	*In situ*	Dative interactions between CNT-PAMAM and Cd^{2+}/Ag^+	CdS, Ag_2S	1.5	MWNT	Polyamidoamine (PAMAM) functionalised	*ca*. 25
7	*In situ*	Electrostatic interactions between CNT-polymer film and Cd^2	CdS	25-30	MWNT	Polymer (chitosan) nanocomposite	8
24	*In situ*	Dative interactions between CNT-NH_2 and Cd^{2+}	CdS	Clusters (20 nm)	MWNT	1-Aminopyrene coated	60
25	*In situ*	Dative interactions between CNT-PAMAM and Cd^{2+} or Ag^+	Ag_2S and CdS	2-19(Ag_2S), clusters (CdS)	MWNT	Polyamidoamine (PAMAM) functionalised	*ca*. 60
26	*In situ*	Electrostatic interactions between CNT-COO^- and Cd^{2+}	CdTe	1-9	MWNT	Carboxylic acid functionalised	35±10
27	*In situ*	Electrostatic interactions between CNT-COO^- and Cd^{2+}	CdS	10	MWNT	Carboxylic acid functionalised by oxidation with O_2 or HNO_3	30-40

Table 1. (*continued*)

Ref.	*In Situ*/ *Ex Situ*	Nanotube/QD interactions	QD	D_{QD}/nm	Capping group	CNT	Functionalisation to CNT	D_{NT}^{EXT}/ nm
28	*Ex situ*	Electrostatic interactions between CNT- NH_3^+ and QD(COO^-)	CdSe	3	Mercaptoacetic capped	MWNT	Carboxyl-, hydroxyl-, and amine-functionalised	20-30
29	*Ex situ*	Electrostatic interactions between CNT-COO^- and Cd^{2+} (electrophoretic deposition)	CdSe	*ca*. 5-15	Poly(methylmethacrylate), with and without surfactant	MWNT	poly(3,4-ethylenedioxythiophene) (PEDOT) wrapped	20-80
30	*Ex situ*	Electrostatic interactions between CNT-polymer(NR_4^+) and QD-COO^-	CdTe	3-5	Thioglycolic acid capped	MWNT	poly(diallyldimethyl-ammonium chloride)(PDDA) wrapped	30±15
31	*Ex situ*	Electrostatic interactions between CNT-triethylammonium groups and QD-COO^-	CdTe	5.0, 2.4, 3.4	Thioglycolic acid capped	SWNT, MWNT	1-(trimethylammoniumacetyl)pyrene functionalised	*ca*. 50
32	*Ex situ*	Covalent- reaction between CNT-amine and QD-COOH	CdSe	15-40	Oleic acid	MWNT	Amine functionalised	80-110
33	*Ex situ*	Covalent- CNT-COOH reacts with QD-NH_2	CdS	5	Cysteamine capped	SWNT	Carboxylic acid functionalised	1.2-1.5
34	*Ex situ*	Nucleophilic addition reaction between CNT-COOCl and QD-NH_2	CdSe, CdSe/ ZnS	2.8-4.3	Cysteamine capped	SWNT	Thionyl-chloride functionalised	*ca*. 1.5
35	*Ex situ*	Van der Waals between grooves in bundles of SWNT and QD	InP, CdSe	InP 4.3, CdSe 2.4, 3.4	TOP/TOPO capped	SWNT	None	1.4
36	*Ex situ*	Van der Waals/ hydrophobic Oleylamine-oleylamine interactions	CdS	5-10	Oleylamine capped	SWNT	Oleylamine functionalised	*ca*. 3
37	*Ex situ*	Hydrophobic oleylamine-oleylamineinteractions	PbS	*ca*. 5	Oleylamine capped	MWNT	Oleylamine functionalised	30±15

The general approaches for formation of QD/CNT hybrids can be split into two distinctive methods: i) *in situ* and ii) *ex situ* (Figure 53). *In situ* approaches can provide a convenient and effective route to CNT hybrid materials with high QD coverage, formed in the absence of stabiliser. *Ex situ* methods involve the synthesis of QD followed by adhesion to the surface of CNT, which allows effective control of the QD size through colloidal chemistry. Thus, QD in solution can be directly compared to those adsorbed on a surface. However, methods of attachment to CNT can be much more complex, and QD have to be capped during preparation in order to prevent aggregation. These capping ligands have to be carefully selected or modified post-synthesis to maximise attractive interactions that will drive self-assembly with other materials, such as CNT.

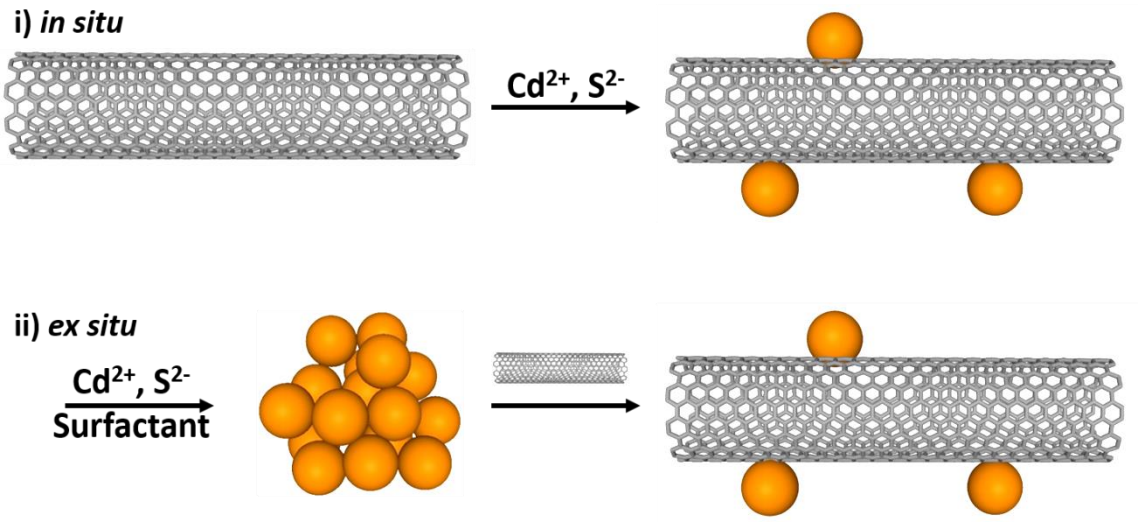


Figure 53. Schematic representation of *in situ* (i) and *ex situ* (ii) formation of CdS/CNT hybrid materials.

In situ synthesis is believed to be aided by electrostatic interactions between a functionalised CNT and ions dissolved in the reaction mixture (Figure 54). Most

commonly, carboxylic acid groups are introduced to the surfaces of CNT through oxidation in air[12, 27] or acid treatment,[12, 19, 22, 26, 27] resulting in electrostatic attractions between CNT-COO^- and cations in solution e.g. Cd^{2+}. When combined with counter ions from solution (S^{2-}, Se^{2-}) QD form on the CNT (Figure 54).

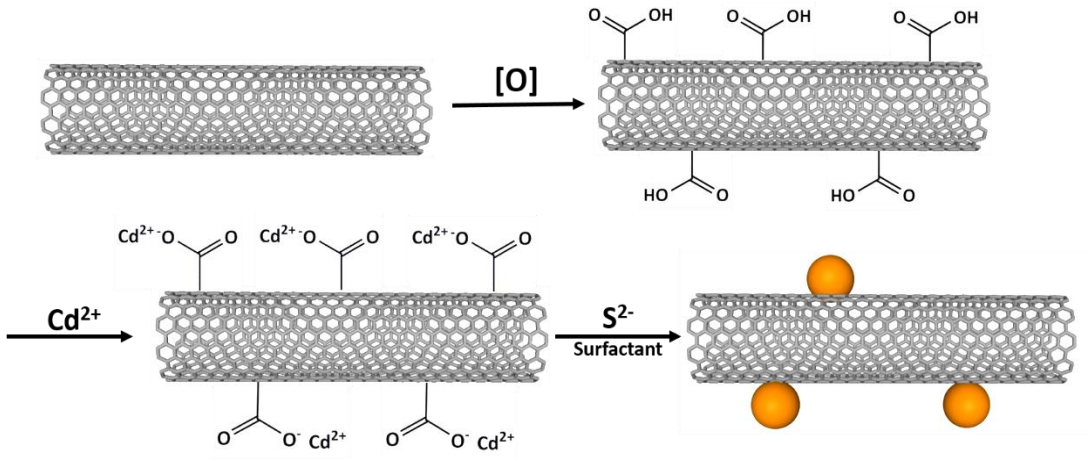


Figure 54. Schematic depicting the formation of CdS on CNT through oxidation of CNT.

Polymer wrapping of CNT is another common approach, which introduces functional groups capable of interacting with QD-precursors. In some cases, the polymers also improve the stability of CNT in aqueous suspensions. Incorporating a polymer will result in a polymer coating on the QD, which may also be advantageous for controlling the growth of QD by acting as a surfactant to passivate the QD surface and limit the growth phase, or even as a conductive coating for high hole mobility[38] but could block access of molecules to the surface of the nanotubes, and reduce the nanotube's internal volume.

In contrast, *ex situ* methods involve the use of QD that are predominantly capped with carboxylic acid/ amine-containing molecules, which then form

interactions with functionalised CNT. For example, Pan *et al*. proved the importance of electrostatic interactions by comparing the self-assembly of carboxyl-capped QD on the surface of carboxyl-, alcohol-, and amine-capped MWNT. The group reported the formation of a dense coating of carboxyl-capped QD on the surface of amine-capped MWNT, yet very few nanoparticles bound to the surface of carboxyl- or alcohol-capped MWNT.[28]

As with *in situ* approaches, polymer wrapping of MWNT is another method of introducing functional groups to CNT. Grzelczak *et al*. report attaching QD to MWNT utilising the electrostatic interactions between ammonia cations ($R_2N^+(CH_3)_2$) from the polymer (poly(diallyldimethylammonium chloride) -PDDA) adsorbed on nanotubes, and thioglycolic acid groups ($RCOO^-$) on CdTe.[30]

Engtrakul *et al.*[35] exploit van der Waals (vdW) forces between bundles of single-walled carbon nanotubes (SWNT) and InP and CdSe QD (capped with trioctylphosphine/ trioctylphosphine oxide (TOP/TOPO)). The grooves in the bundles of nanotubes act as a one-dimensional template for QD to attach to. While many NP are formed on the surface of SWNT through this method, no further examples of QD/NT hybrids have been reported using this approach.

4.2.2 Scope for further investigation

Despite polymers being commonly used during the *in situ* formation and solubilisation of photoactive hybrids, the use of surfactants (or capping group) as a method of controlling the crystal structure of QD formed through the *in situ* approach is comparatively underexplored. This is slightly surprising given that surfactants are widely recognised to improve the structure of QD grown in isolation in solution, and

that the specific nature and even the length of surfactant chosen can significantly alter the size, shape and crystal structure of the QD.[39-42] Through the use of surfactants during the *in situ* formation of CdS on nanotubes, control over the structural characteristics of the QD could be significantly improved and warrants further investigation.

When QD are formed on CNT, there are several competing forces acting between the reactants and the nanotube, including electrostatic interactions and vdW forces; as such, formation mechanisms are often complex and difficult to confidently determine experimentally. However, the encapsulation of QD reduces the number of competing forces and simplifies the mechanism. If QD are formed in the internal cavity of nanocontainers, where the surface is very inert, [13] it is possible to simply harness vdW interactions, which are enhanced due to the greater contact surface area between QD and CNT.

The formation of QD on the external surface of CNT is of significant interest and has been reported comprehensively, yet the formation of QD inside the internal cavities of CNT is significantly underexplored and has the potential to form far superior materials. For example, the QD on the concave surface of the CNT (i.e. encapsulated inside the CNT) could exhibit enhanced electron transfer from QD to CNT, compared to QD on the external surface, through increased contact surface area and by being attached to the more electron deficient surface of the carbon nanotube.[43, 44] This phenomenon has been shown for encapsulated ruthenium, [45] iron (III) oxide[46, 47], and metallic iron.[48] It is therefore reasonable to predict that photogenerated electron-hole pairs produced in QD will be stabilised through charge transfer to the concave surface of the CNT.

Additionally, entrapment of QD inside CNT could lead to the enhanced stability of the QD, possibly shielding them from the external environment and making their removal under applied conditions less likely. This increased stability of encapsulated NP, compared to NP on the surface of carbon supports, has been recognised to improve the recyclability of nanoparticles in nanotubes, such as copper NP inside graphitised nanofibers in the cycloaddition of azides to alkynes.[49]

The nanotube host could template the QD and control its size and shape, as observed for the formation of CNT from the thermal decomposition of C_{60} inside boron nitride nanotubes (BNNT) (Chapter 3), either by physically limiting the size of the encapsulated CdS to grow, or by helping to stabilise CdS leading to larger nanoparticles.

While CNT have been explored as supports for CdS, the use of boron nitride nanotubes as an alternative vessel has never been investigated and no reports of encapsulating QD inside BNNT have been documented. The most likely reason being that BNNT have not been synthesised on a large scale until recently. Moreover, effective opening methods are not widely available, hence the encapsulation of any materials inside BNNT is very limited. The structural differences between BNNT and CNT, such as the polarity of interatomic bonding, delocalisation of π electrons and polarizability, may result in altered interactions between the nanotubes and the QD or QD precursors, which in turn could change the structure of the resulting QD on the host. Formation of CdS QD on the surface of boron nitride nanosheets (BNNS) has been reported,[50] with the authors stating that strong B-O-S covalent bonds between QD and edges of BNNS are responsible for their self-assembly. Hence, QD may also selectively form at the edges of BNNT.

4.2 Aim and Objectives

The aim of this study is to probe the assembly of QD inside nanoscale tubular containers. This will involve an exploration of how the encapsulation of QD can be controlled as a result of reaction conditions and nanocontainers used. Consequently, new materials with improved properties can be designed for targeted applications.

It is critically important to carefully select the type of QD studied, as this affects the properties, and hence applications, of the resulting composite. CdS absorbs visible light,[16] making CdS an ideal candidate for solar light driven devices. Cadmium chalcogenides are a popular choice and have proven to possess a number of outstanding properties for a photoactive nanoparticle; they absorb light across a broad spectrum and have high molar absorptivity *ca*. 10^5-10^7 M^{-1} cm^{-1}.[51-53] The bandgap can be controlled by changing structural parameters, and the solubility can be controlled by functionalising the surface of the chalcogenides with groups that can impart solubility in water.[54] Therefore, the construction of superstructures based on CdS will be explored.

CNT, specifically MWNT, and BNNT are chosen as the nanocontainers, since both are chemically stable in common reaction conditions, so will not be damaged during QD formation reactions. The nanotubes selected are wide enough to allow encapsulation of nanoparticles (inner diameter MWNT = 5.1 ± 1.5 nm, inner diameter BNNT = 2.45 ± 1.19 nm) yet narrow enough to impose spatial confinement effects. MWNT form a dispersion in water more readily than narrower CNT and can be exposed to harsher conditions, without completely destroying their structure.

The first objective is to open CNT to maximise the efficiency of filling. By opening the ends of the nanotubes, QD precursors should be able to enter and

react to form QD, where they are stabilised by vdW forces. Increasing the number of entry points, by creating pores in the side walls, is expected to further enhance the filling efficiency.

For CNT, acid-mediated oxidation will open the caps, which are the most reactive part of the nanotube, and subsequently corrode the surface to form pores. It is important to note, however, that oxidation introduces carboxylic acid groups to the outer walls of CNT, which increases the number of sites for cationic QD precursor ions to attach. This subsequently could increases the coverage of QD on the outer wall of the CNT as oppose to encapsulating them. Since there are two competing factors which both result from the oxidation of CNT, it is important to determine the optimum level of oxidation to maximise the extent of encapsulation and limit the external surface adsorption.

The second objective is to explore the effect of CNT diameter and the internal structure. The internal diameter of the CNT determines how large an encapsulated QD can grow, or if it can even form in the first place. While the internal structure can affect the stability of encapsulated NP, for instance, graphitised nanofibers (GNF) interior resembles stacked cups, and these step-edges provide anchoring points for NP. Therefore, a range of carbon nanocontainers with various internal diameters and internal structures should be investigated to understand its effect on the size, shape and location of the QD formed.

The third objective is to investigate how the type of nanotube used to form the hybrid material can affect the structure. The nature of the nanotube selected will result in specific interactions with QD and contribute different chemical, physical and optical properties to the hybrid. For instance, the ionic character of interatomic bonding, polarisability and delocalisation of the π electrons varies significantly between BNNT and CNT, so interactions between the NT and QD will be different.

In order to probe the efficiency of different filling strategies both liquid and gas phase filling will be explored. The difference between the filling conditions and how QD precursors are transported to the inner cavity of the nanotubes will affect the concentration of encapsulated material, and hence the filling efficiency. For instance, gas phase filling may have a higher filling efficiency as no solvents may block the cavity of the nanotube or interact with the precursor molecules.

4.3 Results and Discussion

4.3.1 The effect of oxidation of nanotubes

To determine the optimum level of oxidation to the nanotubes required for maximum QD filling, the MWNT were treated in nitric acid for various durations. Aqueous nitric acid is commonly used to oxidise CNT and is an established method for effective oxidation.[55, 56] Nitric acid breaks the C=C bonds of graphitic MWNT and introduces oxygen-containing groups, such as carboxylic acids, aldehydes, alcohol and carbonyl groups. The acid then continues to attack sequential graphitic layers to eventually form craters.[57] This allows Cd^{2+} ions to enter, increasing the filling yield. The level of oxidation can be controlled through varying the reaction time or concentration of acid. In these experiments, the durations were chosen to produce CNT which span a range of levels of oxidation, from mild to extreme. Longer oxidation or higher concentrations are likely to result in significant structural disruption to the carbon nanotube.

MWNT were heated in 5 M nitric acid to reflux for 1, 16 or 96 h (Figure 55). The black solid was collected by vacuum filtration and washed until the filtrate was pH neutral.

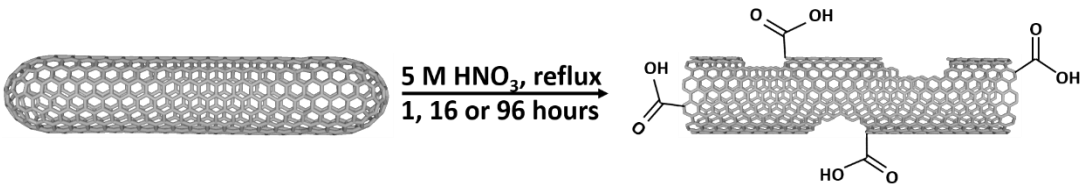


Figure 55. Functionalisation of CNT by oxidation in refluxing acid.

To evaluate the success of these procedures, the most oxidised (96 h-treated) and least oxidised (0 h-treated) MWNT were characterised using a range of spectroscopic and gravimetric approaches.

Raman spectroscopy was the first technique used to examine the structure of the nanotubes. The Raman spectrum of MWNT exhibits a number of key bands: the G band is a C-C stretching vibration of E_{2g} symmetry, present in all graphitic structures at *ca*. 1600 cm^{-1}; the D band is a ring-breathing mode of A_{1g} symmetry in a disordered graphitic lattice at *ca*. 1350 cm^{-1}, activated by a defect e.g. sp^3, heteroatom, vacancy.[58] By measuring the relative intensities of these two bands, I_D:I_G, a quantitative measurement of the degree of disorder in the CNT is provided. From this analysis (Figure 56), it is clear that extensive treatment in nitric acid results in the formation of a more defective MWNT, as I_D:I_G increased from 0.73 to 1.26 in the untreated and 96 h-treated samples respectively. Bands observed at 1138 cm^{-1} and 1544 cm^{-1} in 96 h-treated MWNT, which were not present in 0 h-treated MWNT, have been tentatively assigned to C-O stretches. This also signifies a high level of oxidation to the MWNT after treatment.

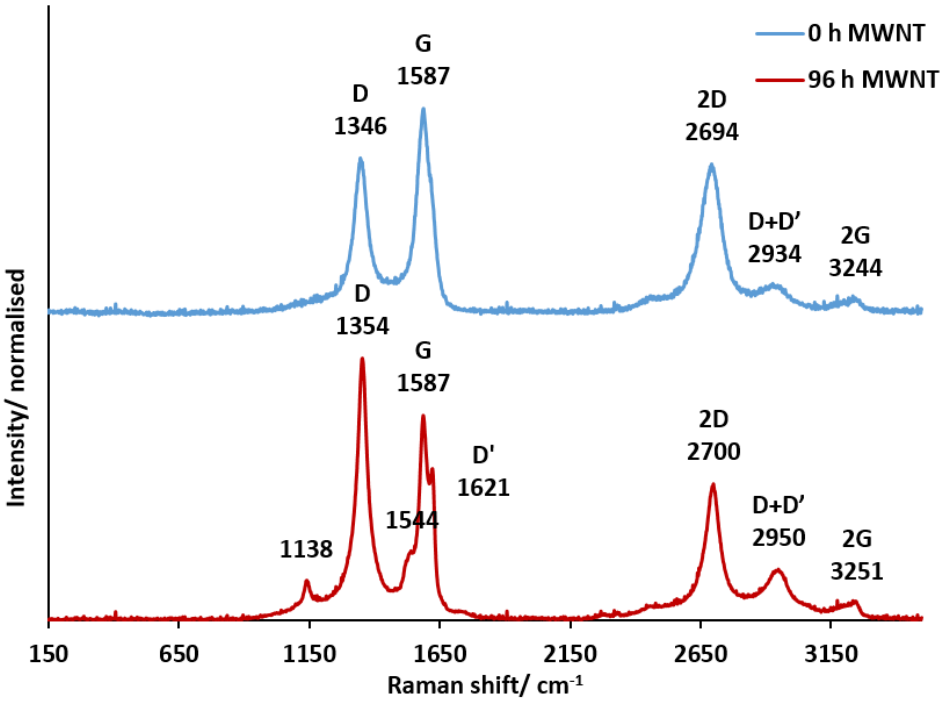


Figure 56. Raman spectra for 96 h-treated MWNT (normalised to the G band). The spectrum was acquired at excitation wavelength, λ_{ex}=532 nm.

Thermogravimetric analysis (TGA) could further probe the structure of the MWNT. For example, carbon nanotubes react with oxygen to form carbon dioxide when heated, but the temperature of this reaction depends on a range of factors, such as the diameter of the CNT, the number of graphitic layers and whether any metal catalyst remains from CNT synthesis. The oxidation of 0 h-treated MWNT was expected to occur at a lower temperature than the 96 h-treated MWNT because the defects and holes make the nanotubes easier to oxidise.

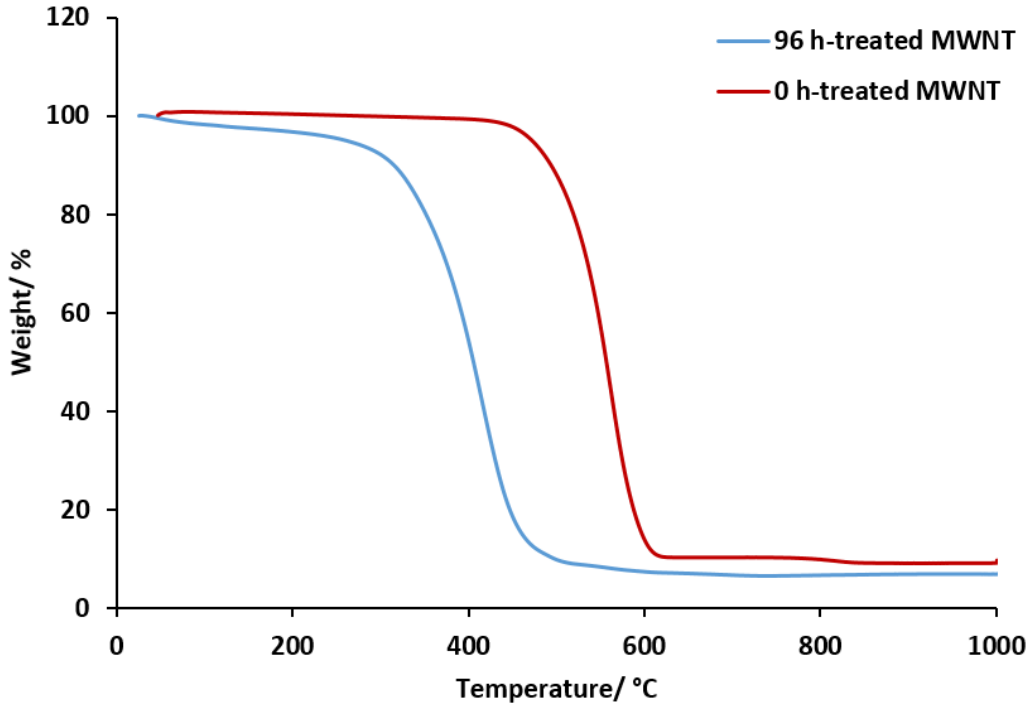


Figure 57. TGA of 0 h-treated MWNT and 96 h-treated MWNT. The weight loss at 400 °C (96 h-treated) and 550 °C (0 h-treated) correspond to the oxidation of carbon of the CNT to CO_2. A higher level of oxidation introduces more oxygen groups to the surface of the MWNT, weakens C=C bonds and creates a higher surface area, which leads to combustion at a lower temperature. Residual weight of 9.8% for 0 h-treated MWNT due to residual iron catalyst, and 6.9% for 96 h-treated MWNT.

Oxidation of 96 h-treated MWNT occurred at a lower temperature (400 °C) than 0 h-treated MWNT (550 °C) as a result of weakened C=C bonds, more oxygen-containing functional groups on the surface of the MWNT, and a higher surface area for oxygen to react with, which made the structure more susceptible to combustion. Also, while the 0 h-treated MWNT remained the same mass before combustion, the 96 h-treated analogue lost mass between *ca*. 25-300 °C, indicative of the loss of functional groups from the surface of the MWNT through decarboxylation reactions.

After heating to 1000 °C, the MWNT synthesis catalyst (iron) was not removed but was likely oxidised to Fe_2O_3, with residual wt.% calculated at 9.8% for 0 h-treated

MWNT and 6.9% for 96 h-treated MWNT. This discrepancy demonstrates that refluxing MWNT in nitric acid for 96 hours also removes some of the iron catalyst.

Through the analysis of both 0 h-treated MWNT and 96 h-treated MWNT, it is clear that the oxidation significantly changed the structure of the MWNT by introducing oxygen-containing functional groups and structural defects. To see how this affected the structure and location of QD synthesised with these nanotubes, a series of experiments was carried out.

Adapted from a method reported by Park. *et al*,[12] a typical experiment involved dispersing MWNT (oxidised for 0, 1, 16 or 96 h) in water, followed by the addition of cadmium acetate dihydrate, which readily dissociates into Cd^{2+} in water. The mixture was stirred for 90 minutes, before the addition of 1-thioglycerol and 1,2-dithioglycerol as surfactants. The mixture was then allowed to stir for 16 hours. Sodium sulfide nonahydrate was then added to the mixture and stirred for 16 hours, while the S^{2-} ions diffuse to Cd^{2+} leading to nucleation. Further diffusion of S^{2-} ions allows QD growth, while the surfactants stabilise the growth and prevent aggregation (Figure 58).[59] The equation for the reaction can be expressed as (Equation 2):

$$Cd(OAc)_2.2H_2O + Na_2S \rightarrow 2NaOAc + CdS + 2H_2O \qquad (2)$$

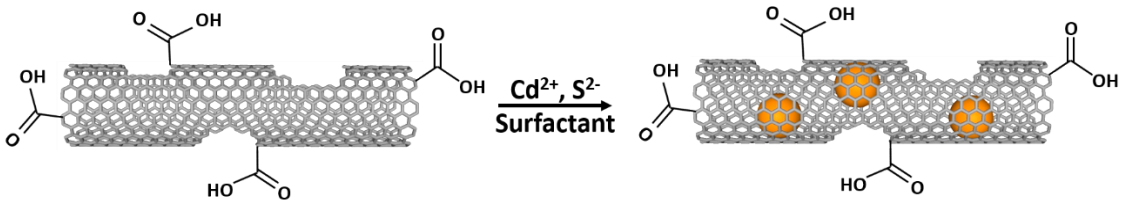


Figure 58. Schematic representation of the formation of CdS QD inside CNT.

The reaction product was collected by vacuum filtration to yield a black powder. It is interesting to note that during the QD formation reaction the suspensions remained black due to the CNT absorbing all of the visible light, masking any macroscopic aggregates of CdS suspended in the solutions. However, after filtering the mixtures to separate the hybrid material from the aqueous phase, a weak orange colour was always observed in the filtrate presumably from QD suspended in solution.

The resulting black powder was analysed using transmission electron microscopy (TEM) as it is the only technique that allows the location of NP (inside or outside of nanotubes) to be accurately determined. In addition, the sub-nanometre resolution images can provide information about the size, shape, crystallinity and distribution and was therefore used as the principle technique for analysis of the structures.

Figure 59 shows the structure of the MWNT after oxidation for 96 hours in nitric acid. Pores were created in the walls, ranging from the 1 nm to 6 nm in size.

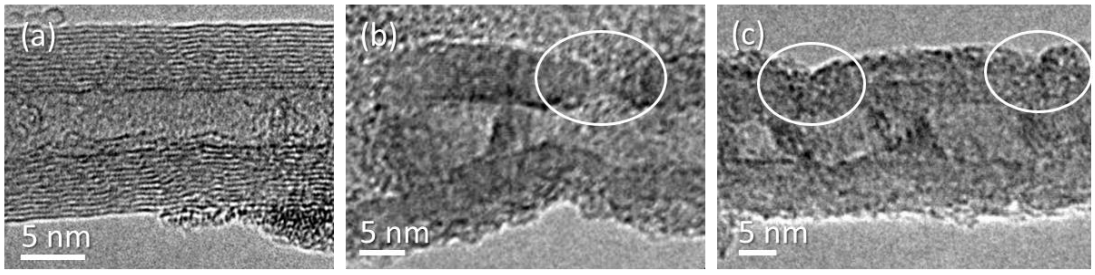


Figure 59. TEM images of (a) CdS/MWNT with smooth, intact walls and (b-c) pores in the walls of MWNT, caused by 96 h oxidation in 5 M nitric acid.

The structure of the 0 h-treated MWNT appeared smooth and intact (Figure 60). Whereas, the 96 h-treated MWNT were much more damaged and irregular as

the prolonged acid-treatment had altered the physical structure of the nanotubes and etched away at the graphitic layers. This shows that defects were introduced to the nanotubes through prolonged acid treatment, supporting Raman spectroscopy and TGA data.

TEM images for the range of acid-treated MWNT (0, 1, 16, 96 h treated) are displayed below.

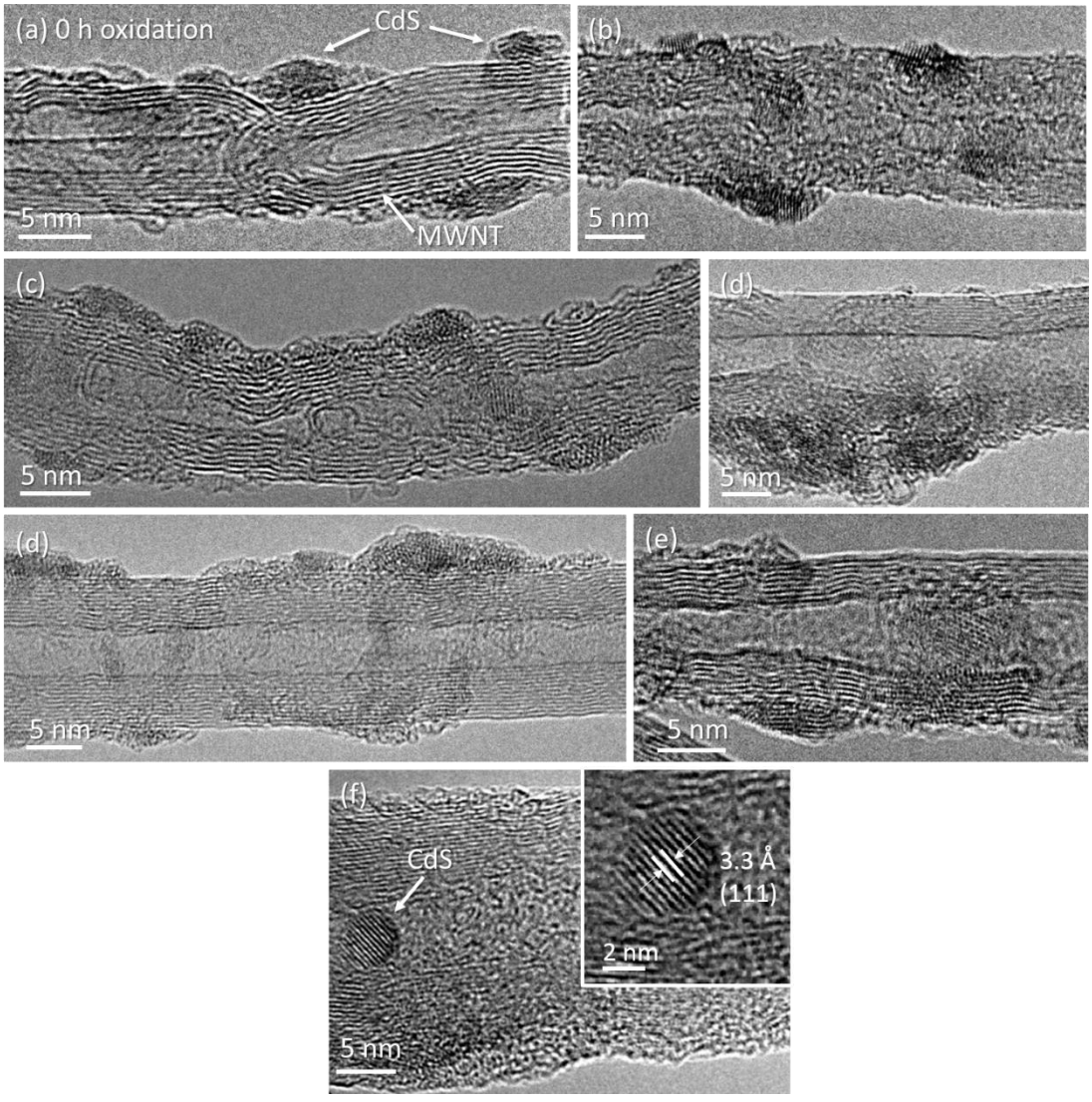


Figure 60. (a-f) TEM images to show hybrid of NP and 0 h-treated MWNT. A d-Spacing of 3.3 Å is clearly observed across the nanoparticle, corresponding to the (111) crystal planes of CdS.

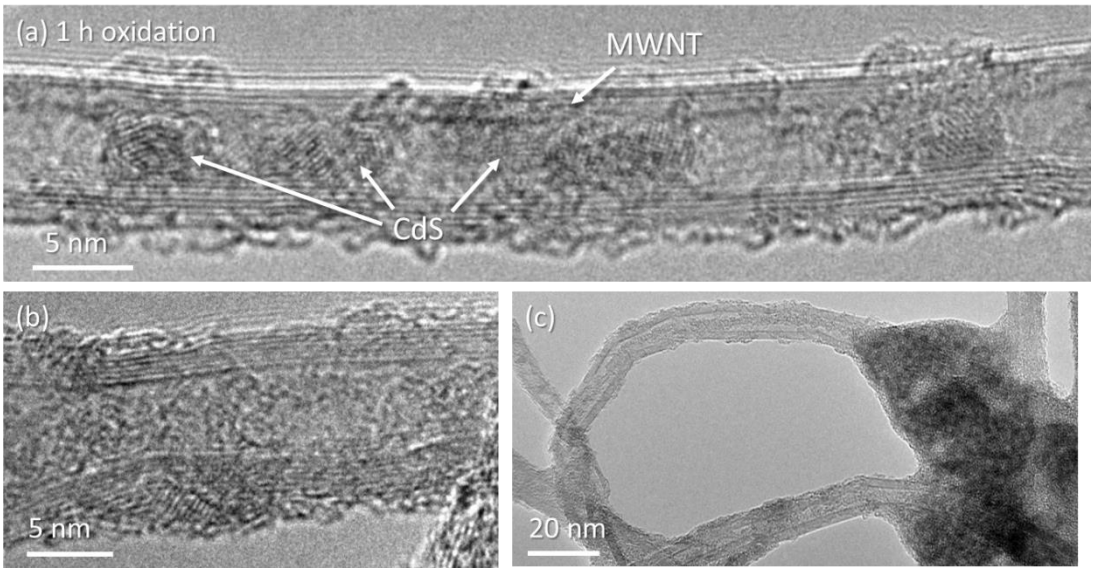


Figure 61. (a-c) TEM images to show hybrids of QD and 1 h-treated MWNT.

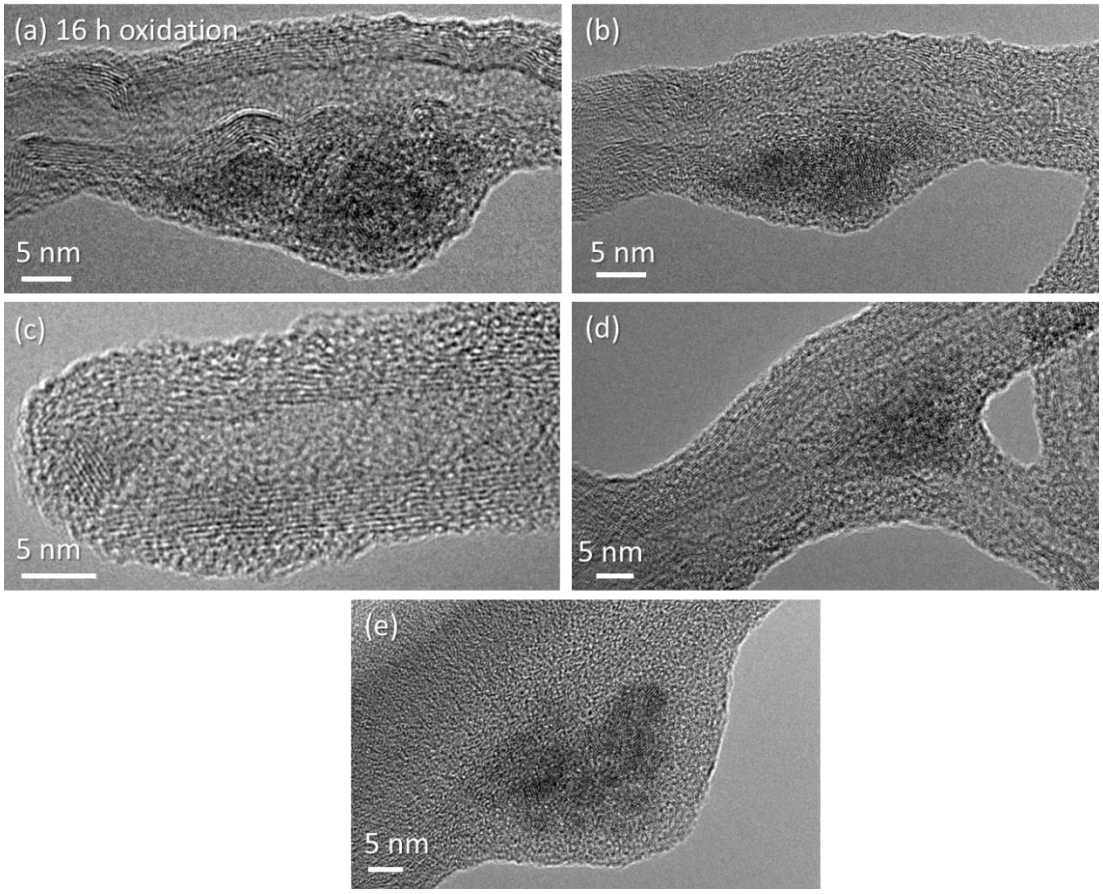


Figure 62. (a-e) TEM images to show hybrids of NP and 16 h-treated MWNT.

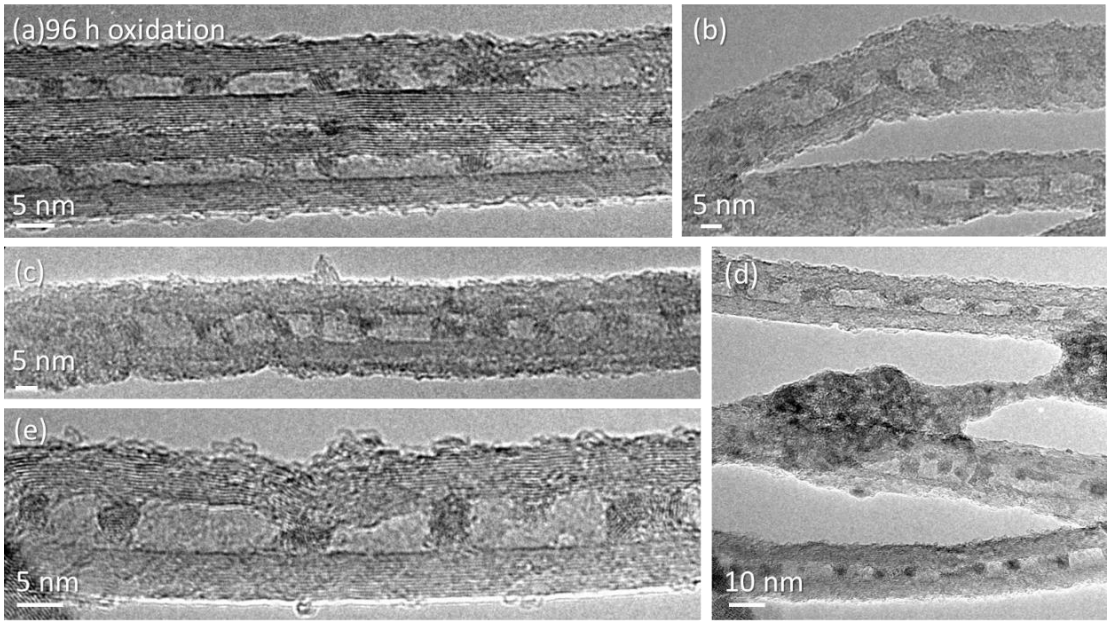


Figure 63. (a-d) TEM images to show hybrids of NP and 96 h-treated MWNT.

Statistical analysis of the coverage and size of NP associated with the MWNT was carried out by counting the number of discrete NP on the MWNT for a measured length of nanotube. This was repeated until a statistically significant number of measurements were recorded. The coverage was then calculated as the number of discrete NP on the MWNT per μm of the nanotube length. Similarly, the filling rate of discrete NP encapsulated within the MWNT was also calculated. The mean diameters of the NP were determined by measuring both the long and short axis. These two measurements were recorded because most of the NP were not spherical, and this method provides information about the shape of the NP as a result of the interactions with the MWNT. The results are presented in Table 9.

Table 9. Coverage of QD on MWNT, with variable MWNT oxidation.

Reflux time/ hours	**0**	**1**	**16**	**96**
NP (discrete) on per µm	83	12	0	19
NP (discrete) encapsulated per µm	5	22	3	70
NP size/ nm	5.0 x 2.4	*	*	4.6 x 3.5

*NP size could not be accurately determined due to the formation of clusters.

The highest number of discrete NP associated with the MWNT resulted from 0 and 96 h-treated MWNT. The former has no functionalisation to the outer walls of the MWNT so NP are likely to be attached through vdW forces. However, when the coverage of carboxylic acid groups on the external surface of the MWNT increased through increased treatment time in acid, the number of NP associated with the MWNT decreased and NP formed large clusters. This could be the result of unfavourable interactions between thiols on the NP and carboxylic acids groups on the MWNT, destabilising individual NP. Many NP then clustered together, thereby increasing the vdW forces between several NP. As the oxidation time of MWNT was further increased to 96 hours, MWNT were opened, creating an accessible route for NP precursors to enter the MWNT. NP then formed inside the MWNT preferentially as they are stabilised by van der Waals forces between the NP and the concave surface of the MWNT.

It was remarkable to discover an incredibly high NP filling rate of 70 NP per µm in 96 h-treated MWNT. The capability to form NP encapsulated within MWNT almost exclusively, shows how powerful the pre-treatment of MWNT is as a tool for controlling the interactions between the nanotube and NP to tailor the hybrid.

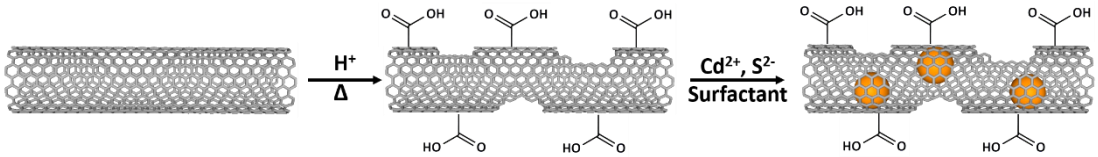


Figure 64. Schematic to show the opening (through oxidation in HNO_3) and subsequent filling process for the formation of NP inside MWNT.

When pores are formed in the walls of MWNT, capillary forces drive NP precursors inside the MWNT. As the nanocrystals grow, they interact with the nanotube walls through vdW forces, the cumulative effect of these forces is much higher when nanoparticles are encapsulated, as oppose to on the outer wall, as the contact surface area significantly increases. It is clearly the structure of the MWNT that affects the location of these NP on MWNT, rather than its surface.

Since highly filled nanotubes, as formed with 96 h-treated MWNT, were the target material, only this structure was characterised further. Having found that QD were encapsulated inside MWNT, further TEM was warranted in order to study the structure in more detail. To confirm that the NP thought to be inside 96 h-treated MWNT were definitely encapsulated, the material was rotated inside the electron microscope, around the nanotube growth axis, and images collected at a range of angles, producing a tilt series (Figure 65).

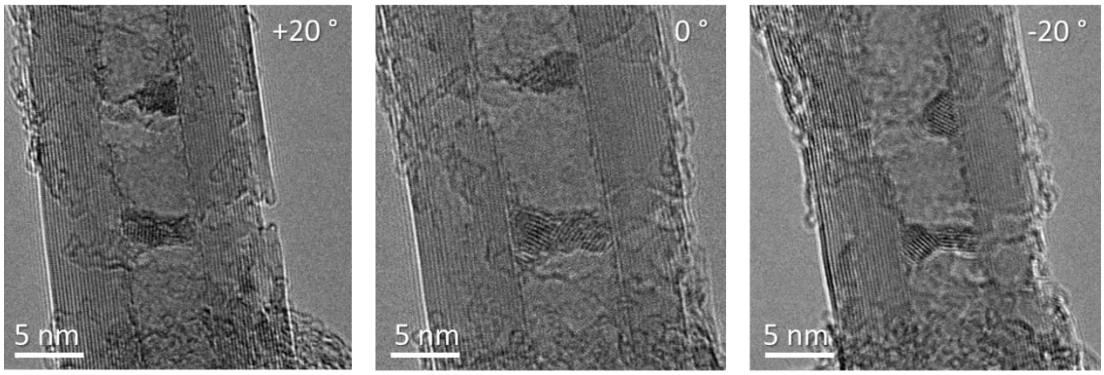


Figure 65. Tilt series (+20° to -20°) of TEM images of NP in 96 h-treated MWNT.

The amorphous material coating the MWNT was presumably excess 1-thioglycerol and 1,2-dithioglycerol used as a surfactant. From the TEM analysis the average diameter of these NP was measured to be 4.6 ± 1.0 x 3.5 ± 0.9 nm, with a long axis and a short axis, i.e. the NP were non-spherical. The inner diameter of the MWNT was measured to be 5.1 ± 1.5 nm, suggesting that MWNT templated the long dimension of the NP (4.6 ± 1.0 nm) when the standard deviation is considered.

To confirm that encapsulated NP were templated by the MWNT, the size of NP in solution was probed. Analysis of the filtrate using UV-vis spectroscopy showed a peak maximum at 512 nm, correlating to CdS with the mean diameter of 8.34 nm.[52] This method for analysing the diameter of CdS is a bulk scale technique, so was representative of the entire sample. The diameter of CdS in the filtrate was much larger than the NP encapsulated within MWNT (4.6 nm x 3.5 nm), suggesting that MWNT limit the growth of NP. This clear size discrimination between NP encapsulated in CNT and CdS in solution, must also mean that QD can grow simultaneously in solution, and in CNT.

Comparisons between the long and short dimensions of NP in MWNT are reported to highlight the distribution of diameters formed. The results were measured from TEM images, recorded for both the long and short NP axis, shown in the histogram below (Figure 66).

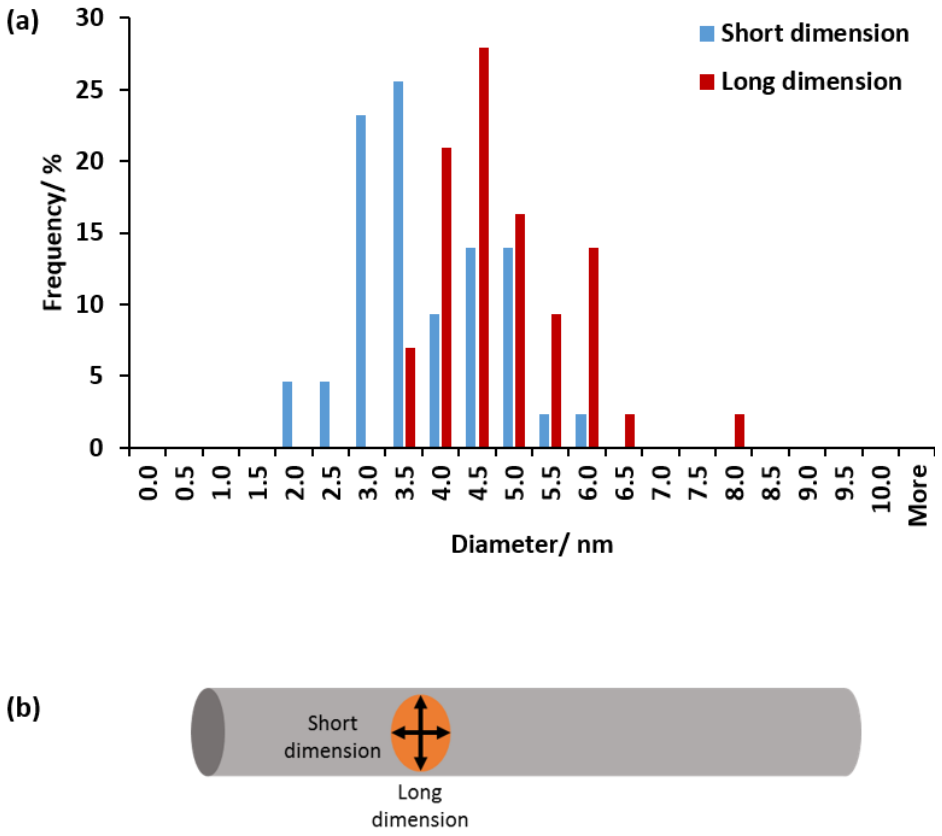


Figure 66. (a) Histograms to show the size distribution of NP in MWNT for dimensions measured along both the short and long axis of the NP, d_{NP}= 4.6 ± 1.0 nm x 3.5 ± 0.9 nm. (b) Schematic representation of the short and long dimensions of QD measured inside MWNT.

The aspect ratio (long dimension/ short dimension) was calculated to be 1.38, representative of the elongated shape of the QD. The long dimension of the NP appear to be templated by the concave surface of the MWNT, completely filling the

cross section of the nanotube. It is likely that the length of the QD parallel to the MWNT is then dependent on the amount of NP precursors available.

The NP formed showed clear lattice spacing of 3.3 Å, consistent with the (111) crystal planes of cubic CdS (Figure 67).[60] Here, the atomic contrast from CdS was much higher than of carbon forming the walls of the MWNT, resulting from the higher atomic number of cadmium and sulfur, compared to carbon. Thus, while graphitic CNT walls and CdS have very similar d-spacing, the encapsulated NP was not composed of carbon.

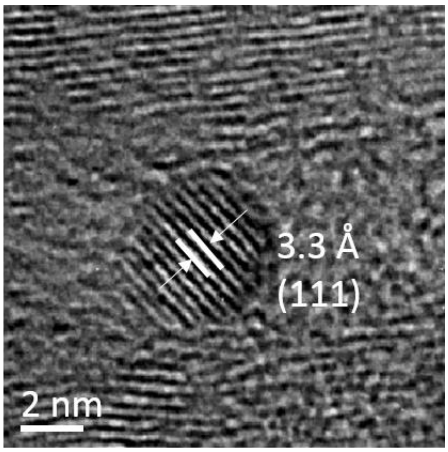


Figure 67. TEM micrograph of CdS quantum dots showing d-spacing. A lattice spacing of 3.3 Å corresponds to the (111) crystal planes of CdS.

CdS QD in this size range (*ca*. 4 nm) are most commonly formed as zinc blende crystals,[61, 62] with factors such as the molarity of the capping agents[63] also playing a part. In our experiments, the concentration of thiols (<0.2 M) was consistent with the formation of a zinc blende crystal structure of CdS.

Energy-dispersive X-ray spectroscopy (EDX) was used to appraise the elemental composition of a material (Figure 68).

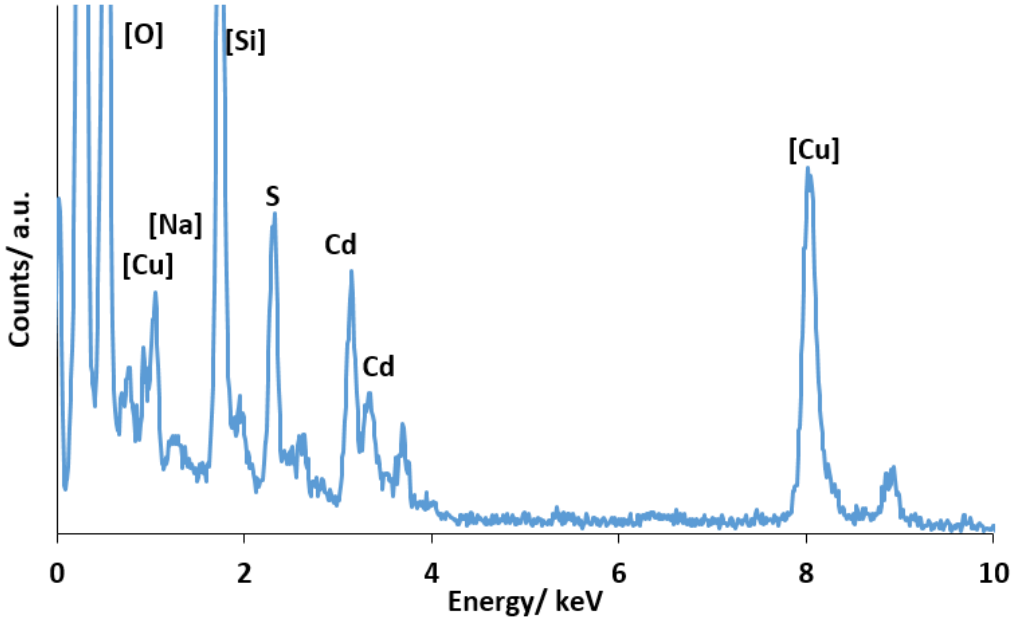


Figure 68. EDX spectrum of CdS in 96 h-treated MWNT, showing the presence of cadmium and sulfur.

As expected, both cadmium and sulfur were detected in this material. The ratio of Cd:S was found to be 1:1.6, with the excess sulfur attributed to the thiol coating, observed in TEM images. Combining this with the information obtained through TEM, the circular structures inside the MWNT could confidently be identified as CdS. Having confirmed that CdS QD were encapsulated within the 96 h-treated MWNT, the material can now be referred to as CdS@MWNT.

EDX and TEM are useful techniques for determination of the elemental composition and visualisation of the morphology of QD on CNT. As both are local probe techniques, it was important to use bulk analytical methodologies to appraise the chemical properties of the entire sample. The first example of such a characterisation technique is powder X-ray diffraction (PXRD). A peak corresponding to the graphitic planes of MWNT was expected, along with crystal planes from CdS QD.

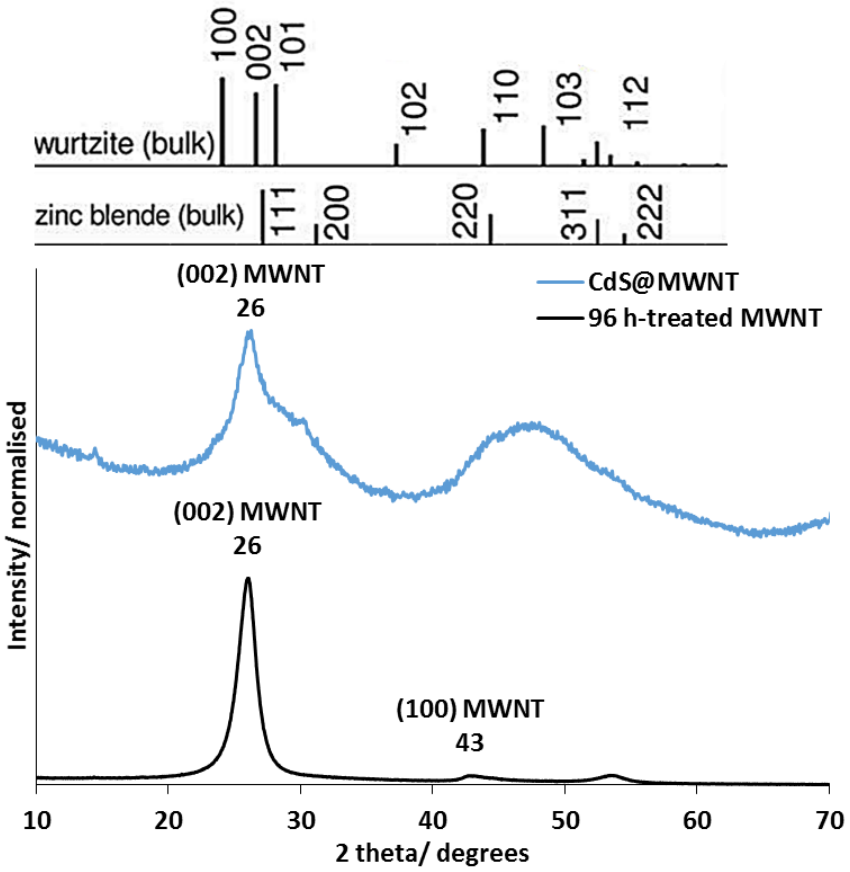


Figure 69. PXRD for CdS@MWNT (blue), and MWNT only (black). The XRD patterns of bulk wurtzite and zinc blende CdS are included for reference, reported by Dzhagan *et al*.[64] (JCPDS no. 75-0581 and JCPDS no. 80-0019).

As expected, the highest intensity peaks were present for CdS@MWNT at 26˚ and *ca*. 43˚, corresponding to MWNT (002) and (100) planes respectively.[12, 65] However, the peak at 26° was also the result of the (111) crystal planes of zinc blende CdS,[8] with a clear shoulder which could be the contribution from the (200) plane. The broad diffraction peak is a direct result of the small diameter of the QD, with peak broadening observed as the nanoparticle size decreases.[41] An additional, broad peak was present at *ca*. 47°, which is not from MWNT and instead is likely resulting from the (220) and (311) crystal planes of cubic (zinc blende) CdS,[8] but may also be a contribution from wurtzite crystal planes (110) and (103). Similarly broad peaks were

observed by Neelgund and coworkers who formed CdS on MWNT,[25] and Wageh *et al*.[66] Due to the peak broadness and overlap, the full width at half maximum cannot be accurately measured, thus the Scherrer equation would not be useful for calculating CdS diameters. Whilst the size of the QD could not be quantified by PXRD measurements, they agree with the TEM analysis that the QD must be very tiny and do not conflict with the size measured through TEM analysis of 4.6 x 3.5 nm.

Raman spectroscopy was another bulk method used to indicate the presence of CdS. In addition to the peaks from MWNT, features corresponding to CdS were also expected in CdS@MWNT.

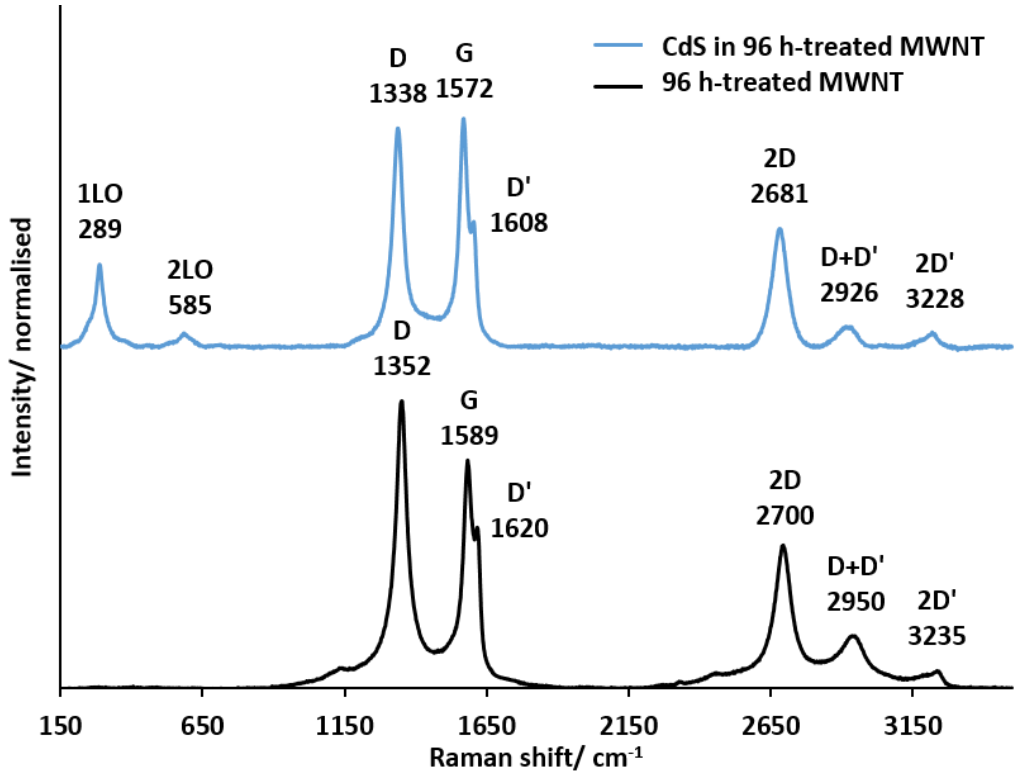


Figure 70. Raman spectra for CdS@MWNT (normalised to the G band). The spectrum was acquired at excitation wavelength, λ_{ex}=532 nm. Bands at 289 and 585 cm^{-1} from the first-order longitudinal optical (1LO) phonon and second-order longitudinal optical (2LO) phonon of CdS QD, respectively.

There was some variation in position and relative intensities for MWNT upon the introduction of CdS (D, G and 2D bands at 1352, 1589 and 2700 cm^{-1} respectively,[67] shifted to 1338, 1572 and 2681 cm^{-1}) due to heating effects. CdS absorbed light from the laser (λ_{ex}=532 nm, corresponding to photon energy of 2.3 eV), and converted phonons into thermal energy. This thermal effect then shifted the D and G bands of MWNT by 14 and 17 cm^{-1} respectively. Studies have shown correlation between the positions of the G bands in SWNT and highly oriented pyrolytic graphite as a function of temperature, agreeing that red-shifting occurs with heating (*ca*. -0.03 cm^{-1} K^{-1}).[68, 69] This downshifting of 17 cm^{-1} indicates a *ca*. 567 °C increase in the temperature of CdS@MWNT compared to MWNT alone.

There was also a decrease in the I_D:I_G ratio from 1.26 to 0.97, also attributable to this heating effect. More interestingly, new bands at 289 and 585 cm^{-1} were observed from the first-order longitudinal optical (1LO) phonon and second-order longitudinal optical (2LO) phonon, respectively. The band position was very similar to that reported by Goswami and coworkers,[5] *ca*. 294 and *ca*. 588 cm^{-1} for 1LO and 2LO phonon modes, respectively, for two sets of QD with diameters of 4.84 and 2.74 nm.

The medium surrounding the QD affects the vibrational properties of the material and if the phonon cannot propagate through the surrounding medium, in this case thiols and MWNT, then the confinement effects are similar to an isolated particle.[70] The bands become broader and red shifted as the QD size decreases (bulk CdS has peaks at 305 cm^{-1} (1LO) and 605 cm^{-1} (2LO)).[71, 72] This is due to a combination of factors, namely, energy-minimization-driven reconstructions, accompanied by changes in the bond lengths and elastic properties upon the reduction in size.[64] A

large QD size distribution, the presence of defects, thermal effects from the laser and phonon confinement also play a part.[73]

There is disagreement in the literature as to whether the size can be accurately determined from the shift, with Zeiri *et al*. showed that the size (between 2-5 nm) and shape (rod or sphere) does not correlate with the band position,[74] in agreement with Shiang and coworkers (*ca*. 1-15 nm).[75] While other studies on larger CdS nanowires (9-22 nm)[76] report a large red shift with decreasing size. Alternatively, theoretical equations by Vasilevshiy and coworkers[77] are backed up by Kostić[78] to calculate the diameter of the QD from the 1LO shift. If this correlation is applied to our Raman spectra, the 1LO band at 289 cm^{-1} correlates with a CdS diameter of around 2.6 nm, which is close to the short dimension of the QD, and could be within the error. But again, disagreement within the literature is noticed as ultrasmall CdS nanoparticles showed 1LO bands at 300 cm^{-1} for both 1.8 nm and 3.0 nm size CdS, with the appearance of a surface optical (SO) mode at smaller diameter, leading to a change in the shape of the band at 300 cm^{-1}.[64]

The 2LO:1LO ratio is often used to determine the electron-phonon coupling strength in polar semiconductors and thus determine the size of the QD.[79] In this case a 2LO/1LO value of 0.165 would be the result of weak electron-phonon interactions, to confirm the zinc blende structure of CdS observed in TEM images.[80] It is also within the range of values reported for 5 nm QD over a range of excitation wavelengths (0.14-0.38).[74] However, other works have reported independence of the 2LO/1LO value,[81, 82] and both increases[75] or decreases[83, 84] of the 2LO/1LO value with NP size. The electron-phonon coupling is determined by a mixture of properties, including the QD internal structure, and the electronic coupling between the electronic states of

the QD and the surfactant/capping groups, so cannot be used to determine the size of the QD.

Irrespective of these factors, the Raman bands clearly confirm the presence of CdS in the sample, signifying that the TEM images are representative of the entire material, and show that QD are small, likely in the size determined by TEM analysis.

Further evidence of CdS formation was obtained through TGA analysis of the composite material in air (Figure 71). A series of weight loss steps were expected corresponding the successive evaporation of thiols, combustion of CNT and oxidation and/or evaporation of CdS.

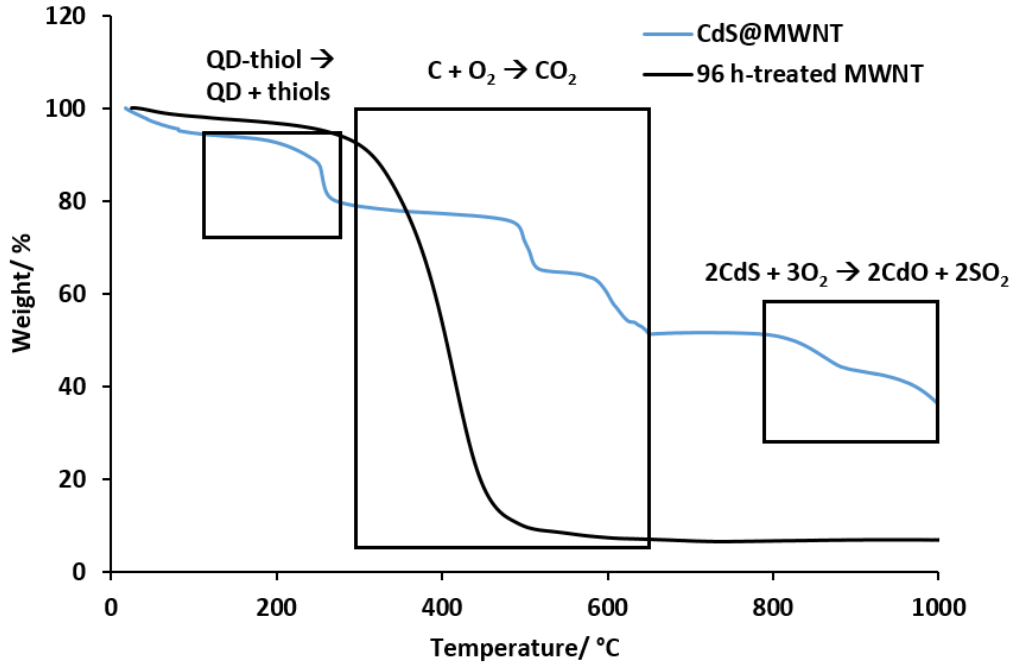


Figure 71. Thermogravimetric analysis (TGA) of CdS@MWNT and 96 h-treated MWNT in air with temperature increasing at a rate of 5 ˚C min^{-1}.

The weight loss between 200-300 °C was assigned to the decomposition of 1-thioglycerol and 1,2-dithioglycerol. This is higher than the reported boiling points

of 118 ˚C for 1-thioglycerol[85] and 140 ˚C for 1,2-dithioglycerol, as the energy barrier to break bonds between sulfur and cadmium had to be overcome. A reduction in mass due to the combustion of CNT was detected as two weight loss steps (500 ˚C then 600 ˚C) for CdS@MWNT. This could be the result of some MWNT filled with CdS, while others are empty. In this case, filled MWNT may combust at a higher temperature as the interactions between CdS and MWNT must be overcome.

Reports in the literature state that between 200-300 ˚C, thiols are removed from the surface of the QD, but sulfur and oxygen coordinated groups are left behind.[86,87] Then, between 640-850 ˚C, the evaporation of sulfur occurs,[87] with a final weight loss step above 840 ˚C resulting from the removal of oxygen from the QD surface.[66] However, the large weight loss of 8% reported herein cannot possibly be due to the removal of surface coordinated groups alone so another explanation must be found.

Alternatively, various endothermic processes are reported to occur in the temperature range 500 ˚C to 1000 ˚C, several of which could explain the observed weight loss.[88]

$CdS_{(s)} \rightarrow CdS_{(g)}$	850 ˚C	**(3)**
$CdS + 2O_2 \rightarrow CdSO_4$	400–800 ˚C	**(4)**
$CdSO_4 \rightarrow CdO + SO_3$	820–1000 ˚C	**(5)**
$3CdS + 5O_2 \rightarrow (CdO)_2.CdSO_4 + 2SO_2$	820–1000˚C	**(6)**
$2CdS + 3O_2 \rightarrow 2CdO + 2SO_2$	820–1000 ˚C	**(7)**

Many of these reactions would result in a mass increase, which indeed is seen in other examples in the literature. For instance, a gain in mass is observed in the 400-750 °C range, as CdS is oxidised to $CdSO_4$.[89] However, no increase in mass was observed in our TGA measurements.

To draw more accurate conclusions about the transformations occurring during the heating process it was beneficial to know how much cadmium was in the sample. Inductively coupled plasma optical emission spectroscopy (ICP-OES) was therefore utilised, with the analysis showing 33% cadmium by weight for CdS@MWNT. Considering the residual mass in the TGA was 37%, 33% cadmium content was calculated to form 37% CdO, so the weight change can now confidently be ascribed to CdS forming CdO through Equation 7. Kristl *et al*. also saw a similar mass loss from isolated CdS QD, but attributed the result to the mixture of new crystal phases CdO and $CdSO_4 \cdot 2CdO$ forming.[90] This, however, was unlikely to cause a large weight loss alone. In our TGA, the mass of 50% at 800 °C was higher than expected for CdS of 33% Cd content (predicted wt.% CdS = 42%), the difference could be the result of incomplete combustion of MWNT which were partially covered with CdS. There is also the possibility of partial CdS sublimation in addition to the oxidation process.

TGA further confirmed the presence of CdS within the material but since several reactions occurred simultaneously and could not be deconvoluted, it was not possible to fully quantify the mass of CdS in the samples through TGA, thus the cadmium content obtained through ICP-OES (33% cadmium by weight) provided a more accurate result.

A large amount of information about the structure and composition of CdS@MWNT was gained through TEM and EDX. Following this, PXRD, Raman spectroscopy and TGA were predominantly used to clarify that the TEM images were representative and consistent with the structure and composition of the bulk material through the detection of CdS diffraction peaks, vibrational bands and weight loss steps respectively.

Having thoroughly and systematically investigated the formation of CdS QD in MWNT, it is evident that the excessive treatment of MWNT produces pores, which drives the formation of CdS exclusively inside MWNT. The MWNT acts as a template resulting in CdS QD with dimensions of 4.6 x 3.5 nm.

4.3.2 The effect of nanotube's diameter and internal structure

The next objective was to discover how the CNT diameter affects the size, shape and distribution of CdS on the CNT, by transferring the optimised formation procedure for CdS@MWNT to other carbon nanocontainers with different diameters and graphitic layers. Single-walled carbon nanotubes are well studied and have been filled with a wide range of different molecules and nanoparticles. Yet, due to the very narrow internal diameter (SWNT, d = 1.3 nm), significant steric restrictions towards encapsulation of precursors for CdS formation is imposed. However, as nanotubes often bundle together in solvent in order to increase the vdW forces between SWNT,[91,92] CdS may form in between the grooves of SWNT, and in turn affect the size and shape of the QD.

As-received SWNT are capped so first needed opening to allow QD precursors to enter the nanotube. The reactivity varies inversely with the diameter of the

nanotube, as such, oxidation in acid can quickly degrade the entire structure, to form fragments of carbon. Therefore, unlike the oxidation of MWNT, which are more chemically robust, the acid treatment must be very short for SWNT. The oxidation procedure would also introduce carboxylic acid groups to the surfaces of the nanotubes, which should increasing their dispersibility in water and may prevent bundling.

SWNT were oxidised by heating to reflux in nitric acid for 1 h or 16 h. The mixture was then diluted with water, collected by vacuum filtration and washed until the filtrate was pH neutral. However, the 16 h-treated SWNT could not be collected as they passed straight through the PTFE membrane, demonstrating that these conditions have cause too much damage to the SWNT, as they had been shortened to <0.2 μm. However, 1 h-treated SWNT could be isolated.

Composites of CdS and SWNT were prepared in a method analogous to CdS@MWNT, using 1 h-treated SWNT. Once the formation reaction was complete the most useful form of analysis to determine the structure of the material formed was TEM. The images revealed that QD formed on the surface of bundles of SWNT, predominantly as clusters (Figure 72).

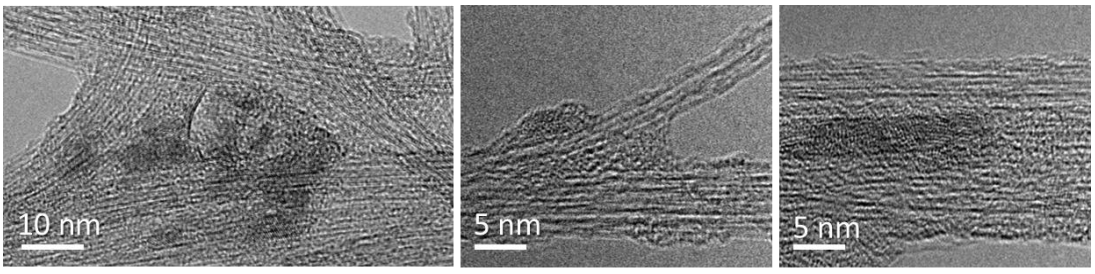


Figure 72. TEM of the composite of CdS and SWNT showing the formation of QD on the surface of clusters of SWNT.

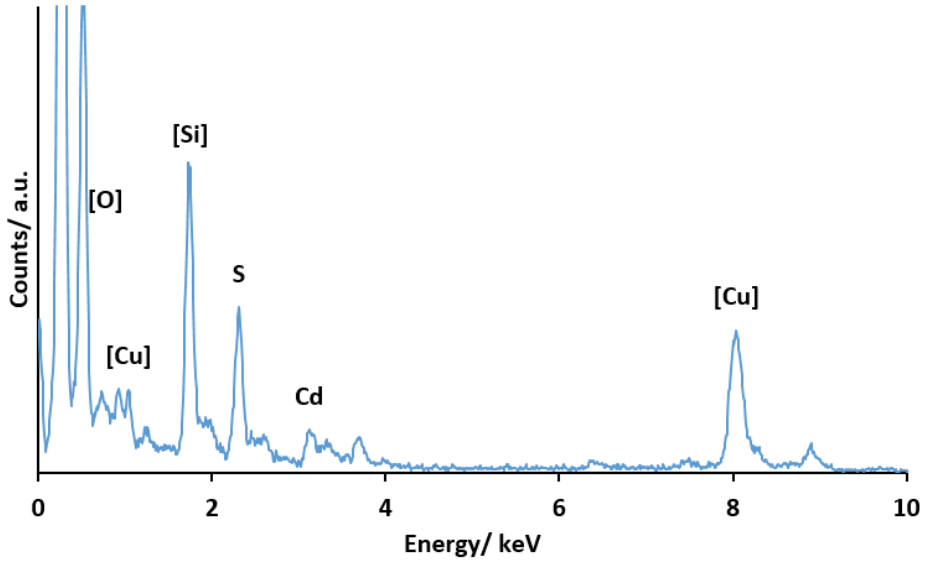


Figure 73. EDX spectra of composites of CdS and SWNT, showing the presence of cadmium and sulfur.

In this material, EDX was also utilised to determine elemental ratios, and showed the percentage of cadmium and sulfur to be 1:3.8. The high ratio of sulfur is demonstrative of large amounts of surfactant coating the bundles of SWNT with only a small numbers of CdS QD attached. Bundling of SWNT is a known phenomenon,[91,92] but one which poses difficulties when forming the hybrid materials. Cd^{2+} and S^{2-} ions could not enter the bundles to form isolated QD on individual SWNT, instead clusters of QD only grew on the surface of the bundles. The cluster size of QD on SWNT bundles ranged between 6 nm x 2 nm to 40 nm x 26 nm with no isolated QD observed in the sample.

The CdS cluster formation was similar to that observed previously for CdS on 1 or 16 h-treated MWNT. When CNT were carboxylic acid functionalised, the formation of individual QD on the MWNT surface was destabilised and as a result clusters were formed. If there are enough accessible pores in MWNT then QD form

inside the cavity of the MWNT. However, this did not happen for CdS on SWNT, either due to insufficient oxidation of SWNT, or because the internal diameter of the SWNT is too narrow to accommodate CdS QD.

This result is consistent with the hypothesis that vdW forces control QD formation; however, the most stable arrangement in this case was the formation of clusters of CdS and bundles of SWNT. Effective contact between QD and CNT is required in order to harness the properties of both in a composite. Yet, as SWNT bundle, effective contact is not possible, and therefore SWNT are not a good material to use to form hybrids of CdS encapsulated in CNT.

In contrast to SWNT, graphitised nanofibers (GNF) are large hollow, carbon nanostructures; they have the highest number of graphitic walls and largest internal diameter (d_{GNF}^{INT} = 30-50 nm). Unlike SWNT, GNF do not bundle in aqueous suspensions which may prevent clusters of QD forming.

QD are likely to form inside GNF for two reasons. Firstly, the size of the cavity in GNF is very large compared to MWNT and SWNT and as-received GNF are not capped. This provides a large opening for Cd^{2+} and S^{2-} ions to enter, and no pre-treatment is required. Secondly, the structure of GNF are slightly different to MWNT in that the interior is corrugated, resembling stacked cups and outer walls are smooth. This corrugated interior of GNF provides step edges; here the vdW forces between the GNF and nanoparticles are highest,[93] and thus provide excellent anchoring points where NP are stabilised.

The method of forming CdS QD encapsulated within GNF was analogous to CdS@MWNT. TEM images showed many dark circles inside the thick GNF walls,

representing an astonishingly high filling of CdS QD inside the GNF as densely packed, discrete particles (Figure 74). Some clusters were also observed on the outer wall.

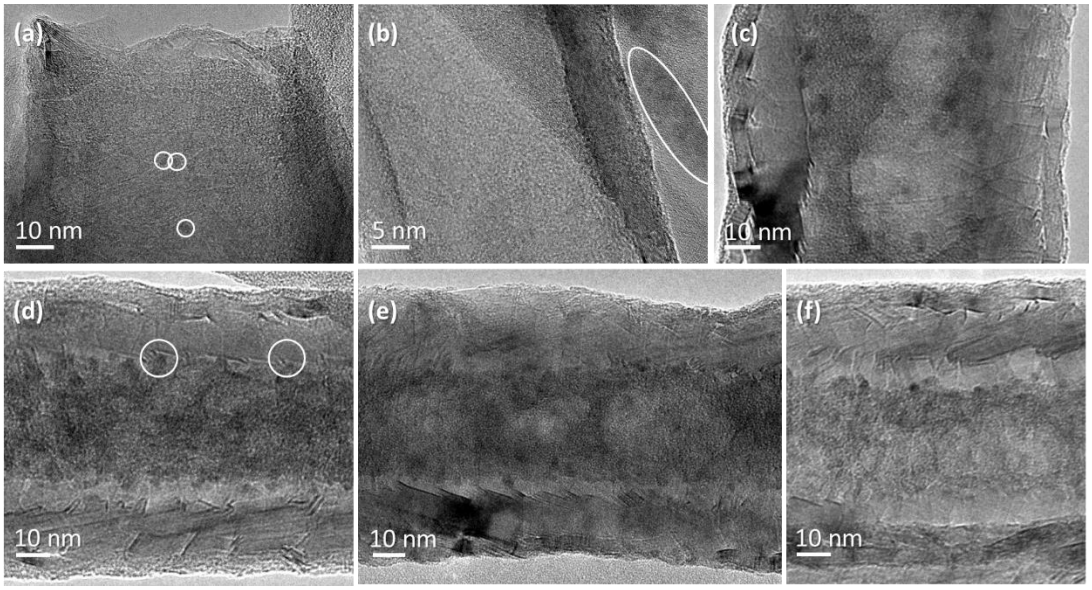


Figure 74. TEM images to show CdS@GNF. White circles show the location of the QD.

Presumably a high local density of precursor ions were encapsulated within the GNF, which allowed a high density of QD to form in the thiol filled cavity of the nanofibre. The vdW forces between QD and GNF would be highest at the step edges, which explains why a number of QD were located here (Figure 74 (d)). But QD were also evenly distributed throughout the GNF cavity, hence, QD interactions with the surfactants may be just as important in controlling the structure of the hybrid material.

It also appears as though the GNF were filled with an amorphous material, most likely attributed to surfactant or solvent. This meant the QD became difficult to visualise through TEM due to the poor contrast between CdS, GNF and surfactant. Hence, analysis of the sample was extremely difficult and the size, shape, coverage and location of most of the QD could not be reliably determined.

The percentage of sulfur and cadmium seen in the EDX spectra was 1:1.7, which is very close to the ratios seen in CdS@MWNT. It could be rationalised that in CdS in GNF and CdS/MWNT, QD were coated with the same amount of surfactant, and what appeared to be amorphous material inside the GNF was just the result of very densely packed QD rather than surfactant. This result agrees with the earlier statement that if enough room is provided for precursor ions to enter the nanocontainer, QD will form inside the cavity.

Whilst the formation of CdS in GNF hybrids showed remarkably high filling, and provided further insight into the interactions with CdS and large carbon nanocontainers, accurate quantitative analysis of the size, shape, and coverage of QD was not possible due to the poor contrast in the TEM images. Due to the thick carbon walls of the GNF blocking interactions/ masking any signal from CdS, analysis using microscopy, spectroscopy and diffraction would not be able to detect CdS. Hence, no bulk characterisation techniques were performed and this material was not taken any further.

4.3.3 Effect of the container and filling mechanism

Having successfully confined CdS QD inside MWNT, it was desirable to develop a procedure for filling BNNT in an effort to make new materials with original and useful properties. BNNT are isoelectronic to CNT, but the intramolecular bonds are more ionic, with more localised π bonding, than in CNT. This would affect the CdS-nanotube interactions and likely impact the size and shape of the QD formed.

As demonstrated earlier, filling MWNT with QD is dictated by the pre-treatment of MWNT to create pores and permit QD precursor ions to enter. Since

BNNT cannot be oxidised in this way, difficulties with encapsulation of CdS into BNNT were anticipated. The dimensions of the BNNT (d_{NT}^{INT} = 2.45 ± 1.19 nm, d_{NT}^{EXT} = 4.32 ± 2.09 nm) are slightly smaller than MWNT (d_{NT}^{INT} = 5.1 ± 1.5 nm, d_{NT}^{EXT} = 30 ± 15 nm) but should still permit filling, though may result in smaller QD if BNNT template the formation of CdS, analogous to that observed for MWNT.

Two filling methods were explored in order to investigate the filling efficiency of gas and liquid filling (Figure 75). The solution method was analogous to CdS@MWNT formation due to the success of this approach. By contrast, a gas filling method, in which materials are sublimed by heating in vacuum, has proven effective for filling CNT with metal halides and organic molecules, as well as filling BNNT with C_{60} (Chapter 3), as molecules become encapsulated due to vdW interactions with the concave surface of the nanotube.[94, 95]

Sublimation methods may be advantageous over solution filling since solvent molecules will not block the nanotubes or interact with other encapsulated molecules, so conceptually, this could be a beneficial approach. However, it is very unusual to form CdS QD in this way, with limited examples of CdS filling in CNT through sublimation of precursors,[96] and no examples inside BNNT.

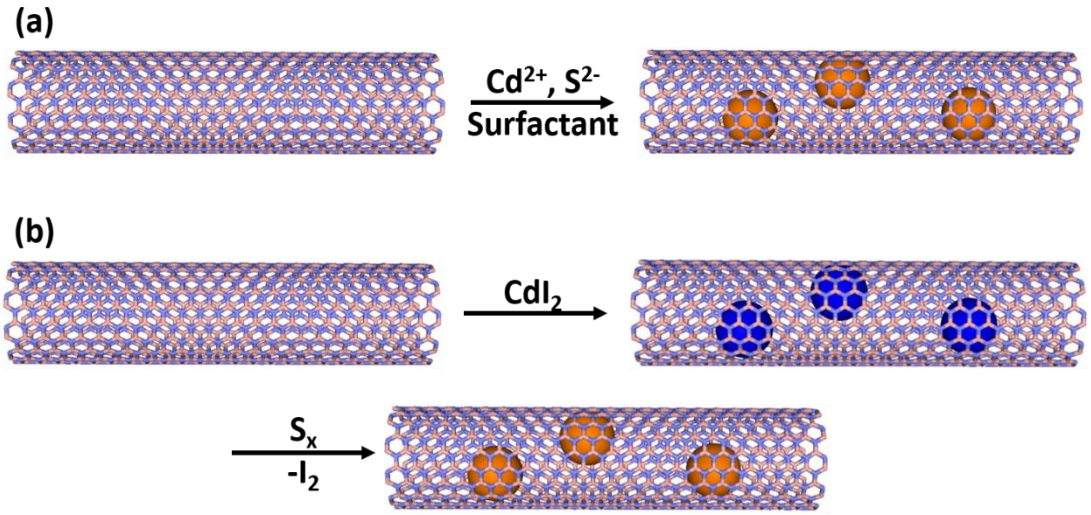


Figure 75. Encapsulation of CdS@BNNT through (a) a solution filling method and (b) a gas filling method.

In both filling experiments, BNNT were already opened through sonication-assisted hydrolysis in ammonium hydroxide solution, followed by thermal oxidation, as described in Chapter 2.

The solution filling method was analogous to the formation of CdS@MWNT. BNNT were stirred in an aqueous solution of cadmium acetate, a source of Cd^{2+} ions, for 90 minutes to allow diffusion of the ions into the BNNT. Thiols were added to control the growth of QD, and sodium sulfide was later added as the S^{2-} source. A pale pink colour was observed, likely due to QD suspended in solution.

While the sublimation route was based on a method reported by Eliseev, in which CdS formed inside SWNT through the sublimation and reaction of precursors.[96] Firstly, cadmium iodide was encapsulated in open BNNT through heating the two materials in a Pyrex ampoule under vacuum. The ampoule was heated well above the sublimation temperature of 448 °C, for 6 hours to allow maximum encapsulation. Secondly, sulfur was encapsulated in the BNNT through sublimation, which could

then react with cadmium iodide to form cadmium sulfide QD inside the BNNT. The two-step process is shown below:

$$\mathbf{CdI_2 + BNNT \rightarrow CdI_2@BNNT\ (+2S, -I_2) \rightarrow CdS@BNNT}$$

Both solution and sublimation filled BNNT were analysed by TEM. Images of solution filled BNNT (Figure 76) indicated that QD formed on both the outer walls and encapsulated in the BNNT, with a greater density located within the internal channel (44 QD are encapsulated per µm compared to 33 QD attached to the external wall per µm of BNNT). The crystal structure of the solution-filled BNNT is clearly that of CdS, as the 3.3 Å d-spacing corresponded to the (111) plane of zinc blende CdS (Figure 76 (l)).

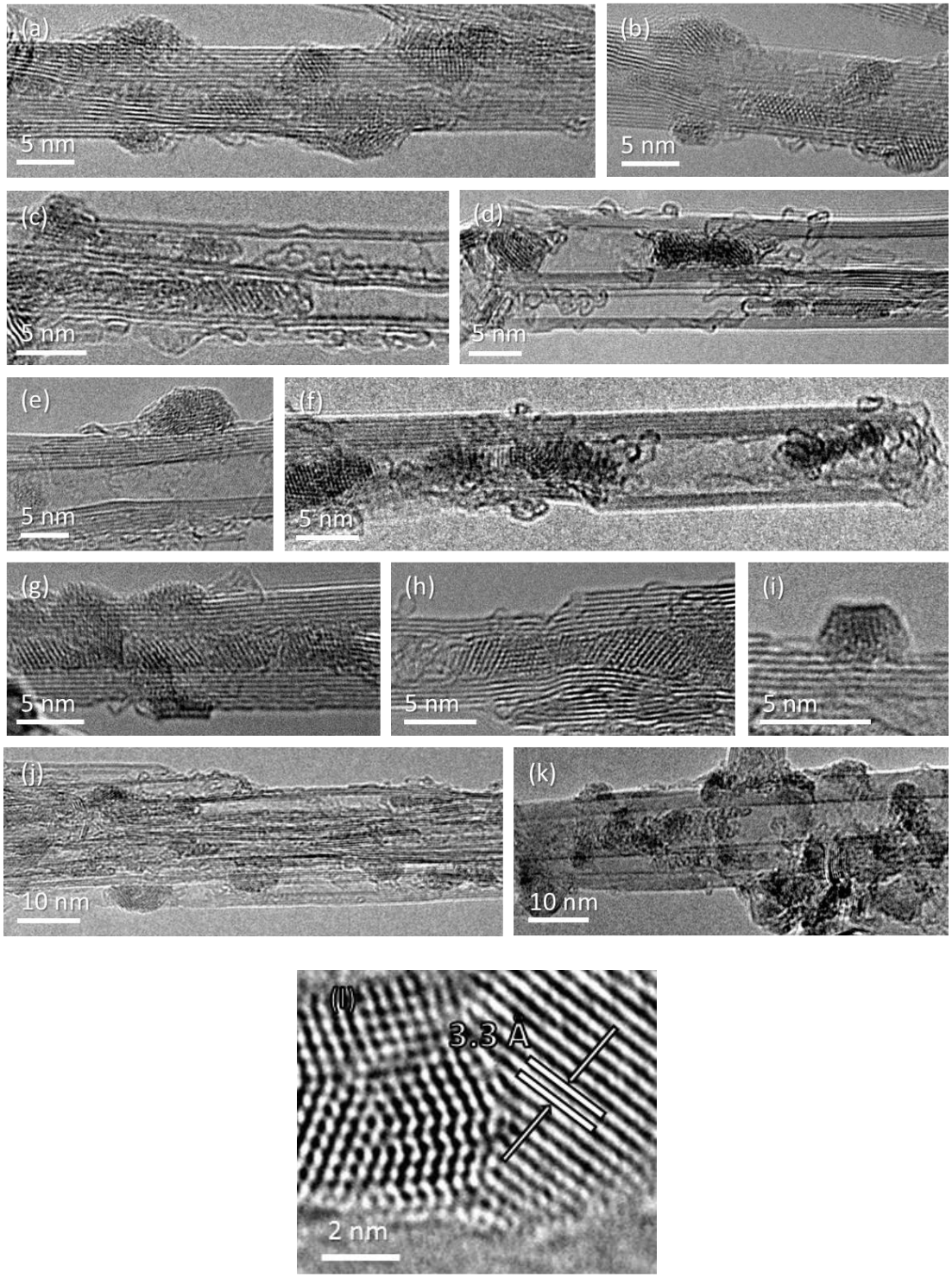


Figure 76. (a-l) TEM images of CdS@BNNT. QD are formed both inside the BNNT and on the external surface with 44 QD encapsulated per µm and 33 QD attached to the external surface per µm of BNNT. (l) The d-spacing of 3.3 Å corresponds to the (111) plane of cubic CdS.

To probe the location of QD further, and thus determine whether QD were inside or outside of the BNNT, the sample was rotated around the BNNT growth axis and imaged at different levels of angular tilt (Figure 77).

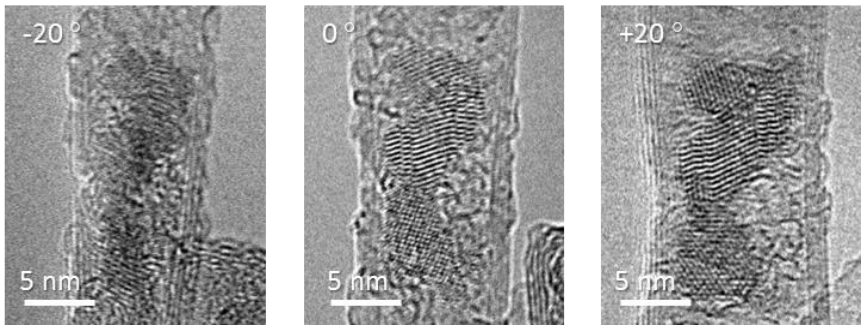


Figure 77. Tilt series of CdS@BNNT.

Interestingly, the internal diameter of BNNT appeared to be templating the width of encapsulated QD, with those encapsulated forming elongated, rod-like structures with mean dimensions of 4.7 ± 2.4 x 2.1 ± 0.6 nm. The inner channel of the BNNT (2.45 ± 1.2 nm) was very similar to the short dimension of the QD, hence, when the vdW radius of the two materials was factored in, QD were restricted to *ca*. 2.1 nm. This is clear when the long and short dimensions are displayed as a histogram (Figure 78), with a narrow size distribution for the short dimension of CdS but a very broad size distribution for the long dimension. The resulting aspect ratio was then calculated as 2.4, clearly much higher than for CdS@MWNT.

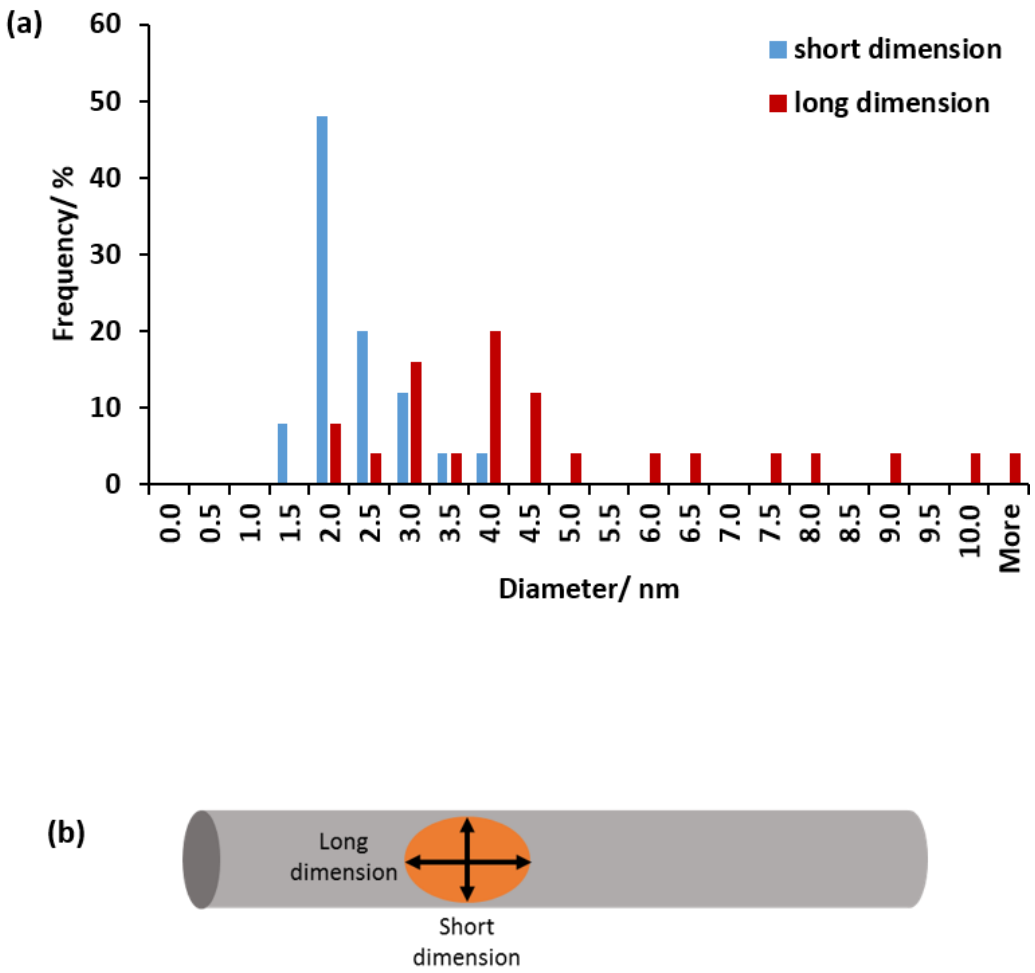


Figure 78. (a) Histograms to show the size distribution of NP in MWNT for dimensions measured along both the short and long axis of the NP, d_{NP}=2.1 ± 0.6 x 4.7 ± 2.4b nm. (b) Schematic representation of the short and long dimensions of QD measured inside MWNT.

In contrast, QD on the outer wall of the BNNT were more spherical, with mean dimensions of 5.9 ± 2.4 x 4.2 ± 1.7 nm and aspect ratio of 1.51, demonstrating that templating did not occur for QD on the convex surface of the BNNT.

Sublimation-filled BNNT were also analysed through TEM (Figure 79). Small, dark circles in the TEM images shown in Figure 79 (a) depicts CdS inside the BNNT.

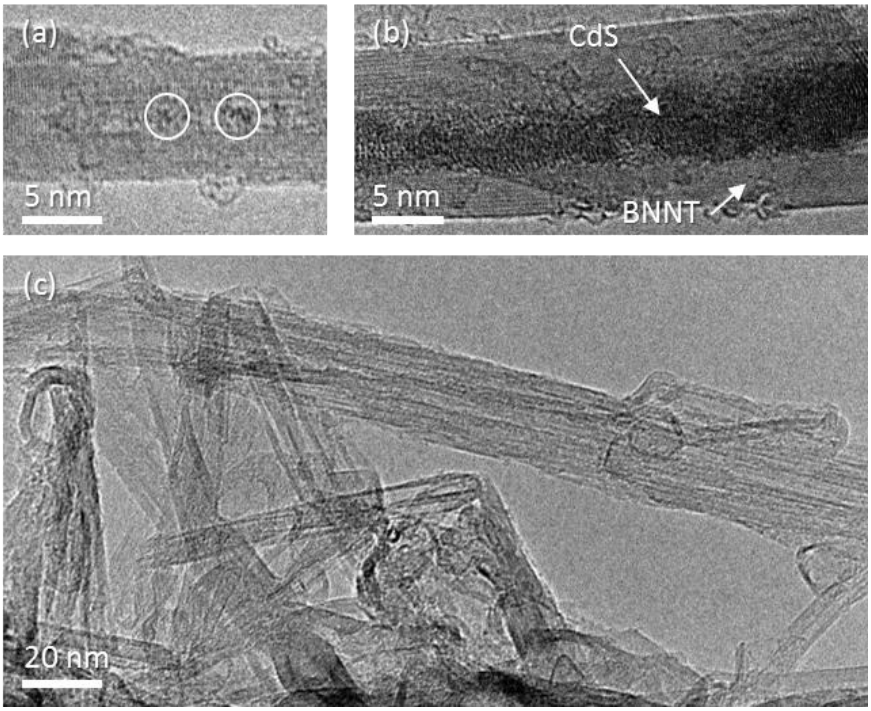


Figure 79. TEM image of CdS@BNNT, filled through sublimation and reaction of CdI_2 and S_x, forming quantum dots (a), continuous CdS crystals (b), with many BNNT remaining empty (c).

In the absence of solvent CdI_2 occupied all available space within the BNNT, resulting in extended CdS structures, rather than QD (Figure 79 (b)). This suggests that the solution filling method prevents elongated CdS structures forming through the use of surfactant to cap the CdS and by dispersing the concentration of precursor ions more evenly throughout the nanotube's cavity.

It must be acknowledged that the TEM images showed the filling rate to be very poor (<1% of BNNT filled- Figure 79 (c)), compared to >90% filling using the solution route.

The elemental composition of the encapsulated species was also explored through EDX analysis (Figure 80).

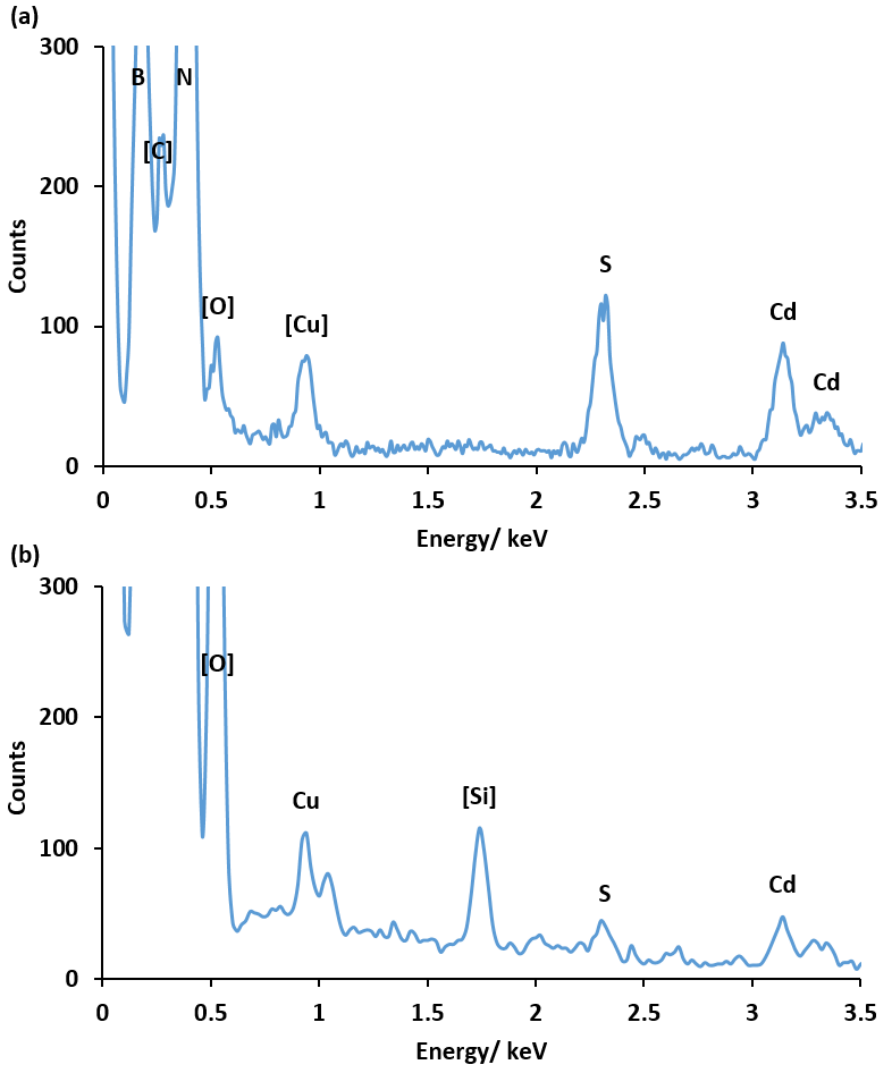


Figure 80. EDX spectra of CdS@BNNT, filled through (a) solution method with Cd:S ratio of 1:3.6, and (b) sublimation method with Cd:S ratio of 1:1.6. The copper, silicon and oxygen signals are from the TEM grid.

The ratio of Cd:S was 1:3.6 in the solution-filling method, which suggested a high excess of thiols on the nanotubes, possibly resulting from preferential interactions of thiols with the surface of BNNT, compared to CNT. In contrast, the Cd:S ratio was almost 1:1.6 when the sublimation method was utilised, making this technique favourable for better controlling the elemental ratios in the QD.

As well as looking at the hybrid structure directly, the dimensions of the QD formed through the solution route could be investigated further through analysing

the filtrate which had been separated from the solid hybrid material by UV/vis spectroscopy. A low intensity peak at 510 nm was detected and from this, the diameter of the QD was calculated as 8.23 nm.[52] This is consistent with analogous experimental analysis on CdS@MWNT. It appears that irrespective of MWNT or BNNT being used, larger QD (*ca*. 8 nm) form in solution, and smaller QD grow inside the nanotube due to templating effects. This is further evidence of the effective size control imposed by nanotubes on QD formation.

To examine the Cd content on the bulk scale, as opposed to the local scale determined through TEM and EDX analysis, ICP-OES was performed. From this, 36 wt.% cadmium in the sample was calculated, which was slightly higher than the 33% measured in the MWNT samples, suggesting higher loading on BNNT.

To probe the crystallinity of the QD and gain further insight into their structure, PXRD was recorded (Figure 81). It was predicted that sharp peaks would be observed from BNNT, with broad peaks resulting from CdS crystal planes, similar to those observed for CdS@MWNT.

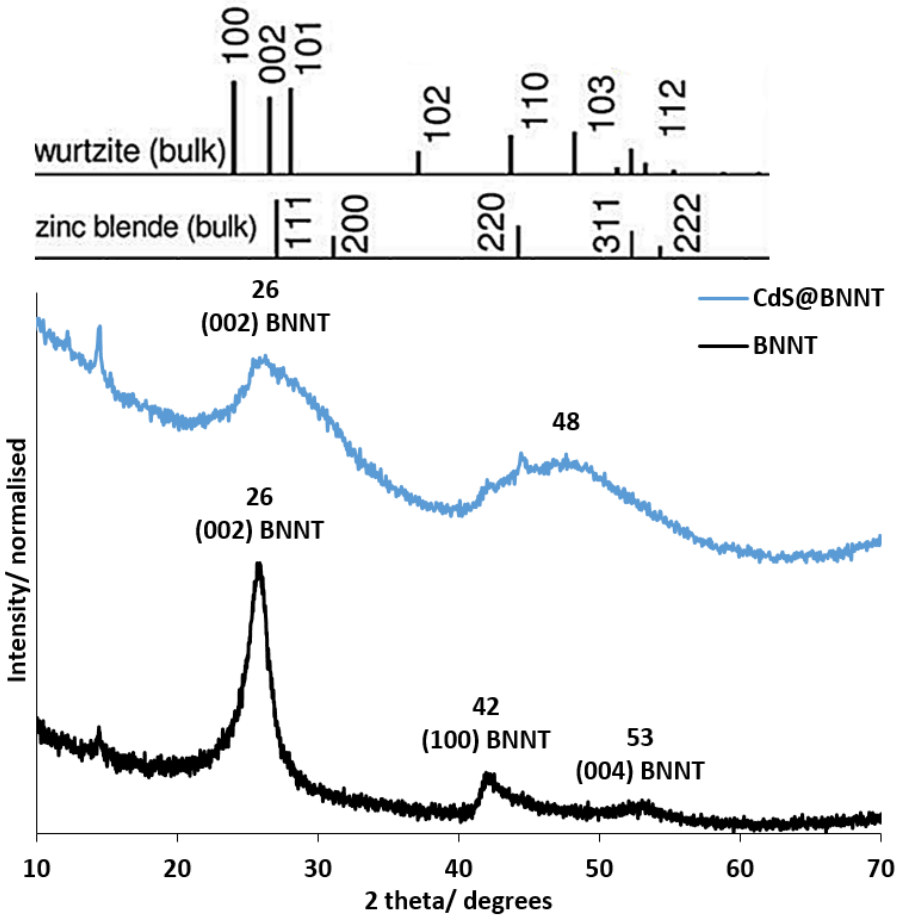


Figure 81. PXRD diffractogram of CdS@BNNT. Broad peaks are the result of the small dimensions of the QD. The weak intensity results from the high percentage of BNNT compared to CdS. The peak at 26˚ corresponds to the (002) planes of BNNT and the (111) plane of cubic CdS. The broad peak at 48˚ is assigned to the contribution of (100) and (004) planes of BNNT, which are expected at 42 and 53˚, and the (220) crystal planes of cubic CdS which is expected at 45˚. The XRD patterns of bulk wurtzite and zinc blende CdS are included for reference, reported by Dzhagan *et al.*[64] (JCPDS no. 75-0581 and JCPDS no. 80-0019).

In addition to the peaks at 26, 42 and 53˚ corresponding to (002), (100) and (004) planes of BNNT,[97, 98] a new peak *ca*. 48˚ corresponding to the (220) and (311) crystal planes of CdS, and broadening of the peak at 26˚, corresponding to the (111) crystal plane of CdS, confirmed the composition of the hybrid material. The peaks resulting from CdS were very broad due to the small dimensions of the nanocrystals,

but could also result from a mixture of zinc blende and wurtzite crystal structures in the sample, consistent with the results observed previously for CdS@MWNT.

Through TEM, EDX and PXRD, it is evident that using the solution method, some CdS QD formed on the surface of BNNT but most of these QD were encapsulated inside the BNNT (57 QD per µm encapsulated compared to 43 QD per µm on the external surface).

To confirm the structure of QD in BNNT as CdS, Raman spectroscopy was performed (Figure 82). It was expected that the spectra of CdS@BNNT would be very similar, whether formed through a sublimation route or a solution route, with peaks corresponding to BNNT, and LO phonon modes of CdS.

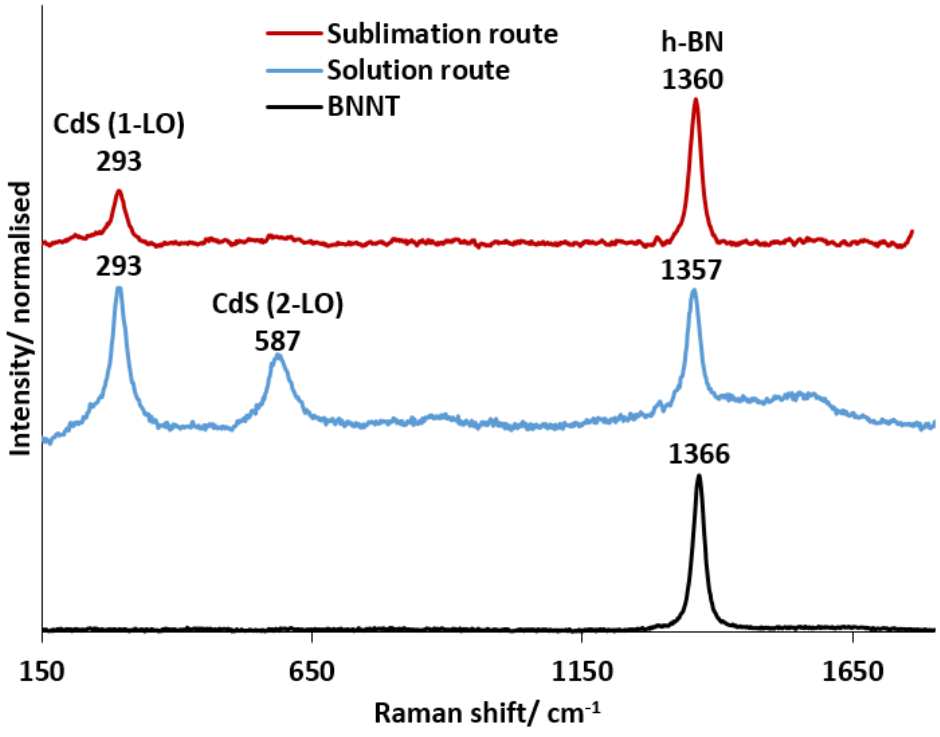


Figure 82. Raman spectra for BNNT and CdS@BNNT formed through sublimation and solution methods. The spectrum was acquired at excitation wavelength, λ_{ex}=532 nm. The peaks at 1360 cm^{-1} results from the E_{2g} mode of BNNT. The feature at 293 and 587 cm^{-1} is a result of the 1LO and 2LO phonon modes of CdS respectively.

In addition to peaks at *ca*. 1360 cm^{-1} observed across all of the samples, corresponding to the E_{2g} B-N stretching mode of BNNT, peaks were clearly visible at 293 cm^{-1} and *ca*. 587 cm^{-1} in CdS@BNNT formed through solution filling. These result from the 1LO and 2LO phonon mode of CdS, indicative of QD formation. The peaks were not shifted as much as CdS@MWNT (1LO =289, 2LO=585 cm^{-1}), which could be due to the QD being slightly larger. Both the 1LO and 2LO modes were weaker when the sublimation method was employed, attributed to the relative concentration of CdS in the sample. Moreover, the broad features between 1300 and 1600 cm^{-1} in CdS@BNNT formed through the solution route were likely to be D and G bands from amorphous carbon. As these were absent when the sublimation method was used, this route can be described as cleaner.

So far, it has been shown that CdS@BNNT can be produced through two different methods. QD@BNNT formation through sublimation was demonstrated, which represented a cleaner route than the solution method, with less amorphous carbon in the sample and better control over the elemental ratio in CdS. However, the poor filling rate highlights the inefficiency of this method, possibly due to cadmium iodide interacting weakly with the interior of the BNNT. Furthermore, the sizes of encapsulated CdS are variable between 0D and 1D nanocrystals, making the sublimation route unfavourable. To take the project forwards and utilise the practical application of the superstructures, the wet-chemistry route is preferred.

4.4 Conclusions

An effective method for forming CdS QD within MWNT is described. A high filling rate of 70 QD per µm occurs through pre-treating MWNT by extended oxidation (96 hour reflux in 5M nitric acid) to form pores in the walls of the nanotubes, followed by the reaction of QD precursors. If an accessible route is provided for CdS precursors to enter the nanotube, QD are predominantly encapsulated. Here, the vdW surface area between the QD and the nanotube is highest, leading to the conclusion that vdW forces are the overriding interaction responsible for the formation and location control of CdS in the hybrid structures. The MWNT also template the growth of QD, with the long dimension of the CdS (4.6 ± 1.0 nm) growing to fit the carbon nanocontainer (5.1 ± 1.5 nm).

The internal dimensions and structure of the nanotube has a significant impact on the filling of CdS. SWNT were too narrow and bundled too much to allow effective filling. Whereas, GNF were well filled but with QD, solvent and surfactant encapsulated, structural characterisation of the material was inhibited.

The filling of BNNT with CdS was appraised using two comparative approaches. The resulting hybrid materials are either inefficiently filled but clean (sublimation filling) or efficiently filled but contain amorphous carbon and a greater excess of sulphur from surfactants (solution filling).

When BNNT are used instead of MWNT, the encapsulated QD size remains similar (4.6 ± 1.0 x 3.5 ± 0.9 nm for CdS@MWNT, compared to 4.7 ± 2.4 x 2.1 ± 0.6 nm for CdS@BNNT); however, the aspect ratio increases from 1.4 to 2.4 as the BNNT restrict the growth of the QD perpendicular to the nanotube. The distribution of

encapsulated QD compared to those on the outer walls of the nanotubes varies between MWNT (70 encapsulated and 19 on the eternal wall per μm) and BNNT (44 encapsulated and 33 on the eternal wall per μm), resulting from BNNT being much less open than MWNT, with no pores along the walls for CdS precursors to enter.

4.5 Experimental

All common reagents and solvents were purchased from Sigma-Aldrich Chemicals®, UK and used without further purification, unless otherwise stated. Water was purified (>18 MΩcm) using a Barnstead NANOPure II system.

MWNT (PD30L520) were purchased from NanoLab, internal diameter 5.1 ± 1.5 nm, external diameter 30 ± 15 nm, Chemical Vapour Deposition (CVD) synthesis, >95% purity, oxidation temperature 560 °C. SWNT were purchased from Helix Material Solutions, internal diameter 1.3 nm, length 0.5-3 μm, arc discharge synthesis, 50-70% purity, oxidation temperature 400 °C. GNF (PR24) were purchased from Applied Sciences, external diameter 96 nm ± 32 nm, internal diameter 30-50 nm, length 50-200 μm, CVD synthesis, 99.99% purity, oxidation temperature 580 °C. BNNT were purchased from BNNT LLC, internal diameter 2.45 ± 1.19 nm, external diameter 4.32 ± 2.09 nm, number of walls = 1 to 5 (2 or 3 is most common).

All experimental procedures were performed using conventional glass apparatus, unless otherwise stated. Heating was carried out using a silicon oil bath atop a ceramic hot plate (Fisher Scientific) capable of heating to 310 ˚C, with the temperature stated referring to that of the reaction mixture as opposed to the heating block.

UV-vis absorption spectra were recorded in solution at room temperature, using 1cm quartz cuvettes, using a Perkin-Elmer Lambda 25 UV-vis Spectrophotometer at a scan rate of 240 nm min^{-1} over the range 190-900 nm. The position and intensity of the absorbance maximum was obtained using the `find peaks' function within the UV WinLab ES software with the threshold set at 0.01.

Powder X-Ray Diffraction measurements were performed on a PANalytical X'Pert PRO Diffractometer equipped with a Cu Kα radiation source (λ = 1.5418 Å) in Bragg-Brentano geometry using a Si zero-background holder. Generator voltage = 40 V, Tube current = 40 V.

Transmission electron microscopy (TEM) imaging was performed by Prof. Andrei Khlobystov, Rhys Lodge or Craig Stoppiello using high resolution TEM on either a JEOL JEM-4000EX (LaB_6 source, information limit < 0.12 nm) or a JEOL 2100F TEM (field emission gun source, information limit < 0.19 nm) at room temperature. Samples were typically prepared by casting several drops of solution onto copper-grid mounted 'lacy' carbon films and allowing the grid to dry on filter paper.

Local EDX spectra were acquired for samples mounted on TEM grids using an Oxford Instruments INCA X-ray microanalysis system. The electron beam was condensed onto areas of specimens (bulk specimen or nanotube bundles) suspended over holes of the amorphous carbon film.

Thermogravimetric analysis (TGA), unless otherwise stated, was performed using a TA Instruments SDT Q600 under a flow of air at a rate of 90 mL min^{-1} at a heating rate of 5 °C min^{-1} from room temperature to 1000°C.

Raman spectroscopy was conducted using a HoribaJY LabRAM HR spectrometer with a laser wavelength of 532 nm. Samples were dropcast from

methanolic solutions onto Si(100) wafers and a minimum of five spectra recorded from different areas of the sample.

Inductively coupled plasma optical emission spectroscopy (ICP-OES) was recorded on a Perkin Elmer, Optima 2000 DV ICP-OES with S10 autosampler. Samples and standards were prepared with a final solution composition of 2% nitric acid (69%, VWR Chemicals) in deionized water. CdS@MWNT was prepared by heating 5 mg of the hybrid material in a box furnace to oxidise the nanotubes. The remaining material was dissolved in 2 mL of nitric acid, exposed to ultrasonic irradiation for 15 minutes before mixing on an orbital shaker (Grant Instruments Orbital Shaker PSU-10i at 200 rpm) for 16 h and gradually diluted to 20 mL, at an expected concentration of 2% nitric acid. Blank samples were prepared using an identical method, without the addition of the hybrids. CdS@BNNT sample was prepared by adding 4 mL of nitric acid to 1 mg of CdS@BNNT and heating at 100 °C for 16 h, before filtering and gradually diluting to an expected concentration of 2% nitric acid. A blank sample was prepared using an identical method, without the addition of the hybrids. A radial detection method was used at wavelengths of 214.4 nm and 228.8 nm, with 228.8 nm producing the most accurate result, which was used to determine the final concentration of Cd^{2+} in solution. Calibrations were formed from solutions of 0.005, 0.01, 0.05, 0.1 and 0.2 mg mL^{-1} with linear regression coefficient of 0.9998. Blanks show 0.00 mg L^{-1} of cadmium. Corrected coefficients are measured as CdS@MWNT = 0.9998, CdS@BNNT = 0.9967.

4.5.1 Analysis of 0 h-treated MWNT

Raman (532 nm) ν/cm^{-1} 1339 (D-MWNT), 1573 (G-MWNT), 2673 (2D-MWNT), 2915 (D+D'-MWNT), 3216 (2D'-MWNT)

I_D:I_G = 0.73

4.5.2 Oxidation of MWNT

CNT (40 mg) were added to 5 M nitric acid (40 mL) and heated to reflux for 1 h, 16 h, and 96 h durations. The reactions were then allowed to cool prior to filtration. CNT were washed with deionised water (200 mL) until neutral (the addition of sodium hydroxide (7 mL) if necessary) and dried under vacuum. These acid treated CNT were then used for further reactions to form hybrids as indicated in the results and discussion.

Mass/ mg: 1 h-treated (MWNT) = 35.3, 16 h-treated (MWNT) = 31.1, 96 h-treated (MWNT) = 13.4, 1 h-treated (SWNT) = 7.22, (16 h-treated (SWNT) could not be isolated due to extreme oxidation).

96 h-treated (MWNT) = Raman (532 nm) ν/cm^{-1} 1352 (D-MWNT), 1584 (G-MWNT), 1618 (D'-MWNT), 2695 (2D-MWNT), 2945 (D+D'-MWNT), 3243 (2D'-MWNT)

I_D:I_G = 1.26

4.5.3 CdS/MWNT formation

Reactions were based on the synthetic method used by Y. K. Kim and H. Park.[12] To a dispersion of CNT (MWNT oxidised for 0, 1, 16 or 96 h- described above, SWNT oxidised for 1 h, or GNF) (10 mg) in deionised water (16.7 mL) was added cadmium

acetate dehydrate (44 mg), which was stirred at r.t. for 90 minutes before addition of 1-thioglycerol (0.1 mL) and 1,2-dithioglycerol (2,3-Dimercapto-1-propanol, 0.04 mL) and the mixture allowed to stir for 16 h. Finally, sodium sulfide nonahydrate (1.67 mL, 0.1 M stock solution) was added dropwise and allowed to stir for 16 h. The product was collected by vacuum filtration using a 0.2 µM PTFE membrane and dried under vacuum to yield a black power. The hybrid was removed from the PTFE membrane and studied using TEM imaging. Some reactions were carried out on a smaller scale, where stated.

4.5.4 CdS/ 0 h-treated MWNT

Mass/ mg =27

TEM (200 kV) 83 QD per µm, 5 QD encapsulated per µm, d_{NP}/ nm = 5.03 ± 1.7 x 2.35 ± 0.72

4.5.5 CdS/1 h-treated MWNT

(Scaled down to 1/3)

Mass/ mg = 2.8

TEM (200 kV) 12 QD per µm, 22 QD encapsulated per µm, highly clustered QD

4.5.6 CdS/16 h-treated MWNT

Mass/ mg = 18

TEM (200 kV) 0 QD per µm, 3 QD encapsulated per µm, almost exclusively clustered

4.5.7 CdS/96 h-treated MWNT

(Scaled down to 1/3)

Mass/ mg = 3.0

TEM (200 kV) 19 QD per µm, 70 QD encapsulated per µm, d_{NP}/ nm = 4.6 ± 1.0 x 3.5 ± 0.9

EDX (Cd:S)= 1:1.6

Raman (532 nm) ν/cm^{-1} 289 (1LO-CdS), 585 (2LO-CdS), 1338 (D-MWNT), 1572 (G-MWNT), 1608 (D'-MWNT), 2681 (2D-MWNT), 2926 (D+D'-MWNT), 3228 (2D'-MWNT)

I_D:I_G = 0.97

ICP-OES/ wt.% cadmium: 33

4.5.8 CdS/SWNT formation

(Scaled down to 3 mg SWNT)

Mass/ mg = 3

EDX (Cd:S) = 1:3.8

4.5.9 CdS/GNF formation

Mass/ mg = 44

EDX (Cd:S) = 1:1.7

4.5.10 CdS@BNNT (solution route)

To dispersion BNNT (opened and purified as described in Chapter 2) (10 mg) in deionized water (16.7 mL) was added cadmium acetate dehydrate (44 mg), forming

a white suspension which was stirred at r.t. for 90 minutes. Addition of 1-thioglycerol (0.1 mL) and 1,2-dithioglycerol (0.04 mL) turned the white suspension cloudy, and the mixture allowed to stir for 16 h. Finally, sodium sulphide nonahydrate (1.67 mL, 0.1 M stock solution) was added dropwise and the mixture allowed to stir for 16 h, turning pale pink. The product was collected by vacuum filtration using a 0.2 µM PTFE membrane, producing a pink/red filtrate, and dried under vacuum to yield a pale orange power.

Mass/ mg = 17

TEM (100 kV) 33 QD per µm, 44 QD encapsulated per µm, d_{NP} (external surface)/ nm = 5.9 ± 2.4 x 2.6 ± 1.1, d_{NP} (encapsulated)/ nm= 4.7 ± 2.4 x 2.1 ± 0.6

EDX (Cd:S) = 1:3.63

Raman (532 nm) ν/cm^{-1} 293 (1LO-CdS), 587 (2LO-CdS), 1357 (E_{2g}-BNNT)

ICP-OES/ wt.% cadmium: 36

4.5.11 CdS@BNNT (sublimation route)

Cadmium iodide (50 mg) and open BNNT (10 mg) were sealed in a Pyrex ampoule under vacuum (10^{-5} mbar) and heated and heated at 488 ˚C for 6 hours in a preheated box furnace, then cooled slowly (20 h) to improve crystallinity of CdI_2 in BNNT.

CdI_2 in BNNT (10 mg) and sulfur (10 mg) were sealed in a Pyrex ampoule under vacuum (10^{-5} mbar) and heated from 0 ˚C to 288 ˚C, held at this temperature for 2 hours, then cooled slowly to room temperature.

Mass/ mg = 8

EDX (Cd:S) = 1:1

Raman (532 nm) v/cm^{-1} 293 (1LO-CdS), 587 (2LO-CdS), 1360 (E_{2g}-BNNT)

4.6 References

1. M. R. Travino, *Dye-Sensitized Solar Cells and Solar Cell Performance*, Nova Science Publishers, Inc., Hauppauge, United States, 2011.
2. H. Kisch, *Semiconductor Photocatalysis*, John Wiley & Sons, Incorporated, Erlangen, Germany, 2014.
3. S. Mussa Farkhani and A. Valizadeh, *IET Nanobiotechnol.*, 2014, **8**, 59.
4. L. E. Brus, *J. Chem. Phys.*, 1984, **80**, 4403.
5. M. Goswami, R. Ghosh, T. Maruyama and A. K. Meikap, *Appl. Surf. Sci.*, 2016, **364**, 176.
6. I. Robel, B. A. Bunker and P. V. Kamat, *Adv. Mater.*, 2005, **17**, 2458.
7. H. Y. Zhu, J. Yao, R. Jiang, Y. Q. Fu, Y. H. Wu and G. M. Zeng, *Ceram. Int.*, 2014, **40**, 3769.
8. S. Liu, M. Q. Yang, N. Zhang and Y. J. Xu, *J. Energy Chem.*, 2014, **23**, 145.
9. L. Sheeney-Haj-Khia, B. Basnar and I. Willner, *Angew. Chem. Int. Ed.*, 2005, **44**, 78.
10. T. Mitkina, C. Stanglmair, W. Setzer, M. Gruber, H. Kisch and B. Konig, *Org. Biomol. Chem.*, 2012, **10**, 3556.
11. P. K. De and D. C. Neckers, *J. Photochem. Photobiol. A-Chem.*, 2013, **252**, 8.
12. Y. K. Kim and H. Park, *Energy Environ. Sci.*, 2011, **4**, 685.
13. D. M. Guldi and N. Martin, *Carbon Nanotubes and Related Structures: Synthesis, Characterization, Functionalization, and Applications*, Wiley-VCH, 2010.
14. D. Eder, *Chem. Rev.*, 2010, **110**, 1348.
15. T. Peng, P. Zeng, D. Ke, X. Liu and X. Zhang, *Energy Fuels*, 2011, **25**, 2203.
16. J. Zhang, Y. Guo, H. Fang, W. Jia, H. Li, L. Yang and K. Wang, *New J. Chem.*, 2015, **39**, 6951.
17. J. Munoz, J. Bastos-Arrieta, M. Munoz, D. Muraviev, F. Cespedes and M. Baeza, *J. Mater. Sci.*, 2016, **51**, 1610.
18. X. L. Li, Y. Jia and A. Y. Cao, *ACS Nano*, 2010, **4**, 506.
19. M. Hamadanian, V. Jabbari, M. Shamshiri, M. Asad and I. Mutlay, *J. Taiwan Inst. Chem. Eng.*, 2013, **44**, 748.
20. G. Mountrichas, S. Pispas and N. Tagmatarchis, *Small*, 2007, **3**, 404.
21. G. Mountrichas, A. S. D. Sandanayaka, S. P. Economopoulos, S. Pispas, O. Ito, T. Hasobe and N. Tagmatarchis, *J. Mater. Chem.*, 2009, **19**, 8990.
22. J. Shi, Y. Qin, W. Wu, X. Li, Z. X. Guo and D. Zhu, *Carbon*, 2004, **42**, 455.
23. G. M. Neelgund and A. Oki, *Appl. Catal. B-Environ.*, 2011, **110**, 99.
24. X. L. Li, Y. Q. Liu, L. Fu, L. C. Cao, D. C. Wei and Y. Wang, *Adv. Funct. Mater.*, 2006, **16**, 2431.
25. G. M. Neelgund, A. Oki and Z. Luo, *Colloids Surf., B*, 2012, **100**, 215.
26. S. S. W. Sarbajit Banerjee, *J. Am. Chem. Soc.*, 2003, **125**, 10342.
27. C. Li, Y. Tang, K. Yao, F. Zhou, Q. Ma, H. Lin, M. Tao and J. Liang, *Carbon*, 2006, **44**, 2021.

28. D. C. Bifeng Pan, Cengiz S. Ozkan, Mihri Ozkan, Ping Xu, Tuo Huang, and H. C. Fengtao Liu, Qing Li, Rong He, Feng Gao, *J. Phys. Chem. C*, 2008, **112**, 939.
29. M. Deepa, R. Gakhar, A. G. Joshi, B. P. Singh and A. K. Srivastava, *Electrochim. Acta*, 2010, **55**, 6731.
30. M. Grzelczak, M. A. Correa-Duarte, V. Salgueiriño-Maceira, M. Giersig, R. Diaz and L. M. Liz-Marzán, *Adv. Mater.*, 2006, **18**, 415.
31. D. M. Guldi, G. M. A. Rahman, V. Sgobba, N. A. Kotov, D. Bonifazi and M. Prato, *J. Am. Chem. Soc.*, 2006, **128**, 2315.
32. K. H. Tan and M. R. Johan, *J. Nanopart. Res.*, 2013, **15**, 1920.
33. L. Sheeney-Haj-Ichia, B. Basnar and I. Willner, *Angew. Chem. Int. Ed.*, 2005, **44**, 78.
34. J. M. Haremza, M. A. Hahn and T. D. Krauss, *Nano Lett.*, 2002, **2**, 1253.
35. Y.-H. K. Chaiwat Engtrakul, Jovan M. Nedeljkovic´, S. Phil Ahrenkiel,, J. L. A. Katherine E. H. Gilbert, S. B. Zhang, Olga I. Mic´ic´, Arthur J. Nozik, and and M. J. Heben, *J. Phys. Chem. B*, 2006, **110**, 25153
36. X. L. Li, Y. Jia, J. Q. Wei, H. W. Zhu, K. L. Wang, D. H. Wu and A. Y. Cao, *ACS Nano*, 2010, **4**, 2142.
37. J. K. Baral, A. Sharma, D. Wang, D. Ma, V.-V. Truong and R. Izquierdo, *Eur. Phys. J. Appl. Phys.*, 2014, **65**, 10201.
38. A. A. R. Watt, D. Blake, J. H. Warner, E. A. Thomsen, E. L. Tavenner, H. Rubinsztein-Dunlop and P. Meredith, *J. Phys. D: Appl. Phys.*, 2005, **38**, 2006.
39. B. S. Kim, D. C. J. Neo, B. Hou, J. B. Park, Y. Cho, N. L. Zhang, J. Hong, S. Pak, S. Lee, J. I. Sohn, H. E. Assender, A. A. R. Watt, S. Cha and J. M. Kim, *ACS Appl. Mater. Interfaces*, 2016, **8**, 13902.
40. W. W. Yu, Y. A. Wang and X. Peng, *Chem. Mater.*, 2003, **15**, 4300.
41. A. L. Rogach, A. Kornowski, M. Gao and A. Eychmuller, *J. Phys. Chem. B*, 1999, **103**, 3065.
42. B. T. Huy, M. H. Seo, J. M. Lim, D. S. Shin, Y. I. Lee, S. S. Kim, K. Jang and T. Song, *J. Korean Phys. Soc.*, 2011, **59**, 3293.
43. Z. F. Chen, W. Thiel and A. Hirsch, *ChemPhysChem*, 2003, **4**, 93.
44. X. Pan and X. Bao, *Accounts Chem. Res.*, 2011, **44**, 553.
45. S. J. Guo, X. L. Pan, H. L. Gao, Z. Q. Yang, J. J. Zhao and X. H. Bao, *Chem. Eur. J.*, 2010, **16**, 5379.
46. W. Chen, X. L. Pan, M. G. Willinger, D. S. Su and X. H. Bao, *J. Am. Chem. Soc.*, 2006, **128**, 3136.
47. W. Chen, Z. Fan, X. Pan and X. Bao, *J. Am. Chem. Soc.*, 2008, **130**, 9414.
48. D. Deng, L. Yu, X. Chen, G. Wang, L. Jin, X. Pan, J. Deng, G. Sun and X. Bao, *Angew. Chem. Int. Ed.*, 2013, **52**, 371.
49. G. A. Rance, W. A. Solomonsz and A. N. Khlobystov, *Chem. Commun.*, 2013, **49**, 1067.
50. F. K. Ma, G. Zhao, C. Li, T. L. Wang, Y. Z. Wu, J. X. Lv, Y. Y. Zhong and X. P. Hao, *CrystEngComm.*, 2016, **18**, 631.
51. K. A. Brown, M. B. Wilker, M. Boehm, G. Dukovic and P. W. King, *J. Am. Chem. Soc.*, 2012, **134**, 5627.
52. W. W. Yu, L. H. Qu, W. Z. Guo and X. G. Peng, *Chem. Mater.*, 2003, **15**, 2854.
53. C. d. M. Donega and R. Koole, *J. Phys. Chem. C*, 2009, **113**, 6511.

54. D. V. Talapin, J. S. Lee, M. V. Kovalenko and E. V. Shevchenko, *Chem. Rev.*, 2010, **110**, 389.
55. V. Datsyuk, M. Kalyva, K. Papagelis, J. Parthenios, D. Tasis, A. Siokou, I. Kallitsis and C. Galiotis, *Carbon*, 2008, **46**, 833.
56. A. C. Dillon, T. Gennett, K. M. Jones, J. L. Alleman, P. A. Parilla and M. J. Heben, *Adv. Mater.*, 1999, **11**, 1354.
57. S. Buller, M. Heise-Podleska, N. Pfander, M. Willinger and R. Schlogl, *J. Energy Chem.*, 2016, **25**, 265.
58. P. J. F. Harris, *Carbon Nanotube Science: Synthesis, Properties and Applications*, Cambridge University Press, 2009.
59. A. L. Rogach, *Semiconductor Nanocrystal Quantum Dots*, Springer, 2008.
60. Z. H. Zhang, W. S. Chin and J. J. Vittal, *J. Phys. Chem. B*, 2004, **108**, 18569.
61. A. Veamatahau, B. Jiang, T. Seifert, S. Makuta, K. Latham, M. Kanehara, T. Teranishi and Y. Tachibana, *Phys. Chem. Chem. Phys.*, 2015, **17**, 2850.
62. S. K. Mishra, R. K. Srivastava, S. G. Prakash, R. S. Yadav and A. C. Panday, *Electron. Mater. Lett.*, 2011, **7**, 31.
63. M. Pal, N. R. Mathews, P. Santiago and X. Mathew, *J. Nanopart. Res.*, 2012, **14**, 916.
64. V. M. Dzhagan, M. Y. Valakh, C. Himcinschi, A. G. Milekhin, D. Solonenko, N. A. Yeryukov, O. E. Raevskaya, O. L. Stroyuk and D. R. T. Zahn, *J. Phys. Chem. C*, 2014, **118**, 19492.
65. Y. Chen, X. Y. Liu, X. Y. Mao, Q. X. Zhuang, Z. Xie and Z. W. Han, *Nanoscale*, 2014, **6**, 6440.
66. S. Wageh, M. Maize, A. M. Donia, A. A. Al-Ghamdi and A. Umar, *J. Nanosci. Nanotechnol.*, 2015, **15**, 9861.
67. P. C. Eklund, J. M. Holden and R. A. Jishi, *Carbon*, 1995, **33**, 959.
68. Y. Zhang, L. Xie, J. Zhang, Z. Wu and Z. Liu, *J. Phys. Chem. C*, 2007, **111**, 14031.
69. M. Z. Atashbar and S. Singamaneni, *Appl. Phys. Lett.*, 2005, **86**, 123112.
70. G. Gouadec and P. Colomban, *Prog. Cryst. Growth Charact. Mater.*, 2007, **53**, 1.
71. M. Baibarac, A. Nila and I. Baltog, *Opt. Mater. Express*, 2016, **6**, 1881.
72. J. Trajic, M. Gilic, N. Romcevic, M. Romcevic, G. Stanisic, B. Hadzic, M. Petrovic and Y. S. Yahia, *Sci. Sinter.*, 2015, **47**, 145.
73. B. Schreder, C. Dem, M. Schmitt, A. Materny, W. Kiefer, U. Winkler and E. Umbach, *J. Raman Spectrosc.*, 2003, **34**, 100.
74. L. Zeiri, I. Patla, S. Acharya, Y. Golan and S. Efrima, *J. Phys. Chem. C*, 2007, **111**, 11843.
75. J. J. Shiang, S. H. Risbud and A. P. Alivisatos, *J. Chem. Phys.*, 1993, **98**, 8432.
76. D. Routkevitch, T. L. Haslett, L. Ryan, T. Bigioni, C. Douketis and M. Moskovits, *Chem. Phys.*, 1996, **210**, 343.
77. M. I. Vasilevskiy, A. G. Rolo and M. J. M. Gomes, *Solid State Commun.*, 1997, **104**, 381.
78. R. Kostic and N. Romcevic, in *Physica Status Solidi C: Current Topics in Solid State Physics, Vol. 1, No. 11*, eds. A. Kaplyanskii, A. Akimov and V. Bursian, 2004, vol. 1, pp. 2646.
79. A. M. Kelley, *ACS Nano*, 2011, **5**, 5254.

80. C. L. Hu, Y. Wang, S. Y. Chen, H. Cheng, M. Lin, Y. F. Zhang, D. He, X. Q. Liu and J. Y. Liu, *RSC Adv.*, 2016, **6**, 78053.
81. V. M. Dzhagan, I. Lokteva, M. Y. Valakh, O. E. Raevska, J. Kolny-Olesiak and D. R. T. Zahn, *J. Appl. Phys.*, 2009, **106**.
82. M. C. Klein, F. Hache, D. Ricard and C. Flytzanis, *Phys. Rev. B*, 1990, **42**, 11123.
83. G. Scamarcio, V. Spagnolo, G. Ventruti, M. Lugara and G. C. Righini, *Phys. Rev. B: Condens. Matter*, 1996, **53**, 10489.
84. H. Sekhar and D. N. Rao, *J. Phys. Chem. C*, 2013, **117**, 2300.
85. G. G. Hawley, *The Condensed chemical dictionary*, Van Nostrand Reinhold Co., 1977.
86. S. Wageh, A. A. Higazy and A. S. Hassouna, *Curr. Nano.*, 2013, **9**, 494.
87. S. Wageh, A. A. Higazy and A. S. Hassouna, *J. Mater. Sci. Mater. Electron.*, 2013, **24**, 3049.
88. A. Sabah, S. A. Siddiqi and S. Ali, *World Acad. Sci. Eng. Technol.*, 2010, **4**, 68.
89. V. Thi Thuy Duong, F. Mighri, A. Ajji and D. Trong-On, *Ind. Eng. Chem. Res.*, 2014, **53**, 3888.
90. M. Kristl, I. Ban, A. Danc, V. Danc and M. Drofenik, *Ultrason. Sonochem.*, 2010, **17**, 916.
91. A. Star and J. F. Stoddart, *Macromolecules*, 2002, **35**, 7516.
92. K. Yurekli, C. A. Mitchell and R. Krishnamoorti, *J. Am. Chem. Soc.*, 2004, **126**, 9902.
93. A. La Torre, M. W. Fay, G. A. Rance, M. D. Gimenez-Lopez, W. A. Solomonsz, P. D. Brown and A. N. Khlobystov, *Small*, 2012, **8**, 1222.
94. T. W. Chamberlain, T. Zoberbier, J. Biskupek, A. Botos, U. Kaiser and A. N. Khlobystov, *Chem. Sci.*, 2012, **3**, 1919.
95. B. Botka, M. E. Fuestoes, H. M. Tohati, K. Nemeth, G. Klupp, Z. Szekrenyes, D. Kocsis, M. Utczas, E. Szekely, T. Vaczi, G. Tarczay, R. Hackl, T. W. Chamberlain, A. N. Khlobystov and K. Kamaras, *Small*, 2014, **10**, 1369.
96. A. A. Eliseev, M. V. Chernysheva, N. I. Verbitskii, E. A. Kiseleva, A. V. Lukashin, Y. D. Tretyakov, N. A. Kiselev, O. M. Zhigalina, R. M. Zakalyukin, A. L. Vasiliev, A. V. Krestinin, J. L. Hutchison and B. Freitag, *Chem. Mater.*, 2009, **21**, 5001.
97. S. Kalay, Z. Yilmaz and M. Culha, *Beilstein J. Nanotechnol.*, 2013, **4**, 843.
98. C. Zhi, Y. Bando, C. Tang and D. Golberg, *J. Phys. Chem. B*, 2006, **110**, 8548.

5. Photocatalytic Activity of CdS Quantum Dots Attached to Nanotubes

5.1 Introduction

Composites of quantum dots (QD) and carbon nanotubes (CNT) can be used for a range of photocatalytic reactions, such as for photocurrent generation,[1, 2] hydrogen production[3-5] and water decontamination.[6-10] Their use of light as a source of cheap, clean and renewable energy has rendered photocatalysts as desirable materials, hence significant research efforts have been directed towards understanding and improving the efficiency of these materials.

In these composite materials, QD harvest visible light to generate excitons (electron-hole pairs). [11] The separation of the photogenerated electron from the hole can be achieved by electron transfer to a CNT, helping to prevent recombination and enabling the electron and hole to drive chemical transformations (Figure 83).

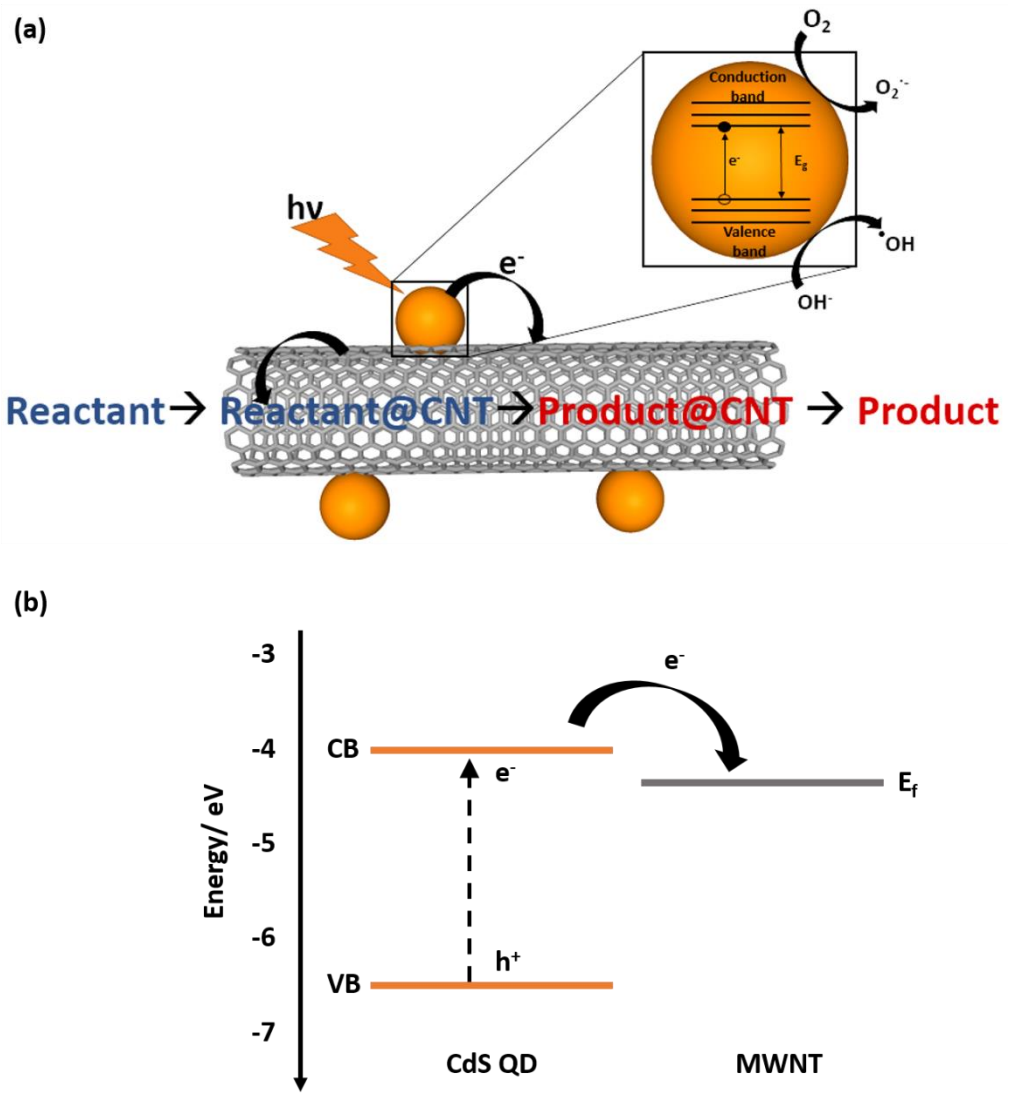


Figure 83. (a) Schematic depicting the mechanism of photocatalysis by CdS/MWNT. QD absorb a photon resulting in excitation of an electron, which is then transferred via the CNT to a reactant. Photogenerated holes are usually removed by either sacrificial reagents[3] or water[7] (b) Band alignment of CdS/MWNT.[12-14]

Some examples of the types of reactions that use CdS-CNT photocatalysts and the associated reaction conditions, are displayed in the table below (Table 1).

Table 1. Photocatalytic reactions of CdS and CNT and reaction conditions, such as the light source and reaction mixture, and the efficiency of the reaction.

Ref.	CNT	Structure	Application	Light source	Reaction mixture	Efficiency	Comment
[1]	SWNT	CdS/SWNT/ Au electrode	Photocurrent generation	300 W Xe No filter	CdS/SWNT modified electrode. Triethanolamine as sacrificial agent, phosphate buffer solution (0.1 M, pH10)	*ca*. 25% quantum efficiency *ca*. 25%	
[2]	SWNT	CdS/SWNT films /Si wafer	Solar cell	150 W Xe No filter	Ti/Pd/Au-coated Si wafer, supporting CdS/MWNT, connected with Cu wires connected with silver paint	1.4% power conversion efficiency	
[3]	MWNT	CdS/MWNT	Hydrogen production	300 W Xe λ≥420 nm	0.35 M Na_2S and 0.25 M Na_2SO_3 as the sacrificial agent. Anaerobic conditions. 0.35 $g.L^{-1}$ catalyst	498 µmol h^{-1} g^{-1} (best average)	
[4]	MWNT	CdS/MWNT	Hydrogen production	350 W Xe λ≥420 nm	0.25 M Na_2SO_3 + 1.0 M Na_2S 0.56 $g.L^{-1}$ catalyst	12130 µmol h^{-1} g^{-1} (NiS cocatalyst, alkali conditions)	NiS and base improve rate
[5]	MWNT	CdS/MWNT	Hydrogen production	300 W λ>400 nm	0.1 M Na_2SO_3 + 0.1 M Na_2S, 1 $g.L^{-1}$ catalyst pH *ca*. 11.5. N_2 purged.	819 µmol h^{-1} g^{-1} (Pt cocatalyst)	Metal cocatalysts improve rate
[6]	MWNT	CdS/MWNT	Methylene blue decomposition	Unspecified	10 $mg.L^{-1}$ dye (50 mL), 0.20 $g.L^{-1}$ cat.	92.2% in 30 min	

Table 1. (*continued*)

Ref.	CNT	Structure	Application	Light source	Reaction mixture	Efficiency	Comments
[7]	MWNT	CdS/MWNT/ polymer	Methyl orange decomposition	300 W Xe	15 mg L^{-1} dye (100 mL), 0.70 g L^{-1} catalyst, 1.0 mM H_2O_2 Under flow of air	99.9% in 90 min	
[8]	MWNT	CdS/MWNT sponge	Rhodamine B decomposition	500 W Xe, λ≥420 nm	5 mg L^{-1} dye (initial volume = 30 mL), 5.5 mg cat (initial conc. = 0.183 g L^{-1})	41% in 30 min	
[9]	MWNT	CdS/MWNT	Brilliant Red X-3B decomposition	300 W Xe No filter	100 mg L^{-1} dye, air pump, 0.15 g L^{-1} CdS content	*Ca*. 70% in 120 min	
[10]	MWNT	CdS/MWNT/ PTFE coated cotton-linen	Methyl orange decomposition	2 x 6 W UV strip lamps, λ=365 nm	HNO_3/NaOH to adjust pH. 20 mg L^{-1} dye (initial volume = 500 mL), 1.4 g CdS content (initial conc. = 2.8 g L^{-1})	*Ca*. 60% in 200 min (neutral pH) (*ca*. 90% at pH 2)	Heat or low pH improve rate

CdS/CNT materials are targeted at photocurrent generation, hydrogen production and dye degradation for water decontamination, with the latter two dominating the field. For hydrogen production, it is advantageous to perform the reaction under anaerobic conditions (because molecular oxygen scavenges photogenerated electrons making them unavailable for the target reaction)[15] and with the addition of a sacrificial agent and metal co-catalyst to assist the transfer of multiple electrons. Whereas dye degradation is achieved in oxygenated conditions, as single photoexcited electrons generate radicals which trigger degradation of organic pollutants. This reaction occurs spontaneously ($\Delta G°<0$) but is shown to be improved at low pH, increased temperature or through the addition of hydrogen peroxide.

Powerful light sources are used in most cases (most commonly 300 W Xe lamps), usually with a filter to cut out UV light. However, there is wide variation in the concentration of catalyst added, contributing to the disparity in catalytic efficiencies.

Current studies on the application of QD-CNT composites for photocatalytic transformations are limited to those where QD are deposited on the exterior surface of CNT, yet QD confined within the internal channel of CNT are predicted to be favourable for photocatalytic applications. The previous chapter has shown the ability to selectively encapsulate QD inside CNT, where it is thought to be stabilised by the nanotube,[16] and more effective for electron transfer[17-20] due to being located on the concave surface of the CNT which is more electron deficient than the convex surface (Figure 84).Thus, this material creates the opportunity to probe the influence

of confinement of QD inside CNT on the mechanisms and pathways of photocatalytic reactions.

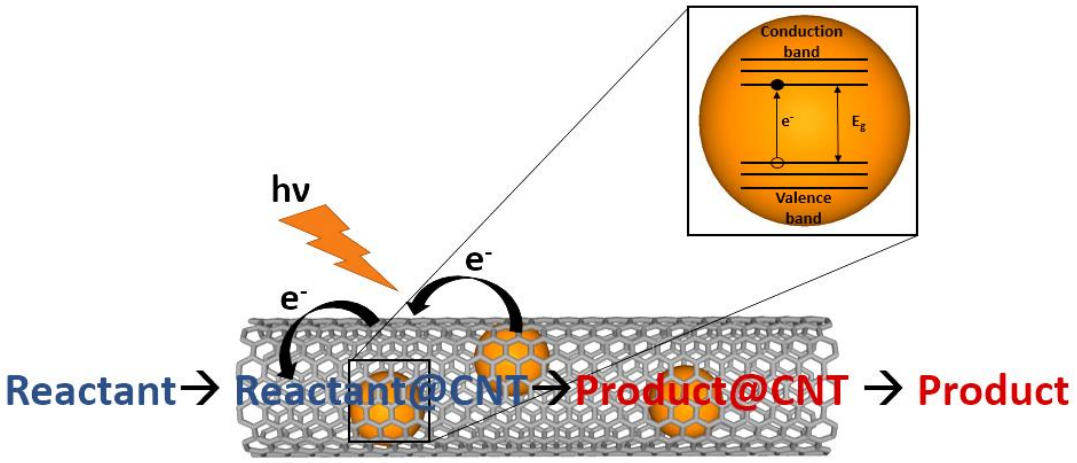


Figure 84. Schematic depicting the mechanism of photocatalysis by CdS@MWNT. QD absorb a photon to excite an electron, which is then transferred via the CNT to a reactant.

5.2 Aim and Objectives

The aim of this study is to explore the effect of confinement of QD inside hollow tubular nanoscale containers (multi-walled carbon nanotubes (MWNT) and boron nitride nanotubes (BNNT)) on photocatalytic reactions.

The first objective is to prepare a control sample comprising of CdS on the outer surfaces of CNT (CdS/MWNT). This material can be prepared in an analogous fashion to that used to fabricate CdS@CNT (Chapter 4), with the use of closed, as-received CNT as opposed to those opened in nitric acid, thus ensuring no internal CNT surfaces for formation of CdS.

The second objective is to develop a probe reaction and methodology to study the photocatalytic properties of our composites. An ideal reaction must adhere to several criteria in order to be suitable for photocatalysis using the hybrids formed: (i)

it must involve a reduction reaction, so that photogenerated electrons are transferred to the reacting species; (ii) the reduced product must be measurable and quantifiable in order to reliably monitor the effect of the catalyst, e.g. a chemical change resulting in distinct NMR shifts or the detection of a measurable volume of gas produced; (iii) the photocatalytic reaction must use a visible light source, since CdS QD are activated by absorbing light in this region; (iv) the reaction must be carried out under ambient conditions, which should prevent changes to the catalyst i.e. growth of QD through Ostwald ripening.[21]

Of the three main reactions reported for composites of CdS and CNT (photocurrent generation, hydrogen production and dye degradation) the first is unsuitable, since metallic nanotubes must be in contact with an electrode for photocurrent generation, excluding the use of CdS encapsulated in BNNT (CdS@BNNT- Chapter 4). While the second requires a metal co-catalyst to be attached to the nanotubes, which is not present in the photocatalysts formed and would introduce an additional variable, thus making it more difficult to distinguish the effects being explored in this study. However, composites of CdS and CNT are also commonly targeted at the degradation of brightly coloured dye molecules, such as Brilliant Red,[9] Rhodium B,[22] methylene orange[7] or methylene blue.[6] These dyes are used in the textile industries and are released in significant amounts as waste, which then contaminate water supplies.[23] Photocatalysts, without the addition of metal co-catalysts, degrade the dyes through a spontaneous reaction which results in decolourisation. This is very convenient for analysis as it creates the opportunity to monitor the degradation of dye in solution using UV-vis spectroscopy.

Methylene blue (MB) (Figure 85) has been explored previously in the literature as a probe for photocatalytic reactions[6, 24, 25] and is known to adsorb onto CNT due to the extended π structure of both MB and CNT.[26] The surface of nanotubes is thought to be the site of catalysis,[27] so good adsorption should help degradation of the dye. MB will therefore be an ideal candidate to measure the photocatalytic activity of the hybrid structures.

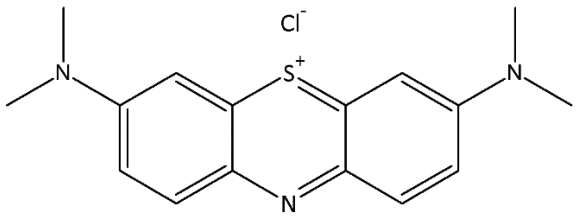


Figure 85. Structure of methylene blue.

The experimental conditions will require some method development in order to optimise the experimental set-up, such as modifying the amount of light reaching the photocatalysts, or the volume of the reaction mixture, in order to discriminate between the activities of each of the photocatalysts.

The third objective is to appraise the photocatalytic abilities of CdS on CNT (CdS/CNT), CdS encapsulated in CNT (CdS@CNT) and CdS encapsulated in BNNT (CdS@BNNT). Doing so will permit examination of the effect of location on the photocatalytic properties of the material to be assessed. It will also show how the nature of the nanocontainer effects the functionality of the hybrid, specifically between MWNT and BNNT since their photocatalytic mechanisms of action and optical properties are quite different: metallic MWNT can accept photoexcited electrons from CdS, whilst BNNT, are wide band gap semiconductors, which are

predicted to act purely as supports for CdS with no electron transfer. However, studied have shown that defects in BN nanostructures can significantly decrease this band gap,[28] thus allowing electronic communication between CdS and BN.[29]

5.3 Results and discussion

CdS/MWNT was formed using an analogous method to CdS@MWNT (called CdS/96 h-treated MWNT Chapter 4), replacing oxidised MWNT with the as-received equivalent. Since these MWNT were not open, QD precursors had no entry route into the MWNT so were expected to from on the external wall (**Figure 86**).

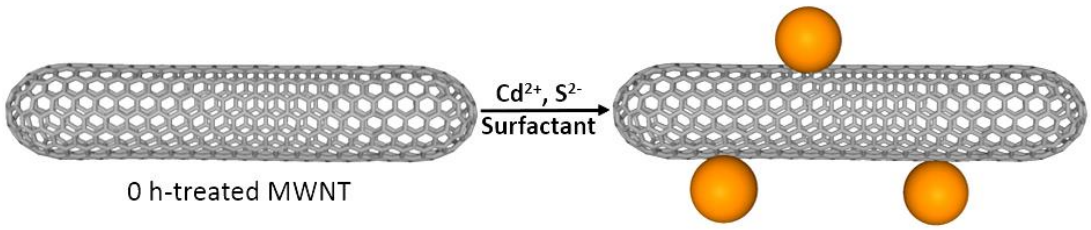


Figure 86. Schematic to show the formation of CdS on MWNT.

After dispersing MWNT in water, cadmium acetate dihydrate was added and the mixture stirred for 90 minutes. 1-thioglycerol and 1,2-dithioglycerol were added as surfactants, and the mixture stirred for 16 hours before the addition of sodium sulfide nonohydrate with 16 hours of stirring. The product was then isolated by vacuum filtration as a black powder.

The outer walls of the CNT comprise carbonyls and carboxylic acids as a result of imperfections and are present in most CNT. These oxygen-containing groups can sequester Cd^{2+} from solution, leading to a higher concentration of Cd^{2+} on the nanotubes surface.[30]

Analysis using TEM was the primary technique to probe the structure of the material formed as this is the only technique which can accurately probe the location of the NP, but also allows the size, shape, crystallinity and coverage of the QD to be simultaneously determined (Figure 87).

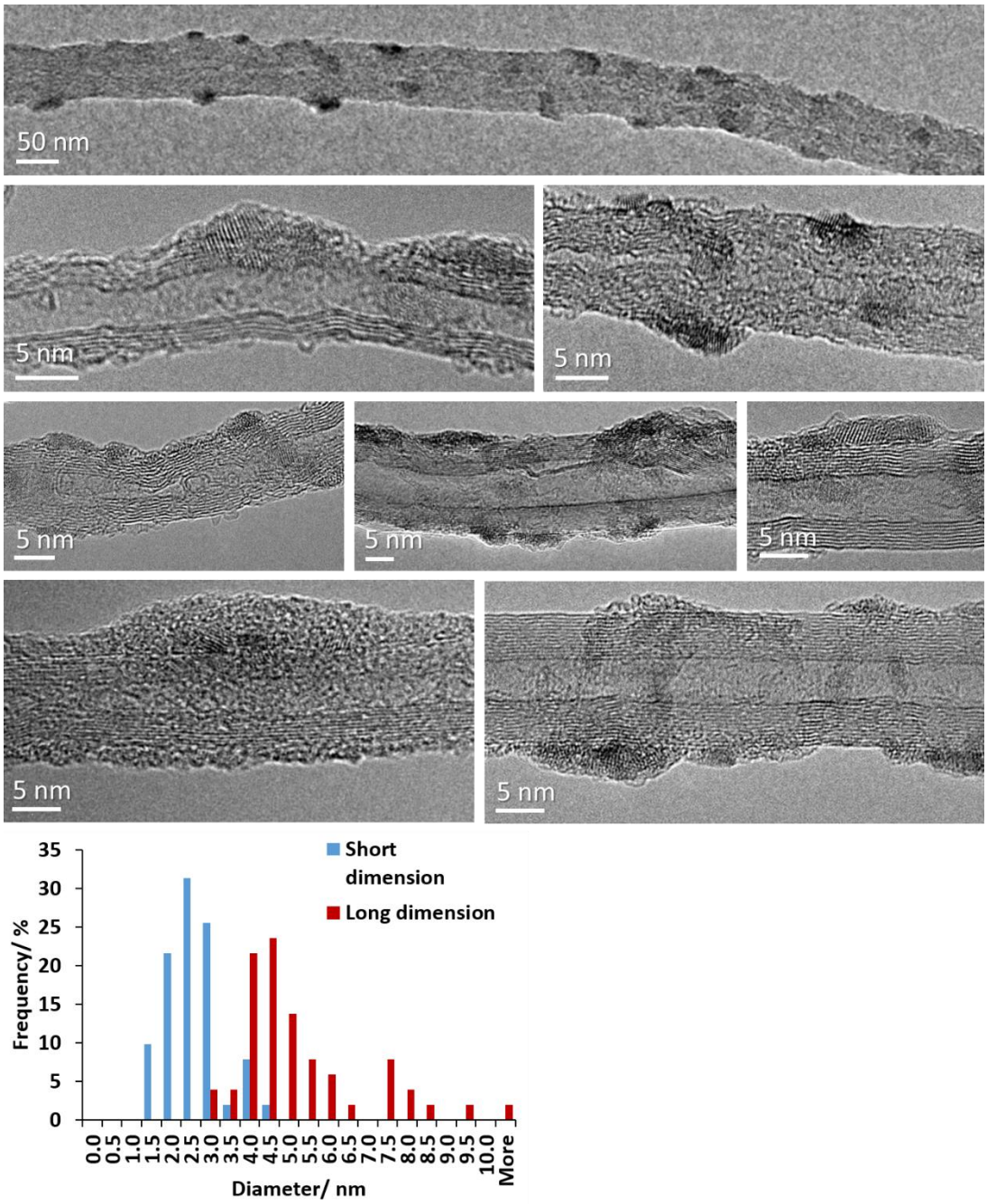


Figure 87. TEM images to show QD/MWNT hybrid materials. The mean QD diameter, recorded as a short and long axis, is measured as 5.0 ± 1.7 x 2.4 ± 0.7 nm. 83 QD are attached to the surface per µm, with only 5 encapsulated per µm of nanotube length.

Statistical analysis of the images revealed a high coverage of 83 QD per µm of MWNT with only few QD encapsulated (5 QD per µm), attributed to pre-existing defects within the CNT, which allowed a small amount of ions to diffuse into the internal volume during synthesis. Moreover, most of the QD were isolated nanoparticles, as oppose to clusters, which is important for good contact between the CdS and nanotube.

Both the long and short dimensions of individual QD are measured from the TEM images and the results are displayed as a histogram (Figure 87). The formation of elongated QD, with dimensions of 5.0 ± 1.7 x 2.4 ± 0.7 nm and aspect ratio (long dimension/ short dimension) of 2.31, was the result of the maximised vdW contact area between the QD and MWNT. As a comparison, QD encapsulated within MWNT (Chapter 4) were more spherical, with dimensions of 4.6 ± 1.0 x 3. 5 ± 0.9 nm and aspect ratio of 1.38, stabilised and templated by the cavity (5.1 nm).

For further characterisation and analysis a range of spectroscopic and gravimetric techniques were employed (Figure 88).

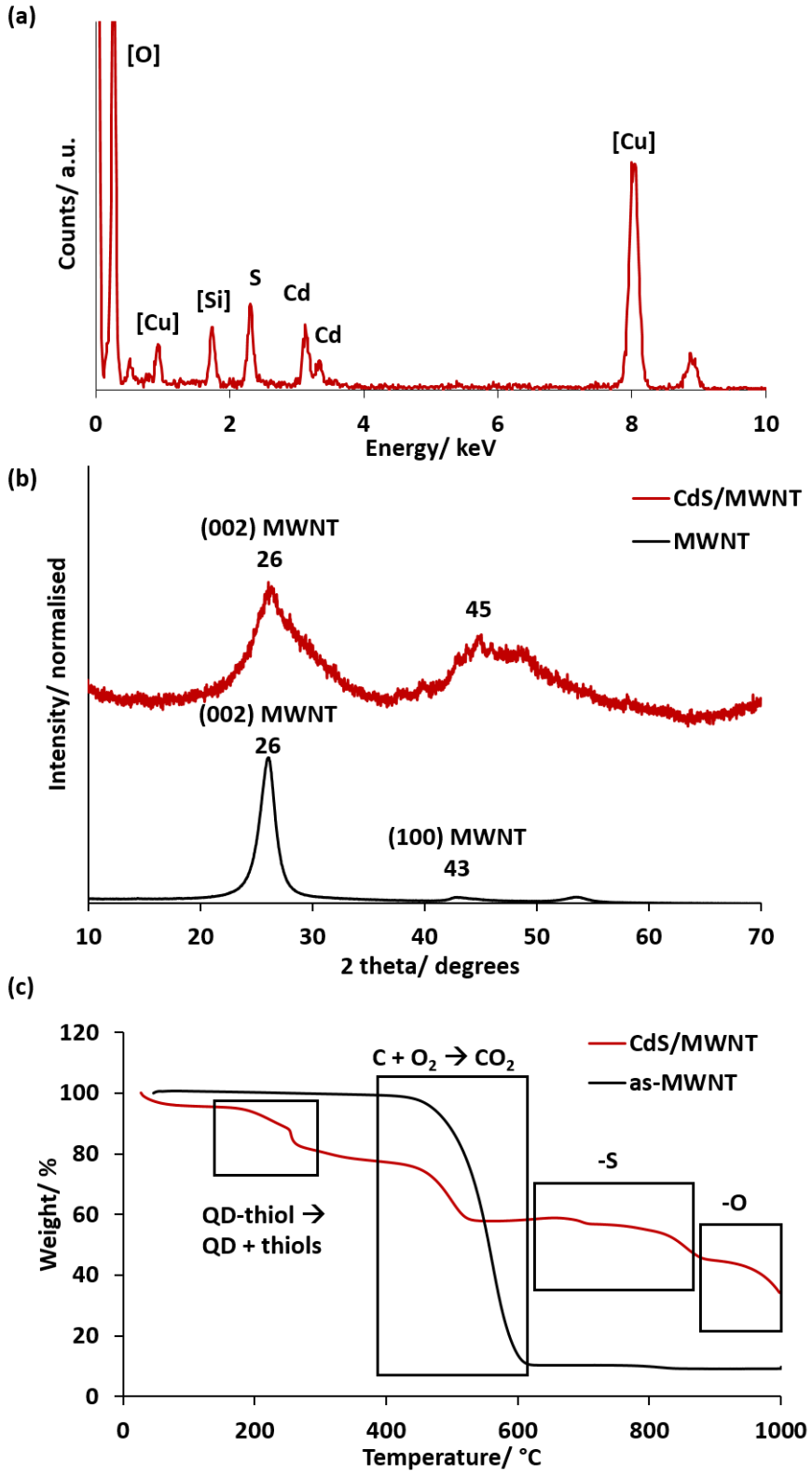


Figure 88. Analysis of CdS/MWNT. (a) EDX spectroscopy showing the presence of cadmium and sulfur, measured at a ratio of 1:1.6, (b) PXRD diffractogram with peaks at 26˚ and ca. 43˚, corresponding to MWNT (002) and (100) planes, and broader peaks at 2Θ values of 26˚ and 45˚, which are likely to be a contribution from the (111) and (220) crystal planes of cubic (zinc-blende) CdS. (c) TGA of MWNT and CdS/MWNT at a heat rate of 5 ˚C.min^{-1} in air, weight loss between 200-300 °C is assigned to the decomposition of 1-thioglycerol and

1,2-dithioglycerol, oxidation of the CNT occurs at 500 °C, the oxidation of CdS to CdO (800 °C - 1000 °C)- similar to those in CdS@MWNT in Chapter 4.

EDX spectroscopy was used for elemental identification, confirming cadmium and sulfur were both present at a ratio of 1:1.6, with the excess of sulfur arising due to the presence of sulfur-containing surfactant. PXRD detects small, polycrystalline CdS in the spectrum of CdS/MWNT in addition to the MWNT (26˚ and 43˚, corresponding to MWNT (002) and (100) planes). The broad peaks at 26˚ and 45˚ are likely to be a contribution from the (111) and (220) crystal planes of cubic (zinc-blende) CdS. The peak broadness indicates very small QD, since broadness increases as the diameter of the nanoparticles decreases.[31] TGA showed CdS loading and complex thermal behaviour of CdS, consistent with CdS@MWNT (Chapter 4). A weight loss between 200-300 °C was assigned to the decomposition of 1-thioglycerol and 1,2-dithioglycerol. Oxidation of the CNT occurred at 500 °C, and the oxidation of CdS to CdO occurred between 800 °C and 1000 °C with partial sublimation of CdS.[32] Additionally, ICP-OES quantified the Cd^{2+} content as 34%, similar to that obtained for CdS@MWNT (33%) in Chapter 4. This thorough characterisation confirmed that CdS had successfully formed on the surface of MWNT with high coverage and dispersion.

5.3.1 Development of probe reaction

The decolourisation of MB was used to probe the photocatalytic activity of the materials. This is an important reaction for the decontamination of polluted water[23] and is suitable as a probe reaction owing to its ability to adsorb onto CNT.[26] Its bright colour in water is lost after reduction/ decomposition allowing the concentration to be monitored using UV-vis spectroscopy.

The mechanism of MB degradation using CdS QD is shown below. Having generated excitons, sequential reactions eventually lead to the formation of hydroxyl radicals resulting in the degradation of MB (Figure 89, Equation 1-5).[33, 34] The $OH^{\bullet}$ radicals can attack the $C\text{-}S^{+}\text{=}C$ functional groups of MB,[35] which degrades the dye (Figure 90).

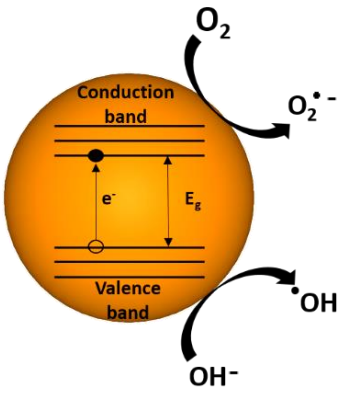


Figure 89. Photocatalytic mechanism for the degradation of MB by CdS QD.

$$CdS + h\nu \rightarrow CdS\,(h^{+} + e^{-}) \quad (1)$$

$$O_2 + e^{-} \rightarrow O_2^{\bullet -} \quad (2)$$

$$H_2O \rightleftharpoons H^{+} + OH^{-} \quad (3)$$

$$OH^{-} + h^{+} \rightarrow {}^{\bullet}OH \quad \text{or} \quad O_2^{\bullet -} + (H_2O \rightleftharpoons H^{+} + OH^{-}) \rightarrow OH^{\bullet} \quad (4)$$

$$MB + {}^{\bullet}OH \rightarrow \text{degradation}\,(CO_2 + H_2O + H_2SO_4 + HCl + HNO_3) \quad (5)$$

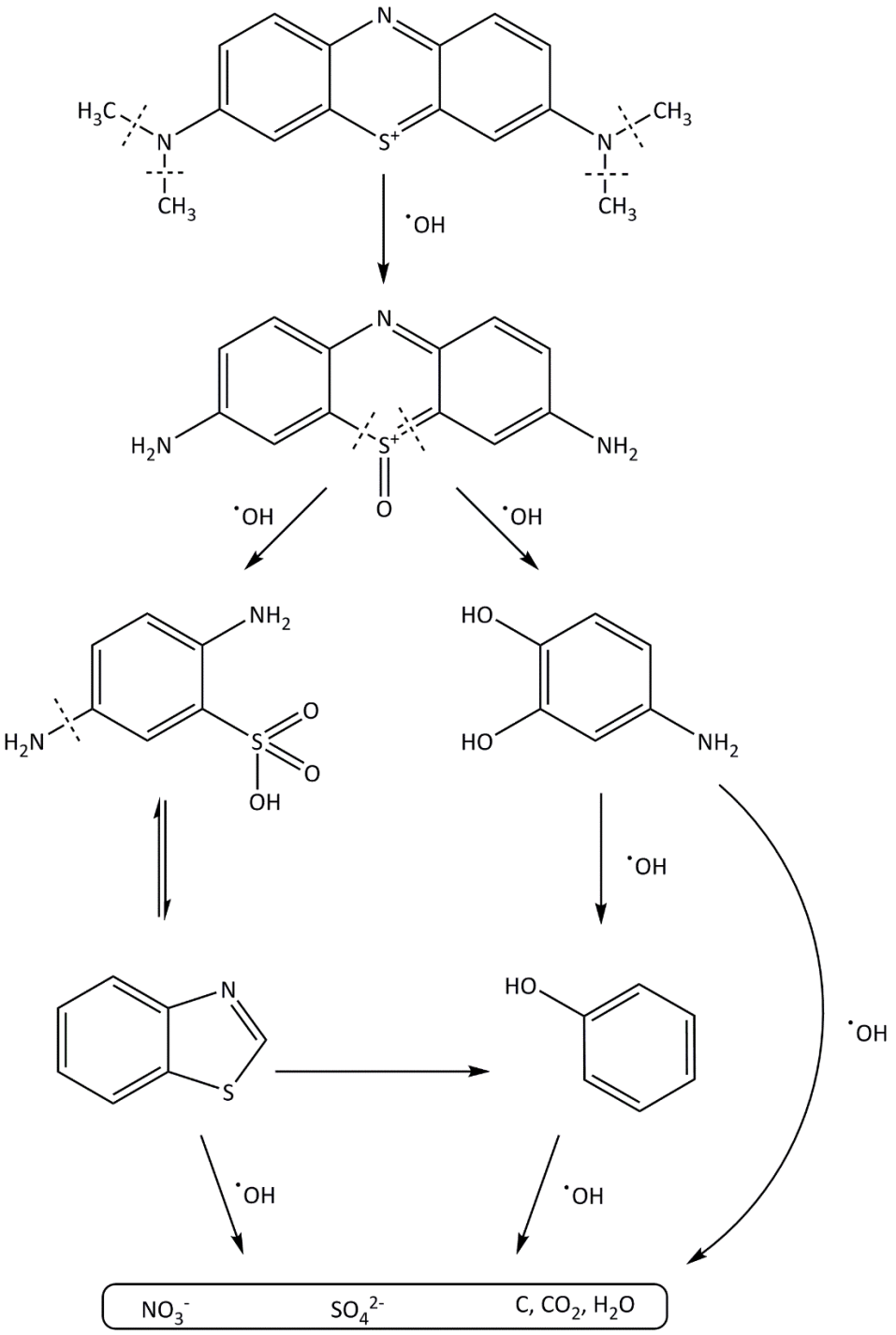


Figure 90. Proposed mechanism for the degradation of methylene blue.

However, two processes act to reduce the concentration of MB (i) the adsorption of dye onto the nanotubes and (ii) the photocatalytic degradation of MB.

While both are important for dye removal it is necessary to delineate the two processes.

For effective catalysis, is it key that dye molecules adsorb strongly onto the surface of the nanotubes since this is the site of catalysis.[27] A high content of MB adsorbed onto BNNT would provide a concentrated dye environment around the QD to contribute to the rate of photocatalysis. In order to gain insight into the amount of dye which could be adsorbed onto the hybrid materials, a series of adsorption tests were performed. Nanotubes without QD attached were tested in order to make the experiments comparable and rule out any effect from non-equivalent QD coverage. Nanotubes were suspended in aqueous solutions of methylene blue and stirred for 16 h. This exceeds the time required for an equilibrium to be reached between adsorbed molecules and those in solution, as theoretically most of the MB molecules assemble around the surface of CNT in water after 1 ns.[26] All samples were kept in the dark during this time to eliminate premature photocatalysis from ambient light in the laboratory. The stirring was stopped and the nanotubes were allowed to settle, thus separating them from the solution of methylene blue. Aliquots were taken for analysis by UV-vis spectroscopy, in order to quantify the change in MB concentration and hence the amount adsorbed onto the nanotubes. The amount of MB adsorbed at equilibrium, Q_e (mg g^{-1}), was calculated using the equation below (Equation 6), where C_0 (mg L^{-1}) is the initial concentration of MB in solution, C_e (mg L^{-1}) is the equilibrium concentration of MB in solution, V in L is the volume of MB solution and W in g is the mass of nanotubes used in the experiment. The results are summarised in the table below (Table 2).

$$Q_e = V(C_e - C_0)/W \quad (6)$$

Table 2. Adsorption of methylene blue (MB) by different nanotubes. Ɛ=58711 L mol^{-1} cm^{-1}, 0.20 mg of MB in 30 mL of water at 25 °C.

Material	Q_e/ mg g^{-1}	MB adsorbed/ %
Open BNNT	65.4	33
As-received BNNT	55.0	28
Open MWNT*	157	79
As-received MWNT	85.6	43

*Oxidised through 96 hour reflux in nitric acid. MWNT remained dispersed in the solution and could not be removed prior to recording the UV-vis spectra. Consequently, the absorbance reported is obtained from the difference in absorbance (CNT in MB solution and CNT in aqueous solution of the same concentration). The concentration of MB was determined using the Beer-Lambert law and experimentally determined ε. For MB (at 664 nm) ε=58711 L mol^{-1} cm^{-1}.

Appraisal of the adsorption of MB onto different nanotubes elucidated the strength of interactions and the available surface area for MB to attach. Open nanotubes adsorbed more MB than closed nanotubes for both CNT and BNNT. Upon opening of the MWNT through oxidation, the surface area of the MWNT available to MB almost doubled and, consequently, the percentage of MB adsorbed increased from 43% to 79%. Open MWNT (i.e. 96 h-treated in nitric acid) also possess more functional groups with negative charge (e.g. carboxylate) on its surface to improve the adsorption of cationic methylene blue through electrostatic interactions. BNNT have a smaller increase in adsorption of 5% after opening, as MB mostly adsorbs to the outer walls. This is where the majority of the electron density of the π bonds (electrons provided by nitrogen lone pair) are situated, and are more available to interact with MB.

The increases in MB adsorption upon opening nanotubes is consistent with surface area effects but also proves that MB can access all surfaces of the nanotube, which is crucial if they are to function as nanoreactors.

When comparing the adsorption behaviour for CNT and BNNT, it is clear that more MB is adsorbed onto CNT than BNNT, suggesting the π- π interaction between MB and CNT are stronger than for MB and BNNT. Seemingly, the extended π structure of CNT is favourable to the more ionic character of BNNT.

MB is known to be very stable on CNT. Simulations showed how MB forms strong interactions with the nanotube (interaction energy, ΔE = -32.8 kcal mol^{-1}) (Figure 91), as it bends around the convex wall to maximise surface contact.[26] Movement in the form of sliding along the nanotube and rotation of dimethylamino-groups are reported, yet the strong interactions between the tricyclic plane of MB and the CNT prevent dissociation. It is the combination of hydrophobic interactions, π-π and cationic-π interactions, along with charge transfer interactions that create such stability.[26]

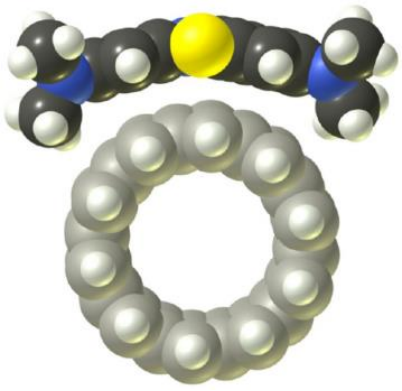


Figure 91. Optimised structure of MB^+ with CNT determined by Chagovets *et al*. using molecular mechanics method for optimisation modeling.[26]

The simulations discussed above were modelled on very narrow (10,10) CNT, rather than larger MWNT used in this report. Although, as the diameter of the CNT increases, the curvature is reduced which in turn will only strengthen the interactions between MB and CNT, as it becomes less strained when positioned on a flatter surface. For instance, graphene-MB interactions are calculated to be much stronger than (10,10) CNT-MB interactions (-42.1 and -45.0 kcal mol^{-1} for the adsorption of MB onto graphene at different orientations).[26] The interaction energy of MB onto MWNT will therefore be somewhere between that of MB onto SWNT and graphene.

The cumulative effect of good adsorption of MB onto the nanotubes, combined with a high photocatalytic decomposition rate, should result in adsorption-photocatalytic synergistic removal of pollutants. Having explored the amount of MB adsorbed onto the nanotubes, the photocatalytic activity of the photocatalysts was investigated.

5.3.2 Method 1:

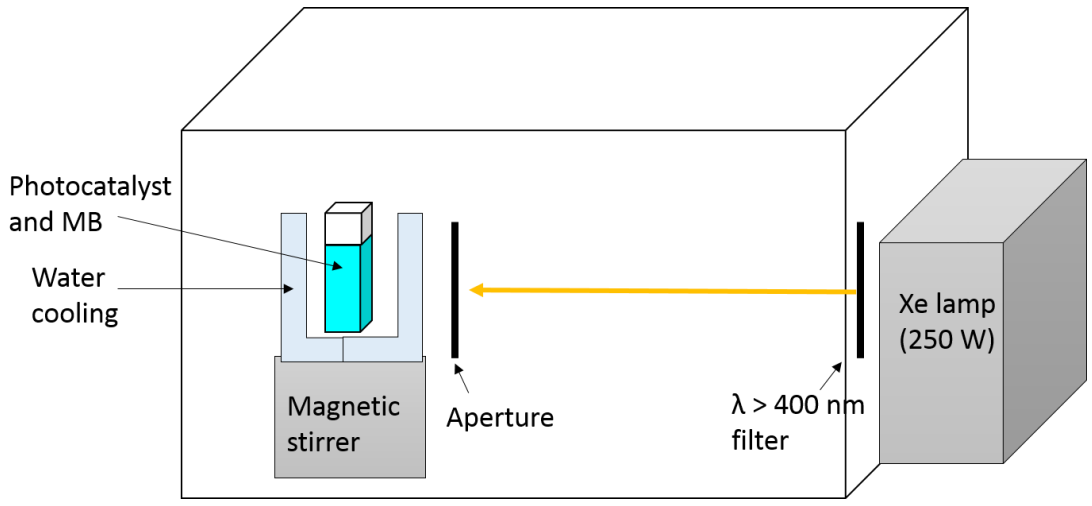


Figure 92. Schematic representation of the apparatus set-up in Method 1.

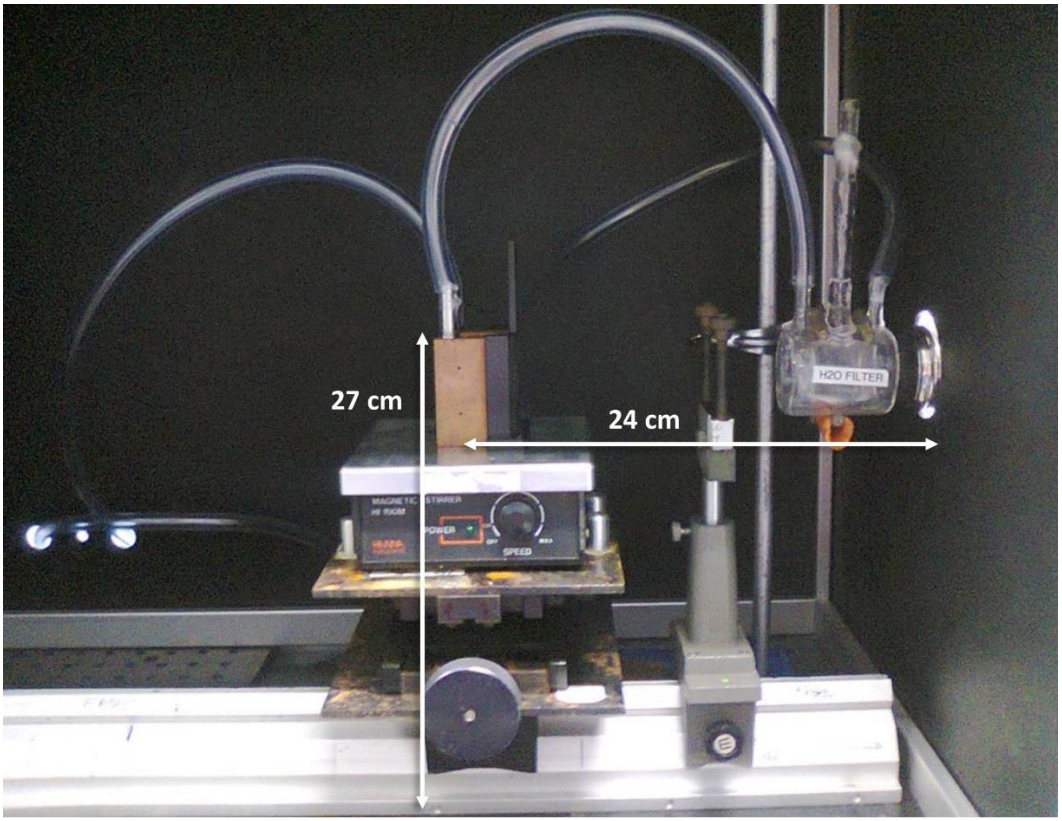


Figure 93. A selection of annotated photographs showing the components of the photocatalytic reaction set-up used in Method 1. The thermostatically controlled cell holder, holder for the filter and water filter. The measurements of the horizontal and vertical positioning of the cell holder are shown. Reproduced from C. A. Clark's thesis.[36]

The design of Method 1, shown in Figure 92 and Figure 93, was based on a similar setup used previously for CO_2 reduction,[36] and the careful consideration of a range of conditions required for photocatalysts. A powerful light source was expected to result in a high rate of photocatalysis, with many literature examples using 300 W Xe lamps for similar reactions.[1, 3, 5, 7, 9] These examples show clear concentration changes over time, therefore a similar lamp (250 W Xe lamp) was employed (Figure 94).

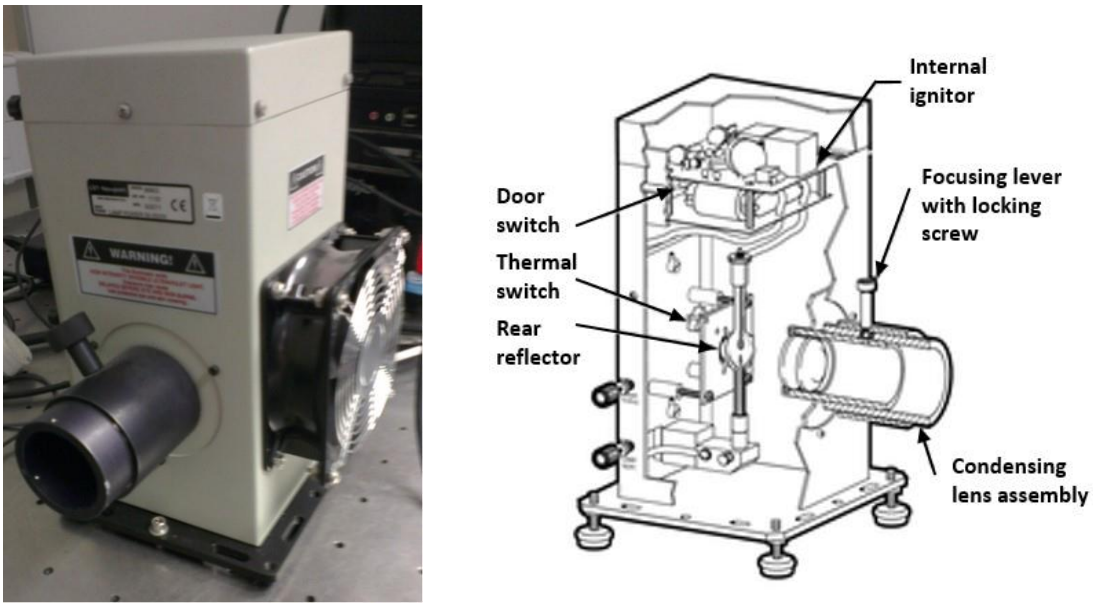


Figure 94. Xenon arc lamp housing, with schematic, used for Method 1.

The lamp housing, in addition to housing the bulb, also contained a rear reflector and two fused silica condenser lenses enabling collimation of the light to an area of *ca*. 25 x 25 mm^2, ensuring the light was directed to the reaction mixture for photocatalysis. The irradiance at 60 cm from the light source is shown in Figure 95. When the reaction mixture is placed at a distance of 24 cm from the light source, according to the inverse square law of light, the irradiance is estimated at *ca*. 937 µW cm^{-2} in the range in which CdS QD will absorb light (590-620 nm). By keeping each sample at the same position and orientation, combined with the known stability of the light source, the intensity of radiation hitting the sample should be identical in each experiment.

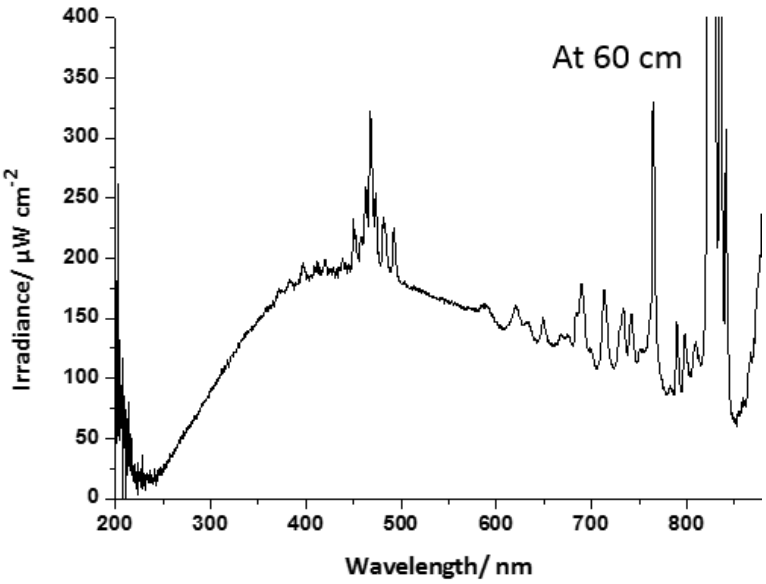


Figure 95. Irradiance from the light source at a distance of 60 cm with no filters present. The irradiance output was measured using a calibrated Ocean Optics Flame UV-vis spectrometer fitted with a cosine corrector.

The broad wavelength light source should excite electrons over the bandgap of QD spanning a broad sizes range. A filter (λ > 400 nm) was employed to cut out any UV light, which would cause the photochemical degradation of MB rather than photocatalysis.

A quartz filter containing water was placed in front of the lamp aperture, which absorbs some of the IR light given out (removing heat) and some of the UV light. The cuvette holder is a custom built copper block with internal pipework which allows cooling water to flow around and maintain a constant temperature of *ca*. 15 °C (Figure 96), removing thermal degradation or temperature fluctuations which are known to effect the reaction kinetics of dye degradation.[10]



Figure 96. Photograph of the thermostatically controlled cell holder, showing the dimensions and pathway for recirculating water. Made by the School of Chemistry workshops.

A rectangular aperture was fixed to the front of the cuvette holder enabling a consistent irradiated area. The cuvette holder sat on top of a magnetic stirrer, allowing the stirring speed to be controlled. This allows the photocatalyst to be dispersed within the mixture to increase the amount of light hitting the photocatalyst.

Prior to the photocatalytic reaction, each photocatalyst (CdS@MWNT, CdS/MWNT or CdS@BNNT, 0.6 mg) was stirred with MB (3 mL of 15 mg L^{-1} or 30 mg L^{-1} MB) in the dark for 16 hours to allow equilibration between MB in solution and MB absorbed on the nanotubes. Monolayers of MB cover the surface of hydrophobic nanotubes and promote dispersion of the hybrid material in water.[26]

The concentration of MB in solution at t=0 (i.e. after equilibration) varied between experiments due to different adsorption capacities of the photocatalysts.

For instance, the adsorption experiments for a range of nanotubes showed the percentage adsorption to range between 28% for as-received BNNT and 79% for open MWNT. Yet, in order to accurately and reliably monitor the concentration of MB throughout the experiment, the concentration must be within a specific range (UV-vis absorbance between *ca*. 0.3-1.0 a.u.). Therefore, the initial concentration was varied (15 mg L^{-1} or 30 mg L^{-1}). In addition to this, to reliably compare the photocatalytic activity of the hybrid materials, MB degradation was plotted as a normalised concentration change over time.

Absorption spectra were measured at the rear of the cell holder using an Ocean Optics Flame spectrometer with the light attenuated using a series of ND filters. In this setup the Xenon arc lamp was used as both the pump light source for the reaction and as a probe for the spectroscopy. The *in situ* approach avoids aliquots of solution being removed, so the reaction volume did not change during the experiment, thus an unlimited number of spectra can be recorded. Typically, UV-vis spectra were recorded every 2.5 minutes producing a high number of data points for an accurate fit on the degradation curve (Figure 97). However, a consequence of the reaction set up is that the reaction volume was limited to the size of a cuvette (1 x 1 x 3.8 cm), so the entire reaction was performed on a small scale.

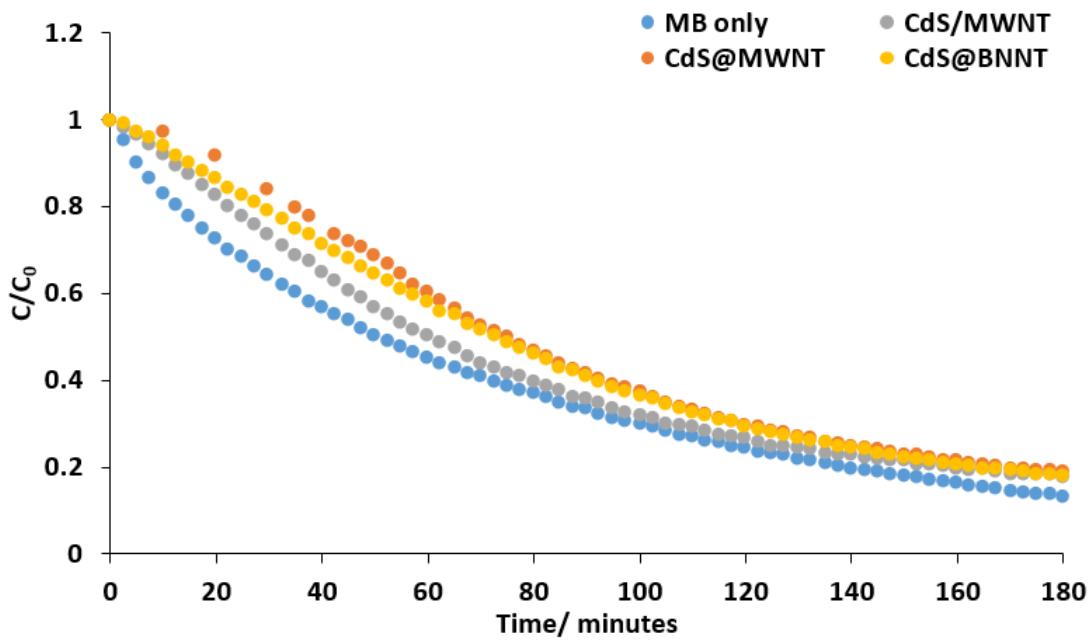


Figure 97. Normalised temporal MB concentration change (C/C_0). Based on Method 1 at 25 °C.

Here, the high intensity of the lamp quickly degraded the small volume of MB in the cuvette across all of the experiments, with no statistically significant changes in the rate of decomposition with the addition of a photocatalyst.

Another drawback with this experimental setup was that the simultaneous photocatalysis and UV-vis analysis resulted in both aspects being compromised. Rapid stirring of the mixture to suspend the photocatalysts would result in nanotubes scattering light and false absorbance values. To compensate for this, stirring was kept relatively slow, however, this limited the amount of light reaching the photocatalyst due to it settling at the bottom of the cuvette, outside of the direct pathway for irradiation. Consequently, Method 1 was dismissed as unreliable and a new method became necessary.

5.3.3 Method 2:

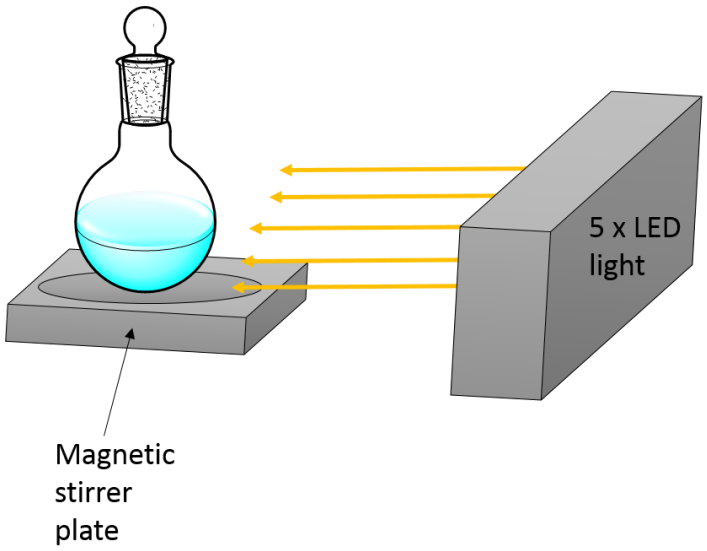


Figure 98. Schematic representation of the apparatus set-up in Method 2.

The new method involved stirring a much larger dispersion of the photocatalyst (*ca.* 11 mg) in an aqueous solution of MB (30 mL, 15 mg L^{-1} or 30 mg L^{-1}). As previously, the mixture was allowed to stir in the dark for 16 h to reach an equilibrium. Subsequently, the suspension was placed at a distance of 20 cm from the lamp and irradiated under visible light with vigorous stirring to create maximum light absorbance from the catalyst.

In this method, an LED light was employed (comprised of 1000 lumen 5* CITIZEN LEDs on a mounted block); while still bright, this light source was less powerful than the Xe lamp used in Method 1, so predicted not to degrade the MB as rapidly. The lamp was fan cooled so the heat emission from the lamp was very low, preventing thermal effects influencing the rate of photocatalysis.

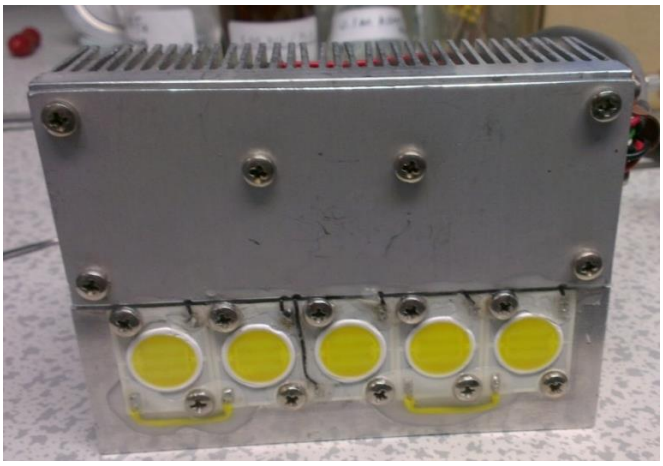


Figure 99. 5* CITIZEN LED block – fan cooled used for photocatalysis using Method 2. Built by the chemistry department workshops. The irradiance output was measured using a calibrated Ocean Optics Flame UV-Vis spectrometer fitted with a cosine corrector.

Another benefit of an LED light source was the production of white light which covers a broad range of wavelengths in the visible spectrum to excite the band gap of CdS QD over a broad size range, but did not produce any UV light (Figure 100) and so a filter was not required.

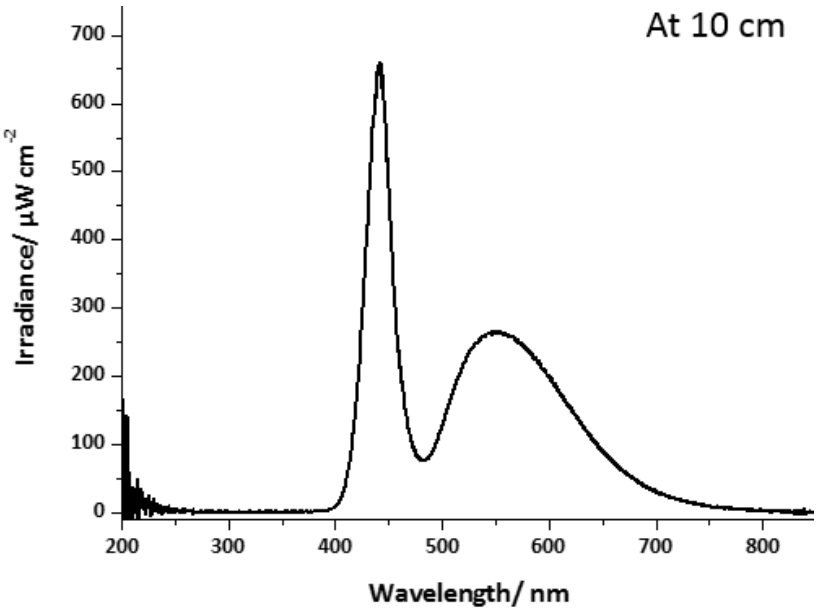


Figure 100. Irradiance from the light source at a distance of 10 cm. At a distance of 20 cm, the irradiance will be ¼ of that measured at 10 cm.

The reaction was performed on a much larger scale than in Method 1 and rapid stirring was permitted to disperse the photocatalyst within the MB solution; the light reaching the photocatalysts should be significant to allow photocatalytic activity to be observed. The irradiance of the LED lamp was estimated from irradiance measurements to be 62 μW cm^{-2} at 550 nm, and reduced only slightly in the range in which the CdS QD absorb light (590-620 nm).

To monitor the degradation of MB, aliquots of the mixture were removed periodically, then stored in the dark while the photocatalyst was allowed to settle at the bottom of the reaction mixture, making separation of the aqueous phase simple. These aliquots were then analysed by UV-vis spectroscopy to determine the concentration of methylene blue remaining in solution.

As with Method 1, MB degradation is plotted as a normalised concentration change over time (Figure 101).

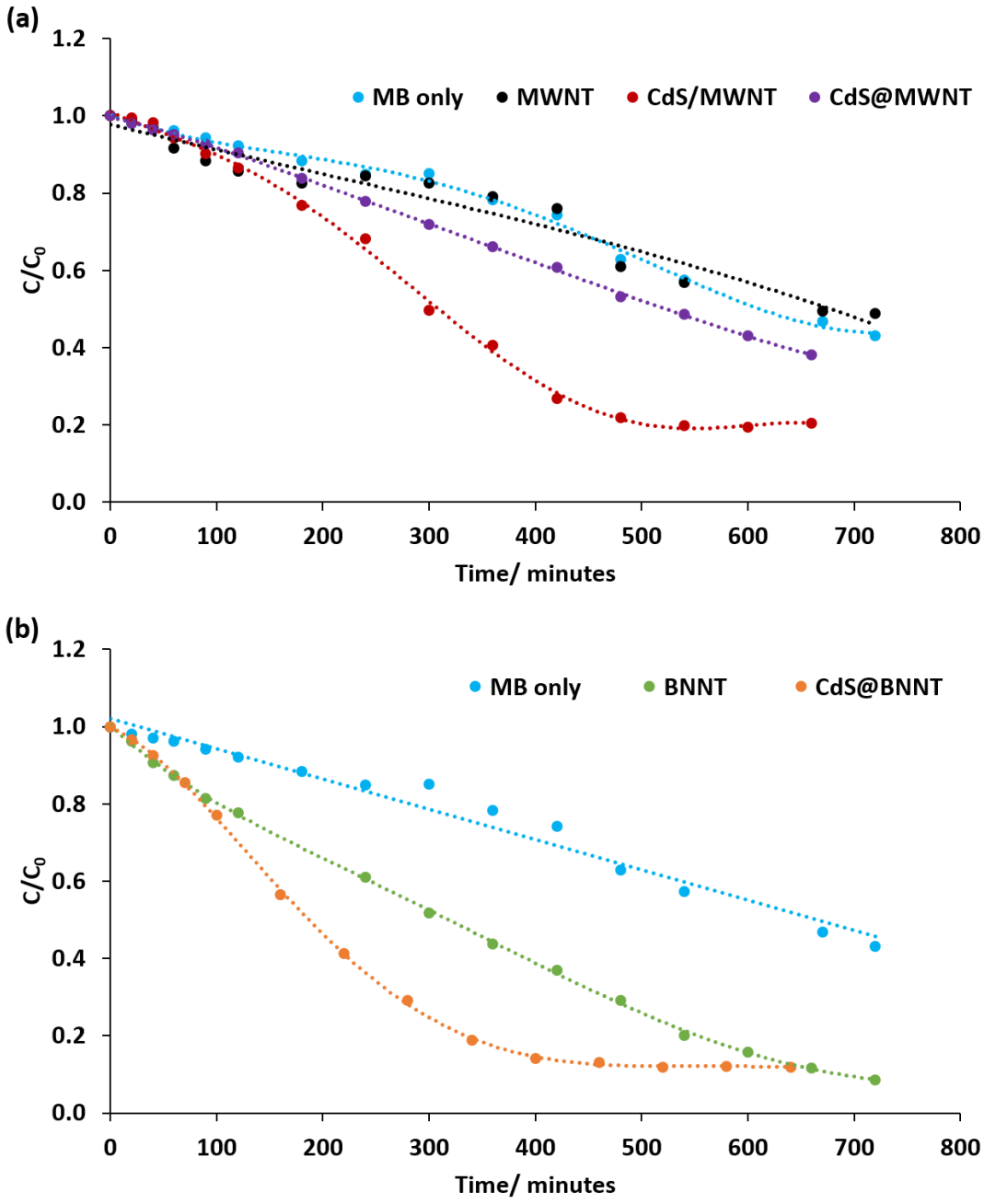


Figure 101. Normalised temporal MB concentration change (C/C_0) based on Method 1 for (a) MB only, MWNT, CdS/MWNT and CdS@MWNT and (b) MB only, BNNT and CdS@BNNT.

A definite variation in the rate of degradation could be seen using this method, and the activity of the catalysts could be clearly discriminated. Quantitative comparisons were made between the photocatalysts, plotted as the percentage MB degradation in the first 360 minutes of the reaction (Figure 102).

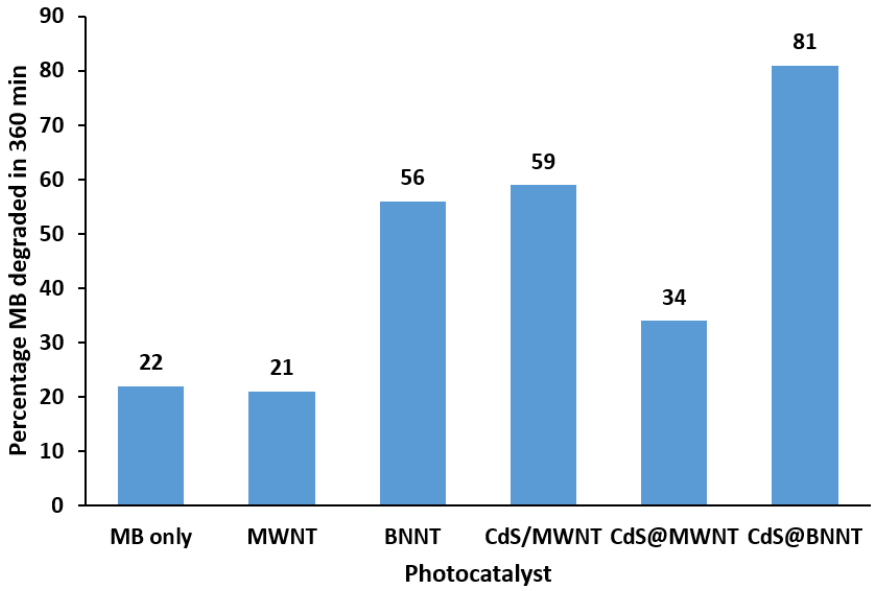


Figure 102. Percentage of MB degraded in 360 minutes using the as-prepared samples under visible light irradiation using Method 2.

Simply by looking at the plots in Figure 101 and Figure 102, it is immediately obvious that the rate of reaction is effected by both the location of the QD and the nature of the nanotube host. As expected, irradiation of MB solution alone showed the slowest degradation rate, since no catalyst was present to increase the degradation rate. The change in absorbance measured over the 700 minute timescale was much slower than in Method 1, and did not prevent photocatalytic effects being observed. Hence, when the photocatalysts were present, the degradation rate increased across all of the experiments.

It is also clear, when comparing CdS/MWNT and CdS@MWNT, that the location of the QD crucially affected the rate of decomposition of MB; with QD on the surface of MWNT outperforming those encapsulated within MWNT. From the proposed mechanism of MB decomposition, the effect of the location of QD on the rate of degradation can be explained by two cumulative effects. Firstly, QD on the external surface of CNT absorb more photons and could therefore produce more

excitons for photocatalysis. Since, 2.3% of light is absorbed by the CNT per graphitic layer,[37, 38] around 42% of incident photons are absorbed by the average MWNT used to produce these hybrids. Secondly, more water is in contact with quantum dots if they are outside of the nanotubes, so the photogenerated holes are able to oxidise water to hydroxyl radicals which in turn degrades MB.

The hybrids composed of CdS and BNNT stood out as the best photocatalyst for MB degradation. The rate was, astonishingly, more than four times that of the carbon analogue (0.270 h^{-1} compared to 0.066 h^{-1} for CdS@MWNT). The most obvious conclusion is that the transparency of BNNT to visible light is very important for photocatalysis.

Another branch of thought is that semiconductors (in this case CdS) can transfer photogenerated holes to the BNNT to increase the rate of photocatalysis. One example reported in the literature showed improved photocatalytic activity of the semiconducting nanoparticle,TiO_2, when deposited on BNNT.[39] Whilst, no other known examples are reported for nanoparticles on BNNT, similar results were reported for BN nanosheets (BNNS) and BN nanoparticles. Xu *et al*. [40] demonstrated that photogenerated holes could be transferred from semiconducting nanoparticles (WO_3) to BNNS, which were then responsible for an increased rate of photocatalytic degradation of RhB. While Fu *et al*.[41] showed hole transfer from TiO_2 to hexagonal-BN nanoparticles, suggesting that N edges, caused by defects in the structure of BN and resulting in negatively charged BN, could be the site that holes migrated to. The transfer could be helped by the electrostatic attraction of the positive holes with the negative charge of BN. Since the nanosheets/ nanoparticles have a very similar structure to BNNT, albeit flat rather than rolled up, the mechanism could be very

similar. Further experiments would be required to determine if this is true, and the band gaps and electronic energy levels of all the materials should be probed.

However, BNNT alone increased the rate of catalysis comparable to CdS/MWNT. This is a fascinating observation as the luminescent and photoactive properties of BNNT are still controversial. One likely explanation is that structural defects/ dopants in a small percentage of BNNT nanotubes can significantly reduce the electronic band gaps,[42, 43] resulting in semiconductors capable of producing excitons for photocatalysis. However, the photocatalytic properties of BNNT are still undetermined so at present, the mechanism can only be speculated.

Using Method 2 for the photocatalytic degradation of MB, it is clear that the efficiency of the photocatalyst is determined by both the location of QD and the nature of the nanotube host. QD on the convex surface of MWNT (CdS/MWNT) are shown to drastically increase the rate of photocatalytic degradation of MB, attributed to significantly more photons reaching the QD than in the encapsulated equivalent (CdS@MWNT – ca. 85% of light is absorbed by the MWNT). If MWNT are exchanged for BNNT (CdS@BNNT), the rate of photocatalysis is significantly increased again. The optical properties of the hybrid structure are thought to be responsible, as BNNT are completely transparent to visible light, increasing the amount of incident photons absorbed by CdS.

5.4 Conclusions

Cadmium sulfide quantum dots have been formed on the surface of multi-walled carbon nanotubes and their size and structure characterised. In contrast to the encapsulated analogue (CdS@MWNT), the QD are elongated as the templating

from the MWNT is lost. However, the coverage and QD content is comparable to CdS@MWNT, making this a good control sample.

A probe reaction has been developed, with two experimental designs (Method 1 and Method 2), to study the photocatalytic decolourisation of methylene blue. Method 1 utilises a high power xenon lamp, with *in situ* UV-vis spectroscopy. Method 2 uses LED lights and *ex situ* UV-vis spectroscopy, allowing the reaction volume to be probed on a larger scale.

Both methods have both been applied to appraise the photocatalytic abilities of CdS/MWNT, CdS@MWNT and CdS@BNNT. Method 1 resulted in such rapid decomposition that the effect of photocatalysis could not be explored. However, Method 2 clearly distinguished the photocatalytic activity of the materials. The catalytic activity of the hybrid materials can be ranked from most to least active as CdS@BNNT > CdS/MWNT > CdS@MWNT, consistent with the intensity of light able to reach the QD. Confinement of CdS in MWNT lowers the photocatalytic activity, compared to the non-confined equivalent, assigned as less light reaching the QD. Encapsulation of CdS inside BNNT results in the highest photocatalytic activity due to favourable photocatalytic properties and the BNNT transparency to visible light.

After these experiments were performed a paper was published detailing a similar photocatalytic reaction, agreeing with the results in this study in which CdS encapsulated within CNT degrades the dye slightly less rapidly than CdS deposited outside the CNT.[44] Although, the difference is much more subtle, possibly due to the shorted timescale of their reactions.

5.5 Experimental

All common reagents and solvents were purchased from Sigma-Aldrich Chemicals®, UK and used without further purification, unless otherwise stated. Water was purified (>18 MΩcm) using a Barnstead NANOPure II system. All experimental procedures were performed using conventional glass apparatus, unless otherwise stated. UV-vis absorption spectra were recorded in solution at room temperature, using 1 cm quartz cuvettes, using a Perkin-Elmer Lambda 25 UV-vis Spectrophotometer over the range 400-700 nm unless stated otherwise.

Powder X-Ray Diffraction measurements were performed on a PANalytical X'Pert PRO Diffractometer equipped with a Cu Kα radiation source (λ = 1.5418 Å) in Bragg-Brentano geometry using a Si zero-background holder. Generator voltage = 40 V, Tube current = 40 V.

Transmission electron microscopy (TEM) imaging was performed by Prof. Andrei Khlobystov, Rhys Lodge or Craig Stoppiello using high resolution TEM on either a JEOL JEM-4000EX (LaB_6 source, information limit < 0.12 nm) or a JEOL 2100F TEM (field emission gun source, information limit < 0.19 nm) at room temperature. Samples were typically prepared by casting several drops of solution onto copper-grid mounted 'lacy' carbon films and allowing the grid to dry on filter paper.

Local EDX spectra were acquired for samples mounted on TEM grids using an Oxford Instruments INCA X-ray microanalysis system. The electron beam was condensed onto areas of specimens (bulk specimen or nanotube bundles) suspended over holes of the amorphous carbon film.

Thermogravimetric analysis (TGA), unless otherwise stated, was performed using a TA Instruments SDT Q600 under a flow of air at a rate of 90 mL min^{-1} at a heating rate of 5 °C min^{-1} from room temperature to 1000°C.

Raman spectroscopy was conducted using a HoribaJY LabRAM HR spectrometer with a laser wavelength of 532 nm. Samples were dropcast from methanolic solutions onto Si(100) wafers and a minimum of five spectra recorded from different areas of the sample.

Inductively coupled plasma optical emission spectroscopy (ICP-OES) was recorded on a Perkin Elmer, Optima 2000 DV ICP-OES with S10 autosampler. Samples and standards were prepared with a final solution composition of 2% nitric acid (69%, VWR Chemicals) in deionized water. CdS/MWNT was prepared by heating 5 mg of the hybrid material in a box furnace to oxidise the nanotubes. The remaining material was dissolved in 2 mL of nitric acid, expored to ultrasonic irradiation for 15 minutes before mixing on an orbital shaker (Grant Instruments Orbital Shaker PSU-10i at 200 rpm) for 16 h and gradually diluted to 20 mL, at an expected concentration of 2% nitric acid. Blank samples were prepared using an identical method, without the addition of the hybrids. CdS in BNNT sample was prepared by adding 4 mL of nitric acid to 1 mg of CdS in BNNT and heating at 100 °C for 16 h, before filtering and gradually diluting to an expected concentration of 2% nitric acid. A blank sample was prepared using an identical method, without the addition of the hybrids. A radial detection method was used at wavelengths of 214.4 nm and 228.8 nm, with 228.8 nm producing the most accurate result, which was used to determine the final concentration of Cd^{2+} in solution. Calibrations were formed from solutions of 0.005, 0.01, 0.05, 0.1 and 0.2 mg mL^{-1} with linear regression coefficient of 0.9998. Blanks

show 0.00 mg.L^{-1} of cadmium. Corrected coefficients are measured as CdS/MWNT = 0.9997.

5.5.1 CdS/MWNT

To a dispersion of MWNT (10 mg) in deionised water (16.7 mL) was added cadmium acetate dehydrate (44 mg), which was stirred at r.t. for 90 minutes before addition of 1-thioglycerol (0.1 mL) and dithioglycerol (2,3-Dimercapto-1-propanol, 0.04 mL) and the mixture allowed to stir for 16 h. Finally, sodium sulfide nonahydrate (1.67 mL, 0.1 M stock solution) was added dropwise and allowed to stir for 16 h. The product was collected by vacuum filtration using a 0.2 µM PTFE membrane and dried under vacuum to yield a black power. The hybrid was removed from the PTFE membrane and studied using TEM imaging. Some reactions were carried out on a smaller scale, where stated.

Mass/ mg =27

TEM (200 kV) 83 QD per µm, 5 QD encapsulated per µm, d_{NP}/ nm = 5.0 ± 1.7 x 2.4 ± 0.7

EDX (Cd:S) = 1:1.6

ICP-OES/ wt.% cadmium: 34

5.5.2 Methylene blue (MB)

Solutions of methylene blue were prepared by adding deionized water (100 mL) to methylene blue (15 mg, 4.69 x 10^{-5} mol, ACROS organics) to form a stock solution (150 mg L^{-1}). The stock solution was then diluted further to produce solutions with concentration 15 mg L^{-1} and 30 mg L^{-1} respectively.

5.5.3 Calibration curves

UV-vis spectra were recorded for samples of methylene blue at concentration of 0.048, 0.24, 1.2, 3.0, 4.0, 5.0 mg L^{-1} to form a calibration plot of concentration against absorbance maximum at 664 nm. The molar absorption coefficient (Ɛ) = 58711 L mol^{-1} cm^{-1} was then calculated. Error (R2) = 0.992.

5.5.4 Adsorption tests

The amount of methylene blue which can be adsorbed onto the nanotubes was determined by adding MWNT (1.097 mg), 96-h oxidised MWNT (0.984 mg), and BNNT (0.957 mg) to solutions of methylene blue (15 mL, 15 mg L^{-1}) and stirring in the dark for 16 hours. After stirring had stopped, nanotubes settled at the bottom of the solution and aliquots of MB were removed for UV-vis spectroscopy.

A control sample was prepared as above, in the absence of nanotubes (MB control) and a blank sample was prepared using MB solution with no additional treatment (MB-blank).

5.5.5 Method 1

Photocatalysts (0.6 mg) were added to MB (3 mL, 15 mg L^{-1}) and stirred in a quartz cuvette in the dark to equilibrate for 16 h. The mixture was then irradiated using a xenon arc lamp (Newport Oriel, Model No: 6258). The lamp housing (Newport Oriel, Model No. 66902), in addition to housing the bulb, also contains a rear reflector and two fused silica condenser lenses enabling collimation of the light to an area of *ca*. 25 x 25 mm^2. The power supply (Newport Oriel, Model No: 69911) is able to vary

the power output of the bulb from 240-330 W, though in practice an output power of 250 W was used for all experiments. A quartz filter containing water was placed in front of the lamp aperture.

A 400 nm cut off filter was used, λ > 400 nm (Newport, FSQ-GG400). The cuvette holder is a custom built copper block with internal pipework which allows cooling water to flow around and maintain a constant temperature (of *ca*. 15°C). A rectangular aperture is fixed to the front of the cuvette holder enabling a consistent irradiated area. The cuvette holder sits on top of a magnetic stirrer (Hanna Instruments, H190M). The position of the setup was kept the same throughout the series of experiments.

Absorption spectra were measured at the rear of the cell holder using an Ocean Optics Flame spectrometer with the light attenuated using a series of ND filters. Absorbance is monitored at 620 nm.

5.5.6 Method 2

Photocatalysts (*ca.* 11 mg) were added to an aqueous solution of MB (30 mL, 15 mg L^{-1} or 30 mg L^{-1}) and allowed to stir in the dark for 16 h. The samples were irradiated using a LED light source (5* CITIZEN LED block – fan cooled) placed 20 cm away from the stirring mixture. Aliquots (2 mL) of the homogenous mixture were removed periodically and stored in the dark to allow the photocatalyst to settle, before recording the UV-vis spectra. The absorbance was recorded at its maxima.

5.6 References

1. L. Sheeney-Haj-Ichia, B. Basnar and I. Willner, *Angew. Chem. Int. Ed.*, 2005, **44**, 78.
2. X. L. Li, Y. Jia, J. Q. Wei, H. W. Zhu, K. L. Wang, D. H. Wu and A. Y. Cao, *ACS Nano*, 2010, **4**, 2142.
3. T. Peng, P. Zeng, D. Ke, X. Liu and X. Zhang, *Energy Fuels*, 2011, **25**, 2203.
4. X. Wang, M. Liu, Q. Chen, K. Zhang, J. Chen, M. Wang, P. Guo and L. Guo, *Int. J. Hydrogen Energy*, 2013, **38**, 13091.
5. Y. K. Kim and H. Park, *Energy Environ. Sci.*, 2011, **4**, 685.
6. A. S. Pawar, S. S. Garje and N. Revaprasadu, *Mater. Chem. Phys.*, 2016, **183**, 366.
7. H. Y. Zhu, J. Yao, R. Jiang, Y. Q. Fu, Y. H. Wu and G. M. Zeng, *Ceram. Int.*, 2014, **40**, 3769.
8. H. B. Li, X. C. Gui, C. Y. Ji, P. X. Li, Z. Li, L. H. Zhang, E. Z. Shi, K. Zhu, J. Q. Wei, K. L. Wang, H. W. Zhu, D. H. Wu and A. Y. Cao, *Nano Res.*, 2012, **5**, 265.
9. L. L. Ma, H. Z. Sun, Y. G. Zhang, Y. L. Lin, J. L. Li, K. W. Y. Yu, Y. Yu, M. Tan and J. B. Wang, *Nanotechnology*, 2008, **19**, 115709.
10. C. S. Li, Y. P. Tang, B. N. Kang, B. S. Wang, F. Zhou, Q. Ma, J. Xiao, D. Z. Wang and J. Liang, *Sci. China Ser. E*, 2007, **50**, 279.
11. H. Kisch, *Semiconductor Photocatalysis*, John Wiley & Sons, Incorporated, Erlangen, Germany, 2014.
12. W. Hou, N. J. Zhao, D. Meng, J. Tang, Y. Zeng, Y. Wu, Y. Weng, C. Cheng, X. Xu, Y. Li, J. P. Zhang, Y. Huang, C. W. Bielawski and J. Geng, *ACS Nano*, 2016, **10**, 5189.
13. A. Hagfeldt and M. Gratzel, *Chem. Rev.*, 1995, **95**, 49.
14. C. L. Hu, Y. Wang, S. Y. Chen, H. Cheng, M. Lin, Y. F. Zhang, D. He, X. Q. Liu and J. Y. Liu, *RSC Adv.*, 2016, **6**, 78053.
15. U. Kang, S. K. Choi, D. J. Ham, S. M. Ji, W. Choi, D. S. Han, A. Abdel-Wahabe and H. Park, *Energy Environ. Sci.*, 2015, **8**, 2638.
16. G. A. Rance, W. A. Solomonsz and A. N. Khlobystov, *Chem. Commun.*, 2013, **49**, 1067.
17. S. J. Guo, X. L. Pan, H. L. Gao, Z. Q. Yang, J. J. Zhao and X. H. Bao, *Chem. Eur. J.*, 2010, **16**, 5379.
18. W. Chen, X. L. Pan, M. G. Willinger, D. S. Su and X. H. Bao, *J. Am. Chem. Soc.*, 2006, **128**, 3136.
19. W. Chen, Z. Fan, X. Pan and X. Bao, *J. Am. Chem. Soc.*, 2008, **130**, 9414.
20. D. Deng, L. Yu, X. Chen, G. Wang, L. Jin, X. Pan, J. Deng, G. Sun and X. Bao, *Angew. Chem. Int. Ed.*, 2013, **52**, 371.
21. M. Kahlweit, *Adv. Colloid Interface Sci.*, 1975, **5**, 1.
22. D. D. Chronopoulos, N. Karousis, S. Zhao, Q. Wang, H. Shinohara and N. Tagmatarchis, *Dalton Trans.*, 2014, **43**, 7429.
23. S. K. Sharma and R. Sanghi, *Advances in Water Treatment and Pollution Prevention*, Springer Netherlands, 2012.
24. J. Zhang, Y. Guo, H. Fang, W. Jia, H. Li, L. Yang and K. Wang, *New J. Chem.*, 2015, **39**, 6951.

25. X. Wang, H. Tian, Y. Yang, H. Wang, S. Wang, W. Zheng and Y. Liu, *J. Alloys Compd.*, 2012, **524**, 5.
26. V. V. Chagovets, M. V. Kosevich, S. G. Stepanian, O. A. Boryak, V. S. Shelkovsky, V. V. Orlov, V. S. Leontiev, V. A. Pokrovskiy, L. Adamowicz and V. A. Karachevtsev, *J. Phys. Chem. C*, 2012, **116**, 20579.
27. X.-b. Hu, Y.-h. Deng, Z.-q. Gao, B.-z. Liu and C. Sun, *Appl. Catal. B-Environ.*, 2012, **127**, 167.
28. S. Azevedo, J. R. Kaschny, C. M. C. de Castilho and F. D. Mota, *Eur. Phys. J. B*, 2009, **67**, 507.
29. F. K. Ma, G. Zhao, C. Li, T. L. Wang, Y. Z. Wu, J. X. Lv, Y. Y. Zhong and X. P. Hao, *CrystEngComm.*, 2016, **18**, 631.
30. Y. H. Li, S. G. Wang, Z. K. Luan, J. Ding, C. L. Xu and D. H. Wu, *Carbon*, 2003, **41**, 1057.
31. A. L. Rogach, A. Kornowski, M. Gao and A. Eychmuller, *J. Phys. Chem. B*, 1999, **103**, 3065.
32. A. Sabah, S. A. Siddiqi and S. Ali, *World Acad. Sci. Eng. Technol.*, 2010, **4**, 68.
33. S. Fang, M. Sun, Y. Zhou, Q. Liang, Z. Li and S. Xu, *J. Alloys Compd.*, 2016, **656**, 771.
34. B. Ahmed, S. Kumar, S. Kumar and A. K. Ojha, *J. Alloys Compd.*, 2016, **679**, 324.
35. A. Houas, H. Lachheb, M. Ksibi, E. Elaloui, C. Guillard and J. M. Herrmann, *Appl. Catal. B-Environ.*, 2001, **31**, 145.
36. C. A. Clark, University of Nottingham, 2013.
37. R. R. Nair, P. Blake, A. N. Grigorenko, K. S. Novoselov, T. J. Booth, T. Stauber, N. M. R. Peres and A. K. Geim, *Science*, 2008, **320**, 1308.
38. F. Bonaccorso, Z. Sun, T. Hasan and A. C. Ferrari, *Nat. Photonics*, 2010, **4**, 611.
39. C. Tang, J. Li, Y. Bando, C. Zhi and D. Golberg, *Chem Asian J*, 2010, **5**, 1220.
40. H. Xu, L. Liu, Y. Song, L. Huang, Y. Li, Z. Chen, Q. Zhang and H. Li, *J. Alloys Compd.*, 2016, **660**, 48.
41. X. Fu, Y. Hu, Y. Yang, W. Liu and S. Chen, *J. Hazard. Mater.*, 2013, **244**, 102.
42. X. L. Li, X. J. Wu, X. C. Zeng and J. L. Yang, *ACS Nano*, 2012, **6**, 4104.
43. A. C. Bevilacqua, C. J. Rupp and R. J. Baierle, *Chem. Phys. Lett.*, 2016, **653**, 161.
44. X. Cui, Y. Wang, G. Jiang, Z. Zhao, C. Xu, A. Duan, J. Liu, Y. Wei and W. Bai, *J. Mater. Chem. A*, 2014, **2**, 20939.

6. Concluding Remarks

As hollow, one-dimensional nanoscale materials, carbon nanotubes (CNT) offer the exciting opportunity to confine guest-species in the internal cavity, and thus study the structure, motion and dynamics of molecules in these nanosized test tubes. Moreover, the spatial restriction imposed inside CNT permits exploration of the templated transformations of guest-molecules into other, potentially more valuable nanoscale materials.

Whilst the properties of CNT as nano test tubes and reactors has been extensively investigated, the applications of the younger, isoelectronic and isostructural analogue boron nitride nanotubes (BNNT) has been comparatively unexplored to date. BNNT possess many of the attractive attributes as CNT, such as high mechanical, thermal and chemical stability, but also present new physicochemical properties, including transparency to visible light and modified interatomic bonding rendering BNNT electronically insulating. BNNT, therefore, offer an interesting host-structure for the formation of new composite materials with potentially enhanced properties, whilst also aiding the analysis of encapsulated guest-species through spectroscopic techniques unavailable for CNT equivalents.

The encapsulation of guest-species into BNNT requires the nanotubes to be open at the end tips and free from impurities which may block the internal channel. Reducing the length of BNNT is also expected to improve the filling efficiency of guest-species, since transport resistance has been shown in CNT to depend on nanotube length. Three classes of methods for treating as-received BNNT were systematically investigated and their effectiveness at opening, shortening and purifying the nanotubes appraised. It was determined that a strategy based on

hydrolysis, followed by high-temperature oxidation in air was most effective, yielding a BNNT material with 83 % of the nanotubes open, lengths of 0.55 ± 0.22 μm and a B:N ratio of 51:49. Thus, this method was applied for all subsequent experiments involving confinement of guest-species inside BNNT.

Following documented literature procedures for the formation of C_{60}@CNT 'peapods', molecules of C_{60}-fullerene were encapsulated within BNNT from the gas-phase. Careful TEM analysis indicated that the packing arrangements of the fullerenes inside BNNT were critically dependent on the nanotube diameter. Furthermore, IR spectroscopy established that the dynamic behaviour and temperature-controlled phase transitions of C_{60} were the same when encapsulated in BNNT as in the bulk crystal. The transformation of C_{60} into CNT at elevated temperature – templated by the internal dimensions of the thermally stable BNNT – resulted in the formation of an electronically conductive CNT confined within an electronically insulating BNNT. Dubbed the world's smallest co-axial cable, this fascinating hybrid nanoscale architecture is predicted to have a wealth of unique functional properties targeted at application such as nanoelectronics and sensing devices.

The encapsulation of photoactive nanoparticles of cadmium sulphide (so-called quantum dots) into both multi-walled carbon nanotubes (MWNT) and BNNT, by both liquid- and gas-phase insertion of cadmium and sulphur precursor molecules into the inner nanotube channels and subsequent confined reaction within the internal volume, was explored, yielding a series of materials to be applied as photocatalytic nanoreactors. Remarkably high filling rates (70 quantum dots per μm of MWNT) were achieved inside MWNT subject to extreme pre-treatment conditions

of oxidation prior to encapsulation. The quantum dots were found to be stabilised by ubiquitous van der Waals forces between host and guest, with nanoparticle dimensions strongly templated by the nanotube. Translation of this strategy to single-walled carbon nanotubes (SWNT, diameter 1.3 nm) was not possible, due to diameter-dependent limitations of access to the internal space by guest molecules and issues of bundling; larger diameter graphitised nanofibres (GNF, internal diameter 30-50 nm) could be filled with quantum dots, however, determination of their structural characteristics by electron microscopy was hampered by the large number of graphitic shells that comprise the external walls. Open and purified BNNT were successfully filled with quantum dots, but significant proportions of the photoactive materials remained deposited on the exterior surfaces (44 encapsulated inside, 33 on the external walls of BNNT per μm length). The templating effects of the nanotube were observed, resulting in the formation of anisotropic CdS quantum dots.

The composites of quantum dots and nanotubes – CdS@MWNT and CdS@BNNT – were then applied as photocatalysts for the degradation of methylene blue, a major source of water contamination from the textile industry. An additional photocatalyst, with cadmium sulfide formed on the surface of MWNT (CdS/MWNT), was also prepared as a control using closed MWNT in a route analogous to that used for the preparation of CdS@MWNT. The efficiency of the photocatalysts was then explored through two experimental designs and the activity determined. The most effective catalyst was CdS@BNNT, followed by CdS/MWNT, then CdS@MWNT, a result that has been correlated with the amount of light reaching CdS from the source.

In conclusion, this study has involved: (i) the development of novel procedures to open and purify BNNT and CNT, thus permitting the encapsulation of guest-species in the internal channel; (ii) exploration of the encapsulation, structural characteristics and thermal transformations of C_{60} molecules inside BNNT, ultimately yielding CNT@BNNT – a nanoscale co-axial cable; (iii) investigation of the confinement, structural attributes and photocatalytic properties of quantum dots of cadmium sulphide inside CNT and BNNT. The new discoveries reported in this thesis demonstrate the controlled formation and applications of innovative nanotube-based hybrid materials, and thus represent an important and substantial contribution to the field of nanomaterials. Moreover, the work described herein provides an essential founding for many areas of further research. As the production of BNNT inevitably improves, to yield BNNT with narrower and more controllable diameter distributions at a lower cost, the applications of BNNT are certain to expand. The route to open and purify BNNT established during these studies is expected to be transferable to BNNT prepared by other methods and therefore provides the opportunity for an almost unlimited number of materials to be confined within BNNT, studied and exploited at the nanoscale. Importantly, the formation of nanoscale co-axial cables needs to be further explored, with determination of the electronic properties absolutely essential if these materials are to be integrated into nanoscale electronic devices. Furthermore, demonstration of the ability of BNNT to act as photochemical nanoreactors, facilitating and controlling the confined reactions of guest-molecules driven by visible light inside this optically transparent host nanoscale reactor, warrants significant further investigation.